LBL-30074

Lawrence Berkeley Laboratory
UNIVERSITY OF CALIFORNIA

Materials & Chemical Sciences Division

Tunable Far Infrared Laser Spectroscopy of van der Waals Molecules in a Planar Supersonic Jet Expansion

K.L. Busarow
(Ph.D. Thesis)

December 1990

LOAN COPY
Circulates
for 4 weeks
Bldg. 50 Library.
LBL-30074
Copy 2

Prepared for the U.S. Department of Energy under Contract Number DE-AC03-76SF00098

DISCLAIMER

This document was prepared as an account of work sponsored by the United States Government. While this document is believed to contain correct information, neither the United States Government nor any agency thereof, nor the Regents of the University of California, nor any of their employees, makes any warranty, express or implied, or assumes any legal responsibility for the accuracy, completeness, or usefulness of any information, apparatus, product, or process disclosed, or represents that its use would not infringe privately owned rights. Reference herein to any specific commercial product, process, or service by its trade name, trademark, manufacturer, or otherwise, does not necessarily constitute or imply its endorsement, recommendation, or favoring by the United States Government or any agency thereof, or the Regents of the University of California. The views and opinions of authors expressed herein do not necessarily state or reflect those of the United States Government or any agency thereof or the Regents of the University of California.

LBL-30074

TUNABLE FAR INFRARED LASER SPECTROSCOPY OF VAN DER WAALS MOLECULES IN A PLANAR SUPERSONIC JET EXPANSION

Kerry Lynn Busarow

Department of Chemistry
University of California

and

Chemical Sciences Division
Lawrence Berkeley Laboratory
Berkeley, CA 94720 USA

December 1990

This work was supported by the Director, Office of Energy Research, Office of Basic Energy Sciences, Chemical Sciences Division, of the U.S. Department of Energy under Contract No. DE-AC03-76SF00098.

Tunable Far Infrared Laser Spectroscopy of Van Der Waals Molecules in a Planar Supersonic Jet Expansion

by

Kerry Lynn Busarow

Abstract

The gas phase high resolution spectroscopic study of weakly bound clusters can provide the information necessary to develop an intermolecular potential energy surface. This surface can then be used to better understand condensed phases. In this work, a tunable far infrared laser spectrometer is used to study weakly bound dimers produced in the newly developed continuous planar supersonic jet expansion apparatus.

The design and optimization studies of the planar jet apparatus will be discussed. This discussion will include the results from the first van der Waals system studied with this experiment, viz. the lowest Σ bend of ArHCl, which demonstrate the sensitivity and versatility of the experimental apparatus. The optimization studies indicate that using the available pumping system, the optimum nozzle length is 4 inches for a slit width of .001 - .003 inches.

The water dimer is an extensively studied hydrogen bonded dimer. It undergoes several tunneling motions which result in splittings and perturbations of the rovibrational energy levels. A review is presented of much of the experimental and

theoretical work done on water dimer, including a description of the combined fit of all the high resolution spectroscopic results by Coudert and Hougen. Also included is a discussion of the measurement of the K=1 lower → K=2 lower band performed using the tunable far infrared laser/planar jet apparatus.

The preliminary results from the study of $CH_4 \cdot H_2O$ will also be presented. $CH_4 \cdot H_2O$ is unique in that unlike a strongly anisotropic complex, such as the water dimer, the monomer subunits are nearly free internal rotors. Seven bands are observed which have very similar band origins and rotational constants. Two energy level diagrams are proposed which are strongly influenced by earlier ArH_2O studies. A brief qualitative discussion of the $CH_4 \cdot H_2O$ binding energy compared to that of ArH_2O is also included.

Acknowledgements

One thing that can be said about Berkeley is that it has never been boring. Berkeley has offered me so many opportunities that I would not have had elsewhere, including the chance to work with two excellent scientists. It has been a pleasure to work with Professor Yuan Lee. His ability and dedication astound me. He has always been very supportive through the lean and not so lean times. He is a marvelous teacher with a great sense of humor and not a bad softball player. Professor Richard Saykally also has a sense of humor, his is just much more twisted. As a chemist, he is never at a loss for new ideas. Experiments in the group tend to have a fairly short lifetime because he is always pushing them in new directions. He keeps the science at the cutting edge.

Being at Berkeley has also afforded me the opportunity to interact with great scientists from around the world. Two which deserve special thanks for their guidance are Dr. Jon Hougen and Dr. Jeremy Hutson. Both have contributed greatly to my understanding of weakly bound clusters.

One thing I learned early in my career is that the department of chemistry is blessed with excellent support facilities. The machine shop staff has been a tremendous help. Fred, Andy, George and Ron have always patiently given great advice to graduate students who know little of designing and even less of machining. The quality of the work has always been excellent, but unfortunately, too many take that for

granted. A special thank you also goes to Bob Dunn who has helped me out at 4:25 pm on numerous occasions.

Life at Berkeley has not always been easy for me. Fortunately, I have worked with many wonderful people who have helped me make it through. Between two research groups, over the course of more than six years, there are just too many people to mention. I cannot express my gratitude to everyone in just a few pages. Several people however, deserve special mention. Howard Nathel, Tim (Twellllve Hz) Minton, Rick (W.B.) Brudzynski, and Rob (Ex-G.H.) Continetti are great friends who, in my early years, showed me the ropes and sometimes how to get around them. They also taught me the proper vending technique. Pam Chu and Barb (Babs) Balko are special friends who have always been willing to listen. Another great listener (I need to talk alot) is Matt (Ah-nold) Côté. I probably could have finished a year earlier if these folks were not so willing to listen. Thanks also to Jim Myers for computer advice during this thesis time. To all the Lee group people, thanks for your help and guidance and for not looking too bored at my group meetings.

The majority of my time was spent working with the Saykally group. I learned so much from all of them, but probably the most important thing was that even though we were all very different people, our experiences together made us very close friends. Speaking of different, I shared my first office with Andy (Oreo) Cooksy and Mike (Sparky) Radunsky. I

Acknowledgements

One thing that can be said about Berkeley is that it has never been boring. Berkeley has offered me so many opportunities that I would not have had elsewhere, including the chance to work with two excellent scientists. It has been a pleasure to work with Professor Yuan Lee. His ability and dedication astound me. He has always been very supportive through the lean and not so lean times. He is a marvelous teacher with a great sense of humor and not a bad softball player. Professor Richard Saykally also has a sense of humor, his is just much more twisted. As a chemist, he is never at a loss for new ideas. Experiments in the group tend to have a fairly short lifetime because he is always pushing them in new directions. He keeps the science at the cutting edge.

Being at Berkeley has also afforded me the opportunity to interact with great scientists from around the world. Two which deserve special thanks for their guidance are Dr. Jon Hougen and Dr. Jeremy Hutson. Both have contributed greatly to my understanding of weakly bound clusters.

One thing I learned early in my career is that the department of chemistry is blessed with excellent support facilities. The machine shop staff has been a tremendous help. Fred, Andy, George and Ron have always patiently given great advice to graduate students who know little of designing and even less of machining. The quality of the work has always been excellent, but unfortunately, too many take that for

granted. A special thank you also goes to Bob Dunn who has helped me out at 4:25 pm on numerous occasions.

Life at Berkeley has not always been easy for me. Fortunately, I have worked with many wonderful people who have helped me make it through. Between two research groups, over the course of more than six years, there are just too many people to mention. I cannot express my gratitude to everyone in just a few pages. Several people however, deserve special mention. Howard Nathel, Tim (Twellllve Hz) Minton, Rick (W.B.) Brudzynski, and Rob (Ex-G.H.) Continetti are great friends who, in my early years, showed me the ropes and sometimes how to get around them. They also taught me the proper vending technique. Pam Chu and Barb (Babs) Balko are special friends who have always been willing to listen. Another great listener (I need to talk alot) is Matt (Ah-nold) Côté. I probably could have finished a year earlier if these folks were not so willing to listen. Thanks also to Jim Myers for computer advice during this thesis time. To all the Lee group people, thanks for your help and guidance and for not looking too bored at my group meetings.

The majority of my time was spent working with the Saykally group. I learned so much from all of them, but probably the most important thing was that even though we were all very different people, our experiences together made us very close friends. Speaking of different, I shared my first office with Andy (Oreo) Cooksy and Mike (Sparky) Radunsky. I

think it took Andy a little while to get used to us. But then he is quite the character himself. Hey Andy, I found a four year old, smashed oreo in a calculator case when I was cleaning out my desk.

The older folks in the group, (I thought they were old at the time) were some of the greatest teacher I've ever had. Doug, Ruth, Chris, Susan, and Neil were a great help. I'm going to miss the science discussions/arguments that went on in the offices. I think Chris was responsible for many of them. Neil (still the world's strongest spectroscopist) has a great sense of humor, is always good for moving heavy equipment, and is smart, too. I used to smile when I heard Susan talking to her computer. Now I have to chuckle when I catch myself doing it. Ruth deserves extra credit, for what that's worth, for helping me through some tough times. I look forward to sharing the challenges ahead. Jeff Owrutsky taught me the important lesson that first impressions aren't always correct. Actually he taught me alot about life, including how to eat with chopsticks. It was either learn or go hungry.

As for my experiment, I've worked with a great bunch of people. Ken Laughlin and Geoff Blake built a fantastic laser that almost made data collection easy. Ken (the original -Bob) has an incredible calm, patient nature, except where sports are concerned. He's a great teacher. Geoff is the type of guy who can really make things happen. As for Ron Cohen, we've been through it all together. From exploding CO_2 power

supplies, to mixing our own cylinders, to Wasco, CA, to collecting lots of data, it's been great, hasn't it? I have great expectations for Ron, there's no stopping him. There are also a number of people who helped out on the experiment including Martina Havenith, Gwo Dz-Hung, Bill Chapman, Jenny Loeser and Dave Steyert. The recent additions to the experiment include Charlie Schmuttenmaer and Nick Pugliano. I've learned from Charlie that when something doesn't work, there's always something else to try. He also deserves a thank you for helping the computer illiterate among us. Nick always has a positive outlook on science and life. I've learned much more than chemistry from these people.

Then there's the rest of the group. They have been great friends. Eric R. Keim has been a terrific office mate. He listens patiently to all of my stories, sometimes two or three times. Mark Polak and Martin Gruebele, those two names will always go together, are both too smart for their own good. Fortunately, they were not only smart, but funny too.

There have been a number of great postdocs in the group, who bring with them a different perspective and always manage to get a lot done in a short time. Les (*.*) Tack brought the Australian perspective, ah-yeah. Jim Coe and Jim Heath have taught us all a great deal and are great for more of those discussions/arguments.

Then there are the young kids, who come along and remind me of how and cynical I am getting. They also remind me that

I've learned a great deal in my time here (PVC machining, pump oil maintenance, etc.) and I enjoy sharing with them, but they all seem to catch up so quickly. Thanks to Jim Lundberg, Bruuuuce DeKock, Nike Agman, Dave Steyert, Roger Sheeks, Dave Cook, Dave Hecht, Matt Elrod, Jim Scherer, and Jeff (J) Rzepiela. (I can spell it correctly, now if you would only say it right).

Also a very sincere thank you goes to the only person left around here who is older than me, Brent Wurfel. If he hadn't been so willing to commiserate with me about thesis writing, I would have definitely beat him. Thanks for keeping my attitude in line.

I must also thank Cheryn Gliebe and Ann Weightman for help and advice, particularly in these last few crazy weeks.

I want to also thank my undergraduate professors, Dr. Jim Davidson and Prof. Nelson Sartoris. Their encouragement and teaching are what got me to Berkeley in the first place. Do I thank them or what?

Probably the smartest thing I did while in graduate school was get up the nerve to call Jeff. We have been through so much together and he's been there for me all the way. I'm looking forward to the challenges ahead, knowing you'll be there. I also want to thank the whole Cogen clan for all their support in our endeavors.

Lastly, I have to thank my parents and family, particularly my father, who taught me everything I know about

chemistry. My family has always been so supportive and when life in Berkeley got a little crazy, they always put things back in perspective.

I also acknowledge the support of the Director, Office of Basic Energy Sciences, Chemical Sciences Division of the U.S. Department of Energy under Contract Number DE-AC03-76SF00098.

For my parents

Table of Contents

Acknowledgements ii

Chapter 1 Introduction 1

Chapter 2 Development of the Planar Supersonic Jet Expansion

2.1 Cluster Spectroscopy in Supersonic Jet Expansions 8

2.1.1 Circular Nozzles 11

2.1.2 Planar Jet Development 14

2.1.2.1 Campargue-type Sources 16

2.2 Spectroscopy in Planar Jets 17

2.3 The Advantages of Planar Jet Expansions 20

2.4 Initial Nozzle Design 25

2.5 The Far Infrared Laser 32

2.5.1 FM Advantage 37

2.6 First Planar Jet Results-H_2S Line Narrowing 38

2.7 The Lowest Σ Bend of ArHCl 41

2.8 Optimization of the Nozzle Design 50

2.9 Conclusion 66

Chapter 2 References 69

Chapter 3 The Water Dimer

3.1 Introduction 73

3.2 Early Experiments 74

3.2.1 Second Virial Coefficients and Thermal

Conductivity 75
3.2.2 Matrix Isolation Technique 81
3.2.3 Molecular Beam Elastic Scattering Measurements 83
3.2.4 Fourier Transform Far Infrared Studies ... 86
3.2.5 Mass Deflection and Initial Microwave Studies 88
3.2.6 Infrared and Coherent Anti-Stokes Raman Spectra 94
3.3 Theoretical Approach to Structure and Potential Surface Determination 97
3.3.1 Structural Determination 98
3.3.1.1 Variational Techniques 99
3.3.1.2 Perturbational Techniques 105
3.3.2 Potential Surfaces 106
3.3.3 Structure of the Trimers and Larger Polymers of Water 114
3.4 Group Theory and Energy Level Diagram 115
3.4.1 Molecular Symmetry 116
3.4.2 Tunneling Paths 135
3.4.2.1 Deuterated Forms of the Water Dimer 146
3.4.3 High Resolution Spectroscopic Studies 148
3.4.4 The Fit of the Spectroscopic Results 166
3.4.4.1 IAM versus PAM 167
3.4.4.2 The Local Internal Axis Method 170

3.5 Future Studies of Water Polymers 178

3.5.1 The Water Dimer Vibrational Spectra 179

3.5.2 The Water Trimer and Larger Polymers 185

3.6 Conclusion 194

Chapter 3 References 198

Chapter 4 The Far Infrared Spectrum of $CH_4 \cdot H_2O$

4.1 Introduction 207

4.2 Lines Observed in a Methane-Water Expansion 208

4.3 The Proposed Energy Level Diagrams 212

4.3.1 The Pure Rotational Spectra for Water and Methane Monomers 213

4.3.2 The ArH_2O Spectrum 217

4.3.3 Comparing ArH_2O to $CH_4 \cdot H_2O$ Spectra 223

4.3.4 Hund's Coupling Cases for Diatomic Molecules 233

4.3.4.1 Hund's Case (a) Energy Level Diagram 239

4.3.4.2 Hund's Case (b) Energy Level Diagram 244

4.3.5 Comparison of the Case (a) and Case (b) Predicted Spectra 246

4.3.5.1 The Case (a) Spectrum 246

4.3.5.2 The Case (b) Spectrum 249

4.4 The Binding Energy of $CH_4 \cdot H_2O$ 253

4.5 Discussion 259

4.6 Conclusion 263

Chapter 4 References 265

Appendix A ArHCl Publications 267

Appendix B Water Dimer Publication 280

Appendix C Unassigned Lines in an Argon/Water Expansion 288

Chapter 1 Introduction

The focus of this thesis is the experimental characterization of intermolecular forces through the study of weakly bound (≤5 kcal/mol) dimer complexes. These weakly bound systems serve as prototypes for condensed phase interactions. To begin to understand the condensed phases, one should first thoroughly understand the corresponding dimer potential surface. Therefore the goal is to collect and interpret the high resolution spectrum of these complexes and to use these results to determine the intermolecular potential energy surface.

The complexes considered in this thesis can be categorized into two groups: van der Waals and hydrogen bonded systems. Van der Waals clusters are generally quite weakly bound. Typically, bond energies are less than 1 kcal/mol (~350 cm^{-1}). Neutral hydrogen bonded clusters are bound by as much as 5 kcal/mol (~2000 cm^{-1}). Still, compared to normal chemical bond energies, which are often 50-100 kcal/mol, both of these clusters are quite weakly bound. As examples, ArHCl is a very thoroughly studied van der Waals complex bound by 0.5 kcal/mole (180 cm^{-1}).[1] The water dimer, $(H_2O)_2$, a hydrogen bonded complex is bound by approximately 5 kcal/mol. There are three different types of attractive forces which can lead to this low energy binding. The first is electrostatic, in which permanent moments on the monomers interact, e.g. dipole-dipole or dipole-quadrupole. This type of interaction cannot occur in

ArHCl. The second type of force is induction, in which the permanent moment on one monomer induces a moment on the other monomer and these moments interact, e.g. dipole-induced dipole. The third force is dispersion, which can be described as the interaction of the instantaneous moments on each monomer. In many cases, the dispersion contribution is the largest, as in the ArHCl case. The water dimer is actually one of the few systems in which the electrostatic contribution is larger than the dispersion term. The induction term is always the smallest contribution.

In the past decade there has been a dramatic increase in the amount of high resolution spectroscopic results available for weakly bound complexes. An enormous number of complexes have been studied using various microwave techniques. The details of these methods will be discussed in Chapter 3, in context with the water dimer work. Microwave techniques provide high resolution and high sensitivity, but are generally limited to the lowest few rotational levels of the ground vibrational state, assuming the clusters are formed in a cold supersonic expansion, as is typically the case. Therefore, microwave results alone can only provide information about a small region near the potential minimum. Quite a few complexes have been studied using various infrared techniques. These spectra are typically combination bands of some high frequency monomer vibration and a low frequency van der Waals vibration. These techniques often allow for the

measurement of several such combination bands rather quickly and provide a good overview of the spectroscopy, although the resolution is generally lower. It is also difficult to extract ground state information from combination bands, because the high frequency vibration can greatly perturb the potential surface. In favorable cases, hot bands of the van der Waals modes can be observed, thus enabling the ground state potential energy surface to be sampled. In the far infrared, the low frequency vibrations or tunneling splittings are probed directly. Because the far infrared can probe many of the low frequency bands, a much larger region of the potential surface is sampled and an accurate ground state potential surface can be determined from these results alone, as in the cases of ArHCl[1] and ArH_2O.[2] Far infrared techniques have been applied less frequently until recently because the experimental difficulties were incapacitating. However, since the advent of tunable far infrared laser techniques, a number of important complexes have been investigated.

The ideal method for generating a high density of weakly bound clusters is to use a supersonic jet expansion in which gas is rapidly expanded through a small nozzle and extensive cooling is achieved in all the degrees of freedom. This cooling not only facilitates the formation of these weakly bound complexes, but also greatly simplifies the spectra because only a small number of vibrational and rotational states will have significant population to be observed.

Chapter 2 will discuss the advances made in our lab in combining the recently developed tunable far infrared laser with a planar supersonic jet expansion. This experiment proved to be extremely successful. Many clusters have now been studied by this method, including ArHCl[3], $(HCl)_2$[4], $ArNH_3$[5], $(NH_3)_2$[6], ArH_2O[7], $(H_2O)_2$[8], $H_2O \cdot CO$[9], and $CH_4 \cdot H_2O$.[10] Our study of the lowest Σ bend of ArHCl will be discussed in detail to demonstrate the advantages of this system over other techniques. The design and testing of the planar jet will also be discussed. The laser system will only be briefly described as it has been thoroughly discussed elsewhere.[11]

Chapter 3 is essentially a review of all of the work that has been done on the water dimer, both theoretical and experimental, with emphasis placed on our far infrared measurement of the $K_a=2\leftarrow1$ $A_2^{\pm}/B_2^{\pm}$ transitions of the ground vibrational state. The dimer spectrum is very unique, complicated by a number of feasible tunneling motions which result in splittings and perturbations of the rotational levels. Understanding of the spectroscopic results came through the combined efforts of a number of theoretical and experimental groups led by J.T. Hougen and his approach to fitting all of the spectroscopic results.

Chapter 4 focusses on the preliminary results we have obtained for the $CH_4 \cdot H_2O$ complex. It is assumed that this spectrum is similar to ArH_2O, which has been studied in our lab[7], however, $CH_4 \cdot H_2O$ will be complicated by the additional

angular momentum associated with the CH_4 rotation. Two energy level diagrams are proposed in an attempt to understand the fairly complex spectra obtained. Although much work remains to be done, this complex should provide some important clues toward understanding hydrophobic interactions.

Chapter 1 References

1. J.M. Hutson, J. Chem. Phys. **89**, 4550 (1988).

2. R.C. Cohen and R.J. Saykally, J. Phys. Chem. **94**, 7991 (1990).

3. K.L. Busarow, G.A. Blake, K.B. Laughlin, R.C. Cohen, Y.T. Lee, and R.J. Saykally, Chem. Phys. Lett. **141**, 289 (1987); K.L. Busarow, G.A. Blake, K.B. Laughlin, R.C. Cohen, Y.T. Lee, and R.J. Saykally, J. Chem. Phys. **89**, 1268 (1988).

4. G.A. Blake, K.L. Busarow, R.C. Cohen, K.B. Laughlin, Y.T. Lee, and R.J. Saykally, J. Chem. Phys. **89**, 6577 (1988); G.A. Blake and R.E. Bumgarner, J. Chem. Phys. **91**, 7300 (1989).

5. D.H. Gwo, M. Havenith, K.L. Busarow, R.C. Cohen, C.A. Schmuttenmaer, and R.J. Saykally, Mol. Phys., in press.

6. M. Havenith, R.C. Cohen, K.L. Busarow, D.H. Gwo, and R.J. Saykally, submitted to J. Chem. Phys.

7. R.C. Cohen, K.L. Busarow, K.B. Laughlin, G.A. Blake, M. Havenith, Y.T. Lee, and R.J. Saykally, J. Chem. Phys. **89**, 4494 (1988); R.C. Cohen, K.L. Busarow, Y.T. Lee, and R.J. Saykally, J. Chem. Phys. **92**, 169 (1990).

8. K.L. Busarow, R.C. Cohen, G.A. Blake, K.B. Laughlin, Y.T. Lee, and R.J. Saykally, J. Chem. Phys. **90**, 3937 (1989).

9. R.E. Bumgarner, S. Suzuki, P.A. Stockman, P.G. Green, and G.A. Blake, Chem. Phys. Lett., submitted.

10. R.C. Cohen, K.L. Busarow, C.A. Schmuttenmaer, and R.J.

Saykally, manuscript in preparation.

11. K.B. Laughlin, Ph.D. Dissertation, University of California, Berkeley, 1988.

Chapter 2 Development of the Planar Supersonic Jet Expansion

2.1 Cluster Spectroscopy in Supersonic Jet Expansions

The amount of literature written on supersonic jet expansions is very extensive.[1] Supersonic jets are routinely incorporated into many different experiments. The advantages are well known. In the isentropic expansion of a high pressure gas through a small nozzle, the gas is extensively cooled. This initial translational cooling is then transferred to the rotational and vibrational degrees of freedom. Typical temperatures obtained in an argon expansion are <1K for the translational temperature, between 1 and 5K for the rotational temperature, and generally less than 50K for the vibrational temperature. Of course, these temperatures are going to depend on the system studied, particularly the vibrational temperature, because cooling is facilitated by low energy vibrations. From a spectroscopic standpoint, the jet provides isolated gas phase molecules with greatly simplified spectra due to the rotational and vibrational cooling. Also, unlike a sample cooled cryogenically with liquid nitrogen or helium, there is typically very little condensation which occurs, particularly in seeded jets, in which the molecule of interest is diluted with a carrier gas such as helium or argon.

Although these jets have been studied for many years by those interested primarily in fluid mechanics or non-equilibrium behavior, it was only within the last fifteen years that these jets were utilized in spectroscopic studies,

particularly for the study of weakly bound complexes. The primary shortcomings of the supersonic jet are that the gas density is very low and the pathlength very short. The sensitivity required in such an experiment is quite high. It is therefore not surprising that the earliest spectroscopic results were obtained using very sensitive, indirect methods, such as laser induced fluorescence[2] and mass detection techniques, such as molecular beam electric resonance (MBER)[3]. This method will be discussed in Chapter 3. Later experiments placed the supersonic jet within the laser cavity, again providing a very sensitive detection method.[4] Direct absorption methods are generally much less sensitive and were only used in ideal cases.[5]

In an attempt to overcome this shortcoming, Jortner and coworkers developed a planar or slit jet to increase the length of the interaction region.[6] This approach, however, presents the new complication that large vacuum pumps are required to maintain the low pressure needed in the chamber. The first slit experiments were pulsed experiments. The advantage being that the gas load is smaller than in a continuous experiment, and also, the pulsed jet provides a detection scheme which incorporates background subtraction, and therefore, higher sensitivity. These pulsed experiments will be discussed in greater detail in Section 2.2. Our experiment was the first to use a continuous planar jet source. The large pumping requirements were met using very

large mechanical pumps. The advantage in using the continuous source is that when the laser is also continuous, the scanning time is greatly reduced. Also, the overall experimental operation is much simpler. It was also determined that these slit jet experiments, both pulsed and continuous, offered a number of other advantages over the circular nozzles, including decreased linewidths, slower cooling rates, slower drop in density, and therefore an increase in weakly bound cluster formation. All of these advantages will be discussed in Section 2.3.

The primary purpose of our experiments was to investigate weakly bound clusters, van der Waals and hydrogen bonded systems, using the continuous planar jet as a source, and the recently developed tunable far infrared laser sideband system as the means of probing these clusters. The far infrared laser allowed for the direct observation of the low frequency vibration and tunneling motions expected for these weakly bound species. In a typical chemically bound molecule, with binding energies between 50 and 100 kcal/mole, vibrational frequencies are several thousand wavenumbers. In ArHCl, on the other hand, the binding energy is approximately .5 kcal/mole and vibrations are at 20-35 cm^{-1}. The far infrared system routinely operates between 15 and 80 cm^{-1}. The spectrum obtained for ArHCl using this method will be thoroughly discussed in Section 2.7. The combination of the tunable far infrared laser and the planar jet expansion proved to be an

extremely successful method of studying clusters.

In this chapter, the development of the planar jet coupled with the tunable far infrared (TuFIR) laser system will be discussed. A background on circular and planar jet expansions will be given followed by a discussion of our first successful van der Waals cluster study, the Σ bend of ArHCl. The last sections discuss a number of experiments directed toward optimizing the planar jet design as well as ideas for further possible improvements.

2.1.1 Circular Nozzles

As was mentioned previously, there has been a great deal written about supersonic jets and it is unnecessary to go into great detail here. Some of the basic characteristics of the circular nozzle will be discussed briefly only to simplify the comparison with the planar nozzle. As a high pressure gas, typically one to several atmospheres, is expanded through a small circular nozzle (1 mm diameter or less), the random motion associated with the gas is converted to directed motion and the gas is cooled. This process requires energy. As the molecules move through the nozzle, they undergo two-body collisions. The molecules are all moving in approximately the same direction and therefore collisions occur at relatively low energy. These low energy collisions result in the efficient transfer of energy among the molecules. In a supersonic expansion, the Knudsen number, Kn, which is the

ratio of the mean free path behind the nozzle to the nozzle diameter, is much less than 1. This implies that as the molecules travel through the nozzle they undergo a large number of collisions and cool. In the case where Kn>1, the flow is effusive, the molecules undergo few if any collisions, do not cool, and essentially move independently. The translational temperature associated with the gas is determined by the width of the velocity distribution. In the limit of an infinite number of collisions, all of the molecules would have the same velocity. Therefore the velocity distribution would be infinitely narrow and the temperature would be zero. However, because the amount of random or thermal energy available in the expanding gas is finite, this cooling process cannot go on indefinitely. Eventually, the density drops to the point where no more collisions occur and the terminal temperature is reached. This terminal temperature depends on the ratio of the pressure behind the nozzle to the pressure outside the nozzle, the nozzle diameter, and the type of gas being expanded (monatomic, diatomic, or large polyatomic).

Figure 2.1 is a diagram which shows the different regions of the jet. The pressure behind the nozzle is referred to as the stagnation or backing pressure. The pressure in the region outside the nozzle and outside of the expansion itself will be referred to simply as the chamber pressure. When the ratio of the backing pressure to the chamber pressure is high, this is

Figure 2.1 A circular nozzle supersonic expansion

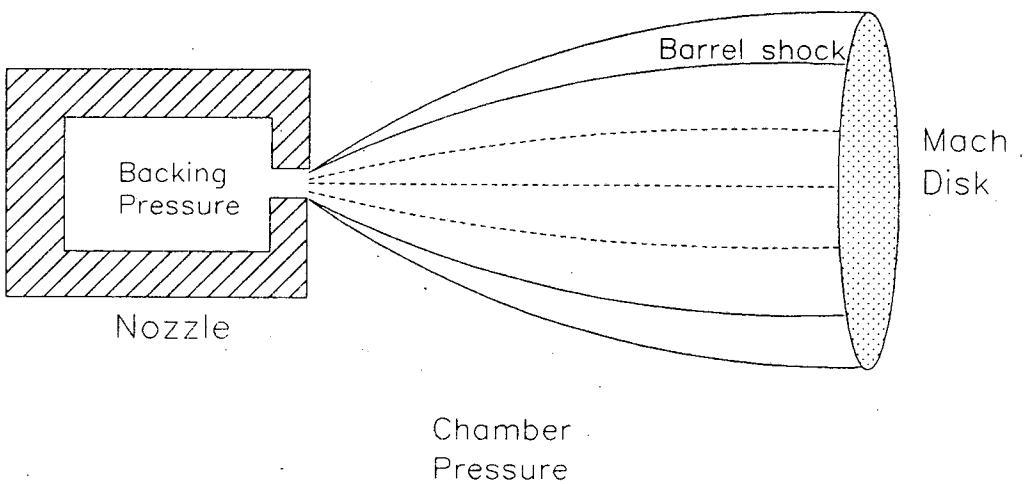

referred to as a hard expansion. The harder the expansion, the colder it tends to get and the expansion process continues further downstream, before the Mach disk appears. The Mach disk is that point along the expansion where the density becomes too low to prevent the warm background gas from entering the jet and heating it up. The distance to the Mach disk can be calculated from the simple formula

$$X_M = 0.67 d \sqrt{\frac{P_B}{P_0}}, \qquad (2.1)$$

where X_M is the distance of the Mach disk from the nozzle, P_B is the backing pressure, P_0 is the chamber pressure, and d is the nozzle diameter. The barrel shock is the boundary region on the edges of the expansion. Both the Mach disk and the barrel shock are discontinuities in the flow and act as boundary layers between the cold expansion and the warm static gas in the chamber.

2.1.2 Planar Jet Development

The initial goal of this project was to develop a source of weakly bound clusters which could be probed spectroscopically. The approach was directed toward designing a planar or slit supersonic expansion, which unlike a pinhole expansion, would provide a long pathlength for observing the clusters. Most of the work on planar nozzles existing at the time these experiments were designed incorporated huge wind tunnels to pump these large jets. The planar nozzles under

development by several groups were pulsed systems, in which the gas load would be sufficiently limited so that large diffusion pumps could be used to maintain the low pressures typically used in molecular beam experiments, roughly 10^{-4} torr. Our approach was to build a much simpler continuous nozzle and operate at a much higher chamber pressure, generally several hundred millitorr. The advantage of working at high chamber pressures was that it was possible to incorporate lower speed mechanical pumps which are simpler to operate and also support a much larger gas throughput. The difficulty with the planar nozzle is that the gas load is much higher than the circular nozzle. To maintain the same chamber pressure, the pumps must be able to accommodate this large gas load increase.

The throughput of a system is the product of the pumping speed and the pressure at the point where the pumping speed is measured. Therefore, to accommodate a moderate increase in the throughput of a factor of ten, the pumping speed must be increased proportionately, or the pressure must be ten times higher. Let us consider as an example the operating conditions of the molecular beam laser electric resonance experiment previously used in our group. Typically a 50 μm circular nozzle was run with approximately 6 atm backing pressure. The chamber was pumped by a 5300 l/sec diffusion pump and the pressure was maintained at 10^{-4} torr.[7] Although diffusion pumps are generally very high speed pumps, a factor of ten increase

would represent a sizable investment, both in cost and rebuilding time, assuming a large enough pump could be found. Simply increasing the chamber pressure by a factor of ten is also not feasible because the range over which the diffusion pump efficiently operates is limited, and at 10^{-3} Torr, the pumping speed is greatly reduced. One possible approach is to operate the system in a pulsed mode and decrease the duty cycle by a factor of ten, making it possible for the existing pump to maintain the low pressure. However, that translates to scanning times which are ten times as long. A different approach is to use large mechanical pumps, viz., Roots blowers, which have a much smaller pumping speed. Generally the largest Roots blowers have speeds approaching 2000 l/sec, however, these pumps can operate up to approximately 1 Torr. Therefore, although the Roots pump is at least ten times slower, the chamber pressure can easily be 1000 times higher giving a factor of 100 in increased throughput.

2.1.2.1 Campargue-type Sources

The idea that a nozzle would work effectively even in a high pressure chamber was strongly supported by Campargue and others in the early 1960's.[8] Campargue demonstrated that as the jet expanded into the high pressure chamber, the Mach disk and barrel shock would form, and contained inside of these shock boundaries was a cold expansion of particles unperturbed by the warm background gas. This region is referred to as the

"zone of silence". However, at that time, nearly all of the applications of supersonic jets were in the generation of skimmed molecular beams. A molecular beam is differentiated from a supersonic or free jet by the use of one or more skimmers or small apertures which transmit only the central portion of the jet. This provides a very narrow jet, eliminating the strongly divergent molecules from the beam and serves to create a nearly monoenergetic, low density, low throughput beam of particles. For a crossed beam scattering experiment, this type of beam is ideal because collision energies are well determined by the narrow velocity distribution. These types of experiments simply do not require these large throughput sources. Also, there was some concern regarding the difficulty in skimming a Campargue source, although Campargue demonstrated that it was fairly straightforward to position the skimmer. The concept was simply not widely considered. For molecular beam applications the concept of the Campargue source was not crucial, but in the case of a large throughput continuous planar jet, in which velocity distributions and skimmers are not considered, the Campargue concept is invaluable.

2.2 Spectroscopy in Planar Jets

The first spectroscopic results obtained using a planar supersonic expansion were performed by Amirav, Even, and Jortner in 1981.[6] They did both direct absorption and laser

induced fluorescence experiments of large organic molecules (aniline and 9,10-dichloroanthracene). The cold jet greatly reduced the complex spectra expected for such large systems and the planar jet afforded them the necessary pathlength to observe the absorption signal. This planar jet was pulsed for several reasons. The first and foremost is that the 35mm long by 0.2mm wide nozzle would require very large pumps if run continuously. Also, a pulsed nozzle can be run at higher backing pressures giving a higher density gas pulse, as opposed to a lower density, constant gas flow. The pulsed scheme also allows for boxcar detection and background subtraction, providing higher experimental sensitivity.

The Jortner pulsed source is quite unique. It consists of two rotating, concentric tubes, each with a 35 by 0.2mm slot cut into them. As one cylinder rotates, the slots align and a gas pulse is formed. The nozzle can also be heated to 200°C, which is important for maintaining an adequate vapor pressure of some large molecules. The nozzle runs at 12 Hz with a 150 μs pulse width. Two mechanical pumps were used with a combined pumping speed of 700 l/min. The nozzle was run with a backing pressure of only 76 torr and the Mach disk was 20mm from the nozzle. This design has two disadvantages. One is that it is extremely difficult to maintain a good seal and the nozzle tends to leak. Also, this rotating cylinder design results in a gas pulse throughout which the nozzle width is constantly changing. Only at the midpoint of the pulse is the nozzle

fully open. Therefore, the nozzle may be difficult to characterize. In a cluster experiment, wherein the cluster concentration may be very dependent on the nozzle width, it is likely that the cluster concentration would vary throughout the pulse.

Veeken and Reuss developed a pulsed, planar nozzle to study linewidths and cluster formation.[9] The nozzle itself was 9.0 mm in length and 0.10 mm wide with a throat depth of 0.1 mm. The nozzle is pulsed at ≤5 Hz by an air-driven piston. The purpose of this work was not to develop an ideal nozzle source for spectroscopic studies, but rather to gain a better understanding of planar sources. Some of their results will be discussed in later sections.

A very successful pulsed, planar nozzle developed by Lovejoy and Nesbitt[10] is similar to the design used in commercially available pulsed circular nozzles. This nozzle features of a solenoid which pulls the nozzle poppet back and opens the nozzle and a spring which closes the valve when the solenoid is shut off. The nozzle is 0.5" long and can run with pulses 150-600 μsec in duration with a repetition rate of up to 60 Hz. The valve is sealed with a piece of o-ring material attached to the poppet which seats against an electric discharge machined (EDM) knife edge on the inner side of the nozzle. Nozzle plates are attached to the front of the nozzle to define the slit dimensions. The nozzle is typically run with 1-2 atm behind the nozzle and a chamber pressure of $\leq 10^{-3}$

torr, pumped by a diffusion pump. In later studies, a Roots blower was incorporated into the system which allows higher stagnation pressures to be used. This is particularly useful for attempting to study clusters larger than dimers. This nozzle has been used for many different cluster studies in the infrared region.[11] Of the pulsed nozzles discussed, this is by far the best designed.

2.3 The Advantages of Planar Jet Expansions

The fundamental advantage of the planar jet is that it provides a long pathlength compared to the circular nozzle. An additional advantage that was predicted and later proven in a number of experiments, is the reduction in linewidths observed due to the reduction in the velocity components perpendicular to the expansion. In Figure 2.2 are simple outlines of a circular jet and a planar jet expansion, including a probe laser directed perpendicular to the nozzle flow and in the plane of the expansion in the case of the planar jet. In the case of the circular nozzle, it is clear that most of the molecules have a substantial velocity component parallel to the laser resulting in significant Doppler broadening. In infrared experiments the Doppler broadening is typically what limits the peak widths. In the planar jet however, because the molecules on the outside of the jet tend to confine the inner molecules, the overall divergence and therefore the Doppler broadening is significantly reduced. In other words, the bulk

Figure 2.2 Outlines of the circular and planar jet expansions

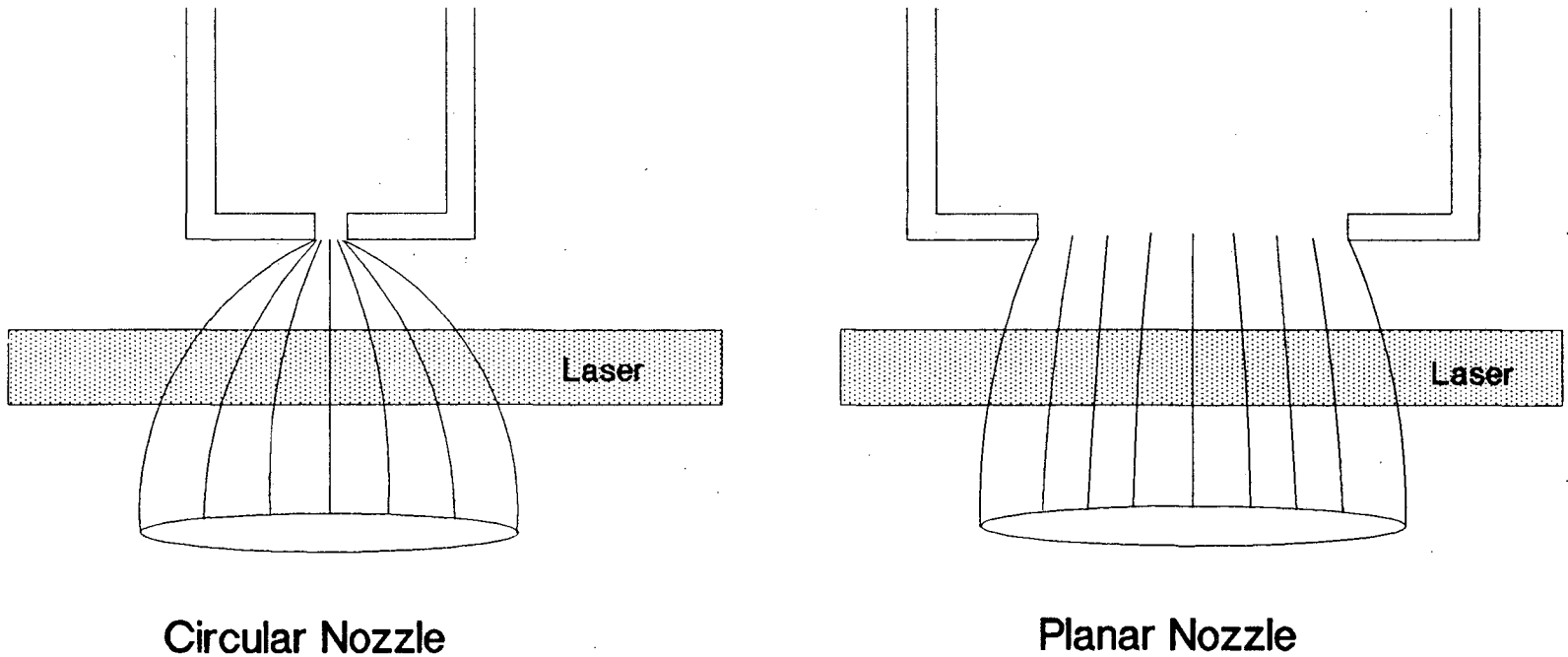

of the absorbing molecules are confined by the molecules further out and are unable to diverge strongly. In the limit of an infinitely long nozzle, the divergence would be zero. Veeken and Reuss[9] measured a CO_2 absorption in a low pressure cell, a circular nozzle, and a 4.4mm planar nozzle. The narrowest lines were obtained with the planar nozzle, the broadest lines were obtained with the circular nozzle, and the gas cell was in between the two. Their observed linewidths are shown in Figure 2.3.

This line narrowing has been observed in many experiments, including our own. From Demtröder[12], one can calculate the expected Doppler broadening expected for a low pressure gas cell

$$\delta\nu_D = 7.16\times10^{-7}\nu_0\sqrt{\frac{T}{M}}$$

knowing the absorber molar mass, M(g), the temperature, T(K), and the absorption frequency, ν_0(Hz). At room temperature, for an ArHCl line at 34 cm^{-1}, the Doppler broadening should be 1.4 MHz. Typical linewidths are 400 kHz (FWHM) in our 1½" planar expansion using argon as the carrier gas. Helium expansions tend to be more divergent and will give a larger Doppler broadening.(Figure 2.4) The Doppler narrowing results obviously in an increased experimental resolution. In a number of experiments, we were able to resolve nuclear quadrupole hyperfine splittings which would have been unobservable without this narrowing. Also, more importantly, as an

Figure 2.3 The linewidths measured for a CO_2 absorption in (a) a low pressure gas cell, (b) a circular nozzle, and (c) a 4.4 mm planar nozzle. This figure is taken from Veeken and Reuss.[9]

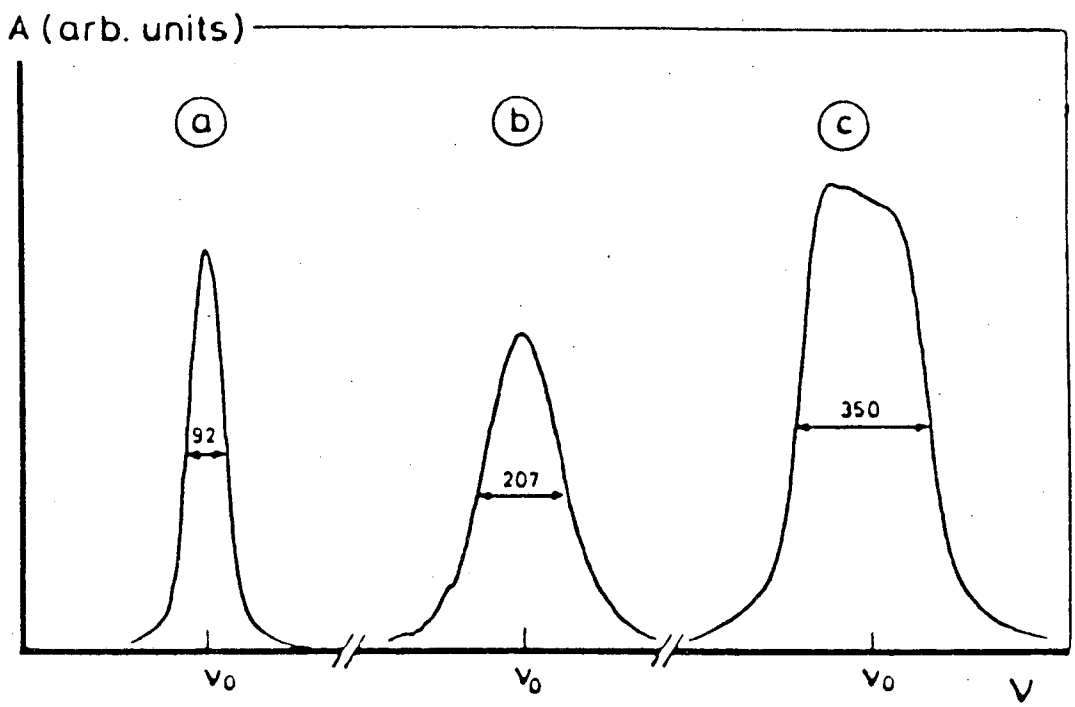

Figure 2.4 A comparison of the linewidths observed in the planar jet for $(HCl)_2$ in an argon expansion and a helium expansion. These scans are of a single rotational line in $(HCl)_2$. The complex structure is due to the Cl-Cl nuclear quadrupole hyperfine splittings.

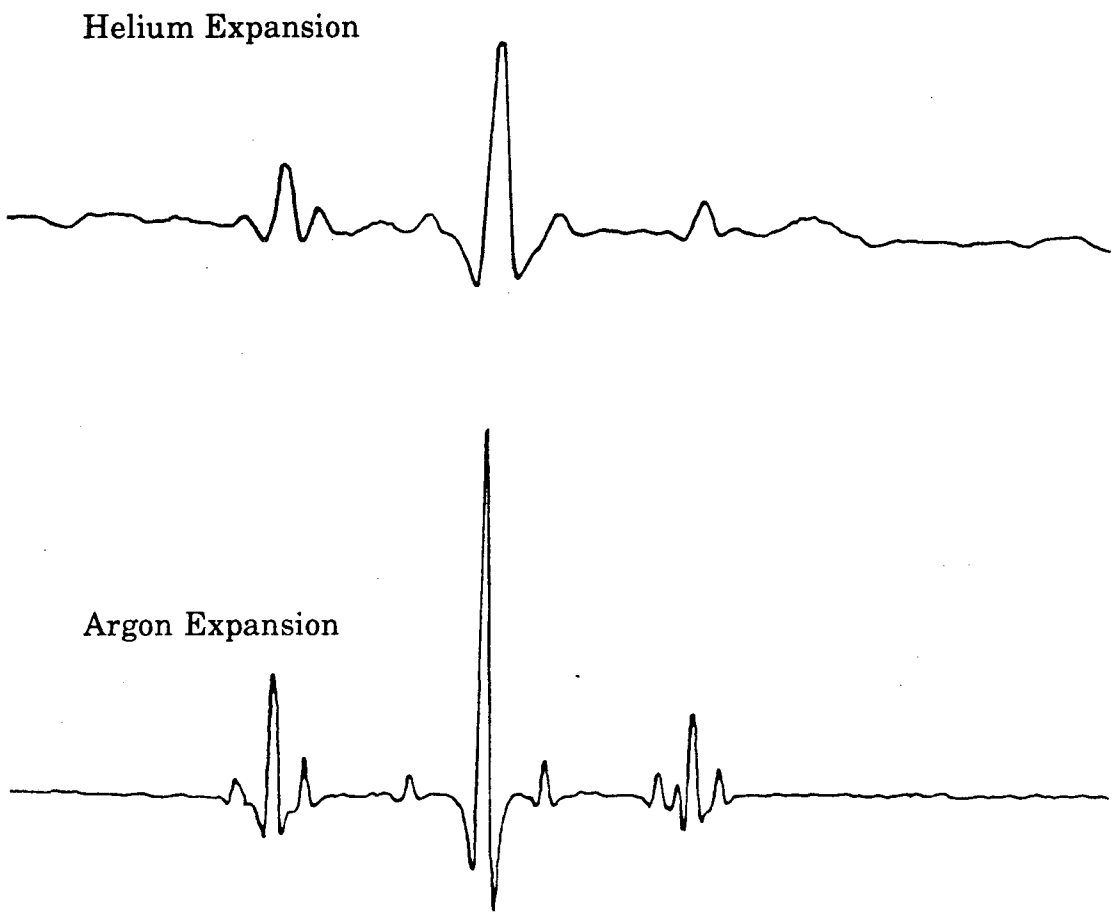

absorption feature narrows, the peak intensity increases. Therefore, the overall sensitivity of the experiment is improved by incorporating the planar jet.

It is also predicted that in the planar expansion the cooling occurs on a slower timescale. According to Hagena, the cooling rate is five times slower in the planar source.[13] Also, in the circular nozzle, the density drop should be proportional to $1/r^2$. In the planar nozzle, expansion parallel to the slit is restricted and therefore the density drop is expected to be proportional to $1/r$. The combination of these two effects, the slower drop in temperature as well as density should result in several advantages in using a planar jet expansion. The first is that one would expect the equilibration of the temperature of the various molecular degrees of freedom, particularly the vibrational temperature, to be more efficient. This could prove helpful in trying to simplify complex electronic spectra with significant vibrational structure. The second advantage is that the extent of clustering should be higher in the planar jet because there are more collisions and better energy equilibration. The disadvantage to a source with increased clustering is that the minimum attainable temperature will be higher because clustering releases energy and heats up the beam.

2.4 Initial Nozzle Design

The original nozzle design is shown in Figure 2.5. The

planar nozzle is constructed entirely of stainless steel to resist corrosion. The body of the nozzle is made from a 2" long piece of 1" square rod. A 0.5" diameter hole is drilled lengthwise through the rod, centered 5/16" (0.312") from the front face of the block. Caps are then made and welded on each end to seal the nozzle body. Through the front face, along the centerline, a 3/16" (0.187") slot is milled which is 1.5" long. Through the back face of the block, a 3/8" (.375") diameter hole is drilled into which a piece of stainless steel tubing is welded. Welded to the other end of this tubing is a mini-Conflat rotatable flange. This is the gas inlet line. On the front face, eight 4-40NC holes are drilled and tapped, 3/16" deep. Four holes are above the slot and four are below it, 0.25" from the centerline. The holes are spaced 0.5" apart. The last fabrication step is to polish the front face to a mirror finish to provide a good sealing surface with the nozzle plates.

The nozzle plates are made from 1/8" stainless steel plate. Each plate is 2" long and 0.5" wide and has four holes drilled through to line up with the four holes on the nozzle body. A beveled step is cut, 1/16" back from the edge of the plate. This step is formed by first milling along the top edge of the plate leaving only 1/64" (0.016"). This thickness is the nozzle throat depth. The step is then beveled back at approximately 30° from perpendicular to minimize the amount of turbulence generated in the jet. It was found that if the step

Figure 2.5 The 1½" planar nozzle design

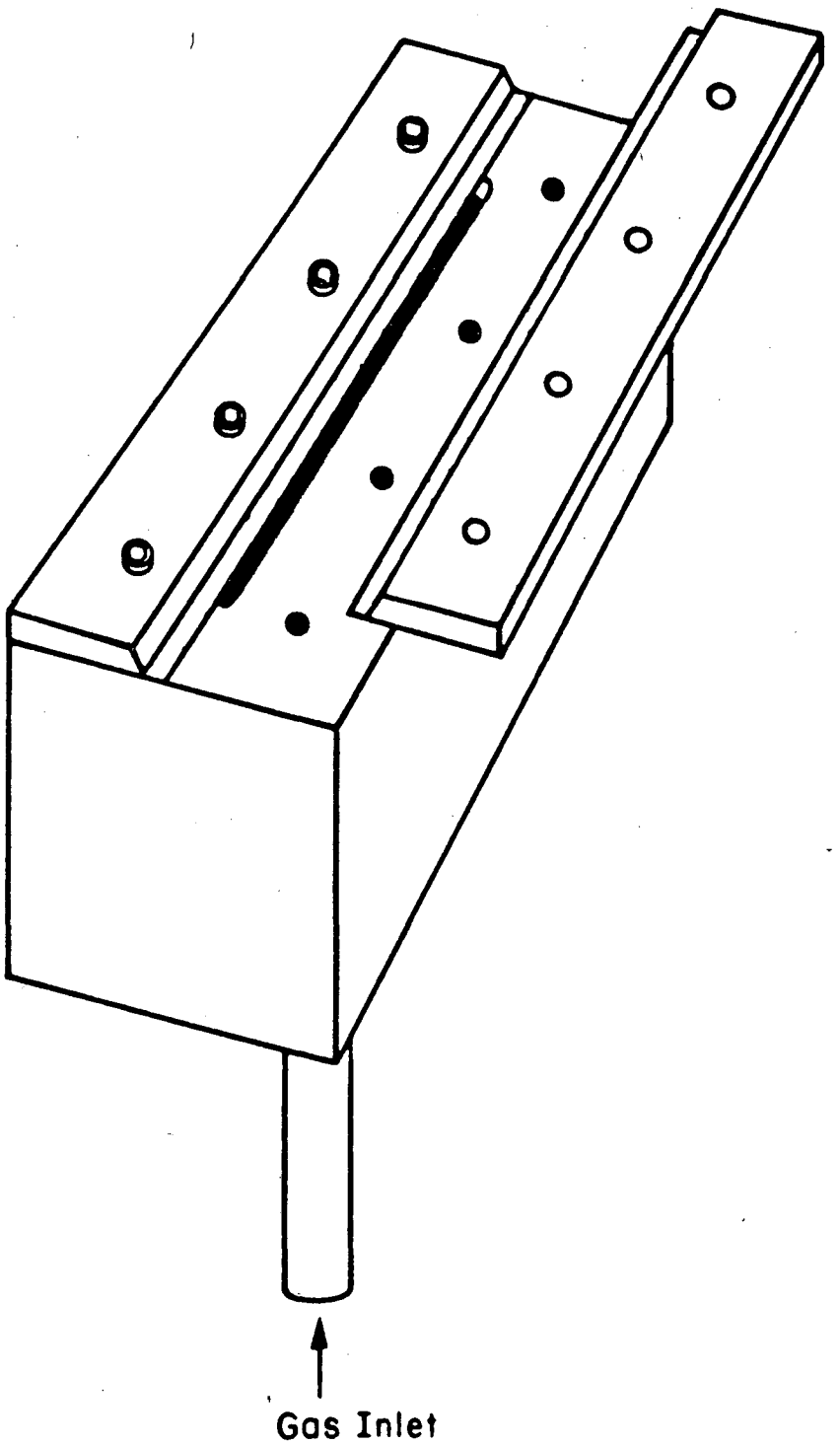

was not beveled back, little or no van der Waals cluster signal would be observed, presumably because the sharp edge interferes with the jet flow. At various times, different nozzle plates have been used. The overall design remained the same except the throat depth was varied. This will be further discussed in Section 2.8. The next step in machining the plates is to polish the sides in contact with the nozzle body also to a mirror finish. There is no sealing element, such as a gasket or o-ring, between the plates and nozzle, only the two smooth surfaces are in contact. Lastly, the two plates are tightly clamped back-to-back and the front edges are lapped together so that they will match up very well to give an evenly spaced slit. It is also very important that the plates remain perfectly vertical during this lapping process. If they were even slightly tilted, the jet itself would flow preferentially in one direction, as opposed to straight out of the nozzle. The holes on the plates are slightly oversized to allow some play when assembling the nozzle. The nozzle width is established by tightening the plates in position with a piece of .001" shim stock between them. It can take some careful adjustment to determine that the shim stock slides smoothly and evenly along the length. Typically, by this method, a slit width of .003" or greater is obtained, as measured using a microscope.

The gas inlet line on the nozzle is connected to a Y-shaped piece of stainless steel tubing. The earliest nozzle

design was for an 8" long slit which was to have two 3/8" gas inlet lines to both improve the conductance as well as prevent the nozzle from rotating out of alignment with the laser. The two gas inlet lines go through 3/8" drilled-through Cajon Ultra-torr fittings which provide a vacuum seal, as well as allow for the nozzle to be slid forward or backward relative to the laser to maximize the observed signal. When the smaller nozzle was designed, rather than changing the chamber flange, the two gas lines were kept and the Y-shaped piece was added. The various segments of tubing are connected with mini-Conflat flanges, all of which are welded to the 3/8" tubing.

A number of van der Waals clusters have been studied on this experiment, including ArHCl[14], $(HCl)_2$[15], $ArNH_3$[16], $(NH_3)_2$[17], ArH_2O[18], $(H_2O)_2$[19], and $CH_4 \cdot H_2O$.[20] We have used several methods for generating the appropriate gas mixtures. In the earlier experiments, pre-mixed gas cylinders (size 1A) were used for the HCl and NH_3 experiments, some of which were ordered from Matheson, many of which we mixed ourselves. The Matheson cylinders lasted roughly three days, while those we mixed lasted only about one day of scanning. This mixing process was very time consuming. Many different percentage mixtures were tested and in all of these clusters, a 2% mixture in argon was adequate. Recently, flow controllers have been installed which allow the gases to be mixed directly in the lines and careful adjustments of the concentration can be performed <u>in situ</u>. These are a valuable addition to the experiment. In the case

of the water experiments, argon is simply blown over the surface of room temperature water in a reservoir. We have bubbled the argon through the water, however, this resulted in large amounts of water being bumped into the gas lines. This most likely resulted in varying amounts of water getting into the expansion over time. Changing to the water reservoir did not result in any decrease in the cluster signal.

The pumping system consists of an Edwards EH4200 Roots blower backed by two E2M275 two-stage mechanical pumps. At 200 mtorr, the Roots blower is capable of displacing 2850 cubic feet per minute (cfm), which is equivalent to 1345 l/sec and each backing pump displaces 145 cfm (68 l/sec). The pumping speed of this combination of pumps is 2500 cfm (1180 l/sec). The pumps are all water cooled and interlocked. The two backing pumps are hooked up such that if one shuts off, the other goes off automatically. This is to prevent one pump from being overworked unknowingly, if something should happen to the second pump. This criterion requires that when turning on the backing pumps, both start buttons must be pushed simultaneously. Also, if either backing pump shuts off, the Roots blower will also shut off automatically. The Edwards Roots blower is designed in such a way that if the pressure gets too high the drive mechanism disengages to prevent the pump from being damaged in the case of accident or stupidity.

The pump maintenance has been minimal in the three years of operation. The Roots blower is essentially maintenance-

free. The oil does not need to be routinely replaced. There are three different oil reservoirs, each with its own sightglass to monitor the oil level and quality. It is extremely important to consult the manual on the proper oil levels in these reservoirs, because they are all different. Over- or underfilling any one could damage the pump. The oil used in the Roots blower is the recommended oil, Edwards No. 16, available from the company. As for the backing pumps, careful attention to the oil is a must. Generally, the oil should be replaced every 4 to 6 months, depending on how often they were run and what types of gases were pumped through them. The best indication is to check the color and consistency of the oil as well as looking for small particulates. Each pump holds roughly six gallons of oil, therefore, it is very unlikely that the oil will ever get extremely dark, because there is such a large volume of it. I would look for a noticeable change in color. This schedule may be somewhat excessive, but we have worked to maintain this schedule to prevent any pump problems from developing. In light of the investment made in these pumps, it seems justified. We have not however, been using the recommended oil (Edwards No. 15 or 17) because of the cost, but instead have used DDO-19, a standard mechanical pump oil available from San Jose Scientific. The mechanical pumps are also equipped with oil filters with filter quality gauges on the front side of the pumps. These wire mesh filters gradually get clogged with

particles and need to be cleaned or replaced. The manual recommends cleaning with standard organic solvents. It has been my experience that there are not good methods for cleaning these filters, including sonicating them in chlorinated solvents. Once "cleaned", the filter degrades again fairly rapidly and after several cleanings must be replaced. These filters are available from Edwards (Code no. A22304032). In the three years that these pumps have been in use, the filters on each pump have been replaced once.

2.5 Far Infrared Laser

The laser sideband experiment after which our system was modeled was developed by Pickett and coworkers in 1985.[21] Prior to the development of this laser sideband technique, very little high resolution far infrared spectroscopy had been done. Far infrared lasers existed, but were very narrow band output and were only line tunable. The general approach to spectroscopy was to use the fixed frequency laser and tune the energy levels of the species being studied with large magnetic or electric fields. The first of these methods, laser magnetic resonance (LMR), only works for open-shell species. The second method, laser electric resonance (LER), works for any neutral species, however the range over which energy levels could be tuned is quite small. Also, only the lowest few rotational transitions can be significantly tuned, limiting the spectra to only these states. This method does however, provide an

immediate measure of the dipole moment. Both techniques are very sensitive but are difficult to implement and spectral assignments are complicated by Stark and Zeeman splittings. The development of the tunable far infrared technique revolutionized far infrared spectroscopy, combining the existing far infrared laser technology with the very well understood techniques of microwave generation to provide a relatively simple method for scanning large regions of the far infrared.

The far infrared laser has been very thoroughly described by Ken Laughlin [22] and only a brief description of the system will be presented here. The experimental set-up is shown in Figure 2.6. To generate the tunable far infrared radiation, tunable microwave radiation is mixed with the same fixed frequency far infrared laser radiation used in the LMR and LER techniques in a GaAs Schottky barrier diode, which acts as a non-linear mixing device. Sidebands are generated at the sum and difference frequency of the microwave radiation and far infrared radiation. As the microwaves are tuned, the sidebands also tune and the spectroscopy is done with these tunable sidebands. The first part of the experiment is very similar to the LER or LMR experiments. A commercially available, 2.5 m, discharge pumped, cw, 150 W CO_2 laser (Apollo Model 150) is used to longitudinally pump the 2.5 m far infrared laser. The far infrared lasing media are generally small organic molecules, such as CH_3OH and HCOOH. This is a gas laser

Figure 2.6 The experimental design of the tunable far infrared laser spectrometer with the planar jet expansion.

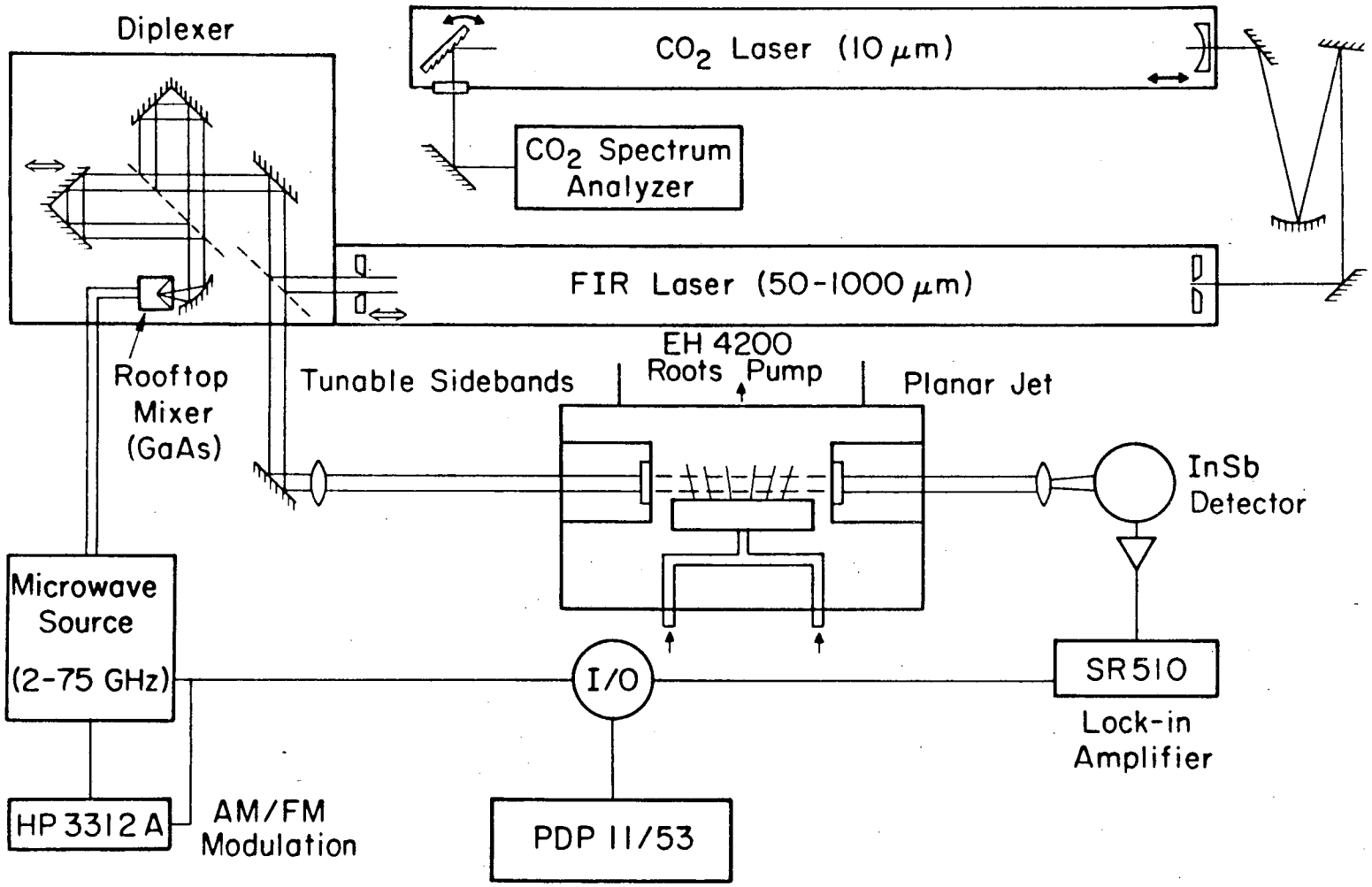

generally run at 100-300 mtorr. The gas is slowly pumped through the laser by a liquid nitrogen trapped mechanical pump. The lasing scheme involves vibrational excitation of the gas by the CO_2 laser, which operates around 1000 cm^{-1} and is frequency tuned using a grating to select the appropriate CO_2 vibration-rotation transition. Often the vibrational excitation of the FIR laser gas will create a population inversion in the rotational manifold and it is stimulated emission within the rotational states of the excited vibrational state that results in the FIR lasing. There are a wide range of gases which can be used as well as the choice of CO_2 pump lines and over 2000 FIR laser lines have been tabulated. In our lab however, we have only been able to make several dozen of these lase with sufficient intensity to be useful. However, our experiment does not require the large numbers of lasers required in the LER or LMR experiments, for which tuning ranges are much smaller.

This FIR laser radiation is then coupled onto the GaAs diode after traveling through the Michelson polarizing diplexer. The GaAs chip is actually an array of diodes, only one of which is used at a given time. The diode is contacted by a Au:Ni wire etched to a fine point. This whisker acts as an antenna for coupling the radiation into and out of the diode, as well as completing the electrical circuit. The Ga:As chip is mounted in an open rooftop cornercube[23] which is mounted on x-y-z translation and rotation stages to optimize

the amount of FIR laser coupled onto the diode. The microwave radiation is coupled onto the diode via coaxial cable connected to the whisker or with the waveguide built into the cornercube, through which passes the post on which the diode is mounted. The mixed radiation - the sidebands as well as a large amount of reflected FIR laser power - radiate out from the cornercube and follow the same path through the diplexer. That radiation which was not simply reflected from the cornercube, but was coupled onto the diode and whisker will have its polarization rotated 90°. It is this rotation which allows the sidebands to be separated from the much more intense reflected FIR laser or carrier. By setting the appropriate difference in the two arm distances of the diplexer, it is possible to selectively send almost pure sidebands out to the chamber and detector. This prevents the detector from seeing large amounts of the carrier, which can saturate the detector.

This microwave mixing technique also provides a very simple modulation technique which allows us to use phase sensitive detection methods. The microwave source can be easily frequency or amplitude modulated. We use frequency modulation (fm) at 50 kHz and detect at 100 kHz. In the case of a continuous nozzle source, this is an extremely valuable feature. With other laser systems, such as the color center or diode lasers there are no simple ways to modulate the radiation and often the source of clusters has to be

modulated. For example, a chopping wheel could be placed in front of the nozzle, however, it must be close enough to the nozzle to leave enough room for the laser. This is an awkward arrangement. Probably the best approach when using a radiation source which cannot be easily modulated is to go to a pulsed nozzle design. This will result in a decrease in duty cycle. The easy modulation scheme afforded by the tunable FIR system is a very important asset.

The laser sidebands are directed through the plane of the jet and detected using an InSb detector. The signal is then demodulated using a lock-in amplifier and then processed and stored on the PDP11/53 computer. More recent experiments are incorporating several new detectors as well as multipassing optics. These developments will be described in detail by Cohen.[24]

2.5.1 FM Advantage

A very important unforseen benefit was obtained which is specific to our tunable far infrared/ planar jet experiment. The laser sideband experiment has some significant baseline fluctuation problems. These fluctuations are generally peak-like structures throughout the scan, typically several MHz wide. When the laser is used in conjunction with a gas cell or discharge cell, absorption linewidths are typically 1 to 2 MHz. The detection scheme involves frequency modulation of the laser. The amount of frequency deviation applied is dependent

on the width of the line being measured: the broader the peak, the larger the deviation required to optimize the signal. The fact that the absorptions and the baseline fluctuations are roughly the same width implies that the fluctuations are detected with nearly the same efficiency. There is no discrimination against this baseline problem. However, reducing the linewidths by a factor of three in the planar jet means that the fm deviation required can be reduced by that amount and the much broader baseline fluctuations are strongly discriminated against and therefore greatly reduced.

2.6 First Planar Jet Results-H_2S Line Narrowing

The first successful experiment using our planar jet and tunable far infrared laser involved measuring H_2S monomer absorptions in a helium beam and observing significant narrowing in going from the static gas absorption to the planar jet. Two lines were measured for H_2S, the first was at 687.303 GHz which has a lower state energy only 15 cm^{-1} above the ground state. The second line was at 689.120 GHz and has a lower state energy 800 cm^{-1} above the ground state. Therefore, the ratio of the intensities of these lines would be expected to be quite different in the cold jet, compared to the room temperature absorption. Two sets of these scans are shown in Figure 2.7. The upper set of lines were taken with the nozzle pulled far back from the laser. This situation imitates the static gas cell in that the absorption is well

Figure 2.7 Two sets of scans showing the line narrowing in the planar jet for an H_2S absorption. In each set, the upper trace is of an absorption with a lower state energy only 15 cm^{-1} above the ground state. The lower trace is of an absorption with a lower state energy 800 cm^{-1} above the ground state. The upper set of scans shows the two absorptions in the warm background gas in the chamber. The lower set of scans shows the two absorptions in the jet expansion. The upper trace clearly shows both the line narrowing and signal increase due to thermal relaxation (the sensitivity is thirty times lower than in the upper set). The lower trace shows no narrowing. The lack of significant intensity reduction is due to absorption in the warm background gas in the chamber on either side of the jet expansion.

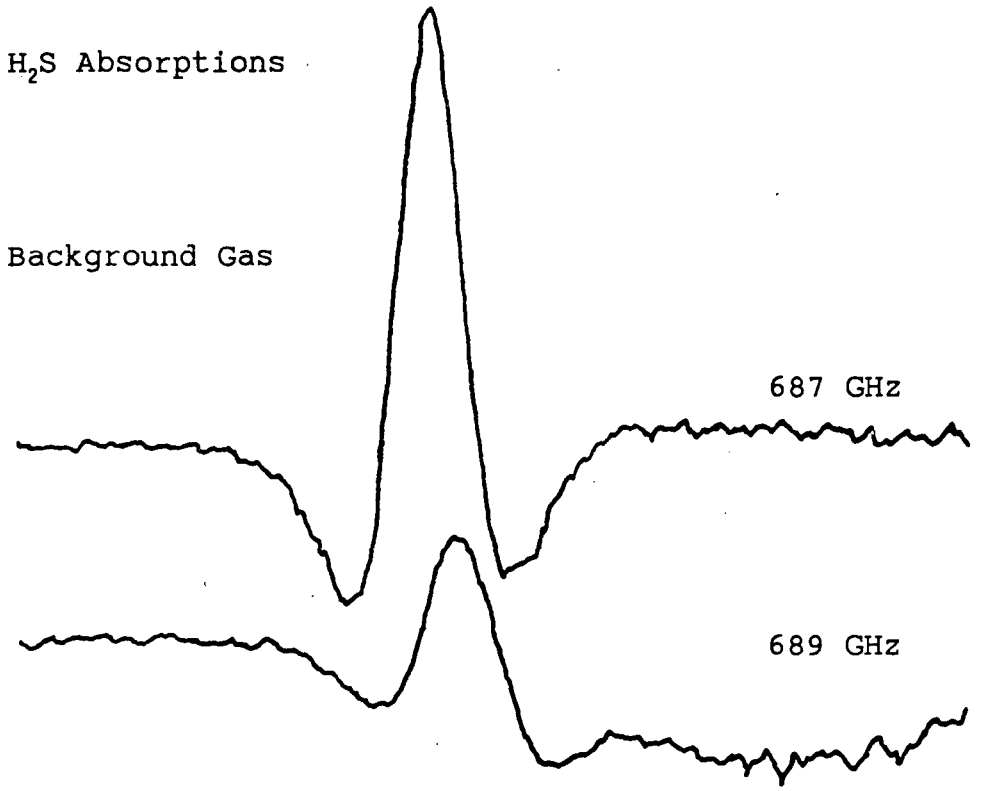
H_2S Absorptions
Background Gas
687 GHz
689 GHz

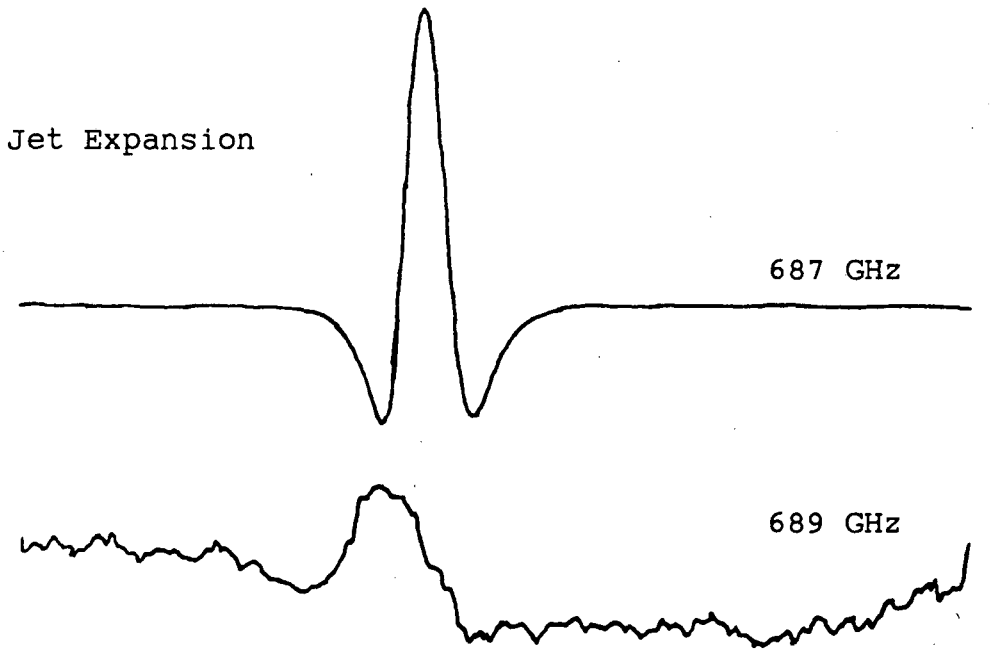
Jet Expansion
687 GHz
689 GHz

beyond the Mach disk, not in the jet, but in the warm background gas in the chamber. The upper line is the 687 GHz line with the low energy ground state. The lower line in the upper set is the 689 GHz line and has the high energy ground state. At room temperature, the predicted ratios of these two lines is 2.5:1 for the 687 versus the 689 GHz lines. The lower set of scans were taken with the nozzle very near the laser path. It is very clear that the 687 GHz line is significantly narrower. In the background gas it is 1.25 MHz, and in the jet it is only 660 kHz. It is also significantly more intense, as the lock-in amplifier sensitivity is a factor of 30 lower in the jet scan. As for the 689 GHz line, in the cold jet, the intensity should be much weaker than observed. The reason it appears fairly intense in the jet scan is that it is most likely the result of absorption in the several inches of background gas on either side of the jet. This notion is supported by the fact that the line does not appear to narrow at all. The small decrease in the intensity of this line over that in the upper set of scans is due to the presence of the cold jet which actually reduces the pathlength of the warm background gas.

2.7 The Lowest Σ Bend of ArHCl

The first van der Waals study undertaken with the newly built tunable far infrared laser/planar jet apparatus was the measurement of the lowest Σ bending vibrational transition in

ArHCl. This molecule was chosen because it had been thoroughly studied by Robinson and coworkers in our group using the molecular beam laser electric resonance spectrometer.[25] The frequencies of the lower J state transitions were well determined, eliminating any possible search problems. We then used this band as a proving ground to determine what the experiment was capable of, in terms of the linewidths, jet temperature, sensitivity, and experimental accuracy.

Theoretical aspects of the ArHCl complex have been thoroughly discussed in a number of papers[26] and will only be briefly described. The well depth (D_e) for the linear ArHCl complex is 180 cm^{-1}. A secondary minimum exists at the linear ArClH configuration which is bound by 120 cm^{-1}. The energy level diagram is shown in Figure 2.8. In this scheme, the van der Waals molecule is described in terms of a "rigid" linear molecule vibrational spectrum. The fact that the Σ bend, which correlates to the overtone of the bend, is lower in frequency than the fundamental, the Π bend, indicates that this is not the most appropriate scheme and is probably better represented by a hindered rotor formalism. However, this model provides a simple language that can be used to describe these transitions.

We measured 37 transitions in $ArH^{35}Cl$ and 31 transitions in $ArH^{37}Cl$ in natural abundance.[14] The two papers describing this experiment are included in Appendix A. In transitions with J" ≤ 6, the nuclear quadrupole hyperfine splitting was

Figure 2.8 The ArHCl energy level diagram

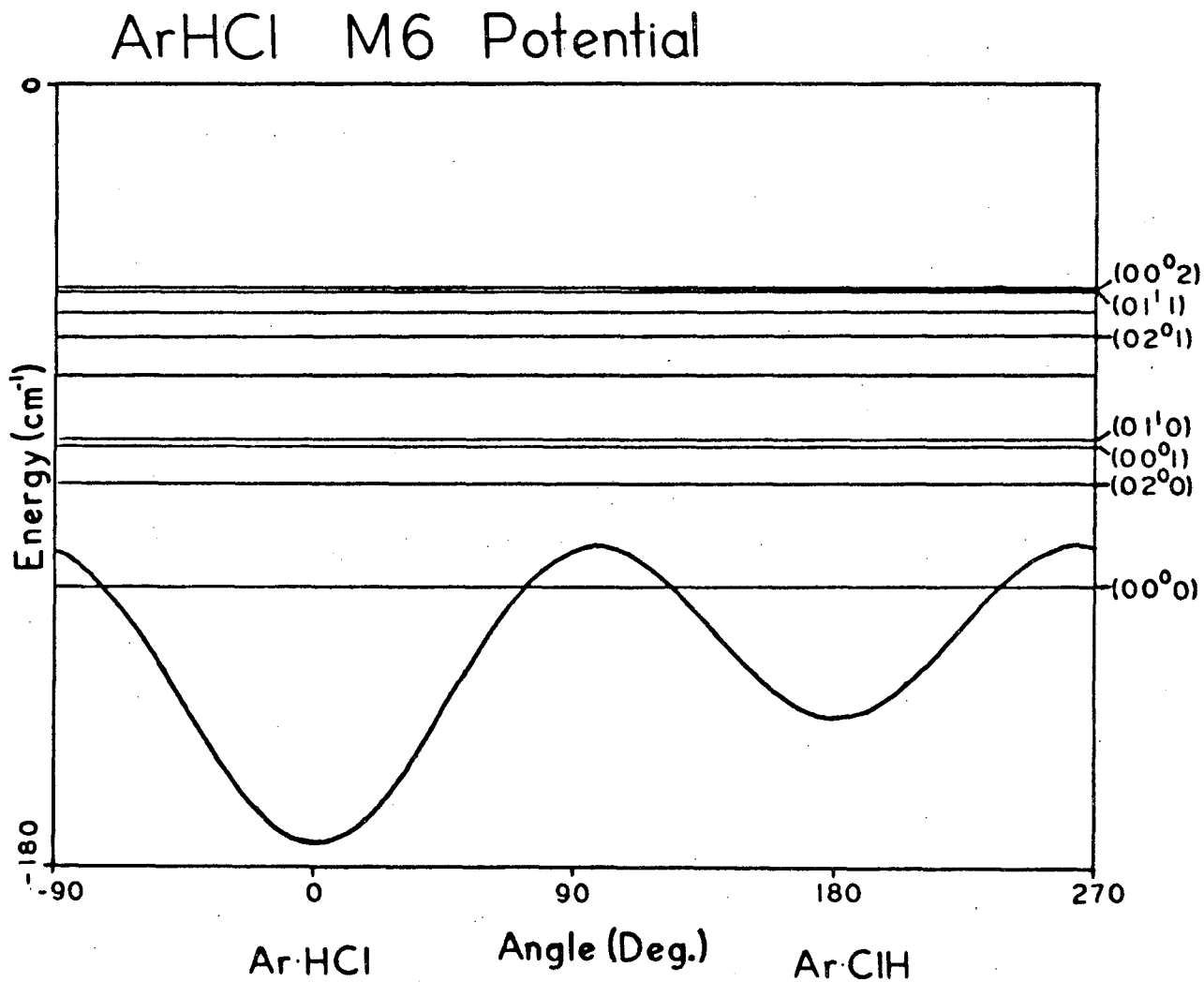

resolved. In the earlier molecular beam laser electric resonance experiment[25], only P(1) and R(1)-R(3) were observed. At higher J, it becomes significantly more difficult to Stark tune the transitions into resonance with the far infrared laser. In our experiment, we do not have that limitation and measured from P(23) to R(17) in the Cl-35 species.

A careful calibration of all of these lines was performed to obtain the best possible fit. The J=0→1 transitions of $H^{35}Cl$ has been measured by DeLucia et al. and is known to approximately 20 kHz.[27] We used this line to calibrate the ArHCl lines observed. First, the HCl line was measured, in the jet as opposed to a gas cell, to reduce the linewidth and improve our measurement of the center frequency. Immediately after measuring this line, P(10) of $ArH^{35}Cl$ was measured to calibrate it. It was assumed that the drift in the far infrared laser frequency was slow on the timescale of the two scans, roughly three or four minutes. Once P(10) was calibrated, the other transitions were referenced to it. The P(10) transition was measured before and after each line measurement. Through this rather tedious process we were able to obtain a fit for the Cl-35 complex with a standard deviation of 85 kHz, and a standard deviation for the Cl-37 dimer fit of only 31 kHz. It is assumed that the Cl-37 fit is somewhat better due to fewer high J lines being measured. These lines tend to worsen the fit. This was the only van der Waals study in which we performed this careful calibration.

In subsequent van der Waals studies, our fits generally had a standard deviation of roughly 1 MHz, due to the large frequency deviations that are encountered with the far infrared laser. This is not the result of laser drift. Simply pulling the laser to determine which sideband is responsible for a given absorption shifts the laser frequency several hundred kHz. Although the laser linewidth is typically less than 50 kHz [28], the range over which the laser can operate is at least several MHz wide. From day to day, the laser frequency can change significantly, giving rise to standard deviations typically 1 MHz or more. In this study we demonstrated that with careful calibration, this frequency deviation can be eliminated and an order of magnitude or more improvement in the standard deviation can be achieved.

As anticipated, narrow linewidths were observed making it possible to resolve the hyperfine structure. Linewidths are approximately 350 kHz. In Figure 2.9 is the scan of P(3) of $ArH^{35}Cl$ with a stick diagram indicating the hyperfine assignment. Significant effort went into optimizing the jet and laser conditions to obtain the best signal to noise ratio possible. With a 1 second time constant, the S/N of this scan is 2000.

One problem encountered with the TuFIR experiment is that it is very difficult to obtain accurate relative peak intensities. As the microwave frequency is changed, the sideband power fluctuates. Peak intensity measurements are

Figure 2.9 The best ArHCl scan showing the P(3) absorption with the nuclear hyperfine splitting. The signal to noise is 2000:1 with a 1 sec time constant.

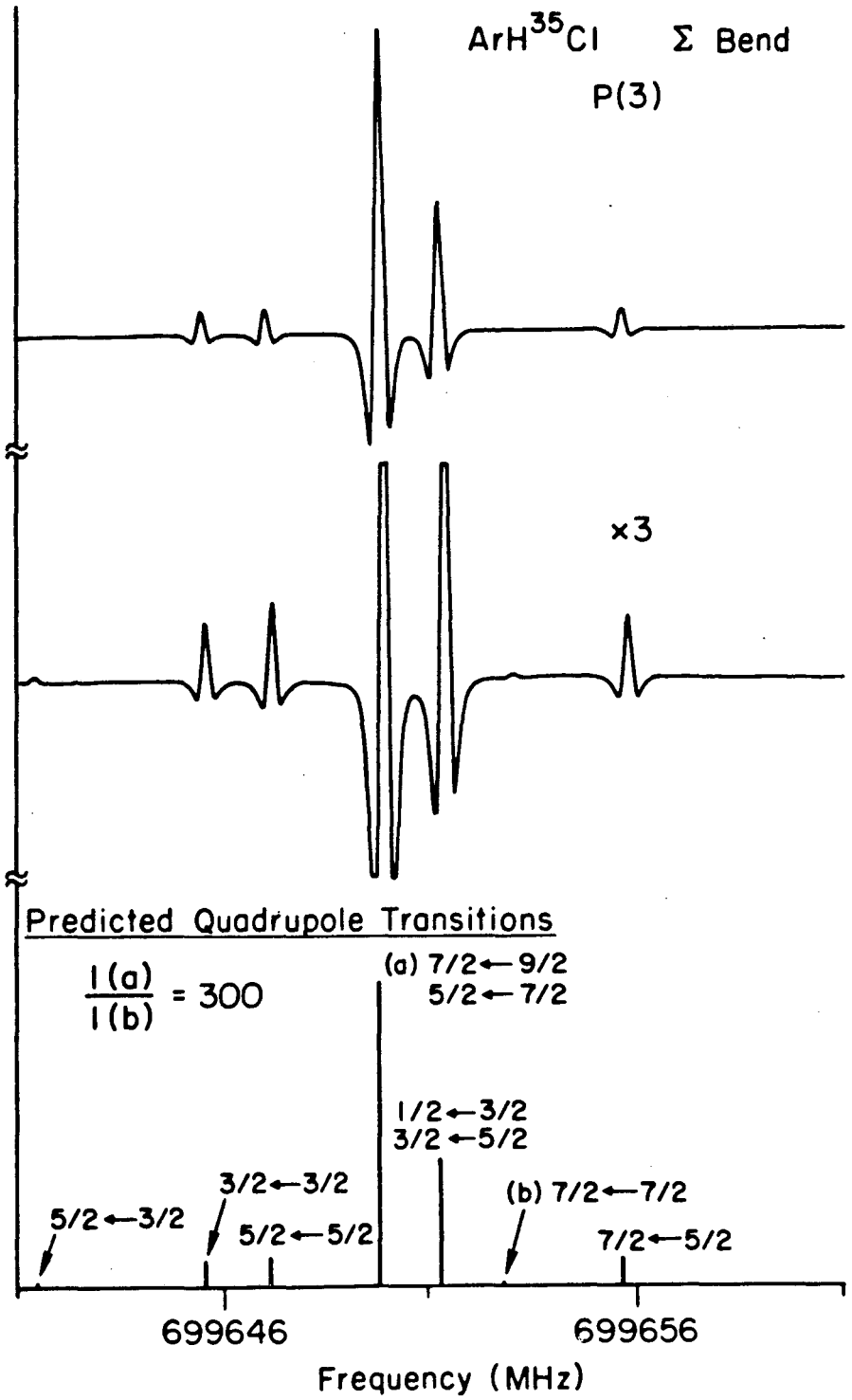

more reliable for closely spaced lines, such as in a Q branch, however, in this band there is no Q branch. This makes obtaining an accurate rotational temperature difficult. However, fortuitously, in a single scan, both the P(2) and P(9) transitions were observed for $ArH^{37}Cl$ (Figure 2.10). In this experiment, both the sum and difference frequency sidebands are scanned and detected simultaneously. The P(2) transition occurs on the upper sideband and the P(9) transition is on the lower sideband. This is an ideal situation for determining the beam temperature. Using a Fabry-Perot etalon, the ratio of the powers of the upper and lower sidebands was obtained and then from the ratio of the peak heights, correcting for the quadrupole hyperfine intensity, a rotational temperature of 3(±1) K was calculated. There have been several van der Waals studies since this one in which we estimated the beam temperature and consistently arrive at 3 K.

An interesting result obtained was that in the higher J transitions, $J \geq 15$, the peaks broadened and gradually split into doublets (Figure 2.11). The proposed explanation for this doubling is that for the highest rotational states there is very little population in the cold jet and the observed spectra is actually due to absorption primarily in the warmer boundary regions of the jet. Because the jet is somewhat divergent, absorptions on either side of it are Doppler shifted, giving rise to the doublets. From the splitting obtained, an angular divergence of the jet was calculated to

Figure 2.10 In this single scan, both the P(2) and P(9) transitions for $ArH^{37}Cl$ were observed allowing for the jet temperature to be determined (3±1 K). The P(2) absorption occurs on the upper sideband and is split by the nuclear quadrupole hyperfine. The P(9) absorption occurs on the lower sideband.

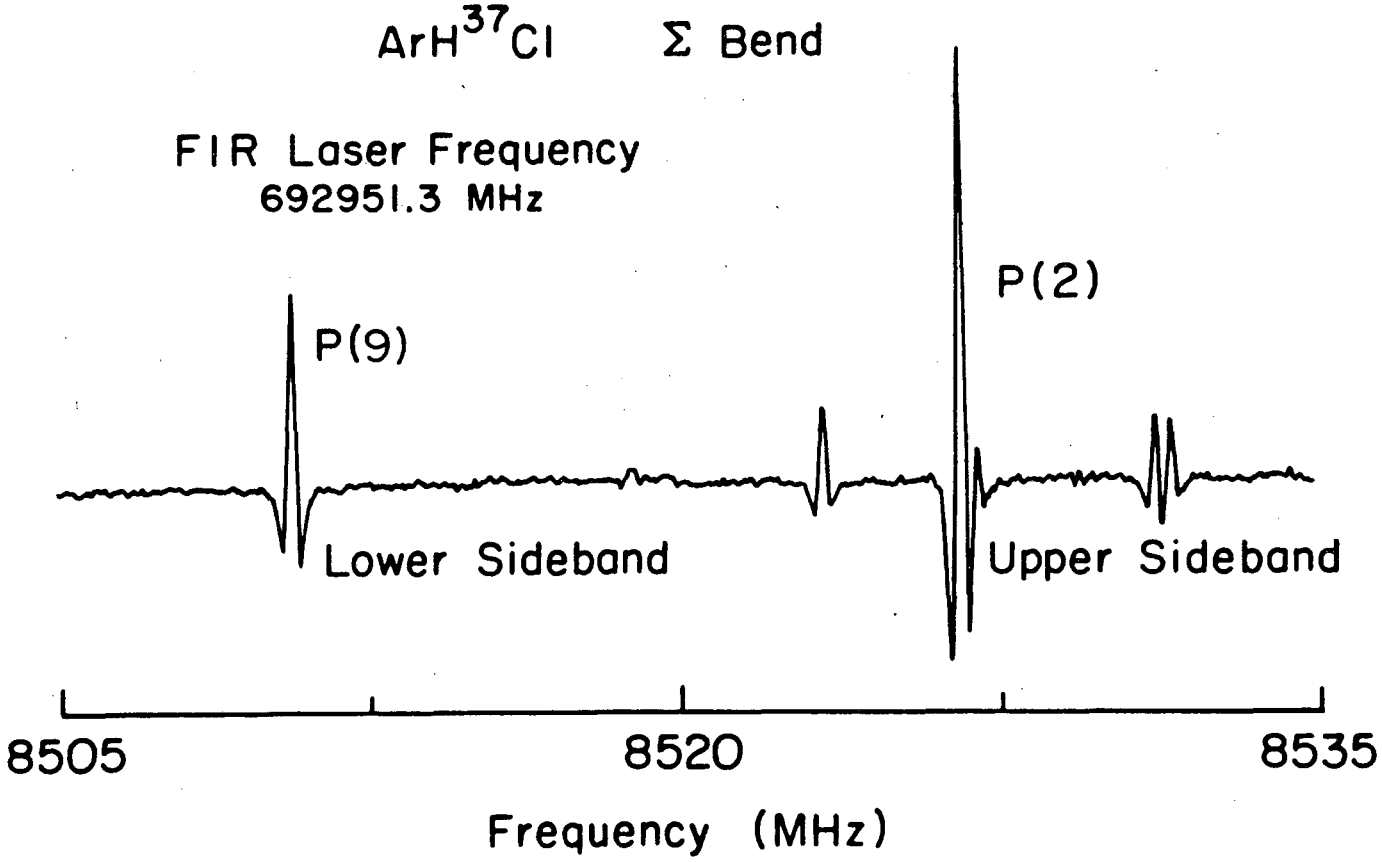

Figure 2.11 This scan shows the Doppler doubling observed in the high J lines of ArHCl.

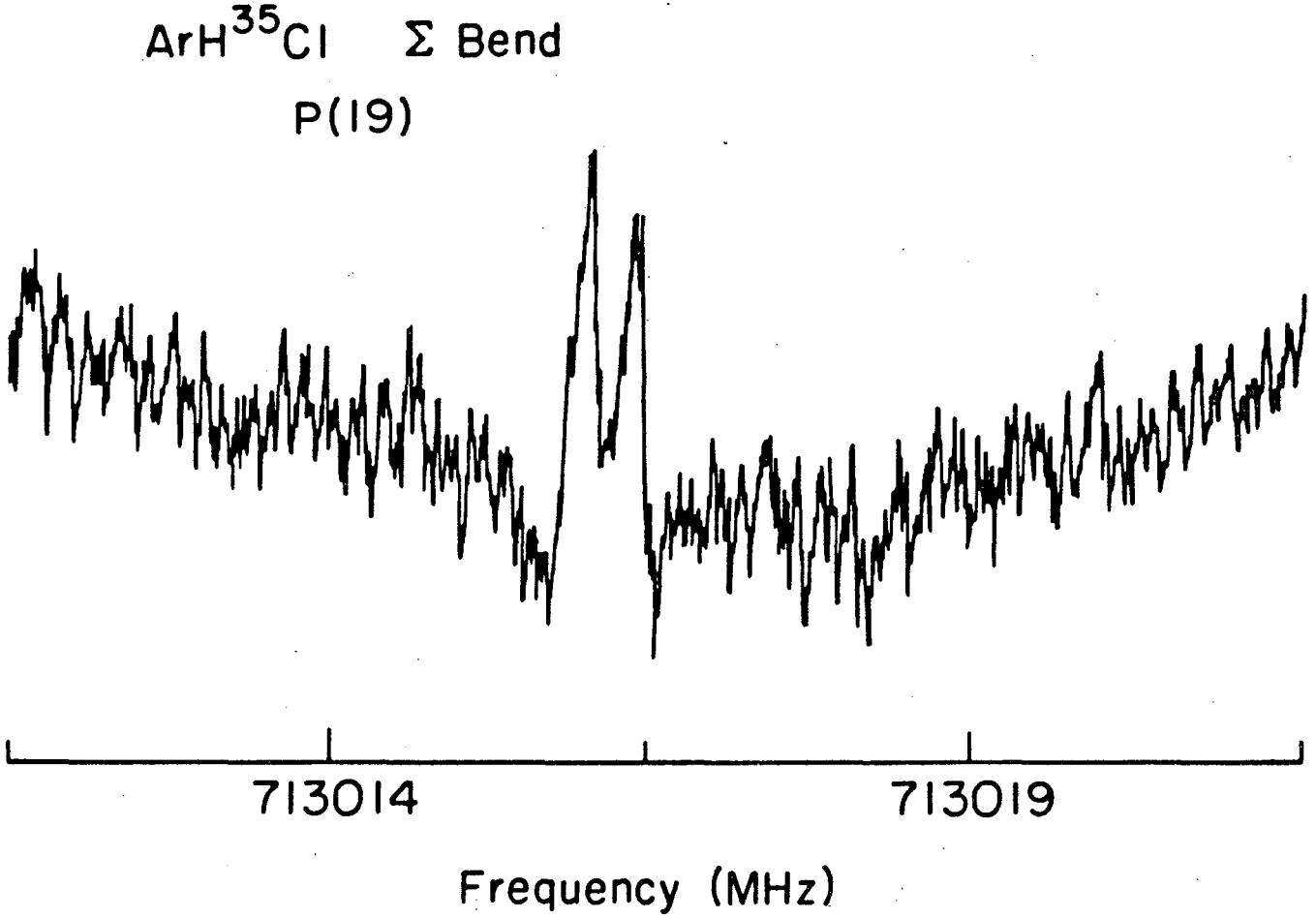

be 7°, assuming that the forward beam velocity was that typically observed for an argon expansion, namely 560 m/sec.[20] Veeken and Reuss measured the divergence of their pulsed planar jet to be 3°.[9]

In this study, the spectroscopic constants for the ground state and the Σ bending state were improved. However, the real value of this work was to demonstrate the power of this new technique, combining the tunable far infrared laser with the planar jet expansion. The laser made it possible to scan large regions of the far infrared with only the strongest laser lines. There were no large electric or magnetic fields to complicate the analysis. The planar jet provided a long pathlength of cold clusters with a very small perpendicular velocity component, giving sub-Doppler linewidths. Spectra could be obtained quickly, in a single pass with an excellent signal to noise ratio. There were few disadvantages. Shortly after the ArHCl project was completed, this versatile technique provided the spectra for other van der Waals complexes, including $(HCl)_2$[15], ArH_2O[18], $(H_2O)_2$[19], $ArNH_3$[16], and $(NH_3)_2$.[17] It became a situation in which the data was easy to obtain but difficult to analyze.

2.8 Optimization of the Nozzle Design

The original 1½" nozzle design worked quite successfully through most of the van der Waals molecule experiments. It was not until many of these experiments were completed that we set

out to optimize the design. This optimization however, proved to be quite difficult for a number of reasons and the results at this point should be considered qualitative. The approach was to look at the effects of length and nozzle plate design on the absorption signal of ArH_2O. This implies that the optimization is not only of the expansion itself, such things as temperature and shape or overlap with the laser, but also, we are optimizing the extent of cluster formation, particularly the dimer formation. Also, it should be noted that the far infrared laser beam is quite large compared to most lasers, it is generally 1 cm or larger in diameter. This size laser does not allow us to get a detailed picture of the various regions of the jet, as would a smaller laser. Also, we are essentially optimizing the nozzle for this large laser. In other words, the nozzle which is best for the far infrared laser system may not be ideal for a color center or diode laser experiment. The most difficult aspect of these optimization experiments is that it is not possible to vary a single parameter. Varying the throat depth, for example, results in a change in the pressure drop across the nozzle. Therefore signal improvement may be the result of increased collisions in the nozzle throat or an overall improvement in the expansion due to the lower chamber pressure. It is not possible to separate these effects. The approach was to carefully install each new set of nozzle plates such that the plate spacing was as similar as possible , and in general, as

narrow as possible, from one set to the next using .001" shim stock. The same person installed each set to minimize the variation. Then each nozzle was optimized for backing pressure and nozzle position relative to the laser beam path. Rather than trying to monitor the variation of a single parameter, several were varied to determine the best possible signal from a given nozzle. Of course, in varying several parameters at once, it is possible that the best signal was not found, but the hope was that we would observe trends in the various nozzle designs pointing toward the best combination of features.

The length optimization was quite straightforward. The first planar jet that we had built has a maximum length of 8". The design was essentially the same as the 1½" nozzle previously described. We used this jet, blocking varying amounts by placing a teflon sheet which had a slot cut to the chosen length, between the nozzle block and the nozzle plates. In this way, we could vary the length up to 8". However, with the 8" nozzle, we have found that it is extremely difficult to machine 10" long, ⅛" thick plates of stainless steel and keep the front edges of the plate parallel to .001" over the entire length. Machining the pieces to that tolerance is difficult but not impossible. As in the case of the smaller nozzle, the plates are carefully clamped back-to-back and the slit edges are lapped together to give an even, parallel surface. The problem is that once the plates are unclamped, they bow. The

stress of machining the holes, in particular, causes the relatively thin plates to distort. The result of this warping is that it is impossible to keep the plates evenly spaced along the entire 8" length. In some of the measurements at the longer lengths, the expansion may have had actual breaks or gaps in it due to the plates touching. The hope was that the results would indicate that we would not need a nozzle that was that long.

The results are given in Table 2.1. All of the measurements were made using the 432 μm HCOOH (692.9513 GHz) laser line. Several R branch lines of the ArH_2O $\Sigma(1_{01})\rightarrow\Pi(1_{10})$ band were used in these measurements.[18] The ArH_2O spectrum will be discussed in Chapter 4. The important point is that this band represents one of the strongest van der Waals complex signals observed with this experiment. The laser line used is one of the strongest lasers we use and the reagents are readily available, making this an ideal system for these studies. Two separate experiments were run. In the preliminary experiment R(5) and R(10) were measured. These results indicated that the optimum length was between 3 and 6". A second, more careful experiment was later performed in which R(3), R(6), and R(9) were measured in the hopes of estimating a beam temperature for each length. The Michelson interferometer was optimized at the R(6) frequency and was not reset in going between the three different lines. This was to maintain a consistent sideband power when comparing one nozzle

Table 2.1 Nozzle Length Measurements

Lines measured refer to R branch lines of ArH_2O $\Sigma(1_{01})\rightarrow\Pi(1_{10})$ band. The R(5) and R(10) measurements were performed at a time when the laser power was significantly better than when the R(6) and R(9) lines were measured. This accounts for the large discrepancy in the peak intensities.

	Peak Intensities (arb. units)			
Nozzle Length (inches)	R(5)	R(10)	R(6)	R(9)
1	40000			
1.5	65000	7200	7100	1680
3	145000	12600	4200	1200
4			13200	3350
5			9400	1700
6	132000	15000		
8	114000	11800		

to the next. This implies that the R(3) and R(9) signals were not maximized and therefore the temperature determination may be slightly off, however, we would be able to observe relative differences between the nozzles. Also, in the second experiment the sideband power was lower than in the earlier experiment. However, it was quite apparent that the 4" nozzle was the best overall. Typical operating conditions for the 1½" nozzle are 700-800 torr behind the nozzle with 100-140 mtorr in the chamber. With the 4" nozzle, the optimum conditions are 500 torr behind the nozzle and 300 mtorr in the chamber, indicating that with larger pumps, it would most likely be possible to go to a longer nozzle.

If the laser sideband power had been better in the second experiment, it would have been possible to get a direct measure of the linewidth by measuring R(6) using amplitude modulated sidebands. Unlike frequency modulation, amplitude modulation gives the true linewidth. However, to observe a line using amplitude modulation, it must be a very strong signal. In general, most lines are not observable using amplitude modulation. In the earlier experiment, the linewidth of the R(5) line was measured with the 8" nozzle to be 650 kHz. This is much larger than we would have expected even for the 1½" nozzle, which because it is shorter should have, in theory, a broader linewidth. Our estimation of the linewidths are 300-400 kHz. The explanation of why the longer nozzle gave such broad peaks is still unclear. It may be related to the

fact that the 8" nozzle is not evenly spaced along the length, as was described above and the gas flow may simply not behave as anticipated.

In addition to the length experiments, a number of experiments were performed to optimize the shape of the nozzle plates. There were several questions we were attempting to answer: 1) What is the effect of varying the throat depth, that is, the plate thickness where the jet is being formed? 2) Is there an added benefit to sloping the plates outward at the throat exit? 3) Is there any added benefit to sloping the plates from the inside of the nozzle? or sloping it both inside and out?

To answer these questions a number of nozzle plates were machined for the 1½" long nozzle. The plates were made of aluminum and the inside face and throat surface were polished to give a smooth finish. As in the length measurements, R(3), R(6), and R(9) of the ArH_2O $\Sigma(1_{01})\rightarrow\Pi(1_{10})$ band were measured for each nozzle. The nozzle plates studied are depicted in Figure 2.12. The nozzle plates are drawn looking end on down the slit, as they would fit on the nozzle at the top of the figure. For example, Nozzle A is beveled outward on the outside or low pressure side of the nozzle, while Nozzle K is beveled from the inside or high pressure side of the nozzle. In the case of the nozzles beveled from the inside, the bevel is not cut along the entire length of the nozzle as in the other nozzles, but only across the center 1½" (Figure 2.13).

Figure 2.12 The various nozzle designs studied in the nozzle optimization studies. The nozzles are depicted looking end on down the slit as the plate would fit on the nozzle at the top of the figure.

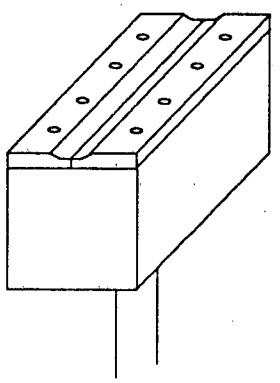

Nozzle	Shape	Angle	Throat depth
1	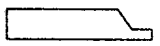		.031
2	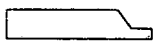		.016
A	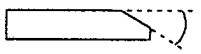	10	.062
B	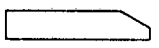	20	.062
C	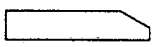	30	.062
D	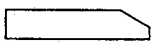	45	.062
E	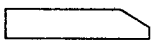	70	.062
F	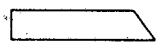	70	.000
G	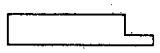		.047
	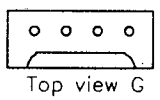 Top view G		
H	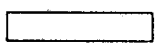	0	.125
K	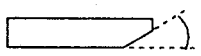	30	>.062
L	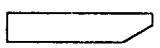	45	>.062
M	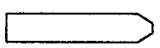	Both 45	.031
N	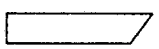	45	.000
P	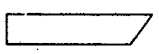	70	.000

Figure 2.13 The design of the nozzle plates beveled on the high pressure side of the nozzle

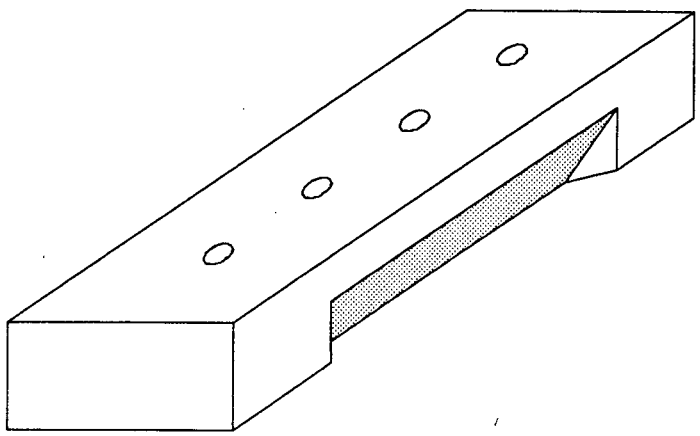

This is to provide a seal for the nozzle. If it was cut along the entire length the gas would flow out of the sides of the nozzle rather than through it.

Nozzles 1 and 2 are the stainless steel plates which have been used in many of the van der Waals experiments. The original plate design was quite similar to these, except that the recessed angled edge was stepped (Figure 2.14). The reason the step design was first considered was to keep as much thickness in the plate as close to the throat as possible, to minimize the warping and distortion of the plate. We have found that the stepped nozzle gives a much lower van der Waals signal. Once the steps are removed, the signal improves by an order of magnitude. Our interpretation of this result is that the sharp edges of the steps create turbulence in the jet and destroy the flow characteristics. Although this type of nozzle was not specifically included in this study, we have in the past observed that it is ineffective for the van der Waals molecule source.

The results of the experiment are shown in Table 2.2. There are several general conclusions which can be drawn. The first is that the throat depth is an important parameter. Nozzles 1 and 2 differ only by a factor of two in the throat depth and Nozzle 1, with the thicker throat, is consistently better. This can also be seen by comparing L to N. Both nozzles are beveled from the inside, L has a .062" throat, and N has no throat. Both nozzles give a fairly strong signal, but

Figure 2.14 The stepped nozzle design

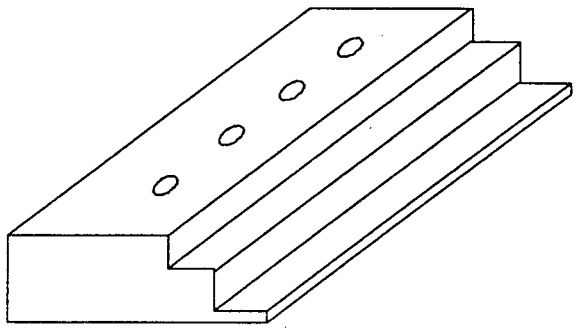

Table 2.2 Measurements of Nozzle Geometries

The various nozzle designs are shown in Figure 2.12. The lines measured refer to R branch lines of the ArH_2O $\Sigma(1_{01})\rightarrow\Pi(1_{10})$ band. Nozzles listed below the double line (K through P) were measured at a later time than the other nozzles. The laser power at that time was not as high and the experiment was optimized for the R(6) line instead of the R(3) line. Nozzle 1 was remeasured at this time to allow for comparison between the data sets.

	Peak Intensity (Arb. units)		
Nozzle	R(3)	R(6)	R(9)
1	27500	15000	6400
2	5300	2400	1700
A	35500	18500	6400
B	25500	13500	5200
C	17500	14000	3200
D	3500	1060	520
E	250	150	105
F	---	135	120
G	11600	5400	2150
H	27000	15000	5500
1	3500	6800	250
K	4200	5500	185
L	6100	9000	280
M	1500	3400	150
N	4300	8500	240
P	4900	8200	430

L is slightly better. However, the reasonably intense signal observed with nozzle N, which has no throat, indicates that a substantial throat depth is not required for cluster formation.

Another trend can be seen in comparing nozzles A through E, in which the throat depth is constant, but the angle of the bevel is varied. There is a consistent decrease in the signal as the included angle between the plates is decreased. The question being addressed with these nozzles was, is there an increase in observed cluster signal when the beam is confined. One motivation for trying these nozzles was that in the carbon cluster experiments performed by Heath and Cooksy in our group, they saw an enhancement in signal when a cone was used to confine the jet.[29] These two experiments are certainly quite different. They are using a laser vaporization source with a large diameter nozzle and a much smaller spot size diode laser. There are several possible reasons for the difference. In our case, the van der Waals clusters are in a very cold jet (~3K) and attempting to confine the jet may only serve to warm it up. In the carbon experiment, the source is a bit warmer, with a rotational temperature of ~15K. Therefore, a small increase in temperature may not be detrimental, or can be more than compensated for by increasing the cluster density in the laser overlap region. In our case, the laser is nearly the same size as the jet and compressing the jet will not increase the number of dimers interacting with the laser, but only make

the overlap worse. For whatever reason, on the far infrared laser system, when looking at van der Waals clusters, the larger the included angle, the better the signal. Nozzles H, K, L, N, and P have no external angle and all give fairly intense signals. Therefore, on the new nozzle, the plates were designed with a flat surface on the low pressure side. Nozzle G was designed to determine the effect of trying to confine the jet in the direction parallel to the laser. We were looking for an obvious decrease in linewidth due to a reduced Doppler broadening, but found none. As was previously mentioned however, it is very difficult to measure accurate linewidths using frequency modulation, therefore, this result is inconclusive.

Nozzles K, L, M, N, and P were used to study the effect of having an angle on the high pressure side. This experiment was suggested by Ken Leopold.[30] The nozzles beveled on the high pressure side showed little variation except for M, which also had a bevel on the low pressure side. This result was interpreted to mean that the high pressure side geometry has little effect. Nozzle M, with the bevel on both sides, did not perform well. The other four were as good or better than nozzle 1. Therefore, it appears that the important criterion is that there not be surfaces on the low pressure side which interfere with the expansion. One type of nozzle that was not investigated is the Laval nozzle in which the nozzle tapers outward on both the high and low pressure sides. There are no

sharp corners or edges on this type of nozzle to create turbulence in the flow. This type of circular nozzle has been shown to yield greatly increased cluster formation.[31] It was not tested because it requires fairly sophisticated machining techniques and this study was focussed on simple nozzle designs. It should be considered in future studies.

The temperature determinations for all of these nozzles were inconclusive in that there was no large temperature deviation with any of the nozzles, even those which performed very poorly. The average temperature was 2.9 K with an average deviation of only 0.6 K.

Based on all of the nozzle results, a new nozzle was designed. It is made of stainless steel. The body of the nozzle is 5" long, the actual slit length is 4". The nozzle and plate design are shown in Figure 2.15. The plates are .125" thick with a .062" throat depth. The front surfaces are flat and for the first time, the screws are recessed to reduce any possible jet turbulence. The .062" thickness was removed from the inside surface of the nozzle so that the low pressure side surface of the plates could be flat, with no steps or bevels, to minimize turbulence. Measurement of several different dimer spectra indicate that this nozzle provides an increase in signal of a factor of two to three over the original 1½" nozzle.

The nozzle can also be temperature controlled. The inlet tubes are jacketed for cooling liquid which then flows through

Figure 2.15 The 4" temperature-controlled nozzle

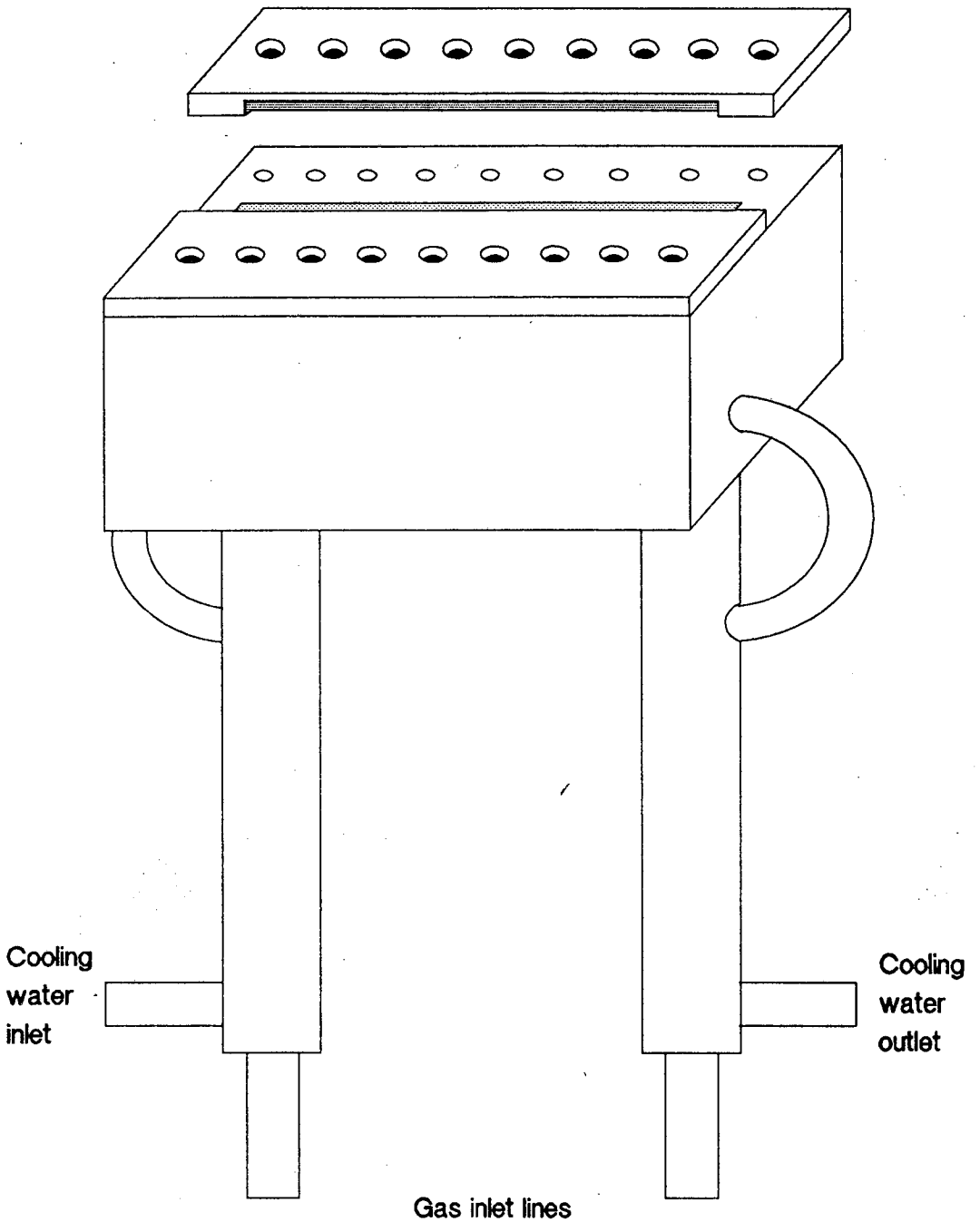

the body of the nozzle. The nozzle was designed such that the connections for the coolant are outside of the vacuum chamber to eliminate the possibility of leaks under vacuum. The vacuum feedthroughs for the gas inlet tubes are ¾" drilled-through Cajon Ultra-torr fittings. These fittings allow the nozzle position to be adjusted, moving the nozzle relative to the laser to optimize the signal. Cooling systems could be either a closed-cycle refrigerator or various dry ice baths. Liquid nitrogen cooling, however, is not feasible because the jacketed inlet tubes are not insulated and would be in contact with air outside the chamber, resulting in excessive condensation and nitrogen loss. Also, the feedthrough fittings have o-ring seals which could easily fail at liquid nitrogen temperature. Even modest cooling of the nozzle should improve the cluster formation, particularly for the larger clusters. In tests recently conducted by Matt Elrod and David Steyert[32], it was observed that dimer signals, ArHCl and $(HCl)_2$, were somewhat reduced when the nozzle was cooled with a -78°C dry ice bath. However, trimer formation, Ar_2HCl, appeared to improve by approximately a factor of two.

2.9 Conclusion

The initial goal of this project was to design and build a planar supersonic jet and use it to study weakly bound clusters using the recently built tunable far infrared laser spectrometer. The combination of these two techniques proved

to be extremely successful. The jet provides a high density, long pathlength source of clusters and the laser makes it possible to probe the low frequency vibrations, tunneling motions, and hindered rotations directly. The technique also proved to be very versatile. Many dimers have been studied including ArHCl[14], $(HCl)_2$[15], $ArNH_3$[16], ArH_2O[18], and $(H_2O)_2$[19]. Very recently the system was also used to study NH_2 radical.[33]

In the first cluster study, the Σ bend of ArHCl, it became apparent that this experiment represented a significant improvement over the other far infrared laser techniques, laser electric resonance and laser magnetic resonance. This technique requires no electric or magnetic fields which can greatly complicate the spectrum. The planar jet also provides a reduction in the Doppler broadening over a circular nozzle due to a reduction in the divergence of the jet. This line narrowing results in both an increase in sensitivity, due to the increased peak intensity, and an increased resolution. The tunable far infrared laser offers the advantage that the tuning range available on a single laser line is much greater and therefore scanning is much simpler.

The later work was directed toward improving the original nozzle design. The intensity of several ArH_2O lines were studied as a function of nozzle length and nozzle plate geometry. For many reasons it is difficult to derive more than qualitative results from these studies. However, based on this work a new 4" long nozzle was built which has demonstrated a

factor of two increase in signal over the original nozzle design.

Chapter 2 References

1. H. Ashkenas and F.S. Sherman, Fourth Symposium on Rarefied Gas Dynamics, Vol. II, J.H. deLeeuw, ed. (Academic Press, NY, 1966), p. 84; O.F. Hagena and W. Obert, J. Chem. Phys. **56**, 1793 (1972); Y.T. Lee and Y.R. Shen, Phys. Today **33**, 52 (1980); O.F. Hagena, Surf. Sci. **106**, 101 (1981); A. Amirav, U. Even, J.Jortner, F.W. Birss, and D.A. Ramsey, Can. J. Phys. **61**, 278 (1983).

2. R.E. Smalley, L. Wharton, and D.H. Levy, Accts. Chem. Res. **10**, 139 (1977); D.H. Levy, Science **214**, 263 (1981).

3. T.R. Dyke, B.J. Howard, and W. Klemperer, J. Chem. Phys. **56**, 2442 (1972); W. Klemperer, J. Mol. Struct. **59**, 161 (1980).

4 W.R. Lambert, P.M. Felker, and A.H. Zewail, J. Chem. Phys. **74**, 4732 (1981).

5. Y. Mizugai, H. Kuze, H. Jones, and M. Takami, Appl. Phys. B **32**, 43 (1983).

6. A. Amirav, U. Even, and J. Jortner, Chem. Phys. Lett. **83**, 1 (1981).

7. R.L. Robinson, Ph. D. Dissertation, University of California, Berkeley (1987).

8. R. Campargue, Fourth Symposium on Rarefied Gas Dynamics, Vol. II, J.H. deLeeuw, ed. (Academic Press, NY, 1966), p.274; H.C.W. Beijerinck, R.J.F. Van Gerwen, E.R.T. Kerstel, J.F.M. Martens, E.J.W. Van Vliembergen, M.R.T. Smits, and G.H. Kaashoek, Chem. Phys. **96**, 153 (1985).

9. K. Veeken and J. Reuss, Appl. Phys. B **38**, 117 (1985).

10. C.M. Lovejoy and D.J. Nesbitt, Rev. Sci. Instrum. **58**, 807 (1987).

11. C.M. Lovejoy and D.J. Nesbitt, J. Chem. Phys. **86**, 3151 (1987); C.M. Lovejoy, M.D. Schuder, and D.J. Nesbitt, J. Chem. Phys. **86**, 5337 (1987); C.M. Lovejoy and D.J. Nesbitt, J. Chem. Phys. **87**, 1450 (1987); D.C. Clary, C.M. Lovejoy, S.V. O'Neil, and D.J. Nesbitt, Phys. Rev. Lett. **61**, 1576 (1988); C.M. Lovejoy and D.J. Nesbitt, J. Chem. Phys. **91**, 2790 (1989).

12. W. Demtröder, Laser Spectroscopy-Basic Concepts and Instrumentation (Springer-Verlag, New York, 1982).

13. O.F. Hagena, Surf. Sci. **106**, 101 (1981).

14 K.L. Busarow, G.A. Blake, K.B. Laughlin, R.C. Cohen, Y.T. Lee, and R.J. Saykally, Chem. Phys. Lett. **141**, 289 (1987); K.L. Busarow, G.A. Blake, K.B. Laughlin, R.C. Cohen, Y.T. Lee, and R.J. Saykally, J. Chem. Phys. **89**, 1268 (1988).

15. G.A. Blake, K.L. Busarow, R.C. Cohen, K.B. Laughlin, Y.T. Lee, and R.J. Saykally, J. Chem. Phys. **89**, 6577 (1988).

16. D.H. Gwo, M. Havenith, K.L. Busarow, R.C. Cohen, C.A. Schmuttenmaer, and R.J. Saykally, Mol. Phys., in press.

17. M. Havenith, R.C. Cohen, K.L. Busarow, D.H. Gwo, and R.J. Saykally, J. Chem. Phys., manuscript in preparation.

18. R.C. Cohen, K.L. Busarow, K.B. Laughlin, G.A. Blake, M. Havenith, Y.T. Lee, and R.J. Saykally, J. Chem. Phys. **89**,

4494 (1988); R.C. Cohen, K.L. Busarow, Y.T. Lee, and R.J. Saykally, J. Chem. Phys. **92**, 169 (1990).

19. K.L. Busarow, R.C. Cohen, G.A. Blake, K.B. Laughlin, Y.T. Lee, and R.J. Saykally, J. Chem. Phys. **90**, 3937 (1989).

20. R.C. Cohen, K.L. Busarow, C.A. Schmuttenmaer, and R.J. Saykally, to be published.

21. J. Farhoomand, G.A. Blake, M.A. Frerking, and H.M. Pickett, J. Appl. Phys. **57**, 1763 (1985).

22. K.B. Laughlin, Ph.D. Dissertation, University of California, Berkeley, 1988.

23. H.R. Fetterman, P.E. Tannenwald, B.J. Clifton, C.D. Parker, W.D. Fitzgerald, and N.R. Erickson, Appl. Phys. Lett. **33**, 151 (1978); E. Sauter, G.V. Schultz, and R. Wohlleben, Int. J. Infrared and Millimeter Waves, **5**, 451 (1984); H.P. Röser, E.J. Durwen, R. Wattenbach, and G.V. Schultz, Int. J. Infrared and Millimeter Waves, **5**, 301 (1984).

24. R.C. Cohen, Ph.D. Dissertation, University of California, Berkeley, anticipated 1991.

25. D. Ray, R.L. Robinson, D.H. Gwo, and R.J. Saykally, J. Chem. Phys. **84**, 1171 (1986); R.L. Robinson, D. Ray, D.H. Gwo, and R.J. Saykally, J. Chem. Phys. **87**, 5149 (1987); R.L. Robinson, D.H. Gwo, D. Ray, and R.J. Saykally, J. Chem. Phys. **86**, 5211 (1987); R.L. Robinson, D.H. Gwo, and R.J. Saykally, Mol. Phys. **63**, 1021 (1988); R.L. Robinson, D. Ray, and R.J. Saykally, J. Chem. Phys. **87**, 5156

(1987).

26. J.M. Hutson and B.J. Howard, Mol. Phys. **43**, 493 (1981); J.M. Hutson and B.J. Howard, Mol. Phys. **45**, 769 (1982); J.M. Hutson, J. Chem. Phys. **89**, 4550 (1988).

27. F.C. DeLucia, P. Helminger, and W. Gordy, Phys. Rev. A **3**, 1849 (1971).

28. G.A. Blake, private communication.

29. J.R. Heath and A.L. Cooksy, private communication.

30. K. Leopold, private communication.

31. O. Abraham, J.H. Binn, B.G. DeBoer, and G.D. Stein, Phys. Fluids **24**, 1017 (1981).

32. M.J. Elrod, D.W. Steyert, and R.J. Saykally, J. Chem. Phys., in press.

33. R.C. Cohen, K.L. Busarow, C.A. Schmuttenmaer, Y.T. Lee, and R.J. Saykally, Chem. Phys. Lett. **164**, 321 (1989).

Chapter 3 The Water Dimer

3.1 Introduction

Water plays a central role in chemical and biological systems, typically acting as the solvent in which chemical reactions occur. However, despite its importance in so many systems, the liquid phase of water is still quite poorly understood, due in part to the lack of an adequate water-water intermolecular potential surface. As was demonstrated by Jeremy Hutson for the Ar-HCl system,[1] it is possible to determine a very good intermolecular potential surface for weakly interacting systems strictly from spectroscopic data. The goal of this research is to provide some of the data necessary to determine an accurate intermolecular potential surface for the water dimer, anticipating that such information could contribute to a better understanding of larger water clusters, and, ultimately, to liquid water.

In the last few years, the water dimer has become one of the most extensively studied hydrogen bonded clusters. It is similar to $(HF)_2$, which is now quite well understood. However, the water dimer is complicated by being larger, and by having the possibility of more feasible tunneling motions. As such, it has served as a testing ground for fairly new theories, based on permutation-inversion groups. Although these approaches were developed in the early 1960's, they have not been extensively used, primarily because the various technologies required to produce and probe very non-rigid

molecules were developed only recently.

It will become apparent that the study of the water dimer has not only spanned over a thirty year period, but has required the application of many different techniques, both experimental and theoretical, and the combined efforts of many scientists. This chapter is designed to review much of this work in something of a chronological sequence. First the earliest experimental and theoretical results which contributed to the structural determination of the water dimer are discussed. Following this is a discussion of permutation-inversion group theory and the development of the energy level diagram for the vibrational ground state. The next section presents the more recent experimental results, including our own far infrared work, all of which support the proposed energy level diagram. The final section of this chapter focusses on important experiments which remain to be accomplished, including high resolution spectroscopy of the intermolecular vibrational modes of $(H_2O)_2$, as well as high resolution studies of larger water clusters, particularly the trimer.

3.2 Early Experiments

The goal of the earliest the water dimer studies was to establish the binding energy and the structure of the complex. The first studies measured the second virial coefficient of water vapor in order to determine the binding energy. Later,

different techniques were employed to obtain the binding energy, as well as the structure, and included matrix isolation, molecular beam mass spectrometric deflection studies, molecular beam scattering experiments, and high resolution microwave spectroscopy. Also at this time, there were a number of theoretical studies aimed at determining the lowest energy configuration. Three plausible structures of the water dimer were considered in many of these experiments, and are shown in Figure 3.1. Of these three, only the open structure has the expected linear hydrogen bond, and therefore, studies which supported the other two structures were rather controversial. These experiments are differentiated from later experiments for one of two possible reasons. The first is that the nature of the experiment resulted in only qualitative or low resolution results. These were useful experiments, but did not give great insight into the details of the potential surface. The second reason is that, as in the case of the microwave spectroscopy experiments, the work preceded the development of the theoretical tools necessary to thoroughly analyze the results. High resolution data were obtained, but they could not be interpreted at that time.

3.2.1 Second Virial Coefficients and Thermal Conductivity

The measurement of such gas phase properties as the second virial coefficient or the thermal conductivity provides

Figure 3.1 Three plausible water dimer structures

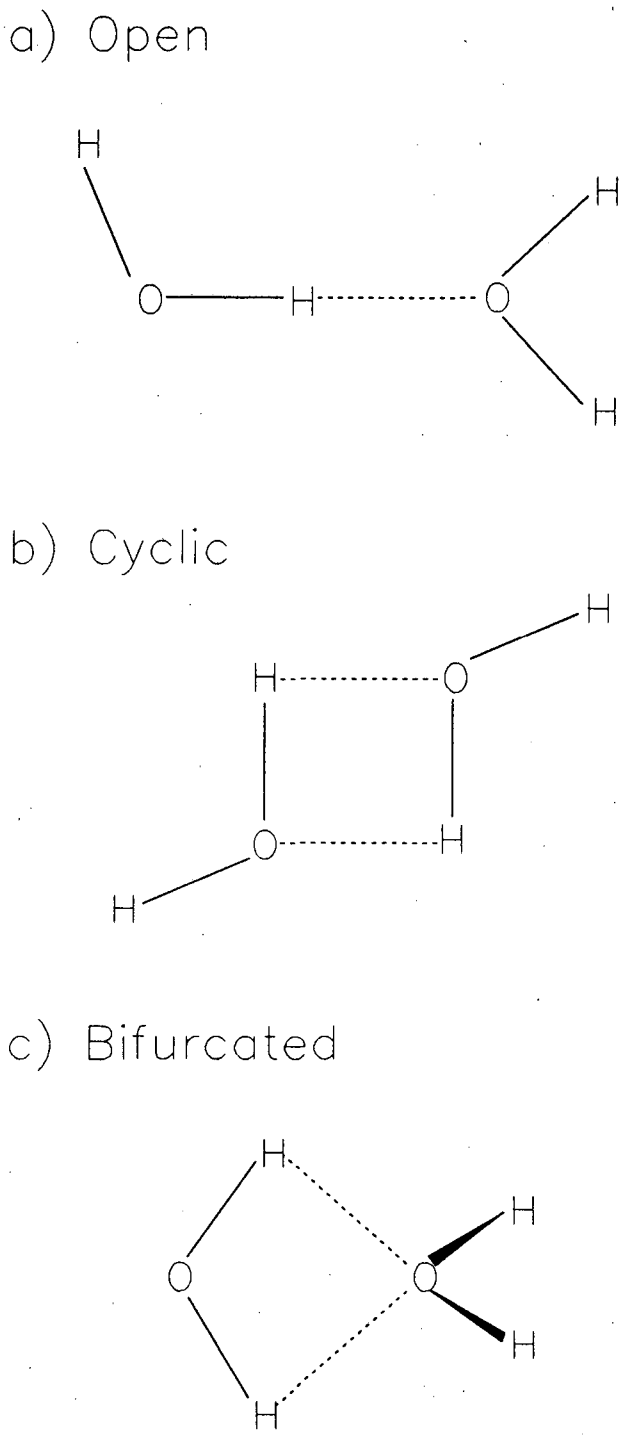

a characterization of the nonideal behavior of gases. Assuming that the nonideality is due to dimer formation allows for an estimation of the binding energy of the dimer. These measurements are simple, and were the first experimental determinations of the water dimer binding energy. The description provided here is a rather simplistic approach, however, the purpose is only to demonstrate how these measurements can be utilized. More detailed descriptions can be found in References 2-5.

The virial equation of state of a gas includes correction terms to the ideal gas law:

$$PV/RT = 1 + B(T)P + C(T)P^2 + \ldots \qquad (3.1)$$

The second virial coefficient (B), is the temperature dependent first order correction and V is the molar volume of the gas. In most cases, the second order term (C(T)) is ignored. Pressure measurements are taken at a variety of temperatures to determine B(T). The next step is then to determine how it is related to the binding energy of the dimer. A rigorous derivation is outlined in Stockmayer's work.[2] A simpler approach comes from a paper by Lambert[3] and is based on the law of corresponding states. This law states that all gases deviate from ideal behavior in a way that is only dependent on the reduced pressure and temperature. The reduced pressure is defined as the measured pressure divided by the pressure at the critical point. Figure 3.2 shows this behavior. In terms of reduced variables, all gases deviate in

Figure 3.2 Taken from Reference 6, this plot shows the deviation from ideal gas behavior of a number of gases.

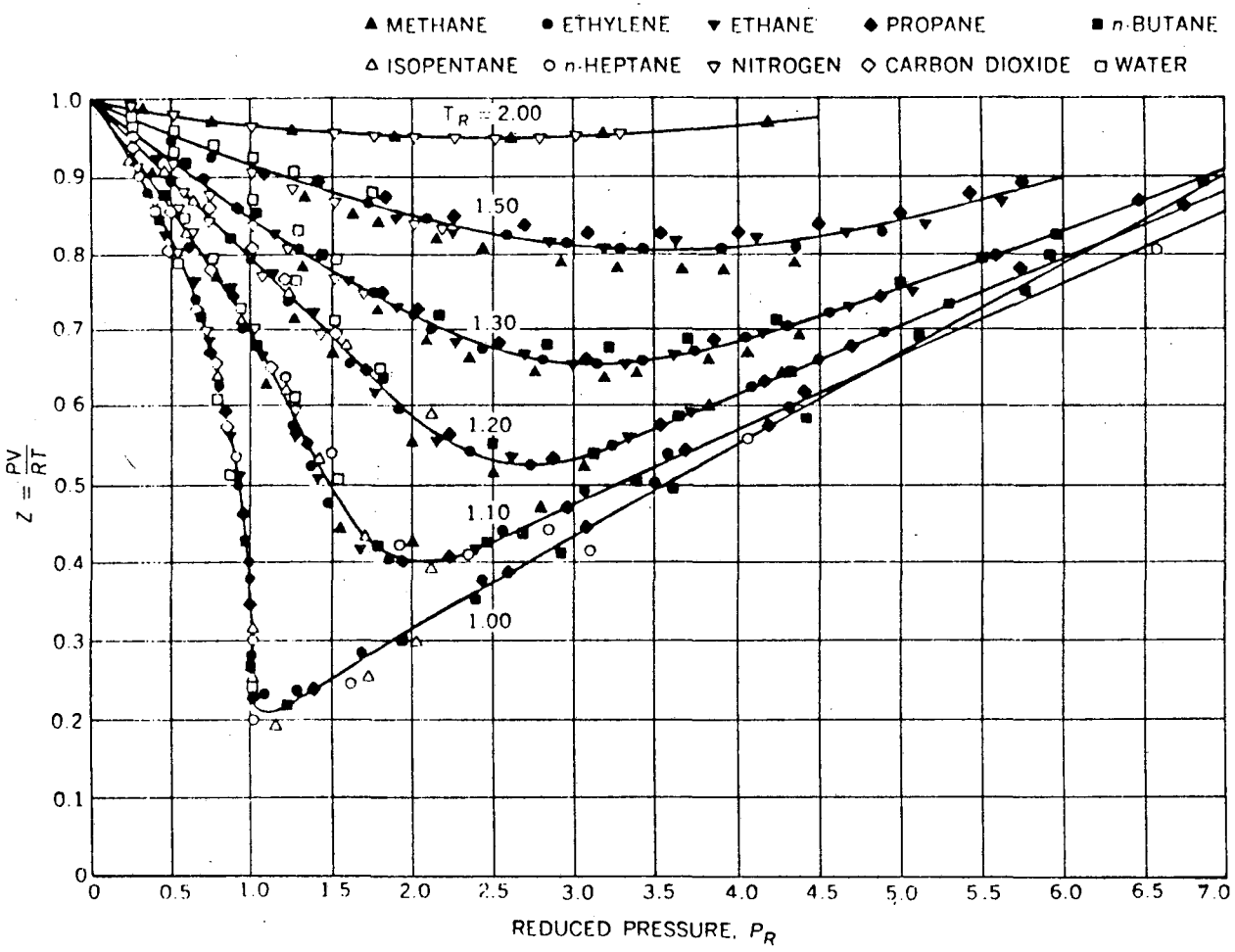

much the same way. The exception is in the case of polar molecules which exhibit strongly anisotropic interactions, such as water. The assumption is that polar molecules do not follow the law of corresponding states due to dimerization. Therefore, the measured second virial coefficients can be considered as the sum of two terms:

$$B_{Obs} = B + B_{Dimer} \qquad (3.2)$$

Here B is the part that conforms to the corresponding states principle and B_{Dimer} is the deviation due to the dimerization. Figure 3.3 shows a plot of second virial coefficients as a function of reduced temperature for a number of gases. The solid line is the predicted value of B; the deviation (B_{Dimer}) is quite apparent, especially at lower temperatures. The deviation is related to the dissociation constant of the dimer:

$$B_{Dimer} = -RT/K_p \qquad (3.3)$$

$$K_p = (p_{Monomer})^2/(p_{Dimer}) \qquad (3.4)$$

From simple thermodynamics, the enthalpy and entropy of association can be calculated:

$$\ln K_p = -\Delta G/RT \qquad (3.5)$$

$$= -(\Delta H - T\,\Delta S)/RT \qquad (3.6)$$

$$= -\Delta H/RT + \Delta S/R \qquad (3.7)$$

Plotting $\ln K_p$ versus 1/T yields $\Delta H/R$ as the slope and ΔS can be calculated from these properties. The values obtained are $\Delta H = -5700$ cal/mole and $\Delta S = -25.8$ cal/mole-deg.[3]

The thermal conductivity measurements are very similar in

Figure 3.3 A plot of the second virial coefficients as a function of reduced temperature for a number of gases, taken from Reference 3.

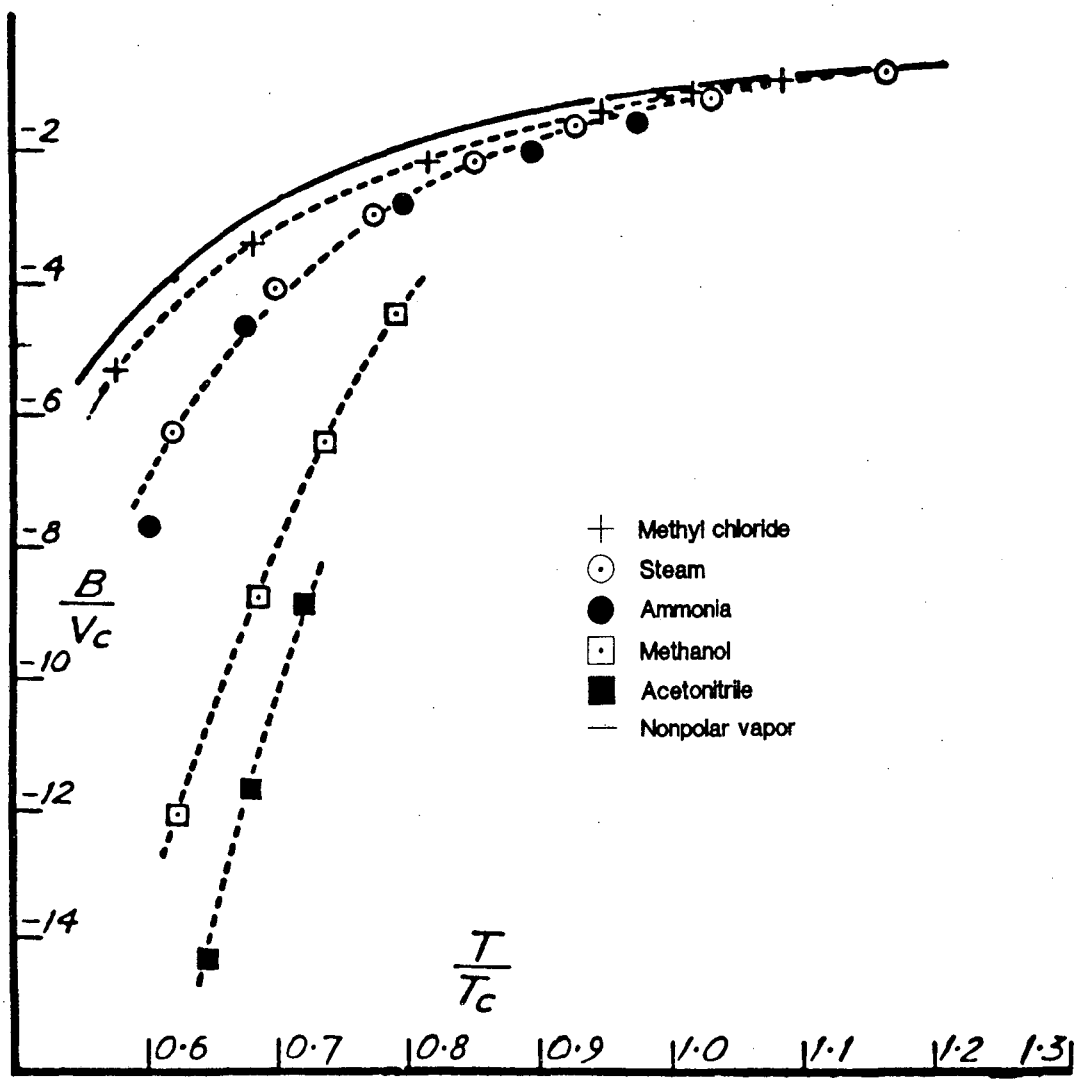

that the nonideal behavior is measured as a function of temperature. The mathematics is somewhat more complicated and is presented in the papers by Curtiss, Frurip, and Blander.[4,5] Their results indicate that the enthalpy and entropy of the water dimer association are $\Delta H = -3.59$ kcal/mole and $\Delta S = -18.59$ cal/mole-deg. Both of these methods make the questionable assumption that the quantity of larger clusters is negligible.

3.2.2 Matrix Isolation Technique

The first spectroscopic observation of the water dimer was made by Van Thiel, Becker, and Pimentel[7] in 1957 using the matrix isolation technique. In these experiments, water is codeposited with nitrogen on a window at 20K. The matrix serves a dual purpose in that it provides a cold environment, facilitating the binding of the clusters as well as providing a cage-like structure in which a given cluster is essentially trapped, and therefore cannot form larger aggregates. The clusters are then probed using a low resolution (approx. 8 cm^{-1} at 3000 cm^{-1} and 2 cm^{-1} at 1600 cm^{-1}) infrared spectrophotometer at a variety of water concentrations. In this manner they could determine the concentration dependence of a given peak and thereby establish the cluster size. Based primarily on the number of peaks observed for the dimer, Van Thiel and coworkers proposed that the water dimer was cyclic (Figure 3.1b). Only two bands were observed in the OH stretching

region; this ostensibly eliminated the open structure, which has three different hydrogen environments. Also, only one band was observed in the bending region, eliminating the bifurcated structure, which would be expected to exhibit two bending bands. The cyclic structure was thus the only one consistent with these matrix observations. In 1969, matrix infrared studies were reported by Tursi and Nixon.[8] These experiments were very similar to the Van Thiel et al. work. These were, however considerably higher resolution studies (approx. 1 cm^{-1}), and deuterium substituted structures were also investigated. This higher resolution experiment revealed new dimer bands not observed in the Van Thiel experiment. These new bands strongly suggested that the open structure was the correct one. Further work by Ayers and Pullin[9] and by Fredin, Nelander, and Ribbegård[10] also supported the findings of Tursi and Nixon that the dimer possesses an open structure. An interesting result observed in the various isotopic studies[8,9,10] was that the deuterium bonded HOD complexes are considerably more stable that the hydrogen bonded DOH complexes. Fredin et al.[11] were able to demonstrate that in a sufficiently cold matrix, it is possible to trap the less stable form by irradiating the matrix. More recent work by Bentwood, Barnes, and Orville-Thomas[12] provides a very thorough investigation of water in argon and nitrogen matrices in the infrared and far infrared regions. This work further supports the proposed open structures and assigns a large number of

bands to the dimer and to larger polymers, including combination bands and several intermolecular vibrational bands observed in the far infrared. These low frequency assignments will facilitate the search for the high resolution intermolecular vibrational studies in the far infrared, which will be discussed in a later section. Their results also indicated that polymers larger than the dimer are most likely cyclic.

Although these matrix studies are limited in resolution, they provided the first spectroscopic observation of the water dimer, revealed the qualitative nature of the hydrogen bonding, and made a significant contribution toward the establishment of the structure of the complex. These experiments also resulted in the assignment of a large number of water cluster bands, including isotopically substituted species, which will simplify the more complex high resolution assignments.

3.2.3 Molecular Beam Elastic Scattering Measurements

Molecular beam elastic scattering measurements can, provide important information about the interaction potential, including the well depth, bond length, and number of bound vibrational states. However, there are a number of assumptions made in this type of an analysis. One assumption is that the potential is isotropic. Also, in a polyatomic system, the results are often fit to a simple radial potential such as a

Lennard-Jones (12,6) form, which can be quite inaccurate for weakly bound systems.[13] Also, for such an analysis to be successful, the molecular beam conditions must be ideal; that is, the velocity distribution, as well as the rotational distribution, must be narrow and well-defined. The extent of cluster formation in the beams must be very small. It is also required that the amount of inelastic scattering must be small. However, this is a property of the system and cannot be controlled by the experimentalist.

In light of these many requirements, it is understandable why very few H_2O-H_2O scattering experiments have been performed, and that among those few, there is a fair amount of disagreement and large discrepancies with other experimental results. Inversion of scattering data works well for rare gas systems and even rare gas-diatomic systems, such as Ar-HCl.[14] In the case of H_2O-H_2O scattering, however, there are two asymmetric top molecules with large dipole moments. The experiment is essentially averaging over very different types of collisions, including favorable ones in which the hydrogen is collinear and between the two oxygens, as well as very unfavorable collisions, in which the two oxygens collide directly. These scattering experiments are presented here for the sake of completeness, even though the results from them are not in agreement with any other experimental or theoretical results.

The earliest molecular beam scattering work was performed

by Kydd in 1962.[15] He obtained the total scattering cross section of H_2O using two effusive gas sources. The effusive source temperature was 65°C, and therefore, the rotational and translational distributions were quite wide. Also, no steps were taken to reduce the dimer formation. The cross section was obtained at four different scattering gas densities, and averaged to give $Q = 615 \pm 65 \times 10^{-16}$ cm^2. This value is then used to calculate C_6, the coefficient of a $1/r^6$ potential. From this experiment, C_6 was $610 \pm 150 \times 10^{-60}$ ergs cm^6. Kydd also calculated the various contributions to the C_6 term, including dipole-dipole, dipole-induced dipole, and dispersion. He obtained an estimated value of 313×10^{-60} ergs cm^6, a factor of two smaller than the experimental result.

In 1973, Snow and coworkers,[16] also determined the total cross section for the water-water system using a supersonic molecular beam scattering from water in a static gas cell. Direct comparison with the Kydd experiment is complicated due to differences in the conditions in the two experiments. However, adjusting for these differences, Snow et al. determine that their cross section is about 50% smaller and their value for C_6 is about six times smaller, implying that their value is also about three times smaller than the estimated value from Kydd's calculations. A third experiment performed by Wendell[17] yields a cross section and C_6 value close to the Snow results, but even smaller.

The first differential elastic cross section measurements

were performed by Bickes and coworkers in 1974.[18] This experiment used a supersonic source crossed by an effusive source, measuring the scattering intensity as a function of angle using a He cooled bolometer detector. The small angle results show an anomalous drop in intensity, which could be due to inelastic scattering. The results were fit, with some difficulty, to a Lennard-Jones (12,6) potential giving a well-depth of 5.8×10^{-14} ergs (292 cm^{-1}), which is six times smaller than theoretical predictions. This well depth was calculated assuming that r_m, the bond length at the potential minimum, was equal to 2.62Å, a value obtained from bulk properties. In 1975, a second study by Bickes and coworkers[19] obtained values of 390 ± 22K (271 ± 15 cm^{-1}) for the well depth and 2.75Å for σ, which is the bond distance at the zero crossing of the potential.

It is apparent from these results that elastic scattering is not an effective means for determining the potential for a strongly anisotropic system like $(H_2O)_2$. The small values obtained for the well depth imply that the anisotropic contributions to the binding energy are quite significant.

3.2.4 Fourier Transform Far Infrared Studies

The earliest observations of the water dimer in the far infrared were atmospheric measurements performed using a Fourier transform spectrometer. Much of the atmospheric far infrared spectrum had been carefully mapped out, many of the

absorptions being assigned to water vapor. In 1957, Gebbie observed anomalous peaks between 7 and 9 cm^{-1}, which appeared to be dependent on the water vapor concentration. However, these results were not published. Later, in 1968, further observations confirmed these results. Gebbie and coworkers also observed an anomalous peak at 22 cm^{-1} and a stronger than expected continuum absorption around 30 cm^{-1}.[20,21] In 1969, Gebbie and coworkers conducted two different laboratory experiments using a long pathlength, low pressure gas cell, which confirmed that at least some of these absorptions were due to water dimers present in the atmosphere.[22] In the first experiment, a Fourier transform far infrared spectrometer was used to monitor the intensity of a peak at 7.5 cm^{-1} as a function of pressure. The intensity was found to be directly proportional to the square of the pressure, indicating that it was due to water dimers. Also, a temperature study was performed; from the Arrhenius plot, a binding energy of 6 ± 3 kcal/mole was determined. The pressure dependence of the intensity of the peaks at 9.3 and 22 cm^{-1} could not be determined due to the small observed signal. In the second experiment, an HCN maser was used to measure the absorbance at 29.71 and 32.17 cm^{-1}. The absorption at 32 cm^{-1} is due primarily to monomer absorption, while at 29 cm^{-1}, the absorption is in the anomalous continuum region. Measuring the ratio of the absorbance at these two frequencies as a function of pressure indicated that the continuum was not wholly due to

monomer absorption, but rather, about half of the signal was due to the dimer and possibly larger clusters. An Arrhenius plot of the data from this region gave an improved value of 5.2 ± 1.5 kcal/mole for the binding energy of the dimer. Several other anomalous absorptions have been observed in the far infrared, however, these are not confirmed water dimer absorptions. For example, Farmer and Key observed lines which were not assigned to the monomer at 317.5 and 359.2 cm^{-1}.[23] They chose not to speculate on the origin of these atmospheric absorptions. These frequencies are listed in Table 3.1.

Although these measurements were made at fairly low resolution, they demonstrated that the dimer was stable enough to exist in a measurable concentration in the atmosphere. Also, these studies provide a simple starting point for high resolution far infrared searches for the water dimer.

3.2.5 Mass Deflection and Initial Microwave Studies

For many years, microwave spectroscopy has been an extremely valuable technique in structural determinations of molecules and complexes. This success is due in part to the high resolution attainable in the microwave region, which provides detailed hyperfine information. Also, the microwave technology is very advanced compared to most infrared laser techniques, making these experiments more straightforward to implement. However, under the extremely cold conditions encountered in the supersonic expansions used in cluster

Table 3.1 The frequencies of far infrared atmospheric absorptions possibly due to water dimer absorptions.

Frequency (cm^{-1})	Reference	Comments
7.5	22	Shows $[H_2O]^2$ dependence
9.3	22	Weak
22	22	Weak
317.5	23	
359.2	23	

experiments, microwave spectroscopy can only probe the lowest region of the potential surface. This is sufficient to determine a vibrationally averaged structure in favorable cases. It does not provide, however, the necessary information to determine a potential surface, which is the ultimate goal in the water dimer experiments. As in the case of the matrix isolation technique, it is important to recognize the limitations of these methods. Yet it is important to realize that these experiments provided extremely important, detailed information about the water dimer, upon which almost every later experiment would be dependent.

One of the earliest studies of the water dimer was a molecular beam deflection experiment.[24] This is not a microwave experiment, but it is included in this section because it is a simplified version of the very powerful molecular beam electric resonance (MBER) technique which will be discussed further, and because it provided the important evidence that the water dimer is a strongly polar molecule. This result supports a non-cyclic structure. This technique employed electrostatic quadrupole fields to direct a molecular beam around an obstacle in the beam path and refocus it onto the detector. Only in the case of polar molecules would a significant signal be observed at the detector. In addition to the observation that the dimer is polar, it was determined that larger polymers were either non-polar or only slightly polar. This implies that in clusters such as the trimer or

tetramer, the structure is either cyclic or that rapid large amplitude motions "average out" the polarity of the complexes.

The first water dimer microwave spectrum was measured by Dyke and Muenter in 1973 using the MBER technique.[25] The MBER technique was developed by Hughes in 1947[26] and has been extensively utilized by many workers since that time. It has been thoroughly discussed in many papers and therefore will only be briefly described. The experiment consists of a molecular beam source, two inhomogeneous electric fields, one homogeneous electric field in which the microwave radiation is introduced, and a mass detector. The first inhomogeneous field, typically a quadrupole field, defocusses the polar molecules in the beam around a beam stop. The second region contains a homogeneous field and the microwave radiation. The third region is again a quadrupole field which refocusses the beam onto the detector. If the microwave absorption causes a change in the state of the molecule, it will no longer reach the detector and is observed as a decrease in the signal. The advantages of this technique are that the spectral assignment is very simple because the initial state of the molecules is selected by the quadrupole field and also the dipole moment of the molecule can be easily determined. The disadvantages are that the experiment is quite complex and difficult to implement, and due to the state discrimination, the signal-to-noise ratios obtainable are very low.

In the 1973 Dyke and Muenter water dimer measurements,[25]

over 50 transitions were observed over the range from 8 to 50 GHz. These transitions were quite randomly spaced, indicative of a system undergoing several large amplitude tunneling motions. Very few of these transitions were initially assigned due to the complexity of the spectrum, and therefore, the initial results were fairly qualitative. In 1976, Dyke, Mack, and Muenter reported significant progress in the assignment of the spectra in this region.[27] Additional lines had been observed in the microwave and radio frequency (rf) regions and many lines were assigned using microwave-radio frequency double resonance. In addition, Dyke had derived much of the permutation-inversion theory[28] that is essential to understanding the spectra of this complex, and which will be discussed in Section 3.4. Although many of the observed lines still remained unassigned, quite a few lines were assigned to K=0,2,3,4. Also studied were the isotopic species $(D_2O)_2$ and $(H_2{}^{18}O)_2$.

It was determined from this work that the trans-linear structure was the most likely, in agreement with the matrix studies and the quantum theorists. This structure is shown in Figure 3.4. The hydrogen bond is nearly linear, the acceptor molecule is tetrahedrally bonded, and there is a plane of symmetry. The value of (B+C)/2 for the various states measured is approximately 6100 MHz, and the oxygen-oxygen bond length is 2.98Å. The O-O bond length in ice is 0.2Å shorter, implying a stronger bond in ice due to the larger induced moments and

Figure 3.4 The trans-linear water dimer structure

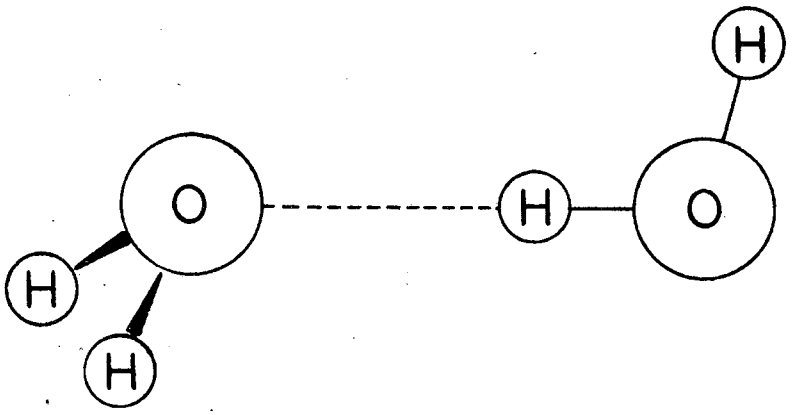

the cooperative effects of many near neighbors in the crystalline structure. The dipole moment along the a axis in the dimer is 2.6D. The dipole predicted from a simple calculation of the projected monomer dipole moments on the cluster a axis is only 2.11D, implying that the induced dipole effects are quite large. The angle between the O-O axis and the symmetry axis of the acceptor molecule is 58°, and the angle with the donor symmetry axis is -51°. The MBER work was thus the first rigorous experimental verification of the structure proposed by the theorists. The assigned transitions in this work all involve E symmetry states that are not strongly shifted by tunneling motions, as will be explained in the next section. Therefore, the spectra of these states can be fit to a standard rigid rotor Hamiltonian. The other symmetry states are expected to be strongly perturbed, which accounts for the apparently random spacing of the unassigned lines.

3.2.6 Infrared and Coherent Anti-Stokes Raman Spectra

In the early 1980's, infrared experiments were performed which took advantage of the fact that when a water cluster absorbed an infrared photon, it would eventually dissociate or vibrationally predissociate. In the experiments by Vernon and coworkers,[29,30] a neat water beam was probed using a pulsed, tunable infrared laser over the range from 2900 - 3750 cm^{-1}. The detector was a rotatable mass spectrometer. When a cluster

absorbed a photon, typically one water monomer would "boil" off. This dissociation would cause the two products to scatter out of the beam. The detector was rotated about the scattering center and fragments would be ionized and then detected. For example, if water tetramer, $(H_2O)_4$ absorbed a photon, in most cases, one water would come off and the remaining trimer could be ionized in the detector. This ionization typically resulted in the loss of OH and an electron, leaving the $(H_2O)_2H^+$ to be detected. It is possible that larger clusters, such as the pentamer or hexamer, could contribute to this signal, but smaller clusters could not. By varying the nozzle source conditions, they were able to obtain the low resolution infrared spectrum of the trimer through the hexamer. In the dimer, however, the detection scheme above would imply that the H^+ signal is associated with the dimer, which is extremely difficult to detect with a mass spectrometer. A second experimental configuration was employed in which the detector is fixed perpendicular to the beam. The IR laser was coaxial with the beam which passes through the ionizer. The various clusters were monitored as their parent mass ions, and when an absorption occurs, a loss in the parent is observed because it predissociates and leaves the beam. This scheme was used to obtain the water dimer spectrum. The H_3O^+, which was easily detected, was monitored and acted as an indicator of the dimer concentration. This signal was monitored as the laser was scanned and a decrease in the signal was interpreted as a

dimer absorption followed by predissociation.

In a later experiment, Page and coworkers[31] used the same apparatus to repeat the dimer experiments. In this work, however, the water was seeded in He, which greatly reduced both the temperature and the percentage of larger clusters formed, and therefore, simplified the spectrum. Also, in this experiment, the laser linewidth was reduced a factor of two. The spectra showed considerable structure and vibrational assignments were made and compared to the matrix work. It is clear from all of these studies that the dimer spectrum is quite different from the spectra of the larger clusters or from liquid water. This is most likely due to the water molecules in the liquid and polymers acting as both hydrogen donor and acceptor. In the dimer each monomer has a distinct donor or acceptor character.

An experiment quite similar to that of Page et al. was performed by Coker, Miller, and Watts.[32] In this experiment the water seeded in helium beam is crossed using a multipass cell with an F-center laser. The detector is a bolometer in the beam path. As in the other experiments, this detection scheme is monitoring the loss of a cluster from the beam as it absorbs, dissociates, and scatters out of the beam. A mass spectrometer was used to determine the cluster composition in the beam. There are some discrepancies between the peak assignments in this work and in the Page et al.[31] experiments. Both groups observed a number of water dimer peaks, but Coker

et al. also observed two peaks at 3357 and 3400 cm^{-1} which they assigned to the trimer. This initial experiment demonstrated the power of their technique. More extensive bolometer experiments will be discussed later in the context of the high resolution studies.

In 1987, a coherent anti-Stokes Raman experiment was performed, producing a spectrum similar to the predissociation spectra discussed above.[33] All of these experiments provided information of the vibrational assignment of the dimer and several trimer bands, but these experiments lacked the rotational and tunneling resolution needed to better understand the dimer potential surface.

3.3 Theoretical Approach to Structure and Potential Surface Determination

The water dimer has long been recognized as a prototypical hydrogen bonded cluster, and as the simplest system for modelling for liquid water. The list of theoretical investigations is extensive. The numerous theoretical investigations can be categorized into roughly four groups, based on the ultimate goal of the study. The first of these groups includes those papers which attempt to determine the lowest energy structure and the binding energy of the water dimer. Many of the earliest papers are in this category. The second group is comprised of those papers in which a potential energy surface is developed and investigated. The third

category consists of those studies in which the authors utilize previously developed potentials to determine properties, such as the vibrational frequencies and intensities. These papers will be fully discussed at the end of this chapter in terms of the predictions for the intermolecular vibrational spectrum. The last category includes those papers in which a detailed energy level diagram is developed, making use of group theory, available potential surfaces, and experimental results. This group of papers is extremely important in understanding the high resolution spectroscopy and will be extensively discussed in a later section. Therefore, the present section will focus primarily on the first two categories, the structural determination and potential energy surfaces developed.

3.3.1 Structural Determination

The earliest theoretical studies of the water dimer focussed on the determination of the structure. A detailed understanding of the water dimer structure is crucial to predicting and interpreting experimental results, particularly the spectroscopic results. In addition, several of these papers include calculations of larger clusters as well, and provide a large fraction of what is currently understood about the higher polymers. Early matrix work proposed that the dimer had a cyclic structure,[7] while other experiments indicated that there was a single, linear hydrogen bond, referred to as

the open structure. Therefore, the early theoretical approach was to determine the binding energy for a number of reasonable structures, including the open, cyclic, and bifurcated structures shown in Figure 3.1. More recently, as the techniques improve and fewer approximations are required, the theoretical results are in excellent agreement with the spectroscopic results and the water dimer structure is considered well determined.

3.3.1.1 Variational Techniques

The earliest *ab initio* studies were variational calculations using the Hartree-Fock self consistent field (HF-SCF) method. The approach is straightforward. The binding energy of the complex is calculated as the difference between the energy of the entire complex, or "supermolecule", and the sum of the energies of the monomers, or subsystems. The fact that the interaction energy is much smaller than the energies of the supermolecule or the subsystems necessitates that these calculations be highly accurate. The standard SCF calculation does not include the electron correlation energy, which is a very important correction to the interaction energy, and somewhat analogous to the dispersion energy in a perturbative calculation.

The first *ab initio* calculation was performed by Morokuma and Pedersen in 1968[34] using a self-consistent field (SCF) method and a rather small Gaussian orbital basis set. The

results indicated that the open structure with the linear hydrogen bond was the most stable. The binding energy (-12.60 kcal/mole), however, was a factor of two larger than the experimental result obtained from the far infrared temperature studies (-5.2 ± 1.5 kcal/mole).[22] They calculated the energy of the cyclic structure minimum (-7.78 kcal/mole) and the bifurcated structure minimum (-9.24 kcal/mole) as well. A second ab initio study was performed by Kollman and Allen.[35] The calculations were similar, however, Kollman and Allen used a larger basis set, and obtained a binding energy for the linear dimer of -5.27 kcal/mole, which is much closer to the experimental value. They also obtained an improved near-linear structure, very similar to that which is now considered correct. The binding energy for the cyclic structure was calculated to be -4.0 kcal/mole and the bifurcated structure energy was -4.45 kcal/mole. At that time, the bifurcated structure was still considered plausible because the energy was not significantly higher.

In the following few years, quite a number of similar calculations were performed.[36-39] In general, each successive paper utilized a larger improved basis set as the available technology improved. Values determined for the binding energy fluctuated, but in almost every study, the open structure was determined to be the minimum energy structure. For example, Hankins, Moskowitz, and Stillinger,[40] using what they described as "the largest practical set" of Gaussian basis functions

calculated the dimer structure and obtained a binding energy of -4.72 kcal/mole, not including the zero-point correction.

Kistenmacher, Lie, Popkie, and Clementi[41] used something of a different approach in determining the lowest energy structure of the dimer. The fundamental assumption used was that the water dimer potential is very isotropic, and therefore, rather than trying to find a single minimum energy structure, they calculated the probability distribution of thousands of possible configurations using a Hartree-Fock potential. They also calculated larger polymers assuming pairwise additivity. They calculated the energy of possible structures of complexes up to the octamer. For the dimer, they determined that the open structure was the most stable, with a binding energy of -3.4 kcal/mole, which includes an estimation of the zero-point energy correction.

The study in 1974 by Kistenmacher, Popkie, Clementi, and Watts[42] was one of the first to include a correlation energy correction. The inclusion of electron correlation energy to the interaction energy is essential for the accurate determination of the binding energy. There are several <u>ab initio</u> approaches to calculating this quantity, including many-body perturbation theory (MBPT), also referred to as Møller-Plesset theory, and configuration interaction (CI) methods. In this study, they investigated several different modified Hartree-Fock potentials by computing the energy of a large number of dimer configurations on these surfaces and

then using a Monte Carlo algorithm to determine the minimum energy structure. The correlation energy corrections were semi-empirical terms incorporated into the potential at short and intermediate range. The long range interaction was parameterized as a $1/r^6$ term. The binding energy of the dimer was calculated on the different surfaces, however, because the large uncertainty in the experimentally determined binding energy, it was difficult to definitively support one surface over another.

The first paper to include configuration interaction in the SCF calculation as a means of determining the correlation energy was published by Diercksen, Kraemer, and Roos in 1975.[43] The intent was also to study the magnitude of the correlation effects in various neutral and ionic clusters. Their study indicated that, although the magnitude of the correlation was small, the fractional change in the binding energy of the dimer due to the correlation was large. The value obtained for the binding energy of the water dimer at the Hartree-Fock level was -5.14 kcal/mole; including the configuration interaction increases it to -6.04 kcal/mole. An estimation was also made for the zero-point vibrational correction, which is approximately 1 kcal/mole and opposite in sign to the correlation, which explains why the simple Hartree-Fock calculations that ignore these corrections were surprisingly close to the experimental value. Their corrected value for the binding energy is -5.1 ± 0.3 kcal/mole.

In 1985, Frisch, Pople, and Del Bene[44] calculated the structures, energies, and vibrational frequencies of a number of dimers, including the water dimer, using Hartree-Fock with fourth-order Møller-Plesset calculations. The binding energy obtained at the HF/6-31+G(d) level is -5.4 kcal/mole. Including the electron correlation, increases the binding energy to -6.1 and including the zero-point vibrational correction reduces it to -3.7 kcal/mole. A later paper by Frisch, Del Bene, Binkley, and Schaefer recalculated the dimer energies at a very high level of theory.[45] The structure was optimized at a number of levels up to 6-311++G(2d,2p) including electron correlation using second-order Møller-Plesset theory. The binding energy was then determined for these structures using up to fourth-order Møller-Plesset theory. At the highest level, the binding energy was -5.36 kcal/mole. Including the correction for the zero-point energy brings this value up to -3.1 kcal/mole. This study indicated that the binding energy was quite dependent on the basis set and method used in the determination. This study also investigated the magnitude of the basis set superposition error (BSSE) as a function of basis set. Briefly, BSSE in these calculations is due to the energy of the subsystems being calculated in one basis and the supermolecule energy being calculated in a second basis which is essentially twice as large. The effect of this error is to overestimate the interaction energy of the complex. One method for overcoming

this problem is to use the counterpoise method of Boys and Bernardi[46] in which subsystems and supersystem energies are calculated with the same basis set. Excluding the vibrational zero-point correction, the best calculations indicate that the water dimer binding energy is approximately 5.4 kcal/mole, including electron correlation (The zero-point correction reduces this value by approximately 2.3 kcal/mole).

In 1988, Bartlett and coworkers[47] published an extensive study of the water dimer. In this study they investigated the interaction energy as a function of the method used, as well as of the basis set incorporated. The first method studied was SCF with and without the counterpoise (CP) correction, including a dispersion term calculated by the variation-perturbation method of Jeziorski and van Hemert.[48] This allowed for a determination of the basis set superposition error for different basis sets. The second method combined SCF with many-body perturbation theory and coupled cluster calculations (MBPT/CC). About twenty different basis sets containing up to 212 basis functions were compared using both methods. One conclusion was that calculations which did not include the CP correction were very unreliable. Also, although the first method, $\Delta E_{SCF} + \Delta E_{DISP}^{(20)}$, somewhat overestimates the interaction energy (-5.7 kcal/mole), the approach is so much simpler than a full CI type calculation that it is probably the best method for large cluster calculations. The interaction energy determined by the MBPT/CC method is -4.7 ± .35 kcal/mole, not

including the zero-point correction.

The most recent results from Radom and coworkers[49] focus on calculating the energy of transition states, or barrier heights between equivalent dimer structures. The level of theory used was MP4/6-311+G(2df,2p), which has a somewhat smaller basis set than the previous paper by Schaefer et al., however, in that paper, the only concern was the minimum energy structure. The binding energy obtained in this study was -5.40 kcal/mole with a zero-point correction reducing it to -3.17 kcal/mole. This result is quite similar to others obtained using this level of theory.

3.3.1.2 Perturbational Techniques

Most of the theoretical work done on the water dimer uses variational methods. Far fewer perturbative techniques have been employed due to the difficulty in determining all of the parameters necessary for an accurate calculation. The perturbation technique essentially determines the interaction energy of a complex as the sum of a number of contributions, both attractive (long-range) and repulsive (short-range).

$$E_{Int} = E_{ES} + E_{IND} + E_{DISP} + E_{EXCH} \qquad (3.8)$$

These contributions include electrostatic contributions consisting of all the possible combinations of the various multipoles of the monomers, such as the dipole-dipole and dipole-quadrupole interaction. Other long-range contributions are the induction and dispersion energies. The short-range

contributions are the various exchange interactions, the exchange-repulsion, the exchange-induction, and the exchange-dispersion energies. One reason these perturbative calculations are not utilized much is that a large amount of information about the monomers is required, including the multipole moments, the polarizabilities, and the ionization potentials. Those quantities which are not or cannot be determined experimentally must be calculated. Also, the short-range interaction energies are very difficult to calculate unambiguously,[50] particularly the exchange-repulsion, and the other two exchange terms have only been calculated for a few small dimers. Calculations on the water dimer which combine perturbational and variational methods have been performed by Jeziorski and van Hemert in 1976[48] and Roszak and coworkers in 1986.[51] In these calculations the induction and dispersion terms were calculated using a variational technique. Jeziorski and van Hemert obtained a binding energy of -5.8 kcal/mole (with no zero-point correction) with R_{O-O} equal to 2.86Å. These perturbative method calculations are somewhat insightful in terms of calculating specific contributions to the interaction energy, however, a complete calculation is prohibitively complicated except for the smallest cluster systems.

3.3.2 Potential Surfaces

There are essentially three possible approaches to developing a potential surface. The first is the *ab initio*

surface, obtained using ab initio methods to determine the energy of the complex at a large number of configurations and then fitting these points to some functional form. The second type of surface, the empirical surface, is determined by fitting experimental results to a parameterized function. A familiar example would be a Lennard-Jones (12,6) potential. The third type of surface, the semi-empirical potential combines ab initio methods with empirical methods. For those interaction energy contributions which are considered well understood, and for which there are accurate functions available, such as multipole-multipole terms, those quantities are calculated directly. For the less well understood contributions, empirical terms are included. These terms are then parameterized and fit to experimentally determined quantities.

A number of groups have reported the binding energy, structures, and vibrational frequencies of water clusters derived from various potential surfaces they have developed. One of the first water potentials was developed in 1972 by Ben-Naim and Stillinger[52,53] and consisted of a Lennard-Jones component containing the same parameters as those determined for isoelectronic neon, as well as an angular component that guaranteed linear hydrogen bond formation. This potential was used in a number of calculations, including molecular dynamics calculations of Rahman and Stillinger[54] in which they obtained a hydrogen bond energy of -6.50 kcal/mole, and an oxygen-

oxygen distance (R_{O-O}) of 2.76Å.

Scheraga and coworkers,[55-58] in 1974, developed two different empirical surfaces. The first of these is the SS surface, developed from macroscopic properties of water. It is not generally applicable to other systems. The second surface, the empirical potential using electrons and nuclei (EPEN), was a more versatile potential than the SS potential. This potential was designed to be easily modified for systems other than water. This was accomplished by breaking up the clusters into combinations of fragments, which once parameterized could be recombined to build different potentials. The open, or trans- linear, structure was found to be the minimum energy structure, with a binding energy of -5.76 kcal/mole on the SS surface and -5.44 kcal/mole on the EPEN surface. The primary flaw with the EPEN surface was that, although it was adequate for hydrogen-bonded systems near the minimum, the long range interactions were poorly characterized. The reason for this problem was that the surface was parameterized using only the gas phase dipole moment and quantities associated with ice, including the lattice energy, x-ray structure, compressibility, and intermolecular vibrational frequencies of ice. The structured nature of ice is quite different from liquid water in that high energy structures far from the minimum are not encountered in the solid phase. Using the EPEN surface, minima were found at non-hydrogen bonded structures predicted by all other theories to be high energy structures.

A new potential was developed which was very similar to EPEN but parameterized differently to eliminate these problems.[58,59] This surface, EPEN/2 predicted a binding energy of 6.480 kcal/mole, which is actually worse than the EPEN value. However, the surface was better for the calculation of liquid water thermodynamic properties, including the internal energy, molar volume, and number of nearest neighbors. It was also proven to work well for a large number of organic liquid systems. In 1984, Sauer and coworkers[60] showed that the general applicability of this potential to other systems was fairly limited. Their method fit the EPEN/2 surface to values determined from ab initio methods, yielding the QPEN surface, the quantum mechanical potential based on interactions of electrons and nuclei. The EPEN/2 surface was good for liquid water calculations, however, the "transferability" of the surface was not as successful as anticipated. The determined O-O distance was 2.880Å (EPEN) and 2.827Å (EPEN/2), compared to 2.76Å in ice and compared to 2.98Å determined by Dyke and Muenter from the microwave spectroscopy.[25]

Matsuoka, Clementi, and Yoshimine, in 1976, developed analytical expressions for the dimer potential surface from the calculated values of the energy for various configurations at the configuration interaction (CI) level.[61] This ab initio surface, the MCY potential was then used to calculate the radial distribution functions of liquid water, as well as the x-ray and neutron scattering intensities, using a Monte Carlo

technique.[62] As for the structure of the dimer, their CI level calculations gave a value of -5.6 kcal/mole for the binding energy of the linear dimer and -4.9 and -4.2 kcal/mole for the cyclic and bifurcated structures, respectively. The correlation energy effect is calculated to be -1.1 kcal/mole for the linear structure, which is nearly identical to the value obtained by Diercksen, Kraemer, and Roos.[43] Several years later, Clementi and Habitz[63] performed very similar calculations to those of Matsuoka and coworkers.[61] The goal of this work was to probe the potential more carefully by calculating the energy of more dimer configurations. However, that reduces the size of the basis set which is manageable. The binding energy for the linear dimer was -5.5 kcal/mole with this method, with the O-O distance 2.97Å. The binding energy is not significantly different, but the authors believe that the potential surface is much improved, particularly in the repulsive region.

In 1981, Reimers, Watts, and Klein[64] developed two semi-empirical surfaces for water, referred to as RWK1 and RWK2. Parameters of the potentials were fit to match experimentally determined macroscopic quantities for the various phases of water, including the second virial coefficient for steam, lattice properties for several ices, the differential cross section for water-water scattering, as well as water dimer properties such as the structure and dipole moment. The calculated binding energy, without the zero-point energy

correction, was -5.90 kcal/mole, which is somewhat higher than that obtained by other methods. An important point to note is that the purpose of many of these potentials is to describe bulk phases of water, not necessarily the dimer. Determining these potentials from the macroscopic quantities of water results in many-body effects being implicitly included in the surface. For liquid phase water, that is not a problem, however, for a two-body system such as the water dimer, this is going to result in significant errors in calculated quantities, particularly, an overestimation of the interaction energy because of the implicit many-body contributions. This error is going to be present in all empirical and semi-empirical surfaces derived from bulk phase properties.

In 1983, Reimers and Watts combined the RWK2 surface with an intramolecular potential consisting of Morse oscillators to describe the high frequency water monomer vibrations.[65] Using this full potential (RWK2-M), they redetermined the structure of the dimer, as well as larger clusters, and also calculated the vibrational frequencies for the clusters. The dimer binding energy calculated (-6.14 kcal/mole) is even larger than from the RWK2 surface, due in part to the fact that this new potential allows for distortion of the monomer subunits to minimize the energy. In 1987, Coker and Watts,[66] again using the RWK2 surface, calculated the vibrational spectrum of the water dimer. They used quantum simulation to generate the basis set, which included electron correlation and determined

that the binding energy was -6.1 kcal/mole. With inclusion of the zero-point vibrational energy, this value was corrected to -3.6 kcal/mole.

The molecular mechanics of clusters (MMC) technique of Dykstra[67] is a unique approach to building a potential for any size or variety of clusters. First, the electric properties of the monomers, the dipole and higher moments as well as the polarizability, are calculated using high level ab initio methods. These properties are then used to generate the surface for any combinations of monomers. This method is much simpler than large ab initio surface calculations, and also is not dependent on bulk phase properties, as are many empirical surfaces, making it suitable for calculating any size cluster, from dimer to liquid. The binding energy obtained using this method is -5.57 kcal/mole, and including the zero-point correction reduces it to -3.25 kcal/mole.

In Table 3.2 is a comparison of some of the better dimer binding energies determined from the various ab initio calculations, potential surfaces, as well as the experimental work. A number of different approaches have been employed to determine a potential surface which can be used for dimer and liquid water calculations. The ab initio potentials are something of a "brute force" technique, accurate but quite expensive. The semi-empirical and empirical surfaces are less expensive but are generally determined from bulk phase properties, which make them less applicable to small clusters.

Table 3.2 The water dimer binding energy determined both experimentally and theoretically.

B.E.(kcal/mole)	R_{O-O}(Å)	Method	Reference
	2.98	Microwave spectroscopy	27
3.59		Thermal Conductivity	4,5
5.4±0.2		2nd Virial Coefficient	64
5.2±1.5		FT-FIR	22
5.8	2.86	Variation-Perturbation	48
4.7±.35 (no zero-point)	3.00	MBPT/CC	47
5.43	2.975	MMC	67
5.4 (w/ zero-point 3.7)	2.96	HF/6-31+G(d) w/MP4	44
5.36 (3.1)	2.911	HF/6-311++G(2d,2p) w/MP4	45

It has only been in the last few years with the large amount of new experimental results, that there is the opportunity to begin to more thoroughly test these various potentials and techniques.

3.3.3 Structures of the Trimers and Larger Polymers of Water

The focus of this chapter is obviously the dimer. Therefore, structural studies of the larger polymers are only going to be discussed briefly. Many of the dimer studies were extended to investigate trimers and larger polymers[66,67,68] and to discuss these methods would be repetitious. There are a several general points which should be made. The first is that there are essentially no experimental results for these larger systems to which we can compare the theory, with the notable exception of the deflection studies of Dyke and Muenter[24]. These studies indicate that polymers larger than the dimer are either nonpolar or only very weakly polar, implying that either they are undergoing rapid tunneling motions, or they are cyclic as opposed to chain structures. Most of the theoretical studies support this conclusion, even in the case of the trimer, which should be a fairly strained cyclic system. A second point to be made is that many studies which focus on the trimer are concerned with the non-additivity of cooperative effects of hydrogen bonding. In their 1970 study, Del Bene and Pople,[38] observed that the charge distribution showed that the hydrogens on the acceptor molecule become more

positive upon dimer formation, making that monomer more likely to become a donor in further complexation. This charge distribution is described in terms of gross atomic populations.[69] For hydrogen in an isolated water molecule, the atomic population is 0.808, for the acceptor hydrogens this value drops to 0.785, indicating that it becomes more positive. The free hydrogen on the donor molecule increases to 0.834, indicating that it becomes more negative. Therefore, this work demonstrates that there is a cooperative effect in the formation of larger polymers. This is clearly an important concept because so many liquid simulations use simply pair potentials that do not explicitly account for this effect. A more detailed look at the predicted spectroscopy and vibrational frequencies of the water trimer will be discussed in Section 3.5.2.

3.4 Group Theory and Energy Level Diagram

From the earliest high resolution spectroscopy studies of the water dimer, it was apparent that the interpretation and analysis was not going to be simple. Theory had predicted that the hydrogen bond strength was only 5 kcal/mole, and therefore it was expected that large amplitude tunneling motions would complicate the spectra. The study of large amplitude motions began long before the advent of molecular beam techniques which made weakly bound clusters spectroscopically accessible. The hindered internal rotations of stable molecules such as

dimethylacetylene (CH_3CCCH_3)[70], hydrazine (N_2H_4)[71], and methylamine (CH_3NH_2)[72] have been studied extensively, particularly in the microwave region. Hydrazine and methyl amine are further complicated due to the possibility of a second tunneling motion, viz. the umbrella inversion of the nitrogen. These systems provided a fundamental understanding of simple tunneling motions, which would later be applied to tunneling motions in weakly bound clusters. $(HF)_2$ was the first hydrogen bonded tunneling system which was thoroughly studied, both experimentally and theoretically.[73,74] The ultimate goal in all of these studies was to derive a Hamiltonian which explained the experimental results and provided insight into the potential surface. These simpler systems will be briefly discussed here to introduce some important concepts and present the language relevant to discussing the more complex water dimer case. In this section, the details of the high resolution spectra of the water dimer will be presented along with the theoretical methods used to understand and analyze the observed spectra. First, the various aspects of the theory of large amplitude motions will be discussed, followed by the details of the several experiments used to obtain the spectra. Finally, results of the combined fit of all the available data for the water dimer will be presented.

3.4.1 Molecular Symmetry

An appropriate place to begin in the spectroscopic study of a complicated system is with the point group theory. An understanding of the symmetry of the system can provide a great deal of information about the spectrum of the molecule. From point group theory one can derive state symmetries and selection rules, as well as spin statistical weights and allowed couplings or perturbations between states. There are many texts written which thoroughly treat group theoretical methods.[75] However, one of the fundamental assumptions in point group theory is that the molecule has essentially a rigid frame; that is, the nuclei undergo only small amplitude motions about an equilibrium position. This clearly is not the case in complexes such as $(HF)_2$ and $(H_2O)_2$, where the nuclei undergo large amplitude motions. This assumption implies that there is little to be learned from a purely point group theoretical approach in these tunneling problem. There is, however, one important exception to note, and that is the case in which the large amplitude tunneling motion takes the original structure through a configuration described by a higher symmetry group, a group which contains as a subgroup the point group of the equilibrium geometry. One of the best known examples is the NH_3 inversion. Ammonia, in its equilibrium configuration has C_{3v} symmetry, and the inversion tunneling takes it through the D_{3h} (planar) configuration. C_{3v} is a subgroup of D_{3h} and therefore, the molecule can be treated using the D_{3h} point group.

Another example in which point groups are applicable to large amplitude tunneling systems is $(HF)_2$.[73] The structure has C_s symmetry and is shown in Figure 3.5. The tunneling motion which occurs exchanges the roles of the proton donor and acceptor molecules. There are two planar paths which can accomplish this interchange, shown in Figure 3.6. The first of these is referred to as the geared path: the acceptor hydrogen moves into the hydrogen bond and essentially, pushes the donor hydrogen out of the bond. At the midpoint of this tunneling motion, the two hydrogens are on opposite sides of the axis which connects the centers of mass of the two monomers, hence, this path is also referred to as the trans path. The second path along which this interchange can occur is the anti-geared path in which the donor hydrogen leaves the bond in the same direction that the acceptor hydrogen moves into the bond. At the midpoint of this motion, both hydrogens are on the same side of the axis containing the centers of mass and therefore, this motion is also referred to as the cis path. If it is assumed that the only one of these motions occurs, then $(HF)_2$ can be treated using only point group theory. For example, if only the trans path is important, then from Figure 3.6 it can be seen that $(HF)_2$ goes through a C_{2h} configuration, which contains the C_s group as a subgroup. In this case, the C_{2h} point group is appropriate for treating the trans tunneling motion of $(HF)_2$. If the cis tunneling is the important motion, from Figure 3.6 it can be seen that it goes through a C_{2v}

Figure 3.5 The $(HF)_2$ structure

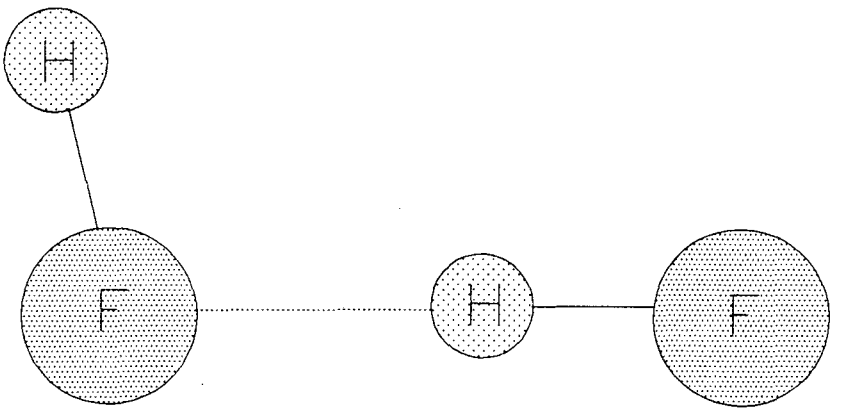

Figure 3.6 The trans and cis tunneling paths in $(HF)_2$

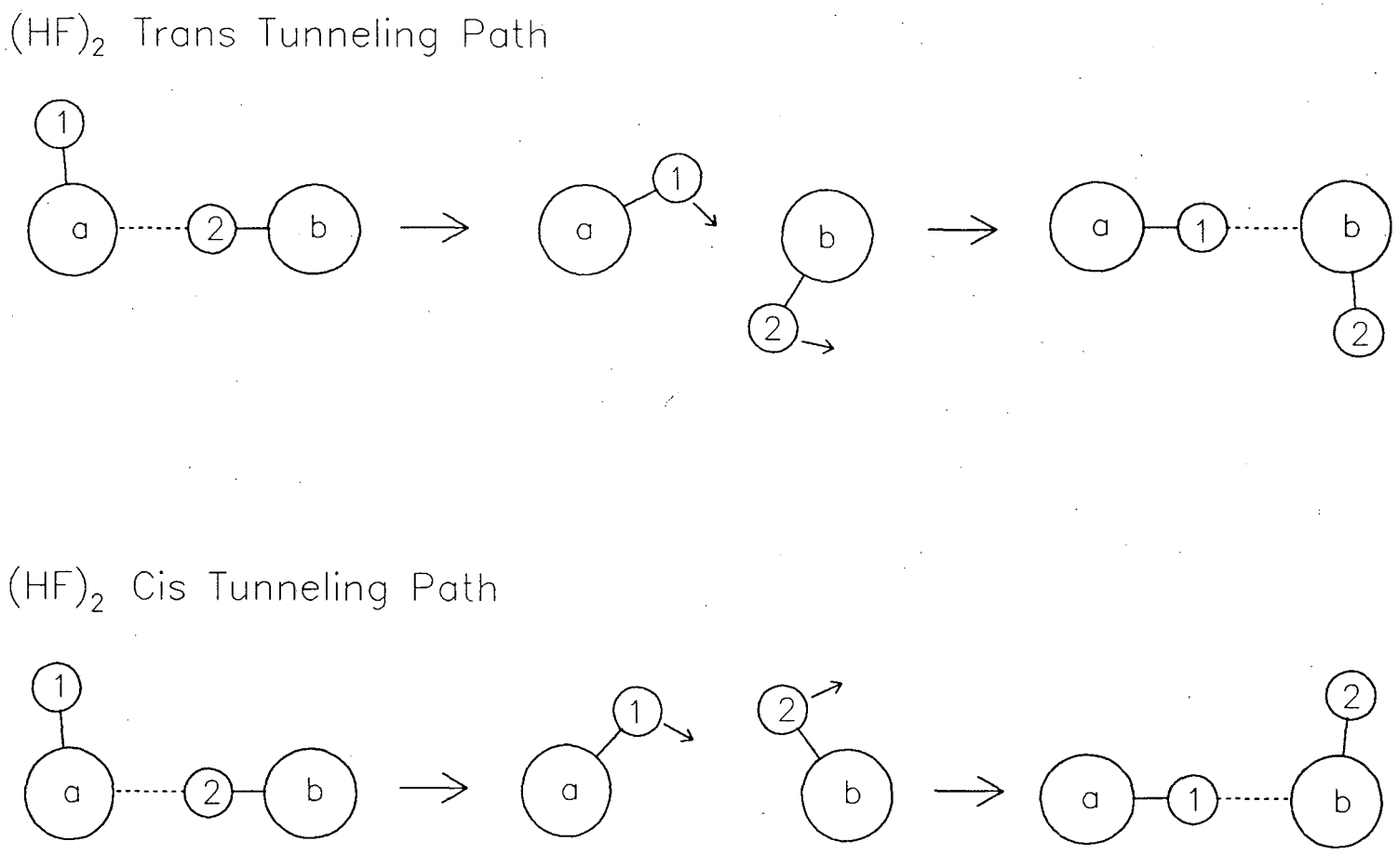

configuration, the group of which also contains the C_s subgroup. The spectra associated with these two different symmetries are likely to be different, and based on the infrared spectrum of $(HF)_2$, and the predicted statistical weights for the C_{2h} and C_{2v} groups, it was determined by Hougen that the trans path with the C_{2h} intermediate is the appropriate tunneling path.[74] This point group approach can be simple and straightforward, but it must be stressed that to apply to large amplitude tunneling systems, two criteria must be met: 1) the intermediate configuration must belong to a higher symmetry group which contains as a subgroup the point group of the equilibrium structure and 2) there can only be one tunneling path. This approach cannot be applied to $(HF)_2$ if both tunneling paths are important, or to a system like $(H_2O)_2$ in which it is anticipated that several different tunneling motions are feasible.

A second approach to the group theory, for those systems which do not meet the point group criteria, is to use molecular symmetry groups or permutation-inversion groups. PI group theory was developed by Longuet-Higgins[76] and Hougen[77] in the early 1960's. One excellent reference text is Bunker.[78] PI group theory is based on the premise that in any system where there are several identical nuclei, there is a type of symmetry that is conserved, regardless of the shape or structure of the molecule. Simply writing down the chemical formula determines the symmetry group. For example, hydrazine

(N_2H_4) is classified with a group of 48 elements (called simply "G_{48}"), from the formula

$$\Gamma = \prod_{i=1}^{k} n_i! \qquad (3.9)$$

where Γ is the number of permutations, k is the number of different nuclei, and n is the number of each particular nuclei, i. For hydrazine, $\Gamma = 2!4! = 48$. The water dimer (O_2H_4) gives the same result. This number of permutations implies that on the $(H_2O)_2$ potential surface there are 48 equivalent minima(called "equivalent frameworks"), and each rovibrational state is 48-fold degenerate provided there is no observable tunneling between these equivalent minima. If there is tunneling, then the degeneracy will begin to split. It is these tunneling splittings that will affect the observed spectrum. Therefore, the problem can be greatly simplified if only the frameworks attainable through "feasible" tunneling motions are considered. Again, considering $(HF)_2$, there are four equivalent frameworks, shown in Figure 3.7. It is clear that the only way to go from Framework 1 to Framework 3 is to break the HF bonds, which are 136 kcal/mole.[79] This motion is considered unfeasible because the associated tunneling barrier is so high that it precludes observation within the timescale of any current experiment. In other words, the frequency at which the tunneling motion occurs is essentially the observed splitting. Therefore, a tunneling motion that occurs once per

Figure 3.7 The four equivalent frameworks for $(HF)_2$

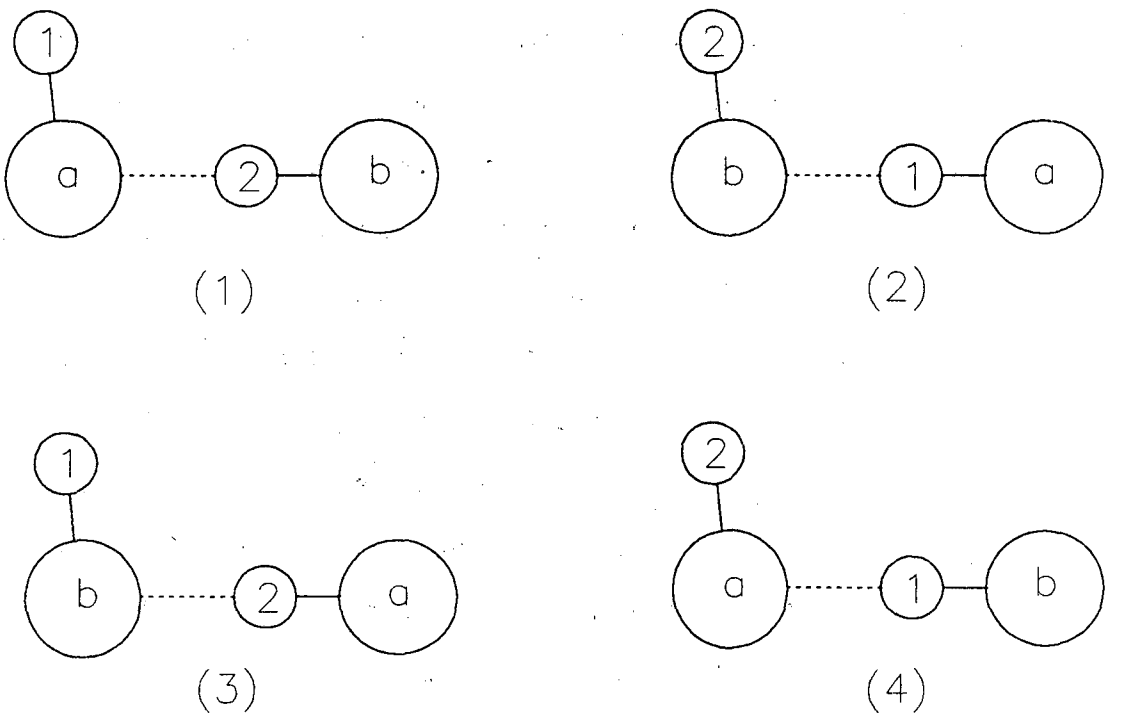

second is going to result in a 1 Hz splitting. A "feasible" motion can therefore be defined in terms of the resolution of the experiment. If any splitting which may occur due to some tunneling motion is not resolvable, it is not a "feasible" motion. The point is that the problem can be greatly simplified if only feasible tunneling motions are considered. For $(HF)_2$, the tunneling between Frameworks 1 and 2 is interchanging the roles of donor and acceptor and as was previously mentioned, this is a feasible tunneling motion which results in a 19 GHz tunneling splitting in K=0 of the ground vibrational state, as measured by Dyke and coworkers.[73] Therefore, for $(HF)_2$, there are only <u>two</u> equivalent frameworks which need to be considered. In hydrazine or the water dimer, considering only feasible motions will also greatly reduce the number of equivalent frameworks involved in the problem.

The concept of "feasibility" is simple in theory, but ambiguous in practice. It is not always obvious what is going to be a feasible motion. From the outset in applying this theory, one must be willing to make assumptions about various tunneling motions and give careful consideration to the possible tunneling paths. One assumption previously mentioned is that breaking a chemical bond is not feasible under ordinary circumstances, while breaking a hydrogen bond may or may not be feasible. As more of these systems are studied our intuition about "feasibility" will improve.

The PI group theory of the water dimer was first worked

out by Dyke in 1977 in an effort to explain the microwave spectra he and his coworkers obtained.[28] In those spectra, there were progressions of lines that appeared to be standard rigid rotor spectra, but most of the spectra exhibited no recognizable pattern. Dyke believed that this random distribution of lines indicated that the water dimer was undergoing large amplitude tunneling motions which were strongly perturbing the rotational states. The details of the PI group theory are thoroughly discussed in Dyke's paper, and only the important results will be presented here.

The first step in understanding the PI theory is to determine the number of feasible operations and the number of equivalent frameworks accessible through feasible motions. The hydrogens are labelled 1 through 4 and the oxygens are labelled a and b as shown in Figure 3.8. Assuming that motions which break OH bonds are not feasible, but those which break only the hydrogen bond are feasible, it is possible to draw eight unique frameworks. It is also assumed that the equilibrium structure is that shown in Figure 3.4, and that the water dimer has a plane of symmetry. Shown in Figure 3.9 are the eight equivalent frameworks taken from Coudert et al.[80] Only the hydrogens are shown, the view is looking down the oxygen-oxygen axis. The center hydrogen is the one which is hydrogen bonded. The circles with the solid lines represent the hydrogens in front and the dashed circles are behind. There are 16 feasible PI operations, and the PI group (G_{16}) is

Figure 3.8 The water dimer structure with the four hydrogens labelled 1 through 4 and the oxygens labelled a and b.

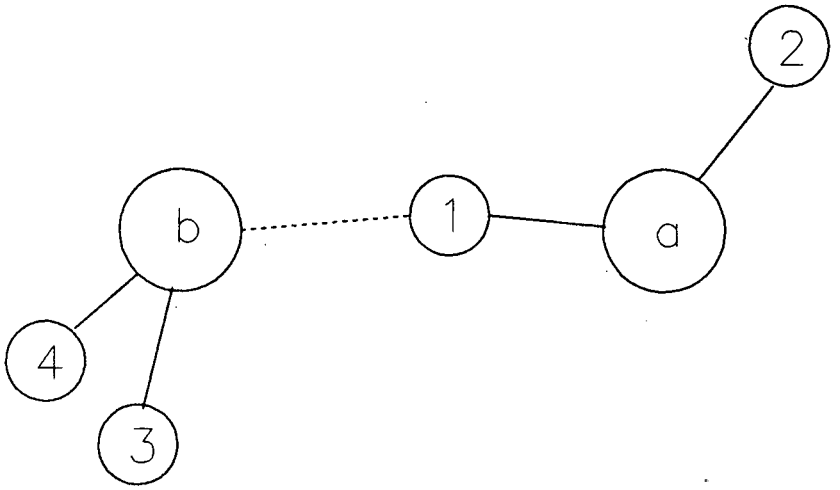

Figure 3.9 This figure is taken from Coudert et al.[80] and shows the eight equivalent frameworks for water dimer. The oxygens are not shown, the hydrogen in the center is the one in the hydrogen bond, and the hydrogens drawn with a solid circle are above the plane, those drawn with a dashed circle are below the plane.

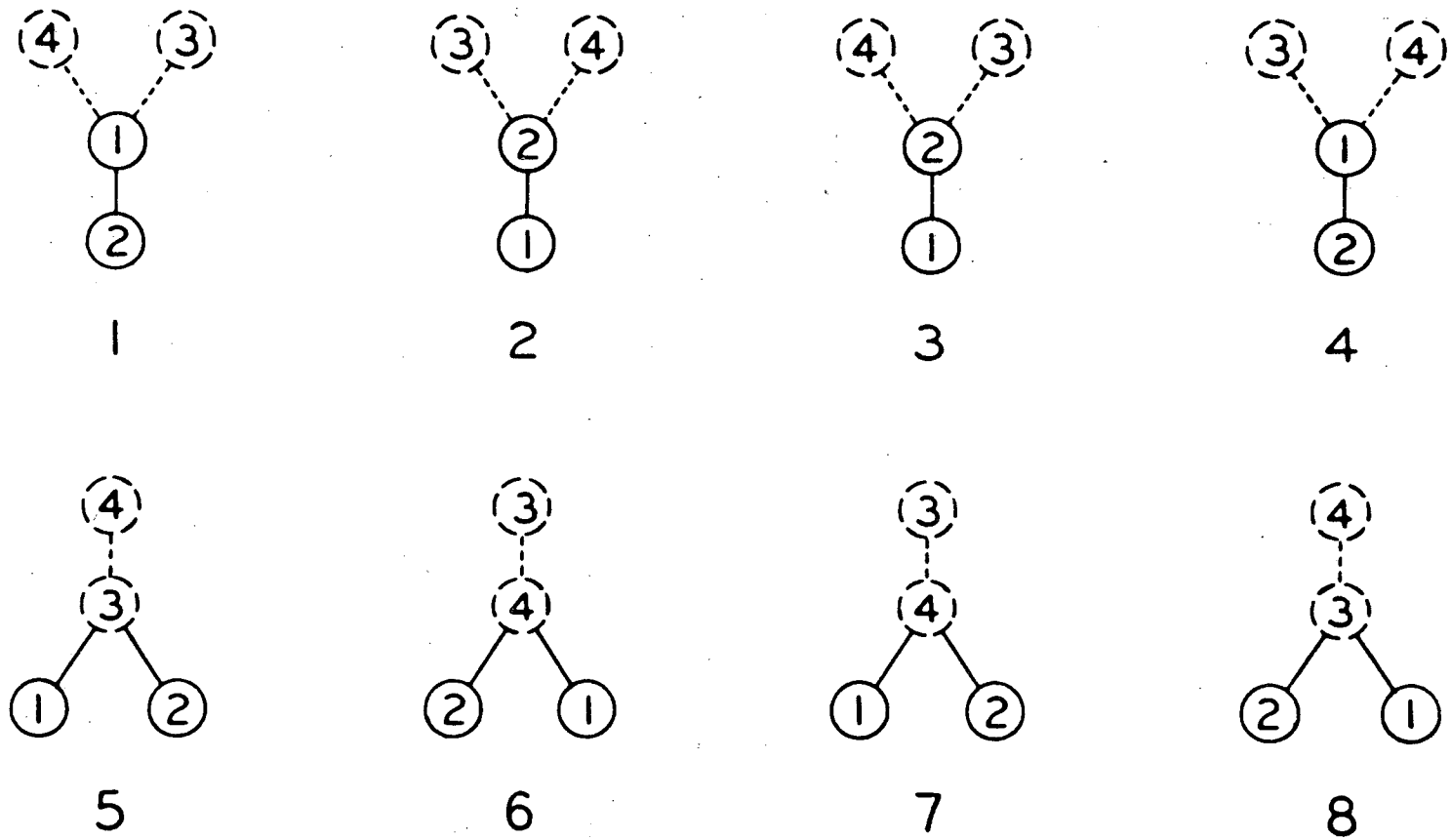

isomorphic with the D_{4h} point group, given in Table 3.3. However, half of these operations do not lead to unique frameworks. This implies that each rotational state is eight-fold degenerate. A second way of expressing this is that there are eight equivalent minima on the water dimer potential surface and tunneling motions are going to move the dimer among the different minima on this surface. This mixing of these wave functions causes a splitting of each rotational level into a maximum of eight states. Actually, each level is going to be split into only six states, two of which are doubly degenerate states of E symmetry.

Considering for a moment the rigid water dimer structure, ignoring any tunneling motions, we see that it has C_s symmetry. Once tunneling is included, the rovibrational states split. Those new states must, however, correlate to the C_s symmetry states in the high barrier limit. In other words, if we start with the completely split levels and gradually increase the height of the tunneling barriers, eventually the infinitely high barrier limit will be reached where there is no tunneling and the water dimer will have eight non-interacting minima with C_s symmetry. The character table for the C_s point group is given in Table 3.4. There are only two types of representations, A' and A". Dyke has shown that the D_{4h} states which correlate with each of these representations can be determined from the behavior under the $(12)^*$ or $(34)^*$ operation which corresponds to the σ_h operation in the C_s point

Table 3.3 The G_{16} character table

	E	(12) (34)	(ab)(13)(24) (ab)(14)(23)	(ab)(1324) (ab)(1423)	(12)(34)	E^*	$(12)^*$ $(34)^*$	$(ab)(13)(24)^*$ $(ab)(14)(23)^*$	$(ab)(1324)^*$ $(ab)(1423)^*$	$(12)(34)^*$
A_1^+	1	1	1	1	1	1	1	1	1	1
A_2^+	1	-1	-1	1	1	1	-1	-1	1	1
B_1^+	1	1	-1	-1	1	1	1	-1	-1	1
B_2^+	1	-1	1	-1	1	1	-1	1	-1	1
E^+	2	0	0	0	-2	2	0	0	0	-2
A_1^-	1	1	1	1	1	-1	-1	-1	-1	-1
A_2^-	1	-1	-1	1	1	-1	1	1	-1	-1
B_1^-	1	1	-1	-1	1	-1	-1	1	1	-1
B_2^-	1	-1	1	-1	1	-1	1	-1	1	-1
E^-	2	0	0	0	-2	-2	0	0	0	2

Table 3.4 The character table for the C_s point group

C_s	E	σ_h
A′	1	1
A″	1	-1

group. Those states which do not change sign under $(12)^*$ are correlated with the A' state, and those which do change sign are correlated with the A" state. Therefore, from the character tables:

$$\Gamma_{A'} = A_1^+ + B_1^+ + E^+ + A_2^- + B_2^- + E^- \quad (3.10)$$

$$\Gamma_{A''} = A_1^- + B_1^- + E^- + A_2^+ + B_2^+ + E^+ \quad (3.11)$$

Dyke also demonstrates that in the ground vibrational state, for K=0, the J_{even} states have A' symmetry and the J_{odd} states have A" symmetry, assuming a totally symmetric (A') ground vibrational state. Therefore, we can draw an energy level diagram, making no assumptions about the magnitude of the tunneling splittings. This is shown in Figure 3.10 for K=0 in an A' vibrational state. For K≠0, one half of the K-type doublet correlates with A' symmetry and the other half correlates with A" symmetry and will alternate with J. The energy level diagram for K≠0, in an A' vibration is shown in Figure 3.11. Included in these diagrams are the spin statistical weights of the states, as derived by Dyke. It is worth noting that for $(H_2O)_2$ the $B_1^{\pm}$ states have no spin weight, and therefore will not be observed. In the perdeutero dimer $(D_2O)_2$, all states have nonzero spin weight and will thus be observable.

From the D_{4h} character table it is determined that the permanent dipole moment will transform as A_1^- (the dipole moment must be invariant under permutation operations, but change sign under inversion, E^*). Therefore, the selection

Figure 3.10 The K=0 state symmetries and spin statistical weights in the ground vibrational state for water dimer making no assumptions about the magnitude of splittings or the ordering of the states.

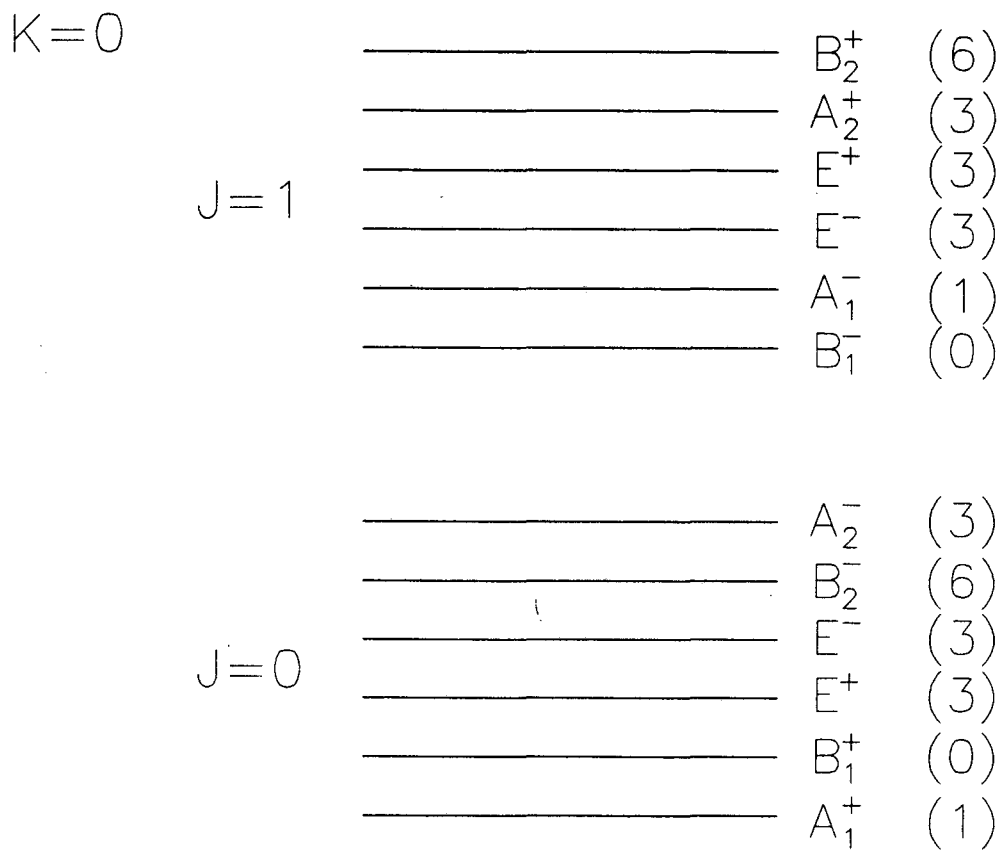

Figure 3.11 The K=1 state symmetries and spin statistical weights in the ground vibrational state of water dimer. No assumptions are made regarding the magnitude of the splittings or the ordering of the states.

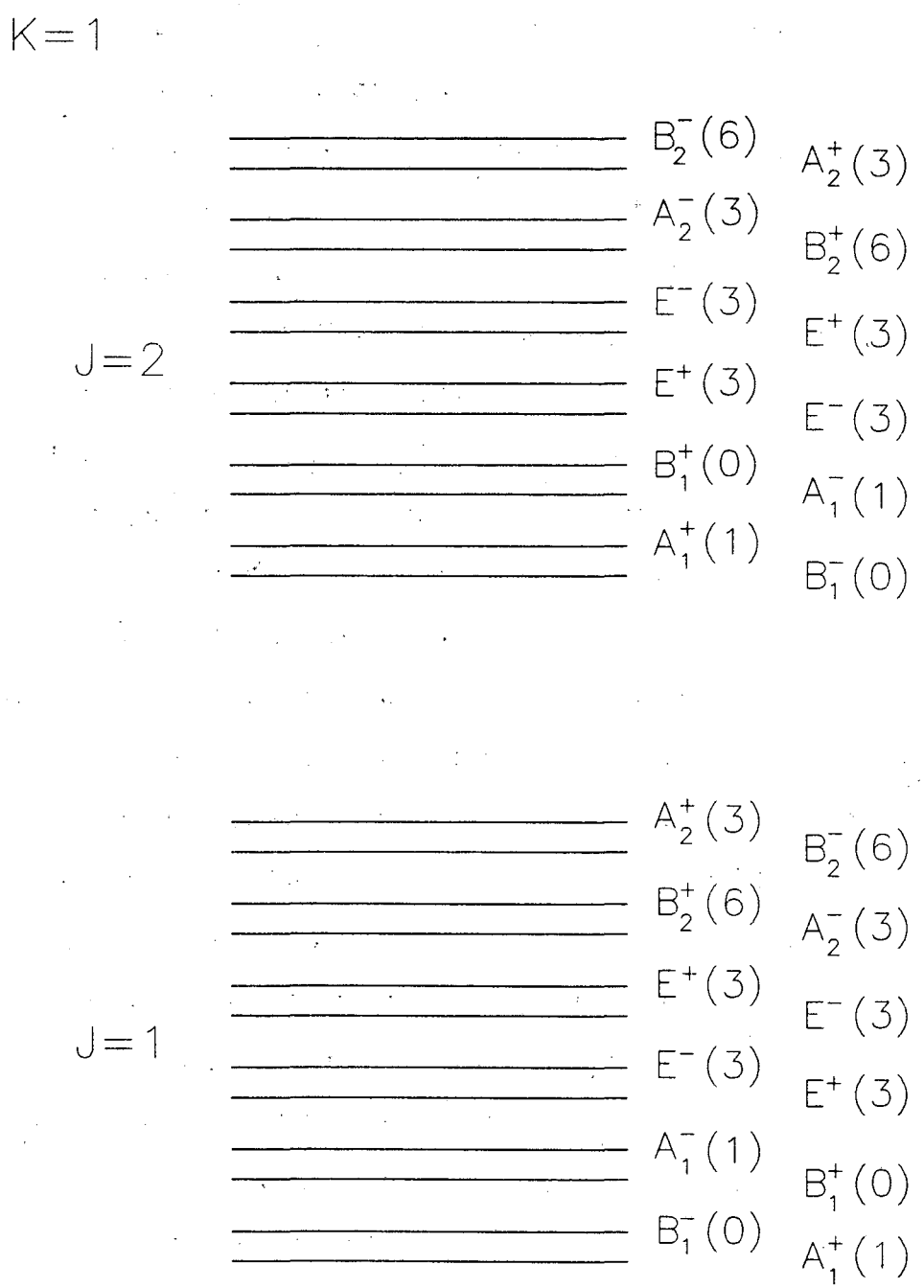

rules for electric dipole allowed transitions are:

$A_1 \leftrightarrow A_1$ $B_1 \leftrightarrow B_1$ $A_2 \leftrightarrow A_2$ $B_2 \leftrightarrow B_2$ $E \leftrightarrow E$ and $+ \leftrightarrow -$.

There are additional restrictions on transitions if we also consider the high barrier C_s symmetry limit. The dipole moment in C_s transforms as A", therefore the selection rule is A'↔A". For the A_1, B_1, A_2, and B_2 transitions, this does not introduce any new restrictions. However, this does add a restriction on the E state transitions. Some authors have chosen to add an extra subscript to the E state label, a 1 or 2, to include this correlation to the A' and A" states. As an example, looking only at the J=0, K=0 state, this additional constraint prevents the observation of the $E_1^+ \rightarrow E_2^-$, because both of these correlate to A' symmetry. This pure tunneling transition is not allowed in the high barrier C_s symmetry limit, even though in terms of only the D_{4h} scheme, there is no such restriction. The high barrier limit as defined by Hougen and coworkers[80] implies that the tunneling splittings are much smaller than the vibrational frequencies of the vibrations associated with the tunneling motions. The question of whether or not the high barrier picture is appropriate will be discussed further in a later section. Essentially, as one moves further from the high barrier limit these restrictions become less rigorous and "forbidden" transitions become weakly allowed. Obviously, there are not infinitely high barriers between the frameworks, or there would be no observable splittings. The selection rules realized in practice are thus dependent on how far the

water dimer is from this limit.

3.4.2 Tunneling Paths

In this section the tunneling paths between frameworks will be discussed. To make an initial assignment of the experimental spectra obtained for the water dimer, it was necessary to make many assumptions about tunneling paths and the relative feasibility of the tunneling motions and hence, the relative sizes of the splittings. Many of the ideas in this section were initially proposed by Coudert and Hougen[80,81] to aid in assigning the spectrum. These ideas are no longer simply proposals, but are considered to be correct because they have since been used in the fit of a large amount of data. Some of the smaller perturbations (less feasible tunneling motions) were not considered until after the spectral assignments were made, and were used to improve the quality of the overall fit. Although some of the concepts presented here were not known prior to the experimental results, it should be stressed that much had to be assumed about the tunneling paths and associated splittings before an assignment could be made. Figure 3.12 illustrates partly why some understanding of the splittings can be instrumental in obtaining an assignment. In this picture, we assume that there are six states for each rovibrational level, and that there are two different tunneling motions which split these levels. If tunneling motion A results in a doubling of each level and tunneling motion B leads to a tripling of the levels,

Figure 3.12 Assuming that there are two tunneling motions which split the rotational levels, one motion results in a doubling of the levels (Motion A) and one motion results in a tripling of the levels (Motion B), two very different spectra will be obtained depending on which motion is more feasible. In (a) tunneling motion A is more feasible and in (b) tunneling motion B is more feasible.

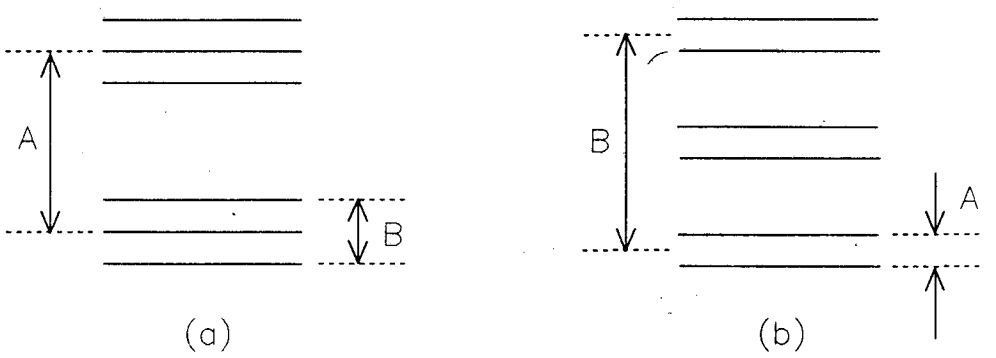

depending on which motion is more feasible, A or B, two very different types of spectra could be obtained.

For the water dimer there are eight equivalent frameworks with a number of different types of tunneling motions connecting them. These different paths are labelled according to the frameworks that they connect and are shown in Figure 3.9. One example is the 1→4 tunneling path, which connects frameworks 1 and 4. There are, of course, identical paths which connect frameworks 2 and 3, 5 and 8, and 6 and 7. The different tunneling motions will be presented in order, from the most feasible, leading to the largest splittings, to the least feasible, which result in only small perturbations to the energy levels. Also presented are the estimated barrier heights for some of these tunneling motions. Using the semi-empirical Coker and Watts potential[66], Coudert and Hougen calculated the barrier heights for the various tunneling motions using simplified two-dimensional surfaces.[81] These calculations will be discussed in a later section. High level ab initio calculations (MP4/6-311+G(2df,2p)) of the energy of the transition state structures were calculated by Smith and coworkers[49] shortly after Coudert and Hougen published their results. These energies will also be presented.

1→4 Tunneling Path

The most feasible (lowest barrier) tunneling motion is that connecting frameworks 1 and 4. At first glance, this path appears to be a simple C_2 rotation about the acceptor symmetry

axis. This motion also involves a change in the angle of the proton acceptor C_2 axis; it moves toward aligning with the O-O axis during the rotation. However, the path can also be envisioned as an ammonia-like inversion of the acceptor molecule and a simultaneous 180° rotation of the donor molecule about the hydrogen bond axis. Hougen proposes that the actual path, based on the potential surface calculations is actually a mixture of both of these motions. However, it is more closely related to the inversion-rotation motion. The barrier height calculated by Coudert and Hougen[81] is only 130 cm^{-1}, the barrier calculated by Smith et al.[49] is 206 cm^{-1}. The splitting associated with this motion is approximately 200 GHz (6.6 cm^{-1}) for K=0. This tunneling motion will result in a doubling of each rovibrational level, as shown in Figure 3.13.

1→5 Tunneling Path

A second tunneling motion is referred to as the 1→5 motion. Again, there are identical paths between many of the frameworks, including 2 and 5, 2 and 6, 3 and 7, 4 and 8, etc. This tunneling can be thought of as a geared internal rotation, similar to that in $(HF)_2$, in which the role of the hydrogen acceptor and donor are switched and is shown in Figure 3.14. In this exchange, one of the hydrogens on the acceptor moves into the hydrogen bond and displaces the donor hydrogen. That hydrogen then leaves the bond, moving in a geared-type motion, i.e., with its motion is in the same direction as the hydrogen which displaced it. At the

Figure 3.13 The 1→4 tunneling motion results in a doubling of the rovibrational levels.

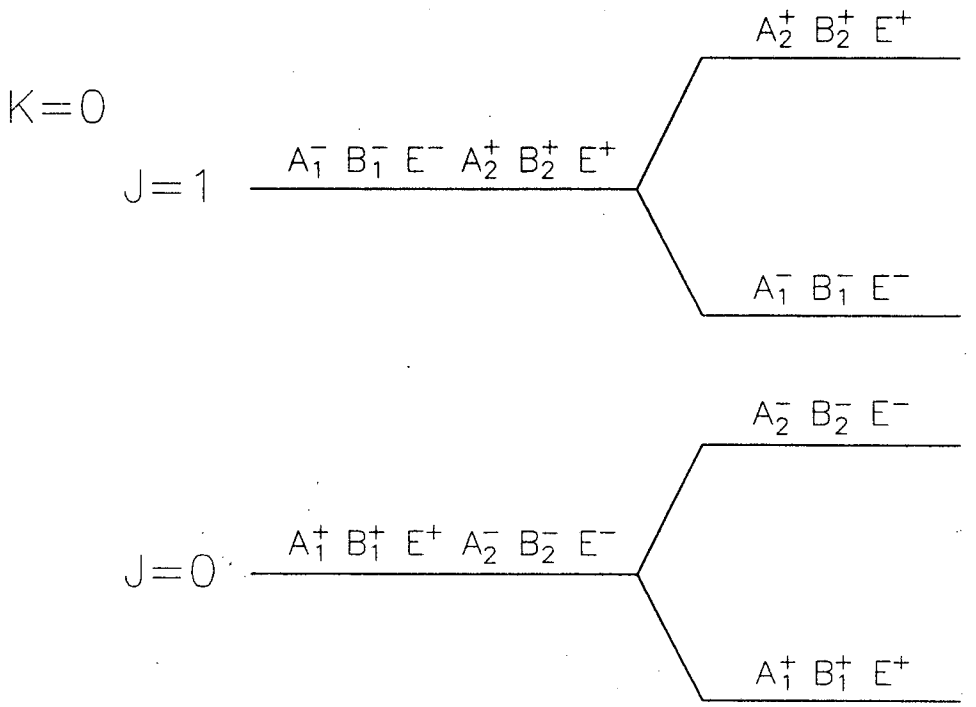

Figure 3.14 The 1→5 tunneling motion, also referred to as the geared internal rotation.

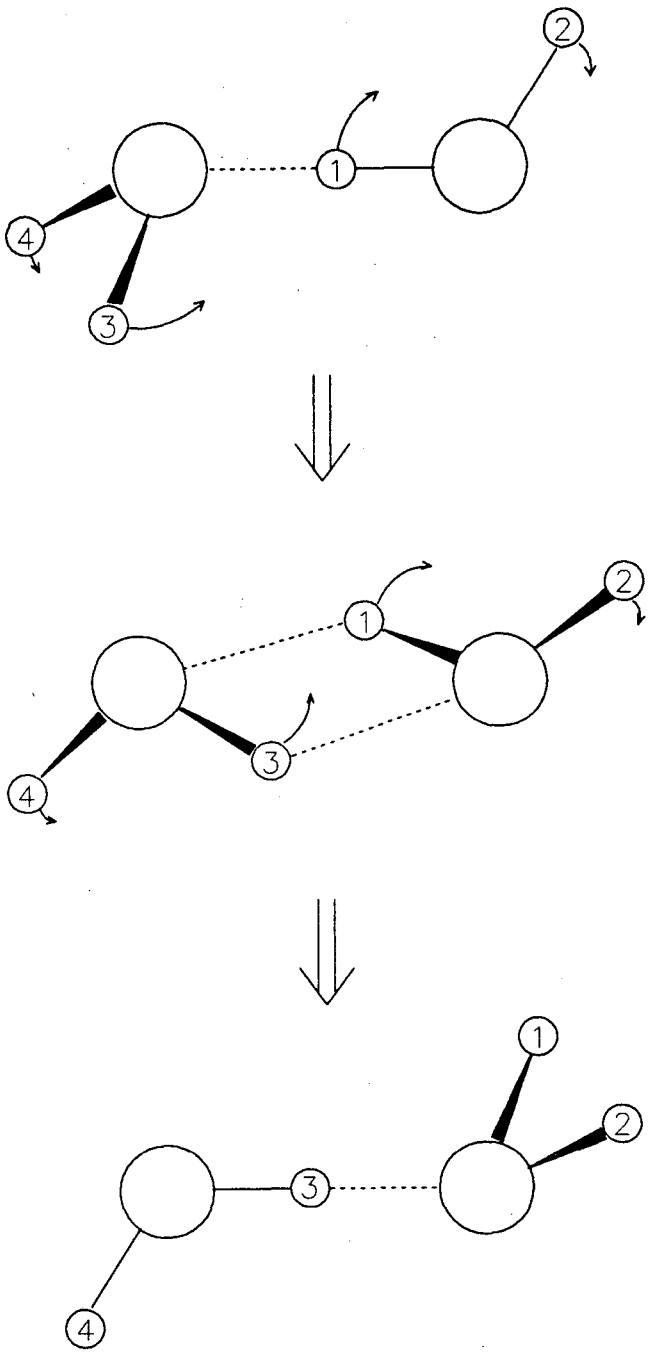

intermediate configuration along this path, the tunneling hydrogens are on opposite sides of the water dimer symmetry plane, and this is referred to as the trans tunneling, as in the $(HF)_2$ case. The 1→5 tunneling motion results in a tripling of each rovibrational level. This motion essentially causes A and B symmetry states to split, while not perturbing the E states, as shown in Figure 3.15. The tunneling barrier for this motion calculated by Coudert and Hougen is 800 cm^{-1}, the barrier calculated by Smith and coworkers is only 304 cm^{-1}. The measured splitting across the three levels in K=0 is 19.5 GHz (~.6 cm^{-1}).

Considering only these two most feasible motions, each rovibrational level is fully split. In other words, any additional tunneling motions will only perturb these existing states. With eight equivalent frameworks, there will be a maximum of eight states. In this case, there are only six, but two are E states, and the E state double degeneracy cannot be broken through tunneling motions.

1→2 Tunneling Path

The 1→2 tunneling motion is a geared motion in which each monomer rotates about an axis parallel to the y axis through its center of mass, assuming that the plane of symmetry is the xz plane (Figure 3.16). In this motion the donor-acceptor roles are not exchanged. This tunneling motion causes a perturbation in which A and B symmetry states shift in one direction and E symmetry states shift in the opposite

Figure 3.15 The 1→5 tunneling motion results in a tripling of each rovibrational level in addition to the 1→4 doubling.

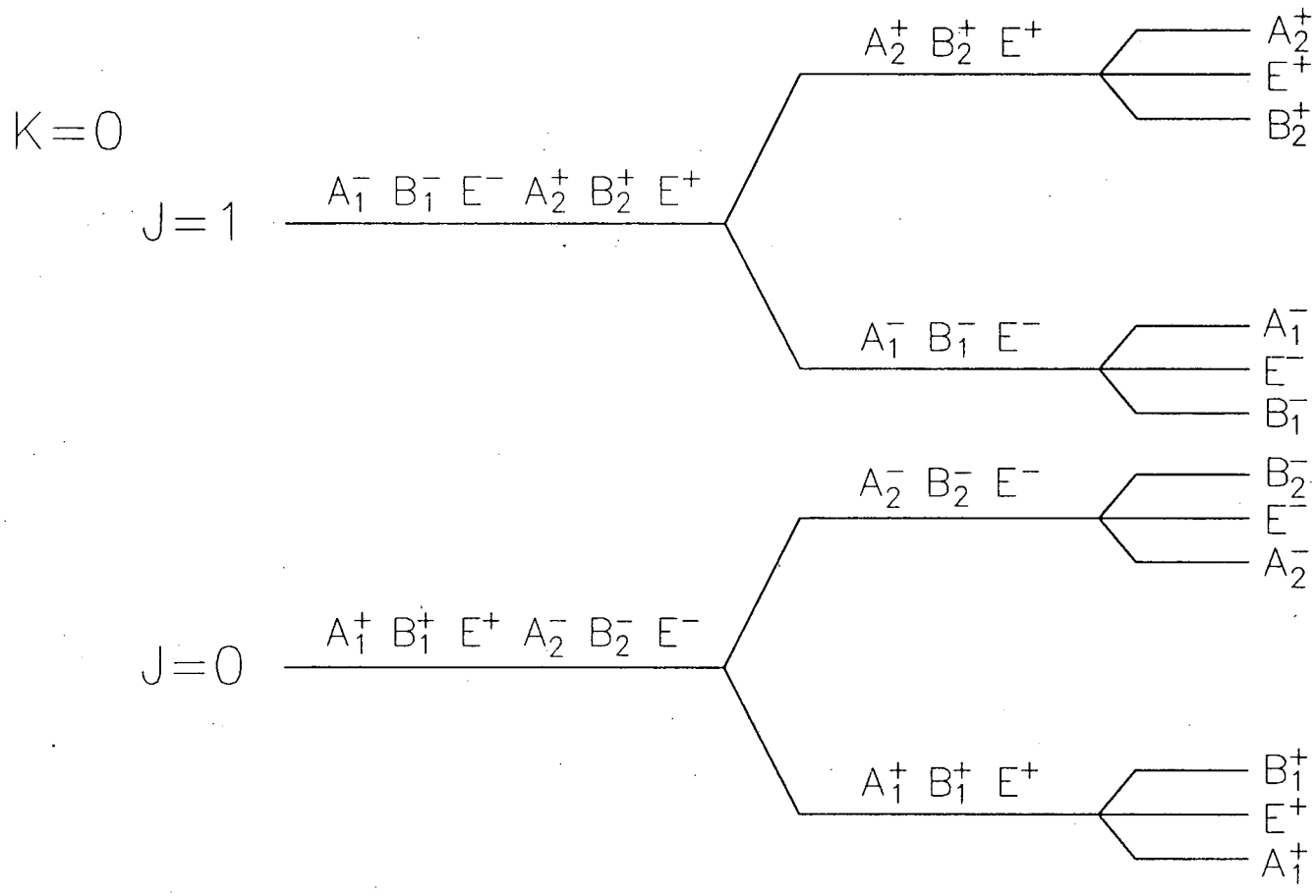

Figure 3.16 The 1→2 tunneling motion

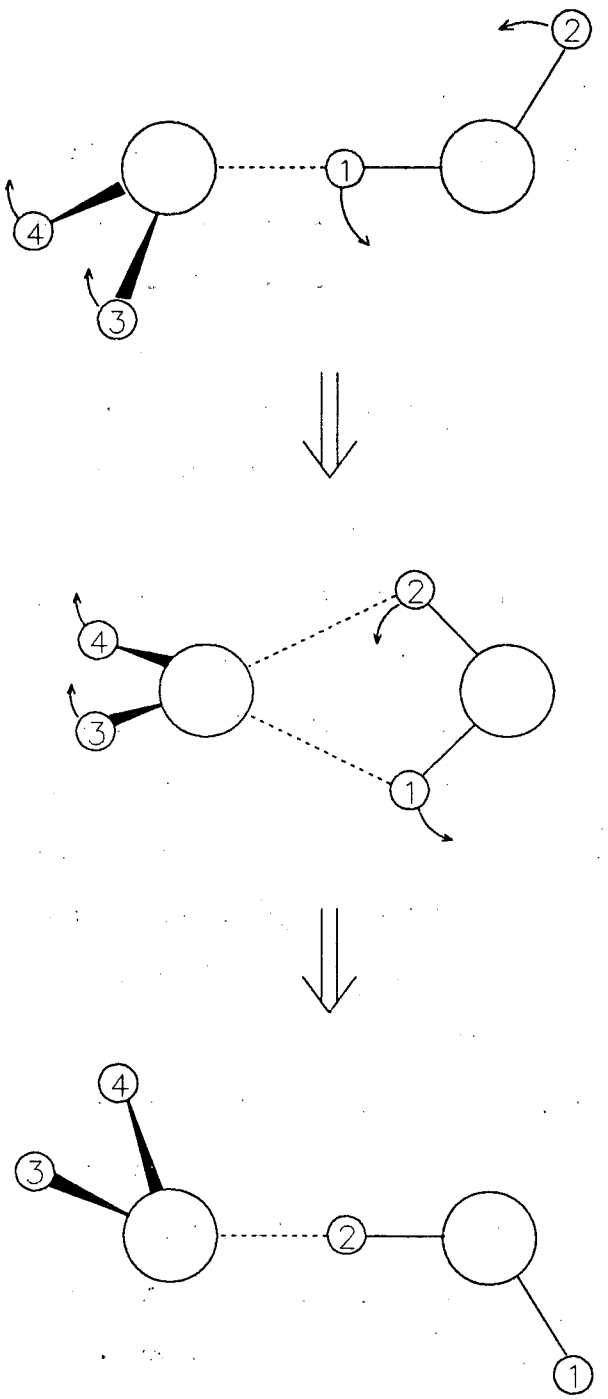

direction. Coudert and Hougen calculated the barrier for this motion to be 1000 cm^{-1}, Smith et al. obtained a value of 658 cm^{-1}. The expected tunneling splitting should be less than 1 GHz (~.03 cm^{-1}).

1→7 Tunneling Path

The 1→7 tunneling is very similar to the 1→5 motion, except that interchanging hydrogens move in an anti-geared manner; the velocity vectors of the hydrogens point in opposite directions (Figure 3.17). The intermediate configuration of this path has both hydrogens on the same side of the water dimer plane of symmetry and therefore this is also referred to, as in the case of $(HF)_2$, as the cis tunneling. In the $(HF)_2$ case, there was no evidence of the cis tunneling motion occurring, and in $(H_2O)_2$ it is probably a reasonable assumption that this motion will be less likely to occur than the trans tunneling motion, and will therefore result in a smaller perturbation to the energy levels. The barrier for this path was not calculated, but it is expected to be much higher than the 1→2 barrier (658 cm^{-1}).

1→3 Tunneling Path

The last motion considered is the 1→3 motion, which is essentially a C_2 rotation about the donor symmetry axis. Intuitively, this does not seem to be a very feasible motion, because unlike in a tunneling such as the 1→5, the hydrogen bond will have to be nearly completely broken before the other hydrogen can reform it. In the 1→5 case, the displacing

Figure 3.17 The 1→7 tunneling motion

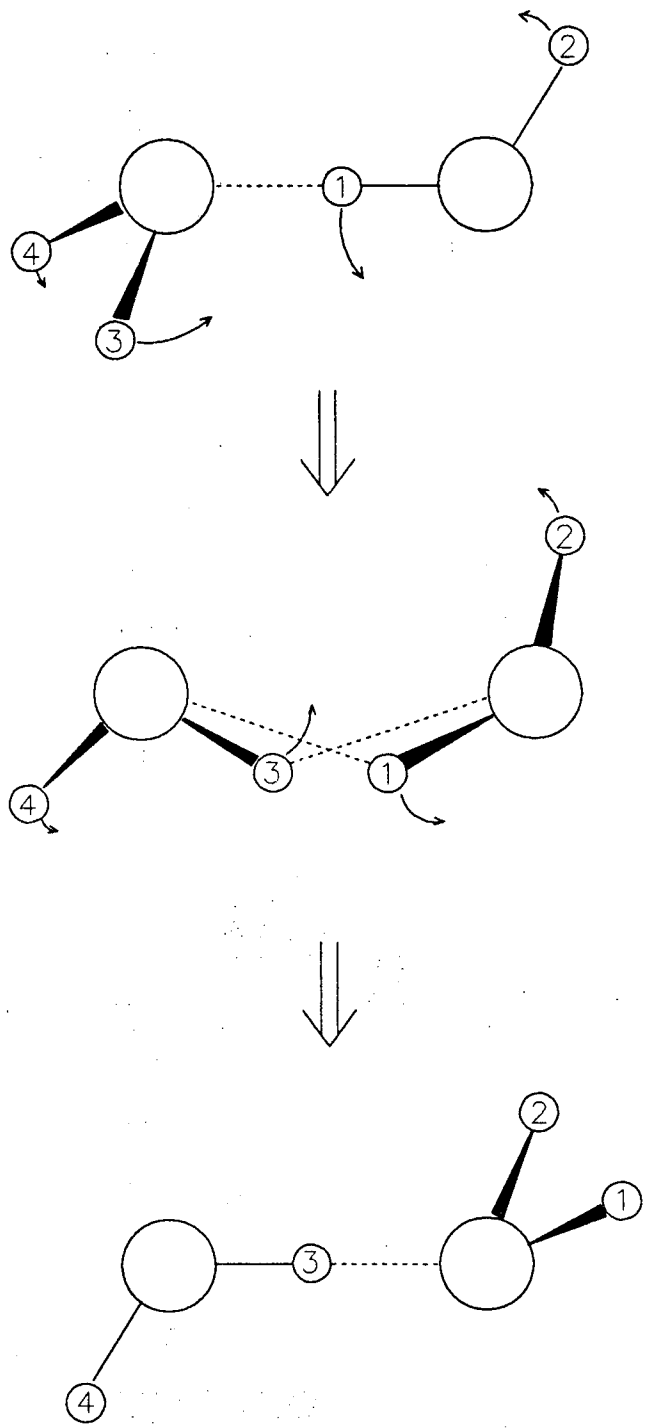

hydrogen is in close proximity to reform the bond. The barrier for this path also was not calculated.

The only two frameworks connections which have not been specifically mentioned are the 1→6 and the 1→8 paths. This is simply because these paths are identical to the 1→5 and the 1→7, respectively, except that the direction of the rotation is reversed, or alternatively, the other acceptor hydrogen moves into the hydrogen bond.

3.4.2.1 Deuterated Forms of the Water Dimer

The deuterated water dimer species are interesting because of the differences expected in the spectra due to symmetry differences. The perdeuterated dimer, $(D_2O)_2$ is expected to undergo the same tunneling motions as $(H_2O)_2$, however, these splittings will be much smaller in the deuterated species due to the reduced feasibility of a deuterium tunneling, relative to a hydrogen tunneling. In the case of the 1→5 tunneling motion, in K=0 for $(H_2O)_2$ the splitting is approximately 19 GHz, while in $(D_2O)_2$ this splitting is only 1 GHz.[27] The spin statistical weights for the states will also be different; the B_1 states will no longer have spin weight zero, but rather, all states will be observable in $(D_2O)_2$.

In the many molecular beam studies which have been performed, there has been no observation of hydrogen bonded dimers when there was a deuterium present, only deuterium

bonded clusters have been observed. In the case of H_2O-HDO, only the H_2O-DOH species is observed. This is due to the fact that with the deuterium in the bond the zero point vibrational energy is substantially reduced and the structure is therefore more stable. Considering only that isomer, it is no longer possible to have 1→5, 1→2, or 1→7 type motions, only the 1→4 motion is possible. Another way of expressing this is that there are only two equivalent frameworks for this structure, and therefore there will only be a doubling of the levels. Presumably, this splitting will be very similar to the $(H_2O)_2$ 1→4 splitting because only the hydrogens are tunneling. This dimer allows for the observation of a pure 1→4 splitting with no additional splitting superimposed on it. The D_2O-DOH dimer will also have only the 1→4 tunneling splitting. However, in this complex, deuteriums are tunneling and therefore this splitting will be significantly smaller. In the H_2O-DOD dimer, both the 1→4 and the 1→2 tunneling motions will exist. This would allow for the investigation of the 1→2 motion without the complication of the 1→5 tunneling splitting.

The other two possible dimers, HDO-DOH and HDO-DOD, are unique in that they do not have the plane of symmetry present in all of the other water dimer species. The symmetry of these two does not correlate to the C_s group in the high barrier limit; therefore the selection rules will be different and the spectroscopy will not be directly comparable. In the HDO-DOD complex the 1→2 type motion can occur, as can a 1→4 type

motion. In the 1→4 motion however, the resulting structure will not be superimposable with the original structure, but the second minimum will be equal energy. Therefore, there will be a four-fold splitting of each level in this complex. In the HDO-DOH, this same 1→4 motion will occur as well as a 1→5 motion in which the deuterium on the acceptor moves into the bond. This is analogous to saying that the 1→5 motion can occur but not the 1→6 motion. Of course, if the 1→5 motion, the geared donor-acceptor interchange can occur, then the 1→7 motion, the anti-geared donor-acceptor interchange is also possible. However, this would result in a very small splitting. In this complex, there would also be a four-fold splitting, assuming that the 1→7 splitting is small. A number of transitions have been measured in the microwave region for these various deuterated species by Dyke and coworkers[27,82] and by Coudert, Lovas, Suenram, and Hougen.[80] At this time, however, the results are still quite limited.

3.4.3 High Resolution Spectroscopic Studies

At this point, with an understanding of the water dimer PI theory and the preliminary experimental results, it is helpful to present a somewhat simplistic energy level diagram. Considering only the two largest splittings, associated with the 1→4 and 1→5 tunneling motions it is possible to arrive at a "first order" energy level diagram which will simplify the explanation of the spectroscopic results. This diagram is

given in Figure 3.18. Shown in this diagram are the K=0, 1, and 2 states of the ground vibrational state. As has been discussed, in each rotational level there are six states in K=0 and twelve states in K≠0 due to K-type doubling. The K-type doubling is not shown on this diagram. The largest splitting is due to the 1→4 tunneling, and is approximately 200 GHz (6.6 cm^{-1}) in K=0. The smaller tripling of these levels is the result of the 1→5 tunneling and in K=0 this splitting is approximately 19 GHz across the three states. The 1→4 splitting separates the A_1/B_1 states from the A_2/B_2 states. Transitions between these states are nearly forbidden, assuming that we are close the C_s limit, and therefore these states are considered separate manifolds and designated as K=n lower and K=n upper states. For example, the K=0 A_1/B_1 states are labelled K=0 lower.

The microwave studies of Dyke and Muenter[25] and Dyke, Mack, and Muenter[27] have already been mentioned several times, as the first high resolution spectroscopic studies done on the water dimer. The spectra were obtained using the molecular beam electric resonance (MBER) technique discussed in Section 3.2.5. In the first study, over 50 transitions were observed between 8 and 50 GHz. Many of the lines appeared to be "randomly" spaced. However, a number of lines formed two rigid rotor-like progressions. From the observed first order Stark effect, these lines were identified as the doubly degenerate E states and were assigned to the K=2 state. The two

Figure 3.18 The energy level diagram for the ground vibrational state of $(H_2O)_2$ including K=0,1, and 2. Included in this diagram are the splittings resulting from the 1→4 and 1→5 tunneling motions. The K-type doubling is not shown.

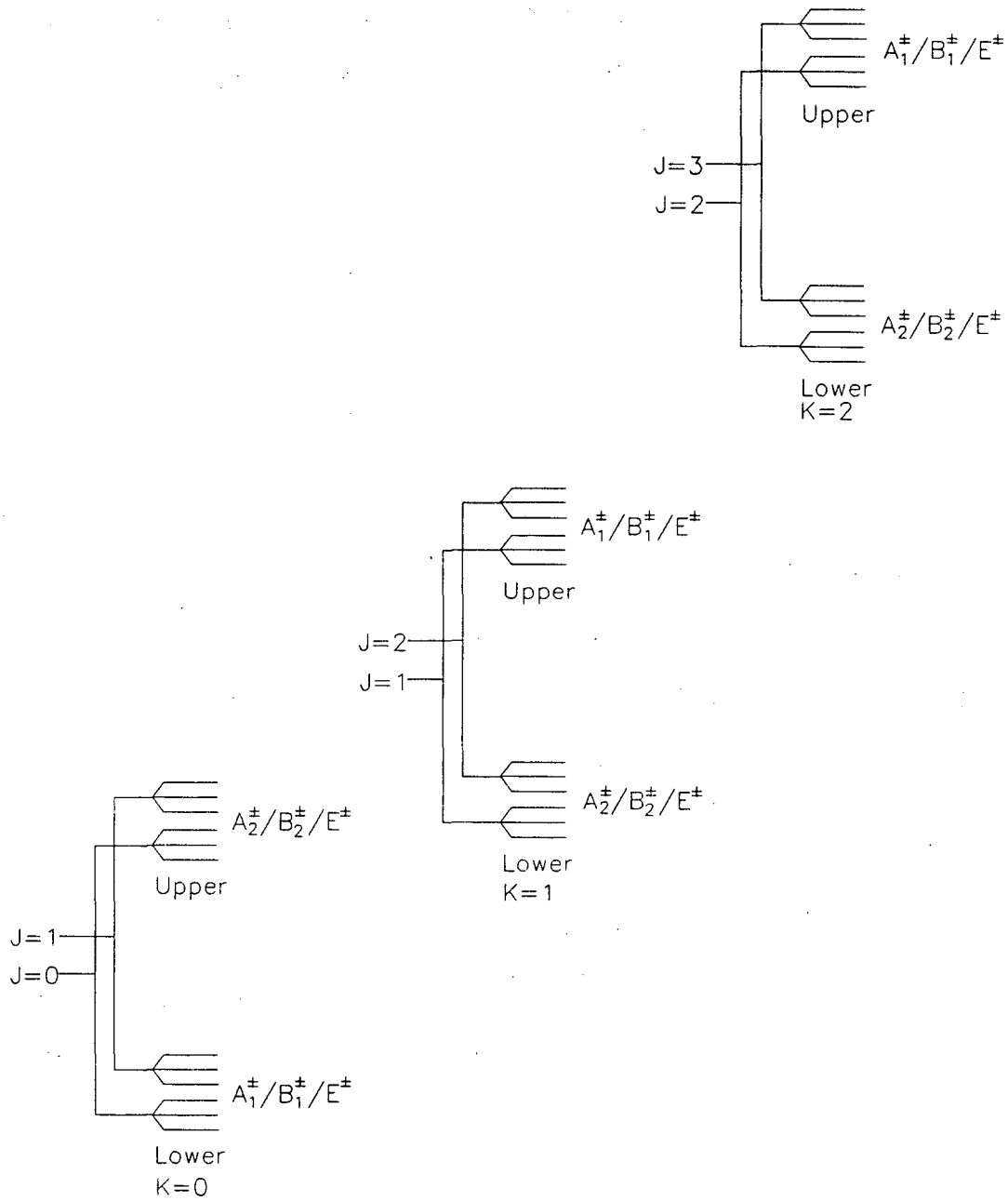

progressions were associated with the K=2 lower and K=2 upper levels. They also observed the K-type doubling of these states. The E states are not strongly perturbed by the tunneling motions and therefore, these spectra appeared to be pure rotational transitions. The rotational constant, ((B+C)/2) is 6160 MHz for K=2, and the associated (D_J) centrifugal distortion constant is 44 kHz. Using the approximation that the dimer is a pseudodiatomic molecule, it is possible to estimate a harmonic stretching frequency from the distortion constant.

$$\omega = \sqrt{\frac{4[(B+C)/2]^3}{D_J}} \qquad (3.12)$$

From this, Dyke calculates a stretching frequency of 149 cm^{-1}. From the rotational constants it was determined that the O-O distance is 2.98Å and the angle between the acceptor molecule C_2 axis and the O-O axis, θ_a, is 60.7°. The MBER technique also allowed Dyke and coworkers to determine the parallel dipole moment, μ_a, which is 2.6D.

This is the only molecular beam experiment that will be discussed that was run with a pure or neat water beam under fairly mild expansion conditions, therefore, these K=2 transitions and even some K=3 transitions were observed. In jets seeded in argon or other carrier gas, the temperature is typically less than 5K and none of these states would have a sufficient population to be observed.

In 1980, Odutola and Dyke published a similar study of

the deuterated water dimers.[82] In this study, again using the MBER technique, they formed the dimers in a 7% water in argon beam. Under these conditions it was no longer possible to observe the K=2 transitions of the previous studies due to the much colder expansion conditions. They repeated the dipole moment measurements, and from the Stark coefficients of the K=0, J=0→1 E state transition and the K=0, J=1, M=0→1 E state transition, they obtained a value for μ_a and the perpendicular component,

$$\mu_{\perp}=\sqrt{\mu_b^2+\mu_c^2} \qquad (3.13)$$

The values determined are μ_a=2.6429(2)D and $\mu_{\perp}$=0.38(10)D.

In 1987, Coudert, Lovas, Suenram, and Hougen reported the study of the K=1 lower states, using a Fourier transform microwave spectrometer.[80] In this study, the A_2/B_2 transitions were observed in K=1 in the 1K expansion. This implies that there is not a significant energy difference between K=0 upper and K=1 lower states. In very cold jets it is generally expected that the population will all be primarily in the K=0 states. The selection rules for thermal relaxation are assumed to follow the dipole moment selection rules, ignoring the +↔- restriction, that is, $A_1 \leftrightarrow A_1$, $A_2 \leftrightarrow A_2$, $B_1 \leftrightarrow B_1$, $B_2 \leftrightarrow B_2$, and E↔E. This implies that dimers formed initially in the A_2 or B_2 states can only relax to the K=0 upper states. In fact, what is actually observed in the water dimer is that both the K=0 upper and K=1 lower states have comparable population, even in the 1K

expansion. Assuming that the collisional selection rules are obeyed, this leads to the conclusion that the K=0 upper states and K=1 states are nearly the same energy, as is shown in Figure 3.18. Unlike the A_2 and B_2 states, the E state population does relax down to the K=0 lower states. In the Coudert et al. study these E state transitions were not observed. It was also observed that the K-type doubling was two orders of magnitude larger than was expected based solely on structural considerations (B-C), implying that there is some sort of perturbation affecting this splitting. This paper also gives an excellent qualitative summary of the tunneling motions and the energy level diagram assuming that only the 1→4 and 1→5 tunneling motions are important.

In very simple terms, the K=0→1 energy difference is approximately equal to the A rotational constant. Therefore, if the K=0 upper and K=1 lower states are nearly the same energy, and assuming that the 1→4 splitting is the same in the K=0 and K=1 levels, then this splitting must roughly equal the A rotational constant which is calculated to be ~200 GHz (6.6 cm^{-1}). The 1→5 splitting (the geared internal rotation) in the K=1 lower state is measured to be 16.2 GHz. Measurements of the K=0 upper states were performed by Dyke and coworkers, again using the MBER technique[83], in 1988. The 1→5 tunneling splitting was measured to be 19.52673 GHz (~.6 cm^{-1}).

Huang and Miller, using infrared vibrational predissociation spectroscopy with bolometric detection,

observed the v=0→1, K=1→0 transitions of the water dimer, where the vibration is one of the OH stretches.[84] In this experiment, an F-center laser was used, but unlike the earlier experiment of Coker, Miller, and Watts[32], the laser resolution was less than the Doppler width of the lines and they obtained rotational resolution. A molecular beam was crossed in a multi-pass configuration by an F-center laser. Situated directly in the beam path was a helium cooled bolometer. The molecular beam strikes the bolometer surface, condenses, and transfers energy to the detector generating a current. In the case of an infrared absorption, one of two things can happen. In the first, the molecule absorbs the photon then strikes the detector and because of the absorption, an increase in the energy transferred to the detector is observed. In the second case, a molecule absorbs the photon and if that photon energy exceeds the binding energy of the molecule, it may predissociate and the fragments will scatter out of the beam before they reach the detector. This will result in an overall decrease in the detector signal due to the decrease in the number of molecules striking the detector. The water dimer spectra were obtained in this latter fashion. The photon energy is typically around 3600 cm^{-1}, and the binding energy of the dimer is only about 2000 cm^{-1}. This experiment offers several unique advantages. The first is that weakly bound, predissociating molecules will be observed as a decrease in detector signal while systems which absorb but do not

dissociate will be observed as an increase in the signal and therefore, these different cases can be identified by the phase of the signal. Also in predissociating molecules, the linewidth is often dominated by lifetime broadening of the line; therefore, lifetimes can be determined from the peak widths and some understanding of the dynamics can be obtained from the absorption experiment. The spectra show three distinct Q branches, which are associated with the three levels of the 1→5 tunneling. The two outer Q branches show a 2:1 intensity alternation, which corresponds to the alternation of the symmetries from B_2 to A_2 (spin weights 6 and 3, respectively). The center Q branch shows no alternation and is therefore assigned to the E states, all of which have the same spin weight. Based on the intensities, it was determined that the ordering of the levels in the K=1 lower J states was reversed from that in the energy level diagram of Coudert and coworkers[80], i.e., the A_2/B_2 states were switched. The authors also point out that the observed linewidths which are limited by the lifetime broadening are very different for the three Q branches. The FWHM of characteristic lines are 93, 220, and 51 MHz, from low to high frequency. This implies that the predissociation rate is very symmetry dependent, and is considerably faster for the E states. A more detailed study will be discussed later in this section.

In demonstrating the usefulness of their newly developed microwave-microwave Fourier-transform double resonance

spectrometer, Martinache and coworkers measured and confirmed the assignment of several lines in K=0 and K=1.[85] The experiment is an adaptation of the one used by Coudert and coworkers, which was originally developed by Flygare and coworkers[86]. Martinache and coworkers incorporate a second Fabry-Perot cavity to enable them to obtain double resonance spectra. Aside from a few $(H_2{}^{18}O)_2$ lines, the transitions measured had been observed previously, but the double resonance technique confirmed the assignment.

The electric resonance optothermal spectroscopy (EROS) technique was developed by Fraser and coworkers.[87] This microwave technique was shown to be versatile and extremely sensitive in important water dimer measurements. The technique is similar to the molecular beam electric resonance (MBER) technique described in Section 3.2.5, in that a quadrupole field is used to focus the appropriate symmetry species onto the detector. In the MBER technique, however, two quadrupole fields are employed, the first of which selects species with the positive Stark shift before the interaction region. The EROS experiment does not incorporate this extra field, therefore the number of molecules actually interacting with the microwave radiation is much higher, increasing the sensitivity. Also, the detector in the EROS experiment is a bolometer, as opposed to the mass spectrometer used in the MBER experiment.

Fraser and coworkers first observed a-type transitions up

to J=9 in the K=0 upper state. They also observed c-type transitions from K=0 upper to K=1 lower. This was the first time these transitions were observed. From these measurements it was determined that the K=0 lower and K=1 upper energy difference is only about 14 GHz. It is apparent from this study that the c dipole moment is very small; the observed transitions were an order of magnitude weaker. Attempts by Lovas and Suenram to measure some of the same transitions using the Fourier-transform microwave experiment were unsuccessful. In the first study, Fraser et al.[87] were unable to observe the c-type transitions from the E states, they only observed A_2 and B_2 transitions. In the second study,[88] with improved microwave power they were able to observe the E states. They then used these results to estimate the tunneling matrix element for the 1→2 tunneling, h_{2v}~743 MHz. The actual splitting is $4|h_{2v}|$ or 3000 MHz.

Fraser et al. also observed a-type transitions among the A_1 states in the K=0 lower state, which had never been observed before by any method. From these spectra they obtained the 1→5 tunneling splitting, 22.6 GHz for the K=0 lower states. These spectra gave significant support to the Coudert and Hougen's proposed energy level diagram.[81]

The K=1 lower to K=2 lower transitions were measured at Berkeley in the far infrared region.[89] This paper is included in Appendix B. The experiment has been fully described in Chapter 2. In this c-type spectrum, only A_2/B_2 states were

observed, again because the E state population can relax to the K=0 lower states. In scanning for the water dimer spectra, over 350 lines were observed from 510 to 835 GHz (17 to 28 cm^{-1}). Many of these still remain unassigned and are listed in Appendix C. In assigning the dimer spectrum from all of these lines, it was crucial to have the K=1 microwave measurements of Coudert et al.[80] from which the combination differences could be calculated. Once the lowest few rotational state transitions were identified from the combination differences, Hougen and Coudert incorporated them into their fit, which will be discussed in the next section, and provided predictions for the higher J transitions. In most cases, we simply found these predicted lines among the unassigned lines. In this manner, we were able to assign 56 transitions up to J=8 for $(H_2O)_2$. Based on Q branch intensities, we also came to the conclusion reached by Huang and Miller[84] that the K=1 lower states were incorrectly labelled, $A_2^{\pm} \leftrightarrow B_2^{\mp}$. We were also able to determine the 1→5 tunneling splitting in the K=2 lower levels. This splitting is 11.1 GHz.

In several studies, it was observed that in K=1 lower states the asymmetry parameter, (B-C), was much larger than expected from structural considerations. This state also required a large number of higher order distortion constants to fit the data. It was speculated that there were "anomalous" tunneling-rotation interactions in the K=1 states. However, observation of several E state transitions in the K=1 upper

levels by Hu and Dyke[90] revealed that there was not this same large asymmetry parameter. This implies that the perturbation involves only the K=1 lower states and not K=1 upper states. It has long been accepted that the K=0 upper and K=1 lower states were nearly the same energy. They are both A_2/B_2 symmetries, therefore it is reasonable to assume that there is Coriolis coupling between these two sets of states. Hu and Dyke fit the E state (rigid rotor-like) transitions including the Coriolis interaction. They were able to fit the lower states of each K-type doublet to an unperturbed Hamiltonian of the form

$$W=\Delta+\frac{(B+C)}{2}J(J+1)-\frac{(B-C)}{4}J(J+1)+D_J J^2(J+1)^2+\ldots, \qquad (3.14)$$

but the upper states of the K-type doublets required an energy expression which included a Coriolis term,

$$W^{\pm}=\frac{W_0+W_1}{2}\pm\left[\frac{(W_1-W_0)^2}{4}+\frac{\zeta^2 J(J+1)}{2}\right]^{\frac{1}{2}}. \qquad (3.15)$$

In this expression W_0 and W_1 are the unperturbed energies of the K=0 and K=1 states, and for the K=0 state, $\Delta=0$. The $\pm$ refer to the parity of the interacting E states. The Coriolis coupling constant ζ describes the extent of mixing between the two states. Essentially, the larger the interaction, the larger the perturbation of the state from W_i. Shown in Figure 3.19 is an energy level diagram from Hu and Dyke which shows how this Coriolis interaction occurs. In K=0 upper and K=1 lower levels, states of the same J and symmetry interact.

Figure 3.19 Taken from Hu and Dyke[90], this diagram shows the states which are perturbed due to Coriolis interaction between K=0 upper and K=1 lower levels. Only states of the same J and symmetry will interact.

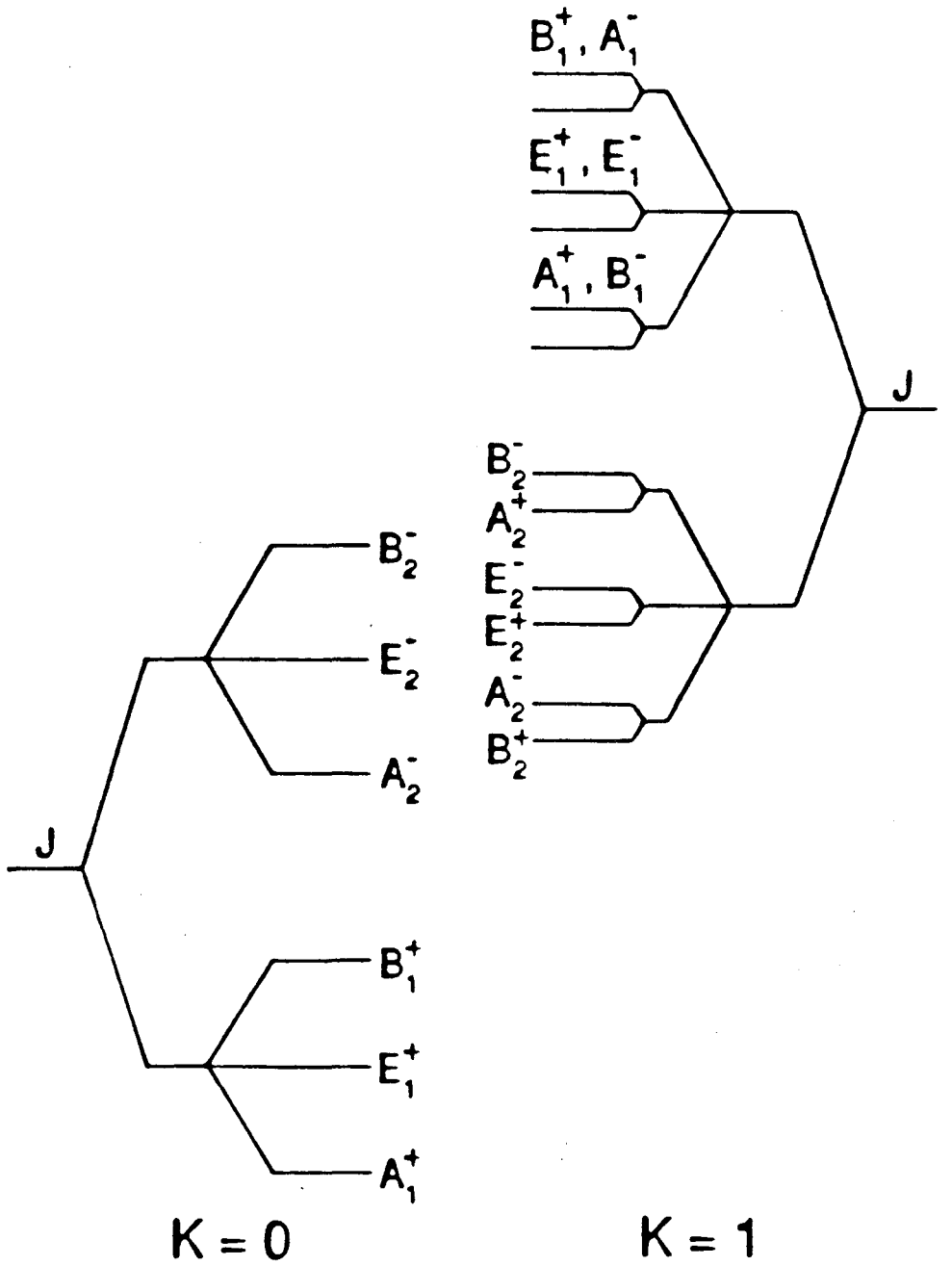

Therefore, as is shown in the figure, only the upper states of the K-type doublets will interact; the lower states are the wrong symmetry. Dyke was treating only the E state transitions, but Fraser et al.[88] also observed a Coriolis perturbation in the A_2/B_2 states, as predicted. They also observed that only the upper states of the K-type doublets were affected. From their fit, Hu and Dyke obtained a value for ζ of 1409.2 MHz for the E states and 1595.6 MHz for the A_2/B_2 states. As was pointed out by Hu and Dyke, the ratio $\zeta/2C \approx 1/8$ indicates that there is considerable vibrational angular momentum, or extensive mixing of the K=0 upper and K=1 lower states. This implies that the assumption of the high barrier limit may not be valid, at least in terms of the 1→4 tunneling motion.

From their fit they also obtained Δ, the spacing between K=0 upper and K=1 lower states. For the E states this value is 10717 MHz and for the A_2/B_2 states it is 14150 MHz. Including this Coriolis perturbation in the fit also results in values for the rotational constant and asymmetry parameter for these states being much closer to those of the K=0 lower and K=1 upper states; that is, the (B-C) is no longer anomalously large, and the rotational and distortion constants among all of the tunneling states are now very similar.

In 1989, Huang and Miller published a second study of the water dimer.[91] In this detailed investigation, they obtained spectra associated with the four CH stretching bands between

3500 and 3800 cm^{-1}, some of which were rotationally resolved. Two of these bands are the symmetric and asymmetric stretches of the acceptor molecule, observed at 3600 and 3745 cm^{-1}, respectively. These are, as expected, close to the free water monomer frequencies of 3651.7 and 3755.8 cm^{-1}.[92] The two bands associated with the donor are expected to be considerably different because one of the hydrogens is in the dimer bond. These bands are discussed in terms of a local mode formalism, that is, one band is the OH stretch of the non-bonded hydrogen, referred to as the "free" OH stretch, and the second is the OH stretch of the bonded hydrogen. The OH stretch of the bonded hydrogen is shifted the farthest to the red, at 3530 cm^{-1}. The "free" OH stretch is at 3730 cm^{-1}. Several different rovibrational bands are observed for these four vibrations. It is important to note that this is the only experiment which has provided rotationally resolved spectra involving these vibrationally excited states.

The acceptor asymmetric stretch proved to be the most insightful, in that three bands were observed, namely, the $K_a=0\leftarrow1$ which was rotationally resolved, the $K_a=1\leftarrow0$ in which some transitions were resolved, and the $K_a=2\leftarrow1$ which was not well resolved. All of these transitions involve the $A_2/B_2/E$ states, what have been referred to as K=0 upper and K=1 lower. The first of these bands has been discussed in their earlier paper.[84] They observed three Q branches associated with the three levels of the geared internal rotation or $1\rightarrow5$ tunneling

motion. From these measurements they determined that the 1→5 splittings in the vibrationally excited states are 1837 MHz for $K_a'=0$ and 473 MHz for $K_a'=1$.

There were two overlapped bands observed for the acceptor symmetric stretch. These were assigned to $K_a=0\rightarrow1$ and $K_a=1\rightarrow0$, and were not well resolved. Similar bands were also observed for the donor free OH stretch. For the proton donor-bonded OH stretch, only broad unresolved transitions were observed. From these measurements, however, they were able to determine a number of tunneling splittings. Figure 3.20 shows all of the states in which the 1→5 splitting has been determined. There is over a factor of ten reduction in this splitting between the ground and vibrationally excited states for $K_a=0$, and a factor of 35 reduction for $K_a=1$.

Huang and Miller point out that in the 1→5 tunneling motions the donor and acceptor roles are interchanged, and in the case of the vibrationally excited state, this interchange requires an exchange of the vibrational excitation between the monomers. Therefore, it is plausible that this vibrational energy transfer greatly reduces the feasibility of this tunneling motion, and therefore the splitting will be reduced in the vibrationally excited state. This hypothesis implies that in tunneling motions where the roles are not interchanged (the 1→4 and the 1→2), the splitting in the ground and excited states should similar. These splitting have not yet been determined in the excited state.

Figure 3.20 An energy level diagram showing all of the states in which the 1→5 tunneling splitting has been determined. All splittings are given in GHz. The excited vibrational state is the acceptor asymmetric stretch.

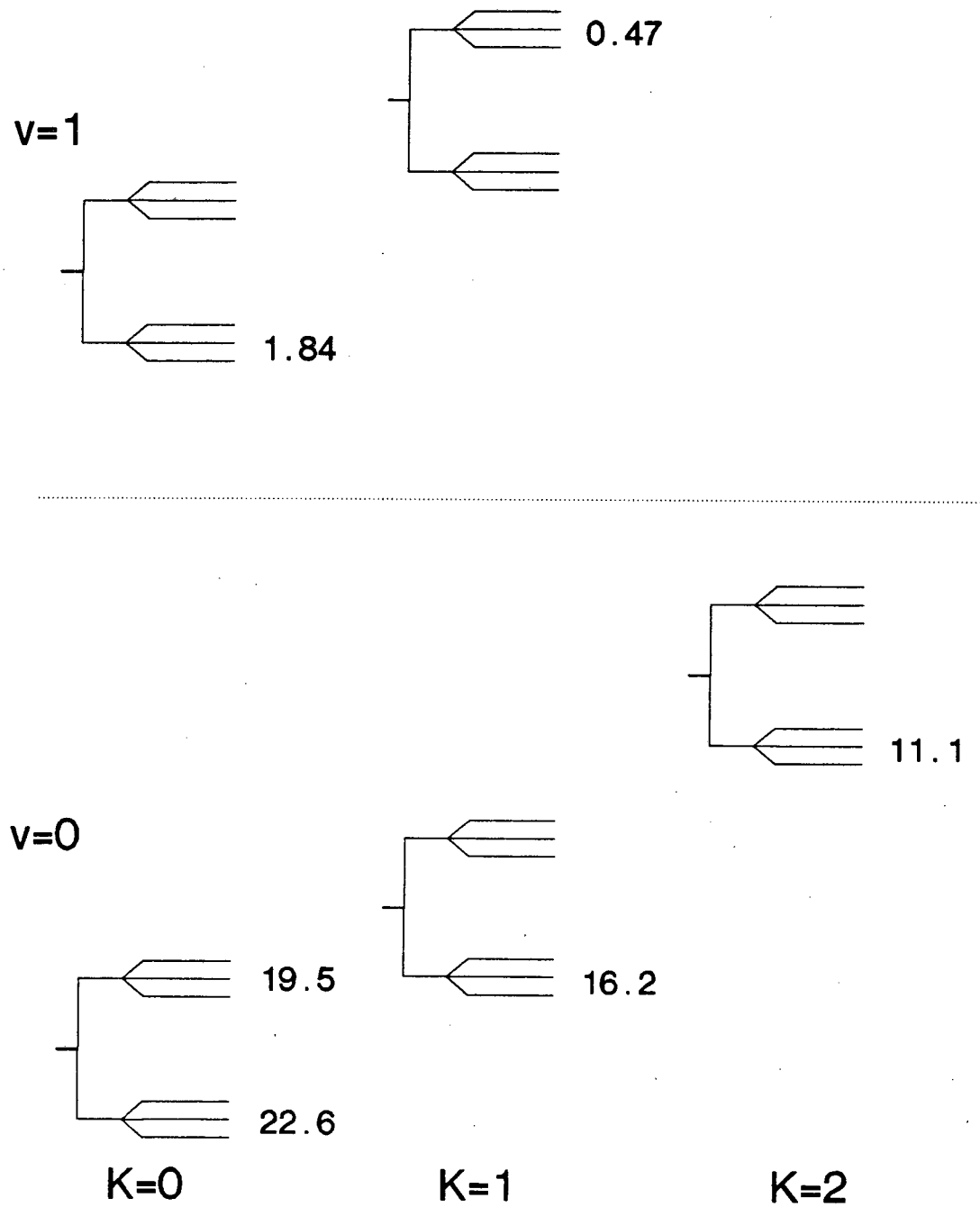

From the linewidths, Huang and Miller determined the lifetimes of the various predissociating states. Some of these lifetimes are predictable; in the case of the proton donor OH stretch, for example, the linewidths are very large, implying that the lifetime is very short. This is presumably due to the fact that the OH stretch is directly coupled to the predissociating coordinate. The spectrum of the asymmetric stretch of the acceptor, conversely, exhibits narrow linewidths indicative of a long lifetime. This vibration is less likely to couple to the hydrogen bond. They observe differences, not only in the lifetimes of the different vibrational states, but also in lifetimes of the different symmetry states within the same band. In the case of the acceptor asymmetric stretch, the linewidths are similar for the E states in the $K_a'=0$ and $K_a'=1$ states, approximately 230 MHz. The A_2 states, however, change dramatically from 50 MHz in $K_a'=0$ to 774 MHz in $K_a'=1$. A similar effect is observed for the B_2 states. The states which are undergoing the 1→5 tunneling (A_2/B_2 states) show a strong K dependence, as opposed to the non-tunneling E states. These results are not yet explained, but may eventually offer insight into understanding the predissociation dynamics of the dimer.

The most recent water dimer spectrum was obtained by Zwart, Ter Meulen, and Meerts.[93] They observed the one remaining set of transitions in the vibrational ground state that is accessible with molecular beam sources. In the cold

jet, only the K=0 lower and upper states and the K=1 lower states will have significant population. Zwart et al. measured the c-type K=0 lower to K=1 upper transitions. These transitions lie in the far infrared between 350 and 500 GHz. The far infrared radiation is generated using a GaAs Schottky barrier diode for harmonic generation of 100 GHz klystron radiation. The dimers were produced in a 40 mm planar cw nozzle. The search for this band was guided by predictions from the Coudert and Hougen fit of the existing dimer data, discussed in the next section. These results gave additional support to Hougen's model and improved the overall quality of the fit. In our lab, we had previously measured a number of the R branch lines, but without P branch lines we could not make the assignment from the combination differences.

3.4.4 The Fit of the Spectroscopic Results

Although the water dimer is a challenging molecule in many different respects, the largest obstacle that had to be overcome in understanding it was ascertaining how to fit the spectroscopic results. Many of the experimentalists fit the individual bands that they observed. However, only in a combined fit of all of the results could the various tunneling splittings be determined. A Hamiltonian had to be developed that could accurately fit all of the obtained results and predict new spectra. The fact that there are at least four feasible tunneling motions, all with different J and K

dependence, makes this problem very complex and very unique. Coudert and Hougen developed such a Hamiltonian, and eventually fit all of the spectroscopic results in a combined analysis. Hougen, in 1985, developed the local internal axis method (IAM), which allowed for the treatment of a system undergoing several tunneling motions.[94] The local IAM is an adaptation of the familiar IAM which has been used successfully in microwave spectroscopy for systems undergoing hindered internal rotation. The first part of this section will briefly discuss the IAM and compare it to a similar method, the principal axis method (PAM), discussing the advantages and disadvantages of each. A basic understanding of both of these methods is helpful in understanding the local IAM. The adaptation of the IAM to the local IAM will then be discussed. This will be followed by a discussion of the results of the fit. The purpose of this section is to provide a qualitative overview of these techniques leaving the reader to examine the rigorous mathematics in Coudert and Hougen.[81,95]

3.4.4.1 IAM versus PAM

The study of tunneling motions did not begin with the study of weakly bound clusters. Hindered internal rotation in stable molecules, such as CH_3SiH_3, has been studied in the microwave for over thirty years. The principal axis method (PAM) and the internal axis method (IAM) were developed to treat hindered internal rotations in such non-rigid molecules.

An excellent review of these methods was written in 1959 by Lin and Swalen.[96] The fundamental difference between these approaches is the choice of coordinate system attached to the molecule. Considering a molecule such as CH_3SiH_3, it can be thought of as being comprised of the rotating methyl group, $-CH_3$ (referred to as the top) and the fixed silyl group, $-SiH_3$, relative to which the methyl group rotates (referred to as the frame). In the PAM, the coordinate system coincides with the principal axes of the molecule and is fixed relative to the frame. In the IAM, one axis coincides with the rotation axis of the top, which does not necessarily coincide with a principle axis. The result of this choice of axes is that in that coordinate system there is no angular momentum generated by the tunneling motion (Figure 3.21). The other two axes are arbitrarily chosen, but typically pass through the center of mass. This choice of axes affects the kinetic terms in the Hamiltonian, which can be separated into an overall rotation term, an internal rotation term, and a coupling term between these two:

$$H = H_{Rot} + H_{Int\ Rot} + H_{Coup} \qquad (3.16)$$

The general approach is then to assume a basis set which is the product of the rotational wave functions and the torsional or internal rotation wave functions, which are calculated from tabulated Mathieu functions.[97] The coupling term is treated as a perturbation. In the PAM, it is straightforward to write down the Hamiltonian and wave functions because the coordinate

Figure 3.21 The choice of axes for the principal axis method (PAM) and the internal axis method (IAM)

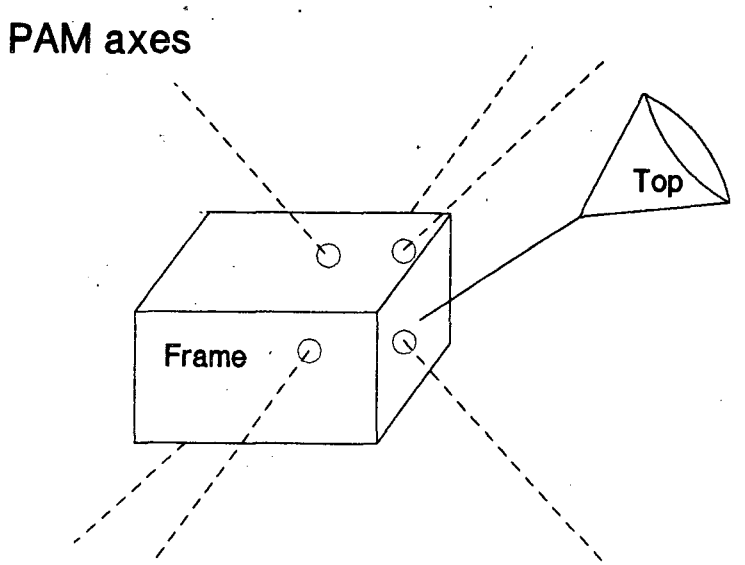

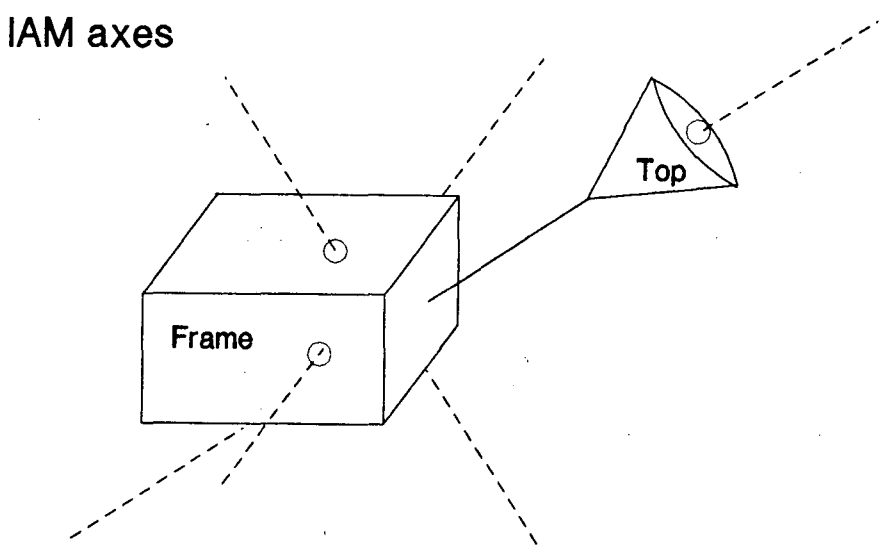

system coincides with the principal axes. However, even in the high barrier limit, the coupling term can be quite large, and in the case of an intermediate barrier, fourth order perturbation theory is typically required. In the IAM, it is much more difficult to write down the operators and wave functions because the coordinate system is shifted from the principal axes. However, the advantage of this method is that the coupling term is zero, through the application of the Neilsen transformation.[98] Therefore, there are no off-diagonal elements in the matrix. Which of these methods is more appropriate depends on the molecule being investigated.

3.4.4.2 Local IAM

In the case of the water dimer, Hougen wanted to use an IAM-like approach, taking advantage of the quality of the zeroth order results. However, in the water dimer, with four or more feasible tunneling motions, it is not possible to choose a single or global coordinate system, such that in any tunneling motion there is no internal angular momentum generated. The basic approach of this method is illustrated in Figure 3.22 taken from Hougen.[94] In the IAM, the focus is to construct an axis system in which internal angular momentum generated by the tunneling motion is zero. In the local IAM, Hougen separates the system into small regions, and in each region an IAM coordinate system is defined. That is, in this small region the internal angular momentum generated by the

Figure 3.22 This diagram, taken from Hougen[94], represents the approach used in the local IAM. In each of the various regions a local IAM coordinate system is defined. Fn refers to a framework coordinate system in which n is the framework number, Pp refers to the path coordinate system where p is the path number, and R is the reference coordinate system.

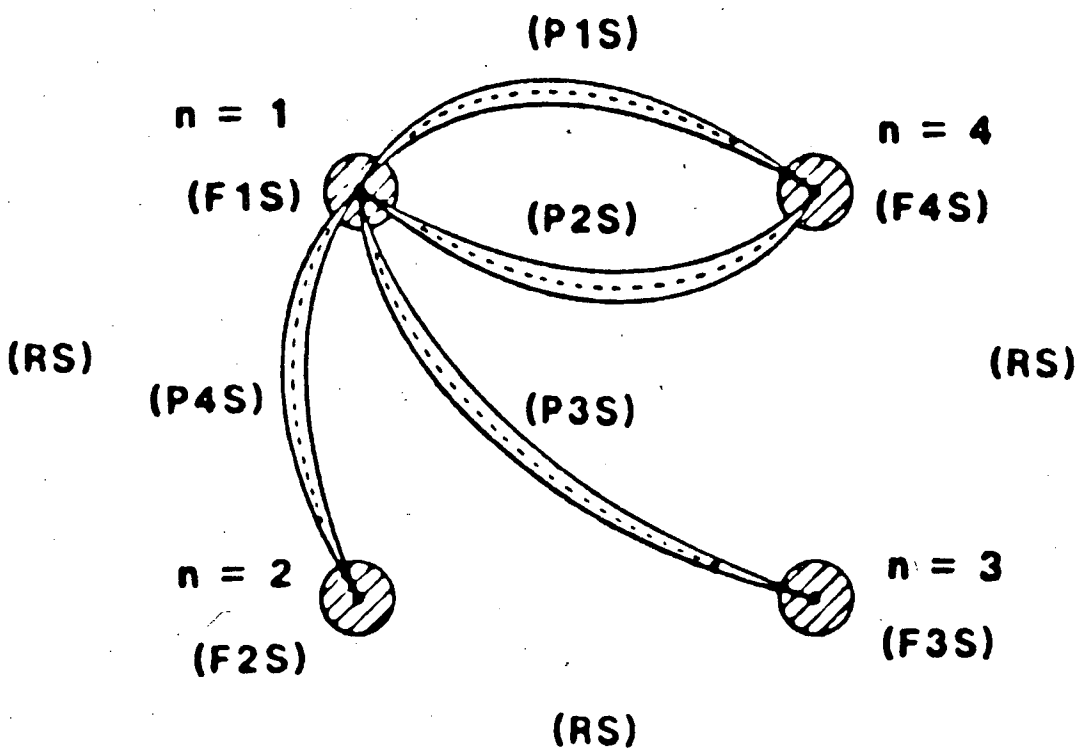

tunneling motion is zero. Local IAM coordinate systems are constructed for each equivalent framework, as well as for each path connecting these frameworks. The framework coordinate systems are labelled Fn, where n refers to the framework number. The path coordinate systems are labelled Pp, where p is a number associated with a specific path between frameworks. Hougen also makes use of a reference coordinate system, labelled as R. The reference system is appropriate near the equilibrium geometry of any framework. The path or framework coordinate systems are appropriate only in the immediate vicinity of the path or the framework, indicated by the shaded regions in Figure 3.22. The difficulty encountered in this method is that for each different coordinate system, there is a different Hamiltonian and set of wave functions which describe the system, and these are only meaningful in the small vicinity of the path or framework.

The approach is to construct a tunneling matrix in which the matrix elements represent the overlap of two frameworks connected by a tunneling Hamiltonian, and then to diagonalize this matrix and fit the spectroscopic results. Hougen writes the individual matrix elements in the form

$$H_{mn}=\int_{Rv}\int_{Rr}[\psi_{vm}(\xi)_{Fm}\cdot D^{(J)}_{K'M}(\chi_{Fm},\theta_{Fm},\phi_{Fm})]\cdot H_R\cdot [\psi_{vn}(\xi)_{Fn}\cdot D^{(J)}_{K''M}(\chi_{Fn},\theta_{Fn},\phi_{Fn})]\,d\tau_{Rr}d\tau_{Rv}\ , \qquad (3.17)$$

where m and n refer to different frameworks, 1 through 8; $\psi_{vm}(\xi)_{Fm}$ is the vibrational wave function in the coordinate system for framework m in terms of the set of large amplitude coordinates ($\xi \equiv (\xi_1, \xi_2, \xi_3)$); the rotation matrices, $D^{(J)}{}_{KM}$, are functions of the Euler angles for a given framework; H_R is the Hamiltonian for the tunneling motion in the reference coordinate system; and the integrals are over the rotational and vibrational degrees of freedom in the reference coordinate system. The first problem encountered in trying to solve this integral is that it is written in terms of three different coordinate systems, namely the reference system (R), the framework system for framework m (Fm), and the framework system for framework n, (Fn). Hougen proposes that this difficulty can be overcome if the integral is rewritten in the coordinate system associated with the path which connects frameworks m and n (Pp). Referring once again to Figure 3.22, it can be seen that only the Pp system is applicable over the tunneling path. The framework and reference systems are only appropriate near the equilibrium geometry. One requirement of the Pp system is that it is equal to the framework coordinate systems, Fm and Fn, at the endpoints of the path. It is straightforward to define the path system such that it is equal to the framework system at one end. However, it may not necessarily match up at the other end. Therefore, a phase factor is introduced to remove the discontinuity in the path. These phase factors are calculated by Coudert and Hougen[81] for

each path assuming that it is the same as the lowest energy trajectory between frameworks on the Coker and Watts[66] potential surface. In the case where there are several possible tunneling paths, the matrix element is the sum of the integrals over each possible path:

$$H_{mn} = \iint Path\ 1\ d\tau + \iint Path\ 2\ d\tau + \ldots \qquad (3.18)$$

The calculation of these integrals requires a fair bit of mathematics and is outlined by Coudert and Hougen.[81,94,95] The Hamiltonian is separated into vibrational and rotational components. The expressions for the various tunneling matrix elements have both pure vibrational and rotational terms. The rotational dependence of the various tunneling splittings are quite complicated, that is, the J- and K-dependence is not strightforward. Therefore, these matrix element expressions are not included here, but are outlined by Coudert and Hougen.[81,95] The tunneling matrix is given in Table 3.5. In the fit by Coudert and Hougen[95], four tunneling motions are included: the 1→4, 1→5, 1→2, and 1→7. This matrix is incorporated into a least squares fitting routine, and all of the available spectroscopic results are included in the fit to give the results of Table 3.6. The different framework numbers refer to the results obtained for the various tunneling motions from framework 1. For example, n=4 results are those associated with the 1→4 tunneling motion along the two proposed tunneling paths. The parameter h_{4v} gives the pure

Table 3.5 The tunneling matrix for $(H_2O)_2$[80]

	1	2	3	4	5	6	7	8
1	$H_{1;1}$	$H_{1;2}$	0	$H_{1;4}$	$H_{1;5}$	$H_{1;5}$	0	0
2	$H_{1;2}$	$H_{1;1}$	$H_{1;4}$	0	$H_{1;5}$	$H_{1;5}$	0	0
3	0	$H_{1;4}$	$H_{1;1}$	$H_{1;2}$	0	0	$H_{1;5}$	$H_{1;5}$
4	$H_{1;4}$	0	$H_{1;2}$	$H_{1;1}$	0	0	$H_{1;5}$	$H_{1;5}$
5	$H_{1;5}$	$H_{1;5}$	0	0	$H_{1;1}$	$H_{1;2}$	0	$H_{1;4}$
6	$H_{1;5}$	$H_{1;5}$	0	0	$H_{1;2}$	$H_{1;1}$	$H_{1;4}$	0
7	0	0	$H_{1;5}$	$H_{1;5}$	0	$H_{1;4}$	$H_{1;1}$	$H_{1;2}$
8	0	0	$H_{1;5}$	$H_{1;5}$	$H_{1;4}$	0	$H_{1;2}$	$H_{1;1}$

Table 3.6 Results of the $(H_2O)_2$ fits of Coudert and Hougen[95] All parameters are given in MHz, except for θ_n and ϕ_n, which are given in degrees. Errors are expressed as one standard deviation and are given in parentheses.

n=1

$A=190327.(450)$

$B=6162.762(130)$

$B-C=29.0219(300)$

$D_{JK}=3.18839(520)$

$D_J=0.049207(120)$

$d_1\times10^3=1.1578(880)$

$d_2\times10^3=0.8444(330)$

n=2

$h_{2v}=-746.0414(780)$

$\theta_2=2.11277(740)$

$h_{2j}=-0.10842(710)$

$f_2=0.05259(440)$

$h_{2jk}=0.01157(450)$

n=4

$h_{4v}=-47353.(250)$

$\phi_4=162.093(230)$

$\theta_4=0.95127(390)$

$h_{4j}=2.6324(120)$

$f_4=-4.2927(320)$

$\phi_{4j}\times10^3=0.751(140)$

$\theta_{4j}\times10^3=-0.05522(150)$

$h_{4jk}=-4.243(130)$

n=5

$h_{5v}=-5260.735(150)$

$h_{5k}=1094.52(110)$

$h_{5j}=1.03691(140)$

$f_5=-0.17026(110)$

$h_{5kk}=-111.228(110)$

$h_{5jk}=-0.19675(350)$

n=7

$h_{7v}=-377.9799(150)$

$\phi_7=116.6871(940)$

$\theta_7=3.68900(630)$

vibrational contribution to the 1→4 tunneling splitting, whereas the actual splitting is $4|h_{4v}|$. The other parameters are associated with the rotational Hamiltonian. Hougen points out that it is difficult to physically interpret the meaning of the Euler angles, χ_n, θ_n, and ρ_n, but they are related to "the amount of angular momentum generated" during the tunneling motion. The n=1 results (tunneling from 1→1), are the non-tunneling, pure rotational parameters. From Table 3.6, it is clear that the pure vibrational terms in the tunneling splittings vary considerably among the four motions. The tunneling splitting for the 1→4 motion (the acceptor hydrogen interchange) is the largest, as predicted to be, approximately 190 GHz. The 1→5 motion (the geared donor-acceptor interchange) splitting is 21 GHz. The 1→2 motion (the donor hydrogen interchange) splitting is approximately 3 GHz. For the 1→7 motion (the anti-geared donor-acceptor interchange) splitting is only 1.5 GHz. The earlier Hougen papers ignored this tunneling motion, assuming that it was too small, Hougen suggests that this anti-geared motion may not be occurring directly, but may occur stepwise, proceeding through an intermediate framework, such as a 1→4→7 motion. These results are not conclusive.

Although some questions remain regarding the application of the local IAM to the water dimer, it must be considered a very successful approach to fitting the data and a successful, although not conclusive, test of the method. It appears

unlikely that the high barrier limit is appropriate to the water dimer, particularly with regard to the 1→4 tunneling motion. However, the overall quality of the fit is good. The success of this method was certainly dependent on the combined efforts of many different groups, experimentalists and theorists. From the earliest microwave results to the most recent far infrared work, each of these experiments provided a necessary contribution to the understanding of this complex system.

3.5 Future Studies of Water Polymers

This section is included as something of a compilation of data and predictions for the water dimer vibrations and the spectroscopy of larger clusters. Obviously, the amount of work done on these projects is quite limited, and therefore there will be much more speculation in this section. The work on the water dimer discussed in this chapter, in the microwave and far infrared regions, probes the tunneling-rotation spectrum. The transitions occur across the various tunneling splittings. The infrared studies have investigated combination bands of the high frequency OH stretches with the tunneling-rotation spectrum. Although these results provide important information about the potential and tunneling barriers, probing the low frequency dimer vibrations would provide much more information about the global potential. High resolution studies of the trimer could answer important questions regarding the non-

additivity of hydrogen bonding, certainly a crucial step in understanding liquid water. There are important water cluster projects remaining which may provide the results upon which a complete water-water potential depends.

3.5.1 The Water Dimer Vibrational Spectra

In the water dimer, there are twelve vibrational modes; six are high frequency vibrations associated with the monomers, and six are low frequency modes associated with the hydrogen bond. It is the low frequency vibrations that are the focus of this section. These modes are more directly related to the hydrogen bonding, to the intermolecular potential. The bond energy of the dimer is about 5 kcal/mole. Although that is a relatively weak chemical bond, the predicted vibrations occur at greater than 80 cm^{-1}, which at the present time is just beyond what is convenient for scanning on the tunable far infrared laser. It is not, however, far out of reach, given the new detectors available, and progress with far infrared output couplers and diodes.

Figure 3.23 shows the water dimer structure with the various angles labelled. Table 3.7 lists the six low frequency modes with a description of the type of motion involved, as assigned by Reimers and Watts.[65] Table 3.8 lists predicted frequencies from several different groups. There is a large discrepancy among the values, but in general, the lowest frequency vibration is the torsion about the hydrogen

Figure 3.23 The water dimer structure including the angles used to describe the vibrations

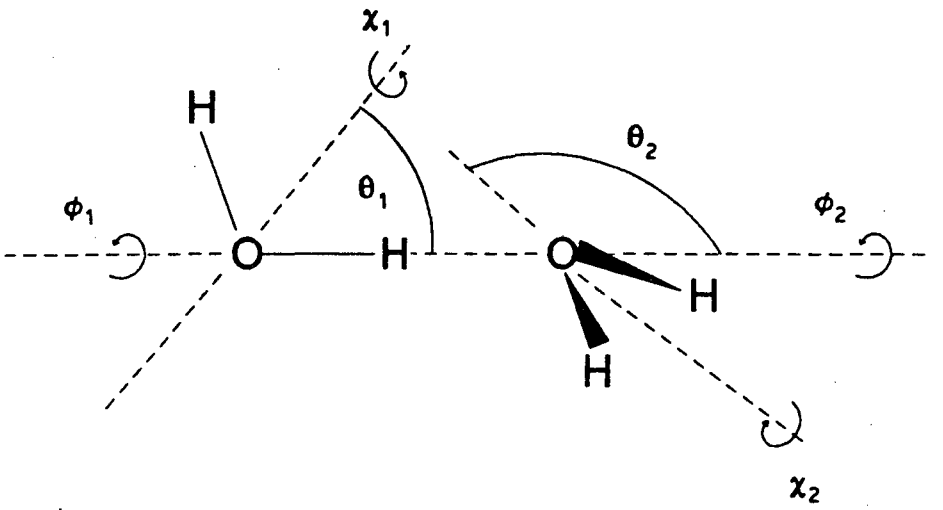

Table 3.7 The six low frequency vibrational modes numbered according to Reimers and Watts[65]

Mode(Symmetry)	Description
ν_6 (a')	In plane bend, θ_1
ν_7 (a')	O-O stretch
ν_8 (a')	Acceptor bend, θ_2
ν_{10} (a")	Out of plane bend, χ_1
ν_{11} (a")	Acceptor twist, χ_2
ν_{12} (a")	Torsion, ϕ_1 and ϕ_2

Table 3.8 The predicted vibrational frequencies for the lowest six modes of the water dimer (cm^{-1})

Mode	Reimer & Watts (Ref. 65)		Curtiss & Pople (Ref.98)	Swanton et al. (Ref. 101)	Slanina (Ref. 99)	Wójcik and Rice (Ref. 100)			Amos (Ref. 102)	Dykstra (Ref. 99)
6	483	482	452	322	345	489	327	334	356	352
7	272	269	204	169	183	283	120	108	174	214
8	169	169	185	96	131	263	281	348	148	135
10	782	780	536	541	615	785	509	708	589	547
11	219	219	118	113	148	297	307	831	153	226
12	115	115	81	105	115	103	87	132	129	147
Method	RWK2-M	RWK2-H	4-31G	MCY II	MCY II	RWK2-M	CF	PM6	4-31G ext.	MMC

bond(ν_{12}). The acceptor bend(ν_8) frequency is also quite low. The dimer stretch(ν_7) is predicted at around 200 cm^{-1}, which is unfortunately higher in frequency than could be expected from the far infrared laser experiment in the near future. The frequencies obtained by Dykstra[67] and by Frisch and coworkers[45] are probably the most reliable. These frequencies are all harmonic, and are therefore expected to be considerably higher than the observed frequencies. Unfortunately the large uncertainties on these frequencies makes the far infrared search problems quite difficult. Although the scanning may be tedious, observed lines can readily be identified with the dimer from the available ground state combination differences. This will not be the case for the trimer.

In Table 3.9 is a listing of the predicted intensities of these vibrational transitions. The first two columns are predicted intensities from the work of Swanton and coworkers[101] and Amos.[102] The third column is the dipole derivative calculated by Dykstra.[67] Although the units differ, it is clear that there is a great deal of discrepancy among these three calculations. Amos predicts the stretch(ν_7) to be the most intense, while Dykstra predicts that it will be the weakest.

There are very few experimental observations of these low frequency modes. Dyke et al.[27] predicted a stretching frequency of 149 cm^{-1}, calculated from the centrifugal distortion constant of the ground state. For such an anharmonic surface, this is a rather poor approximation. Farmer and Key[23], using

Table 3.9 The predicted intensities (km/mole) and dipole derivatives (D) for lowest six vibrational modes of the water dimer

Mode	Intensity[a]	Intensity[b]	Dipole Deriv.[c]
6	88	103	0.45
7	257	102	0.09
8	64	231	0.67
10	154	188	0.29
11	17	148	0.38
12	180	31	0.51

[a] Amos (Ref. 102)
[b] Swanton et al. (Ref. 101)
[c] Dykstra (Ref. 67)

a Czerny-Turner infrared spectrometer, observed broad, unassignable lines at 317.5 and 359.2 cm^{-1}. They were, however, unable to determine the water concentration dependence of the intensity of these lines. In matrix isolation studies by Miyazawa in 1960[103], three peaks between 200 and 270 cm^{-1} were observed. By measuring the intensities as a function of the molar ratio to a known water dimer band at 3725 cm^{-1}, he proposed that the peak at 243 cm^{-1} was due to the dimer. The most extensive study was performed by Bentwood, Barnes, and Orville-Thomas in 1980.[12] They assigned four peaks in a nitrogen matrix to the dimer (ν_6 at 320, ν_7 at 155, and ν_{10} at 520 cm^{-1}). These results, although tentative, serve as a starting point for a far infrared search. Observation of one or more of these low frequency modes would be very important to understanding the water-water potential. It would also be very interesting to ascertain the effect of the hydrogen bond excitation on the various tunneling motions.

3.5.2 The Water Trimer and Larger Polymers

The structure of the trimer is calculated to be cyclic, as are those of the other water polymers which have been calculated.[67] The mass deflection studies of Dyke and Muenter[24] and Kay and Castleman[104] indicated that the larger polymers are only very weakly polar, unlike the dimer, which is strongly polar, and are most likely cyclic. The structure for the trimer is shown in Figure 3.24. The equilibrium structure has

Figure 3.24 The water trimer structure

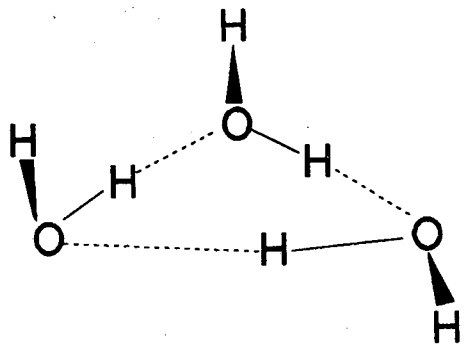

two of the non-bonded hydrogens above the plane of the ring and one below the plane. However, the structures in which all three hydrogens are above the ring, or in the plane of the ring are very close in energy. In the first structure, the complex has no symmetry elements (it has C_1 symmetry). Interestingly enough, it is also chiral, i.e. there are equivalent energy structures which are not superimposable, shown in Figure 3.25. One of the primary questions is: How easily do the hydrogens flip above and below the plane of the ring? Does this flipping occur on a fast timescale, such that the structure can be considered planar from a PI standpoint, in which case it would have C_{3h} symmetry?

Due to the fact the trimer has three more atoms than the dimer, it is reasonable to expect that the group theory is going to be considerably more complex, and this is indeed the case. The CNPI group has an order of 96, compared to the dimer, for which is only 16. The standard Longuet-Higgins PI theory for this complex is so complicated that it has not been completely worked out yet. However, Dyke and Balasubramanian, using Wreath Product Groups have determined the spin species, spin statistical weights and the correlation diagram for the planar (C_{3h}) structure to the symmetry group of the complex, labelled $S_3[S_2]xI$.[105] The explanation of the Wreath Product Group method is well beyond the scope of this thesis. The purpose of this method is to provide symmetry information about large complexes, in a relatively simple and not

Figure 3.25 The non-superimposable left- and right-handed water trimer structures

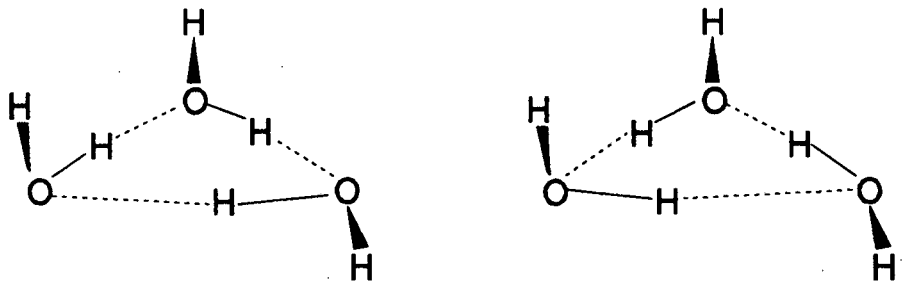

exceedingly tedious way. Dyke and Balasubramanian demonstrated the success of this method by also analyzing the benzene dimer, which has a group order of 586. More information about this method can be found in Reference 105. The correlation diagram for the water trimer is shown in Table 3.10. The spin statistical weights are $A_1(1)$, $A_2(0)$, $A_3(10)$, $A_4(1)$, $E_1(0)$, $E_2(8)$, $T_1(3)$, $T_2(0)$, $T_3(6)$, and $T_4(3)$. This implies that at most, there can be seven observable states for each rotational state, depending on the number of feasible tunneling motions.

Although the group theory is more complicated for the trimer, it is likely that there are going to be fewer feasible tunneling motions, due to the fact that the structure is cyclic and more rigid. Therefore, the spectrum will be simpler to analyze. If we assume that the equilibrium structure is the non-planar structure with two free hydrogens on one side of the ring, then the most feasible tunneling motion will be the flipping of one hydrogen above and below the plane of the ring. Owicki and coworkers calculate the barrier to this motion to be 0.62 kcal/mole.[57] However, including the zero-point energy essentially reduces this barrier to zero. This single hydrogen flip does result in a change in the handedness of the trimer. Although the energy of the two frameworks is certainly the same, the frameworks are not superimposable. Of course, two hydrogens flipping will result in no change in the chirality. In the case of the C_3 structure, in which all three hydrogens are on the same side of the ring, all three

Table 3.10 The correlation table for the water trimer (Ref. 105)

C_{3h}	$S_3[S_2]\times I$
$A_1^+(24)$	$A_1^+(1) + A_2^+(0) + A_3^+(10) + A_4^+(1) + T_1^+(3) + T_2^+(0) + T_3^+(6) + T_4^{+(3)}$
$A_1^-(24)$	$A_1^-(1) + A_2^-(0) + A_3^-(10) + A_4^-(1) + T_1^-(3) + T_2^-(0) + T_3^-(6) + T_4^{-(3)}$
$E^+(20)$	$E_1^+(0) + E_2^+(8) + T_1^+(3) + T_2^+(0) + T_3^+(6) + T_4^+(3)$
$E^-(20)$	$E_1^-(0) + E_2^-(8) + T_1^-(3) + T_2^-(0) + T_3^-(6) + T_4^-(3)$

hydrogens would have to flip at once to arrive at anequivalent energy framework, and again, this would result in a change in the chirality. This chirality associated with a non-rigid molecule appears to be a somewhat unique situation. (Clearly, there are chiral rigid systems, but these systems cannot tunnel through some barrier to change handedness). One well studied example is hydrazine, which has been discussed by Hougen.[71] In this case, the tunneling results in a non-superimposable structure which has the same energy. There will be a tunneling splitting associated with this tunneling motion, even though it is not superimposable on the original structure. The difficulty is in working out the group theory; one must be careful in making certain assumptions in this situation, and Hougen outlines this in the hydrazine case. Spectroscopically, these are very interesting molecules. The planar C_{3h} structure of the water trimer is, of course, not chiral.

A second conceivable tunneling motion, which may be feasible is a simple (12) type switch, essentially an interchange of the bonding and non-bonding hydrogens in a single monomer. However, there should be a sizable barrier to this motion because the hydrogen bond will be nearly completely broken before the second hydrogen comes around to reform the bond. A third tunneling motion is a concerted hydrogen bond displacement. This is similar to the geared hydrogen bond exchange observed in $(HF)_2$ and $(H_2O)_2$, in which

the free hydrogen on monomer 1 displaces the hydrogen in the bond on monomer 2, and the free hydrogen on monomer 2 displaces the hydrogen in the bond on monomer 3 and so on, around the ring. It is difficult to imagine a cis or trans path associated with this kind of motion, especially since with two hydrogens above the ring and one below, there is not a "smooth" displacement as it goes around the ring. Of these three motions, it is likely that the relative feasibility (from most to least feasible) is hydrogen flipping, then the geared concerted displacement, and then the (12) or C_2 of one monomer.

Using the program MOMIRT which is in the group library, the moments of inertia for the trimer were calculated. It is a near oblate top with κ=0.96. The rotational constants are given in Table 3.11 along with the constants for the dimer from Coudert and Hougen.[95] It is clear from the small size of these rotational constants that there will be no pure rotational spectra in the far infrared, if the trimers are formed cold in the jet. Also, it is unlikely that any of the tunneling motions discussed will be so facile that the tunneling-rotation spectrum will be observable on the TuFIR system, occurring at higher than 14 cm^{-1}. The only possible spectra that will be observable are the vibration-rotation-tunneling (VRT) spectra. There are a number of calculations of the vibrational frequencies of the trimer. Once again, although there are more vibrational modes for the trimer

Table 3.11 The calculated rotational constants for the water trimer compared to the experimentally determined constants for the water dimer.

$(H_2O)_3$	$(H_2O)_2$
A=3524 MHz (.1175 cm^{-1})	A=190.3 GHz (6.3 cm^{-1})
B=3492 MHz (.1164 cm^{-1})	(B+C)/2=6163 MHz (.2054 cm^{-1})
C=1784 MHz (.0595 cm^{-1})	(B-C)= 29 MHz(.001 cm^{-1})
κ=0.96	

because the structure is so much more constrained than the dimer, the predicted frequencies are all at fairly high frequency. Some of these frequencies are given in Table 3.12.

3.6 Conclusion

Understanding the water dimer represents the first step in understanding water-water interactions in liquid phase systems. On a more fundamental level, it is also a prototypical hydrogen bonded system. It is also one of the most complicated dimer complexes due to the many feasible tunneling motions. It also proved to be a rather rigorous test of Hougen's local internal axis method (IAM) for interpreting spectra for systems undergoing several tunneling motions.

From a spectroscopic standpoint, the water dimer is well understood in the lowest states of the vibrational ground state. Further study of other bands in the ground state would require using warmer sources. All of the "cold" bands have been observed. This is the result of a unique collaboration of many groups covering the various regions of the spectrum. Excellent work has also been done in the infrared looking at vibrationally excited states, but still more can be done. Hougen and Coudert were able to arrive at a fit of the combined spectroscopic results [95], proving the power of the local internal axis method.

There are several directions in which this work could develop. One is the study of the low frequency hydrogen bond

Table 3.12 The predicted low frequency vibrational modes for the water trimer

	Owicki, Shipman, and Scheraga (Ref. 57)	Dykstra (Ref. 67)	
Mode	Frequency (cm^{-1})	Frequency (cm^{-1})	Dipole Deriv.(D)
1	720	791	0.04
2	556	553	0.53
3	438	490	0.46
4	362	402	0.19
5	345	367	0.11
6	331	326	0.33
7	207	256	0.06
8	192	213	0.11
9	170	194	0.40
10	164	188	0.20
11	135	170	0.45
12	131	164	0.46

vibrations. The vibrational spectra could provide some very important information for improving the potential surface. Unfortunately, the frequency range over which these are predicted to occur is very difficult to access. Most are predicted to be too low in frequency for most diode lasers (less than 400 cm^{-1}) and too high in frequency for the tunable far infrared laser (greater than 120 cm^{-1}). However, improvements in both systems will make these attainable in the not too distant future.

Another direction to pursue is the study of the larger clusters, particularly the trimer and tetramer. In terms of liquid water interactions, these clusters are very important in understanding many-body interactions. The trimer is the smallest cluster in which each water acts as both proton donor and proton acceptor, as would be expected in the liquid. The small rotational constants for these structures imply that bands analogous to those observed in the water dimer, the tunneling-rotation bands, will lie in the microwave region. We cannot expect these bands to be observable in with the TuFIR spectrometer. As for the vibrations, they are predicted to be in a range similar to the dimer vibrations. Dykstra's lowest frequency harmonic prediction is 164 cm^{-1}.[67] Again, this will be difficult to access with the far infrared laser at this time. However, one tetramer band is predicted by Dykstra to be at 30 cm^{-1} [67], which is very accessible. As was discussed for the trimer, because the tetramer is cyclic, tunneling motions

should be rather limited compared to the dimer. Compared to the trimer, it should be somewhat more "floppy" because it is a larger, less strained ring and therefore more motions should be feasible. The tetramer may be one explanation for the unassigned lines tabulated in Appendix C.

Chapter 3 References

1. J.M. Hutson, J. Chem. Phys. **89**, 4550 (1988), and references therein.

2. W.H. Stockmayer, J. Chem. Phys. **9**, 398 (1941).

3. J.D. Lambert, Disc. Faraday Soc. **15**, 226 (1953).

4. L.A. Curtiss, D.J. Frurip, and M. Blander, Chem. Phys. Lett. **54**, 575 (1978).

5. L.A. Curtiss, D.J. Frurip, and M. Blander, J. Chem. Phys. **71**, 2703 (1979).

6. G.-J. Su, Ind. Eng. Chem. **38**, 803 (1946).

7. M. Van Thiel, E.D. Becker, and G.C. Pimentel, J. Chem. Phys. **27**, 486 (1957).

8. A.J. Tursi and E.R. Nixon, J. Chem. Phys. **52**, 1521 (1970).

9. G.P. Ayers and A.D.E. Pullin, Spectrochim. Acta **32A**, 1695 (1976).

10. L. Fredin, B. Nelander, and G. Ribbegård, J. Chem. Phys. **66**, 4065 (1977).

11. L. Fredin, B. Nelander, and G. Ribbegård, J. Chem. Phys. **66**, 4073 (1977).

12. R.M. Bentwood, A.J. Barnes, and W.J. Orville-Thomas, J. Mol. Spect. **84**, 391 (1980).

13. G.C. Maitland, M. Rigby, E.B. Smith, and W.A. Wakeham, Intermolecular Forces-Their Origin and Determination, (Clarendon Press, Oxford, 1981) pp.485ff.

14. J.M. Farrar and Y.T. Lee, Chem. Phys. Lett. **26**, 428

(1974).

15. P.H. Kydd, J. Chem. Phys. **37**, 931 (1962).

16. W.R. Snow, J.T. Dowell, J.G. Chevrenak, and H.E. Berek, J. Chem. Phys. **58**, 2517 (1973).

17. K.L. Wendell, Ph.D. Dissertation, Purdue University, 1970.

18. R.W. Bickes, Jr., G.O. Este, G. Scoles, and K.M. Smith, J. Phys. B: Atom. Molec. Phys. **7**, L19 (1974).

19. R.W. Bickes, Jr., G. Duquette, C.J.N. van den Meijdenberg, A.M. Rulis, G. Scoles, and K.M. Smith, J. Phys. B: Atom. Molec. Phys. **8**, 3034 (1975).

20. H.A. Gebbie, J. Chamberlain, and W.J. Burroughs, Nature **220**, 893 (1968).

21. H.A. Gebbie and W.J. Burroughs, Nature **217**, 1241 (1968).

22. H.A. Gebbie, W.J. Burroughs, J.E. Harries, and R.G. Jones, Nature **221**, 143 (1969).

23. C.B. Farmer and P.J. Key, Appl. Optics **4**, 1051 (1965).

24. T.R. Dyke and J.S. Muenter, J. Chem. Phys. **57**, 5011 (1972).

25. T.R. Dyke and J.S. Muenter, J. Chem. Phys. **60**, 2929 (1974).

26. H.K. Hughes, Phys. Rev. **72**, 614 (1947).

27. T.R. Dyke, K.M. Mack, and J.S. Muenter, J. Chem. Phys. **66**, 498 (1977).

28. T.R. Dyke, J. Chem. Phys. **66**, 492 (1977).

29. M.F. Vernon, D.J. Krajnovich, H.S. Kwok, J.M. Lisy, Y.R.

Shen, and Y.T. Lee, J. Chem. Phys. **77**, 47 (1982).

30. M.F. Vernon, J.M. Lisy, D.J. Krajnovich, A.Tramer, H.S. Kwok, Y.R. Shen, and Y.T. Lee, Faraday Disc. Chem. Soc. **73**, 387 (1982).

31. R.H. Page, J.G. Frey, Y.R. Shen, and Y.T. Lee, Chem. Phys. Lett. **106**, 373 (1984).

32. D.F. Coker, R.E. Miller, and R.O. Watts, J. Chem. Phys. **82**, 3554 (1985).

33. S. Wuelfert, D. Herren, and S. Leutwyler, J. Chem. Phys. **86**, 3751 (1987).

34. K. Morokuma and L. Pedersen, J. Chem. Phys. **48**, 3275 (1968).

35. P.A. Kollman and L.C. Allen, J. Chem. Phys. **51**, 3286 (1969).

36. K. Morokuma and J.R. Winick, J. Chem. Phys. **52**, 1301 (1970).

37. G.H.F. Diercksen, Chem. Phys. Lett. **4**, 373 (1969).

38. J.E. Del Bene and J.A. Pople, J. Chem. Phys. **52**, 4858 (1970).

39. H. Popkie, H. Kistenmacher, and E. Clementi, J. Chem. Phys. **59**, 1325 (1973).

40. D. Hankins, J.W. Moskowitz, and F.H. Stillinger, J. Chem. Phys. **53**, 4544 (1970).

41. H. Kistenmacher, G.C. Lie, H. Popkie, and E. Clementi, J. Chem. Phys. **61**, 546 (1974).

42. H. Kistenmacher, H. Popkie, E. Clementi, and R.O Watts,

J. Chem. Phys. **60**, 4455 (1974).

43. G.H.F. Diercksen, W.P. Kraemer, and B.O. Roos, Theoret. Chim. Acta **36**, 249 (1975).

44. M.J. Frisch, J.A. Pople, and J.E. Del Bene, J. Phys. Chem. **89**, 3664 (1985).

45. M.J. Frisch, J.E. Del Bene, J.S. Binkley, and H.F. Schaefer III, J. Chem. Phys. **84**, 2279 (1986).

46. F.S. Boys and D. Bernardi, Mol. Phys. **19**, 553 (1970).

47. K. Szalwicz, S.J. Cole, and R.J. Bartlett, J. Chem. Phys. **89**, 3662 (1988).

48. B. Jeziorski and M. van Hemert, Mol. Phys. **31**, 713 (1976).

49. B.J. Smith, D.J. Swanton, J.A. Pople, H.F. Schaefer III, and L. Radom, J. Chem. Phys. **92**, 1240 (1990).

50. P.Hobza and R. Zahradník, Studies in Physical and Theoretical Chemistry 52 Intermolecular Complexes-The Role of van der Waals Systems in Physical Chemistry and in Biodisciplines (Elsevier, New York, 1988).

51. S. Roszak, W.A. Sokalski, P.C. Hariharan, and J.J. Kaufman, Theor. Chim. Acta **70**, 81 (1986).

52. A. Ben-Naim and F.H. Stillinger, "Aspects of the Statistical Mechanical Theory of Water," in Structure and Transport Processes in Water and Aqueous Solutions, edited by R.A. Horne (Wiley-Interscience, New York, 1972).

53. F.H. Stillinger and A. Rahman, J. Chem. Phys. **57**, 1281

(1972).

54. A. Rahman and F.H. Stillinger, J. Chem. Phys. **55**, 3336 (1971).

55. L.L. Shipman and H.A. Scheraga, J. Phys. Chem. **78**, 909 (1974).

56. L.L. Shipman, J.C. Owicki, H.A. Scheraga, J. Phys. Chem. **78**, 2055 (1974).

57. J.C. Owicki, L.L. Shipman, and H.A. Scheraga, J. Phys. Chem. **79**, 1794 (1975).

58. J. Snir, R.A. Nemenoff, and H.A. Scheraga, J. Phys. Chem. **82**, 2497 (1978).

59. R.A. Nemenoff, J. Snir, and H.A. Scheraga, J. Phys. Chem. **82**, 2504 (1978).

60. J. Sauer and K.P. Schröder, Chem. Phys. Lett. **107**, 530 (1984).

61. O. Matsuoka, E. Clementi, and M. Yoshimine, J. Chem. Phys. **64**, 1351 (1976).

62. G.C. Lie, E. Clementi, and M. Yoshimine, J. Chem. Phys. **64**, 2314 (1976).

63. E. Clementi and P. Habitz, J. Phys. Chem. **87**, 2815 (1983).

64. J.R. Reimers, R.O. Watts, and M.L. Klein, Chem. Phys. **64**, 95 (1982).

65. J.R. Reimers and R.O. Watts, Chem. Phys. **85**, 83 (1984).

66. D.F. Coker and R.O. Watts, J. Phys. Chem. **91**, 2513 (1987).

67. C.E. Dykstra, J. Chem. Phys. **91**, 6472 (1989).

68. J.E. Del Bene and J.A. Pople, J. Chem. Phys. **58**, 3605 (1973).

69. R.S. Mulliken, J. Chem. Phys. **23**, 1833 (1955).

70. J.T. Hougen, Can. J. Phys. **42**, 1920 (1964).

71. J.T. Hougen, J. Mol. Spec. **89**, 296 (1981).

72. N. Ohashi and J.T. Hougen, J. Mol. Spec. **121**, 474 (1987); N. Ohashi, K. Takagi, J.T. Hougen, W.B. Olson, and W.J. Lafferty, J. Mol. Spec. **126**, 443 (1987); N. Ohashi, K. Takagi, J.T. Hougen, W.B. Olson, and W.J. Lafferty, J. Mol. Spec. **132**, 242 (1988).

73. T.R. Dyke, B.J. Howard, and W. Klemperer, J. Chem. Phys. **56**, 2442 (1972); A.S. Pine and W.J. Lafferty, J. Chem. Phys. **78**, 2154 (1983); A.S. Pine, W.J. Lafferty and B.J. Howard, J. Chem. Phys. **81**, 2939 (1984); H.S. Gutowsky, C. Chuang, J.D. Keen, T.D. Klots, and T. Emilsson, J. Chem. Phys. **83**, 2070 (1985); Z.S. Huang, K.W. Jucks, and R.E. Miller, J. Chem. Phys. **85**, 3338 (1986); W.J. Lafferty, R.D. Suenram, and F.J. Lovas, J. Mol. Spec. **123**, 434 (1987).

74. J.T. Hougen, J. Mol. Spec. **109**, 134 (1985).

75. F.A. Cotton, Chemical Applications of Group Theory (Interscience Publishers, New York, 1963); M. Tinkham, Group Theory and Quantum Mechanics (McGraw-Hill, New York, 1964).

76. H.C. Longuet-Higgins, Mol. Phys. **6**, 445 (1963).

77. J.T. Hougen, J. Chem. Phys. **37**, 1433 (1962); J.T. Hougen, J. Chem. Phys. **39**, 358 (1963).

78. P.R. Bunker, Molecular Symmetry and Spectroscopy (Academic Press, San Diego, 1979).

79. T.H. Lowry and K.S. Richardson, Mechanism and Theory in Organic Chemistry (Harper and Row, New York, 1981).

80. L.H. Coudert, F.J. Lovas, R.D. Suenram, and J.T. Hougen, J. Chem. Phys. **87**, 6290 (1987).

81. L.H. Coudert and J.T. Hougen, J. Mol. Spec. **130**, 86 (1988).

82. J.A. Odutola and T.R. Dyke, J. Chem. Phys. **72**, 5062 (1980).

83. J.A. Odutola, T.A. Hu, D. Prinslow, S.E. O'dell, and T.R. Dyke, J. Chem. Phys. **88**, 5352 (1988).

84. Z.S. Huang and R.E. Miller, J. Chem. Phys. **88**, 8008 (1988).

85. L. Martinache, S. Jans-Bürli, B. Vogelsanger, W. Kresa, and A. Bauder, Chem. Phys. Lett. **149**, 424 (1988).

86. T.J. Balle, E.J. Campbell, M.R. Keenan, and W.H. Flygare, J. Chem. Phys. **72**, 922 (1980).

87. G.T. Fraser, R.D. Suenram, L.H. Coudert, and R.S. Frye, J. Mol. Spec. **137**, 244 (1989).

88. G.T. Fraser, R.D. Suenram, and L.H. Coudert, J. Chem. Phys. **90**, 6077 (1989).

89. K.L. Busarow, R.C. Cohen, G.A. Blake, K.B. Laughlin, Y.T. Lee, and R.J. Saykally, J. Chem. Phys. **90**, 3937 (1989).

90. T.A. Hu and T.R. Dyke, J. Chem. Phys. **91**, 7348 (1989).

91. Z.S. Huang and R.E. Miller, J. Chem. Phys. **91**, 6613 (1989).

92. G. Herzberg, Molecular Spectra and Molecular Structure II. Infrared and Raman Spectra of Polyatomic Molecules (Van Nostrand Reinhold, New York, 1945) p.281.

93. E. Zwart, J.J. Ter Meulen, and W.L. Meerts, Chem. Phys. Lett. **166**, 500 (1990).

94. J.T. Hougen, J. Mol. Spec. **114**, 395 (1985).

95. L.H. Coudert and J.T. Hougen, J. Mol. Spec. **139**, 259 (1990).

96. C.C. Lin and J.D. Swalen, Rev. Mod. Phys. **31**, 841 (1959).

97. Tables Relating to Mathieu Functions (Columbia University Press, New York, 1951).

98. H.H. Nielsen, Phys. Rev. **40**, 445 (1932).

99. Z. Slanina, J. Chem. Phys. **73**, 2519 (1980).

100. M.J. Wójcik and S.A. Rice, J. Chem. Phys. **84**, 3042 (1986).

101. D.J. Swanton, G.B. Bacskay, and N.S. Hush, Chem. Phys. **82**, 303 (1983).

102. R.D. Amos, Chem. Phys. **104**, 145 (1986).

103. T. Miyazawa, Bull. Chem. Soc. Japan **34**, 202 (1961).

104. B.D. Kay and A.W. Castleman, Jr., J. Phys. Chem. **89**, 4867 (1985).

105. K. Balasubramanian and T.R. Dyke, J. Phys. Chem. **88**, 4688 (1984).

106. K. Balasubramanian, J. Chem. Phys. **72**, 665 (1980); K. Balasubramanian, J. Chem. Phys. **74**, 6824 (1981); K. Balasubramanian, J. Chem. Phys. **75**, 4572 (1981); J.A. Odutola, D.L. Alvis, C.W. Curtis, and T.R. Dyke, Mol. Phys. **42**, 267 (1981); K. Balasubramanian, Int. J. Quant. Chem. **22**, 1013 (1982).

Chapter 4 The Far Infrared Spectrum of $CH_4 \cdot H_2O$

4.1 Introduction

There is a great deal of interest and controversy surrounding the nature of hydrophobic interactions. Progress in understanding these forces is seriously hindered by the lack of adequate two-body interaction potentials. These can be obtained through the gas phase study of solute-solvent dimers. In the recent studies of Cohen and coworkers on ArH_2O, a number of bands associated with the hindered rotation of the water were observed and assigned, as well as two van der Waals stretching bands.[1,2] From these measurements, Cohen and Saykally determined an accurate potential surface for ArH_2O using the collocation method.[3] ArH_2O is one of the simplest systems that could be used to investigate hydrophobic interactions. $CH_4 \cdot H_2O$ is a natural extension of the ArH_2O study. It is one of the simplest water-hydrocarbon system, and because CH_4 is essentially a sphere, the spectra are expected to be quite similar to the ArH_2O spectra. $CH_4 \cdot H_2O$ is different however, in that unlike Ar, the CH_4 also can undergo hindered rotations. From a spectroscopic standpoint, this study is unique in that it is the first far infrared investigation of a complex in which both subunits act as nearly free internal rotors. It is immediately apparent from our observed spectra that the CH_4 rotational degrees of freedom greatly complicate the observed spectrum. Our approach toward understanding these spectra draws heavily on our understanding of ArH_2O and its

potential surface. It should be stressed that the results and analysis presented here are only preliminary. There is still a great deal of work that needs to be done before this complex is considered well understood or before a potential surface can be determined.

4.2 Lines Observed in a Methane-Water Expansion

In an $Ar/CH_4/H_2O$ expansion, 225 lines were observed throughout the range from 470 - 820 GHz. The scanning was not continuous. Of these lines, 149 were grouped into bands with typical P, Q, and R structure, or into subbands, in which only one branch was observed. These assigned lines are shown in the stick spectrum in Figure 4.1. Patterns could not be found for the remaining 76 lines. These remaining lines are shown in the stick spectrum in Figure 4.2. A typical spectrum is shown in Figure 4.3.

The experiment has been described in Chapter 2 and elsewhere[4]; however, details specific to $CH_4 \cdot H_2O$ will be briefly discussed. Four far infrared laser lines were utilized in the scanning: 527.9260 GHz using DCOOD as the lasing gas, and 584.3882, 692.9514, and 761.6083 GHz all using HCOOH. The expansion gas mixture was prepared by passing Ar (Liquid Air, 99.99%) over the surface of distilled water in a room temperature reservoir. Flow controllers were used to then mix this Ar/H_2O mixture with CH_4 gas. The methane concentration was typically optimized at 1-2% of the total pressure. The nozzle

Figure 4.1 A stick spectrum of the rotationally assigned lines of $CH_4 \cdot H_2O$.

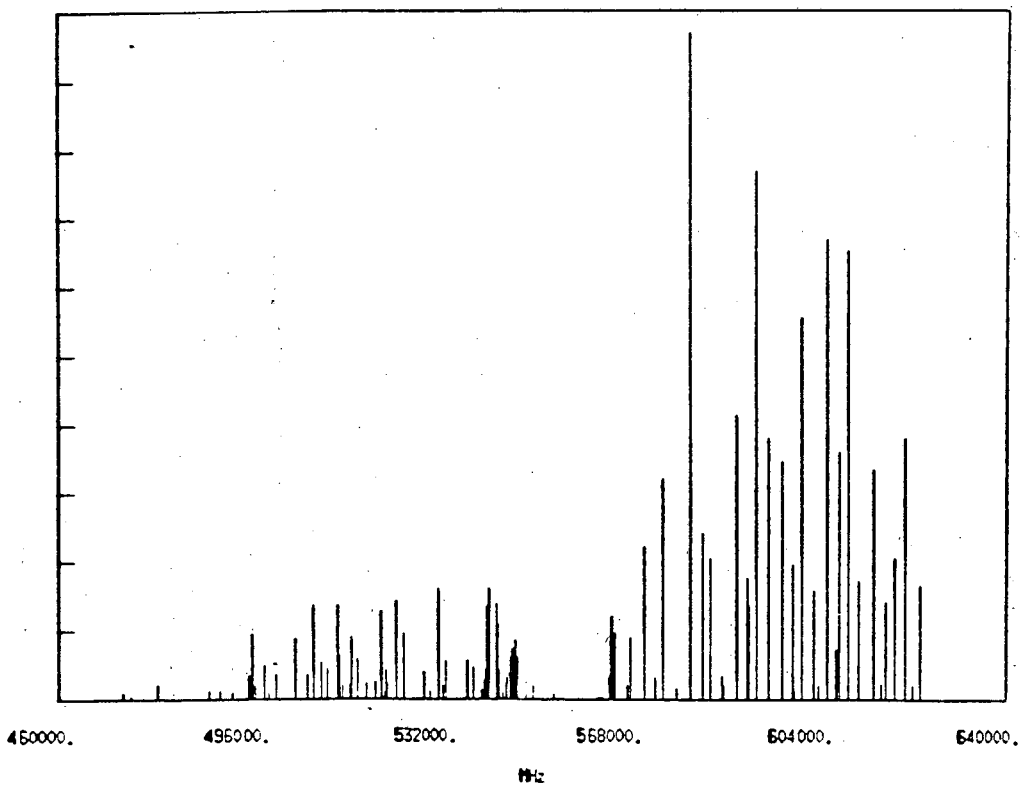

Figure 4.2 A stick spectrum of the unassigned lines observed in an $Ar/CH_4/H_2O$ expansion.

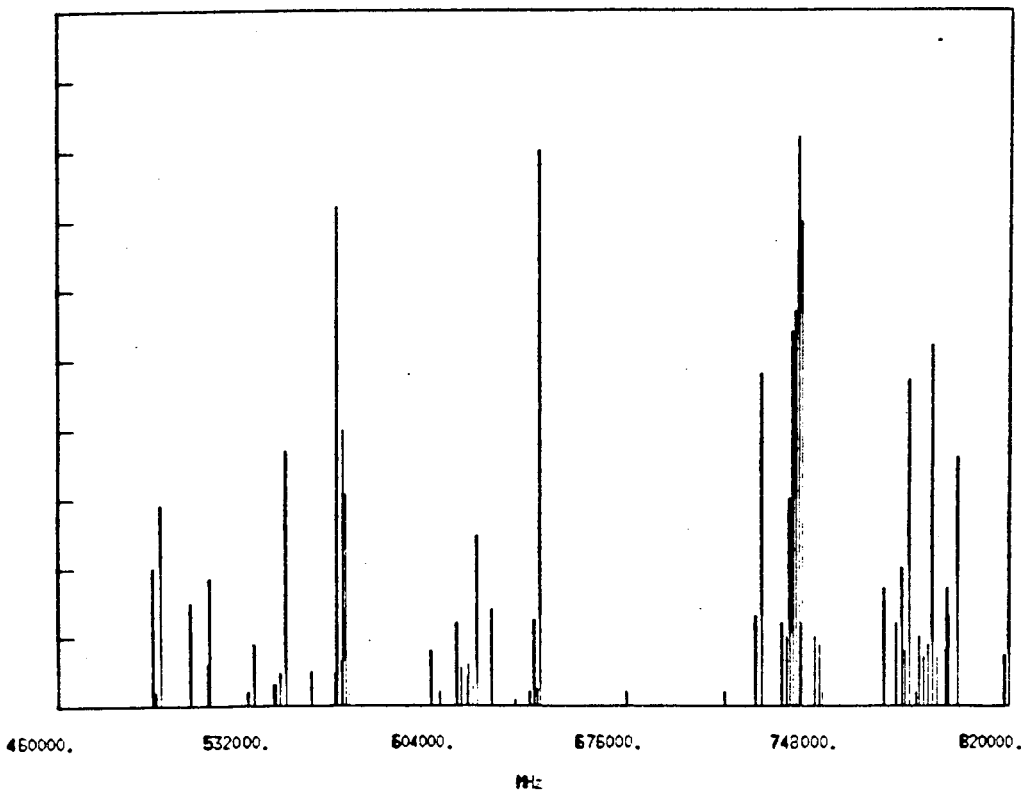

Figure 4.3 A typical spectrum of a $CH_4 \cdot H_2O$ transition (Q(4) of Band A)

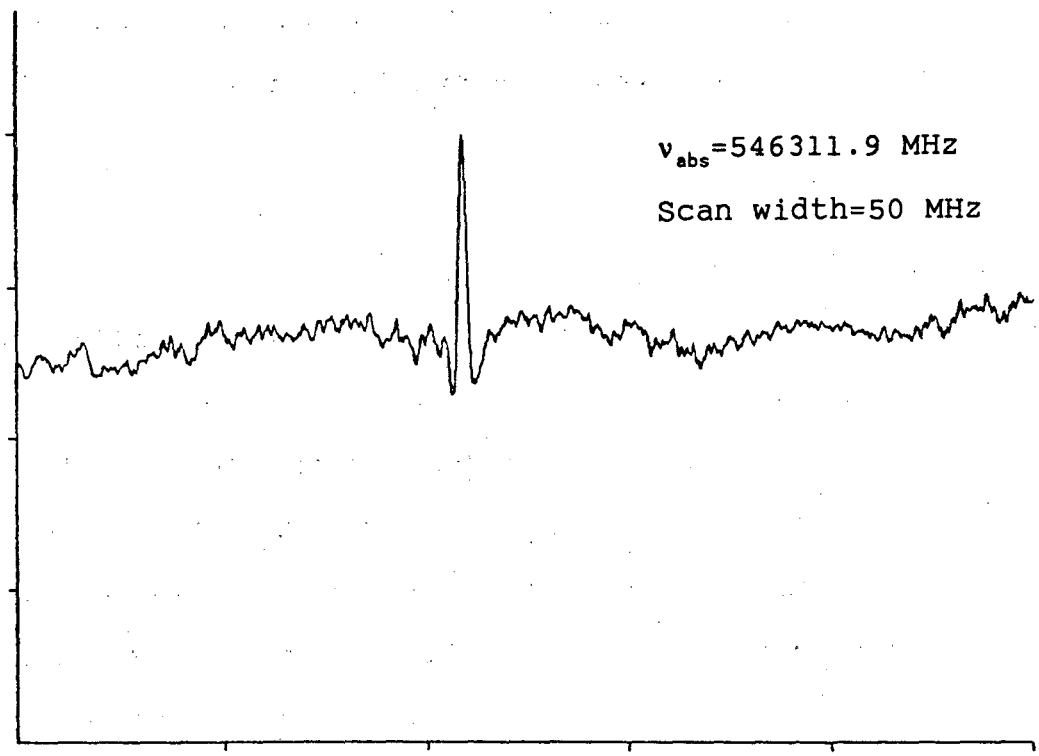

length was 1.5" and the width was .001-.003". The nozzle pressure was typically 700 torr and the chamber pressure was run between 100-130 mtorr. Variations in the nozzle plate spacing as well as the nozzle cleanliness resulted in slight day-to-day pressure variations. The nozzle was run without temperature control. Each observed line was checked to make certain that the signal required both CH_4 and H_2O in the mixture.

4.3 The Proposed Energy Level Diagrams

The first step in attempting to assign these spectra is to develop a proposed energy level diagram. In a system as complex as $CH_4 \cdot H_2O$, there are a number of preliminary steps necessary to presenting the energy level diagram, therefore a brief outline of these steps will be presented. One of the important assumptions that will be made in this development is that the methane and water are nearly free internal rotors in the complex. Therefore, this energy level diagram, to a first approximation, is going to be some type of combination of the pure rotational energy level diagrams of the two monomer units, water and methane. Therefore it is necessary to first understand these monomer eigenstates. The next step is then to review what has been learned from our studies of ArH_2O, in which a single nearly free internal rotor is coupled to a non-rotating sphere. The $CH_4 \cdot H_2O$ project began as an extension of this earlier work on ArH_2O, the assumption being that aside

from the added complication of the CH_4 rotation, the basic foundation for the energy level diagram should strongly resemble the ArH_2O case. The assumptions made in the formulation of the $CH_4 \cdot H_2O$ energy level diagram come directly from the ArH_2O work, therefore this will be discussed in detail. Possible energy level diagrams will then be derived using the ArH_2O example as well as analogies from Hund's cases for the coupling of electronic and rotational angular momentum in diatomic molecules. Finally, some discussion will be presented concerning the future work which remains to be done to help answer some of the many remaining questions about this project.

4.3.1 The Pure Rotational Spectra for Water and Methane Monomers

In Figure 4.4, the lowest few rotational states of the water monomer are shown. Water is an asymmetric top with ground vibrational state rotational constants A=27.79 cm^{-1}, B=14.50 cm^{-1}, and C=9.28 cm^{-1}.[5] Included in the diagram are the asymmetric top labels, J_{KaKc}, nuclear spin statistical weights and the energy spacings. In water, with C_{2v} symmetry and two hydrogens each with spin ½, there are two possible water conformations. One has both hydrogen spins aligned, the para modification and has spin weight equal to one. The second has the two hydrogen spins anti-aligned, the ortho modification and has spin weight equal to three. Transitions between the

Figure 4.4 The energy level diagram showing the rotational states in the ground vibrational state of H_2O. The spin statistical weights are given in parentheses.

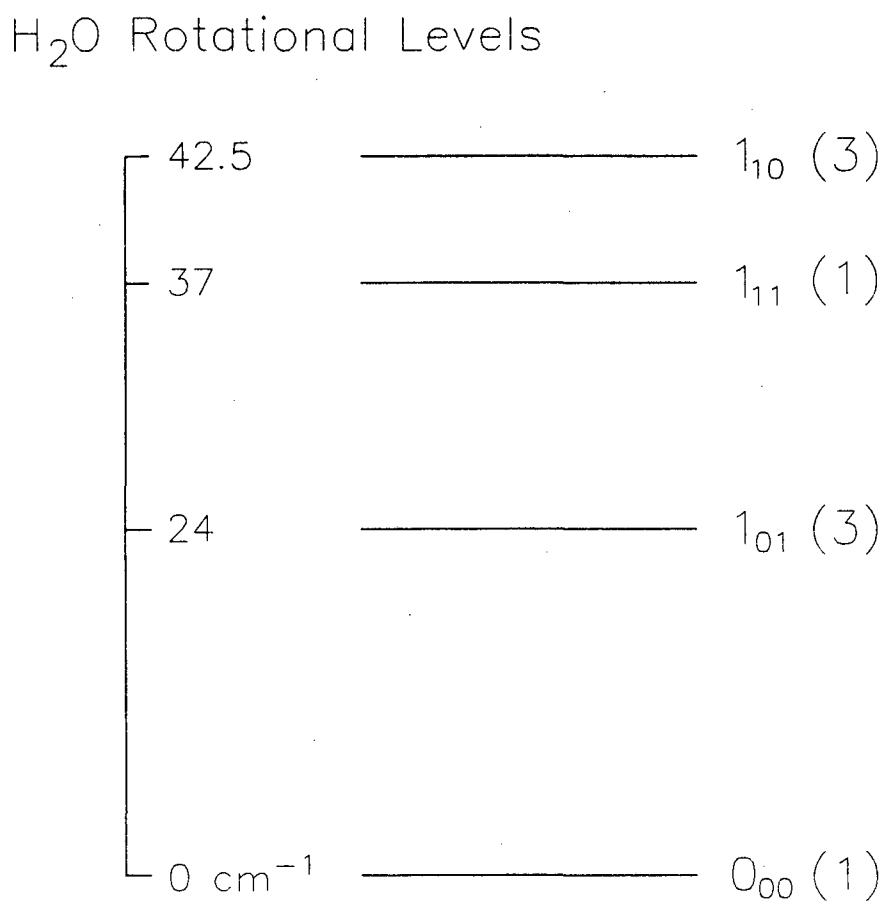

ortho and para states do not occur, either through collisions or dipole transitions, and therefore these states can be thought of as separate unrelated manifolds. This implies that in the cold supersonic expansion there will always be substantial population in the lowest para state (0_{00}) and the lowest ortho state (1_{01}), which is ~23 cm^{-1} higher in energy.

The lowest few rotational levels of the ground vibrational state of methane are shown in Figure 4.5. The state labels, state symmetries, spin weights, and energy spacings are included. Methane has tetrahedral symmetry and has a rotational constant, B, equal to 5.25 cm^{-1}.[5] The spin statistics are rather complicated for a tetrahedral molecule and are described by Herzberg.[5] The rotational states can have A, E, or F symmetry corresponding to all four spins aligned, two spins up and two spins down, and three spins aligned, respectively. Because methane is a symmetric top molecule, the degeneracy with respect to a body-fixed axis, the K degeneracy, must be considered in addition to the degeneracy with respect to a space-fixed axis, the m_j degeneracy. The K degeneracy results in a 2J+1 increase in the number of states for each J. In J=0, there is only a single state with A symmetry which has a spin weight equal to 5. In J=1, 10.5 cm^{-1} higher in energy, there are three F symmetry states which have spin weight equal to two. In J=2, 31.5 cm^{-1} above J=0, there are three F states and two E states. The F states have spin weight equal to two and the E states have spin weight equal to

Figure 4.5 The energy level diagram of the rotational levels of CH_4 in the ground vibrational state. The state symmetries and spin statistical weights are included.

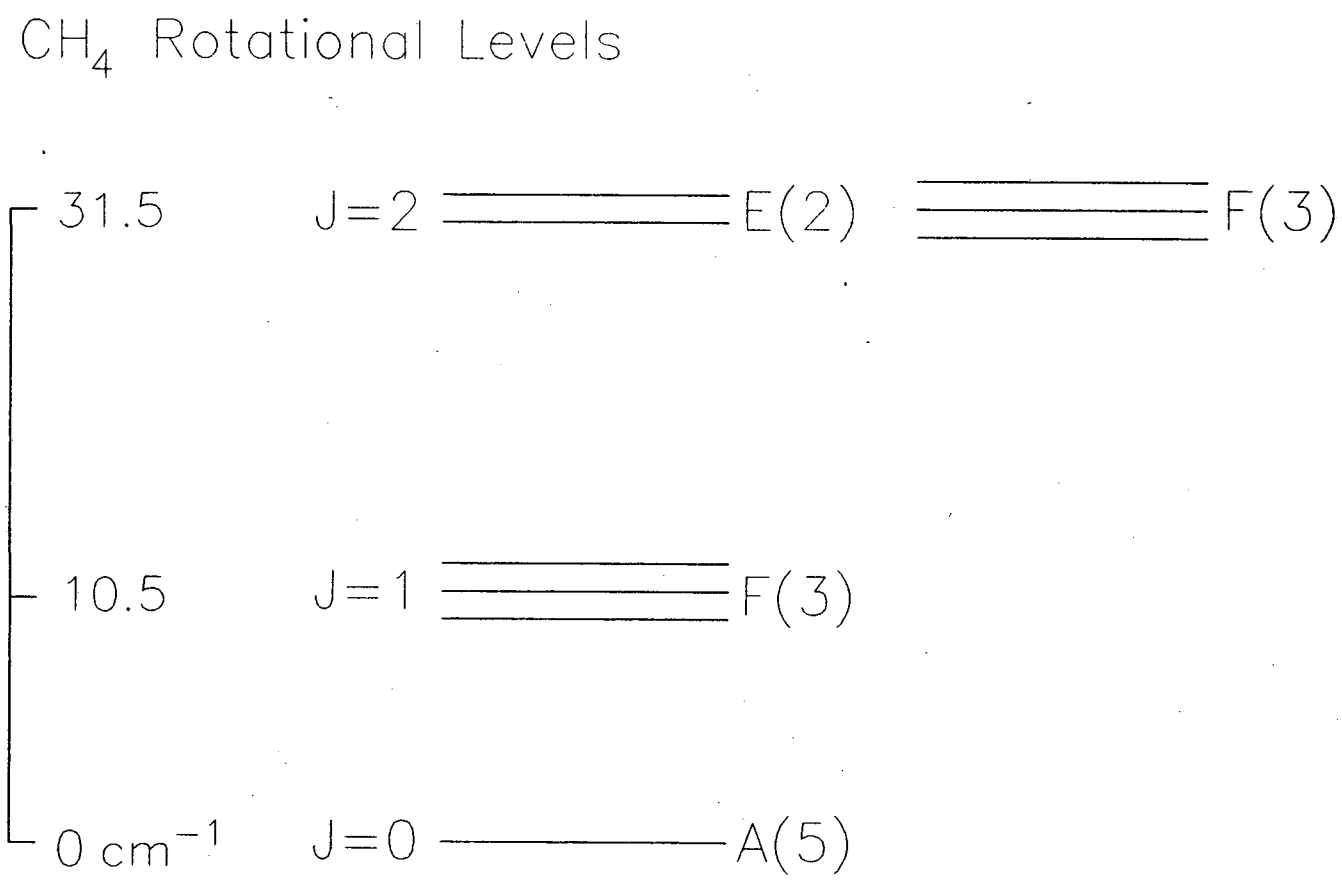

three. As in the water spectrum, there is no interconversion between the different symmetry states. Therefore, in the cold jet J=0 (A symmetry), J=1 (F symmetry), and J=2 (E symmetry) states will all be populated. The J=2 F symmetry states can relax to J=1 and should not have significant population.

4.3.2 The ArH_2O Spectrum

The goal of the ArH_2O study was to determine a potential energy surface for this atom-triatom system solely from spectroscopic results, similar to Jeremy Hutson's potential energy surface determination for the atom-diatom system ArHCl.[6] Our first two papers reported the observation and assignment of several ArH_2O bands.[1,2] Later, Cohen and Saykally determined a potential energy surface from these results using the collocation method.[3] In the experimental studies, four bands in ArH_2O are assigned. Two are assigned as van der Waals stretching bands and the other two are associated with the hindered rotation of the water. In Figure 4.6, taken from Reference 2, three possible energy level diagrams are given. The far left diagram is the energy level scheme if there is no anisotropy. This implies that the argon is an insignificant perturbation to the water and the energy level diagram is identical to the diagram for a freely rotating water molecule. In this limit, the atom-triatom system can be considered a pseudo-diatomic molecule, a freely rotating water molecule, which is essentially a sphere in the isotropic limit, attached

Figure 4.6 The correlation diagram for ArH_2O from Reference 2. (a) On the left is the isotropic limit in which the water is a free rotor in the complex. The water monomer rotational states are unperturbed. (b) On the right is the strongly anisotropic limit in which the water cannot rotate. In this limit, the complex is fairly rigid and motions are restricted to bending vibrations and tunneling motions. The water monomer rotational levels are strongly perturbed and mixed. (c) In the center is the intermediate case in which the anisotropy splits the $J \neq 0$ states, but does not result in extensive mixing of the levels. The motions in this case are hindered rotations of the water subunit. The observed ArH_2O bands were assigned and fit using this scheme and the observed hindered rotation bands are depicted by the arrows. Superimposed on all of the levels in all three cases is the rotational manifold associated with the end-over-end rotation of the complex.

The ArH_2O Correlation Diagram

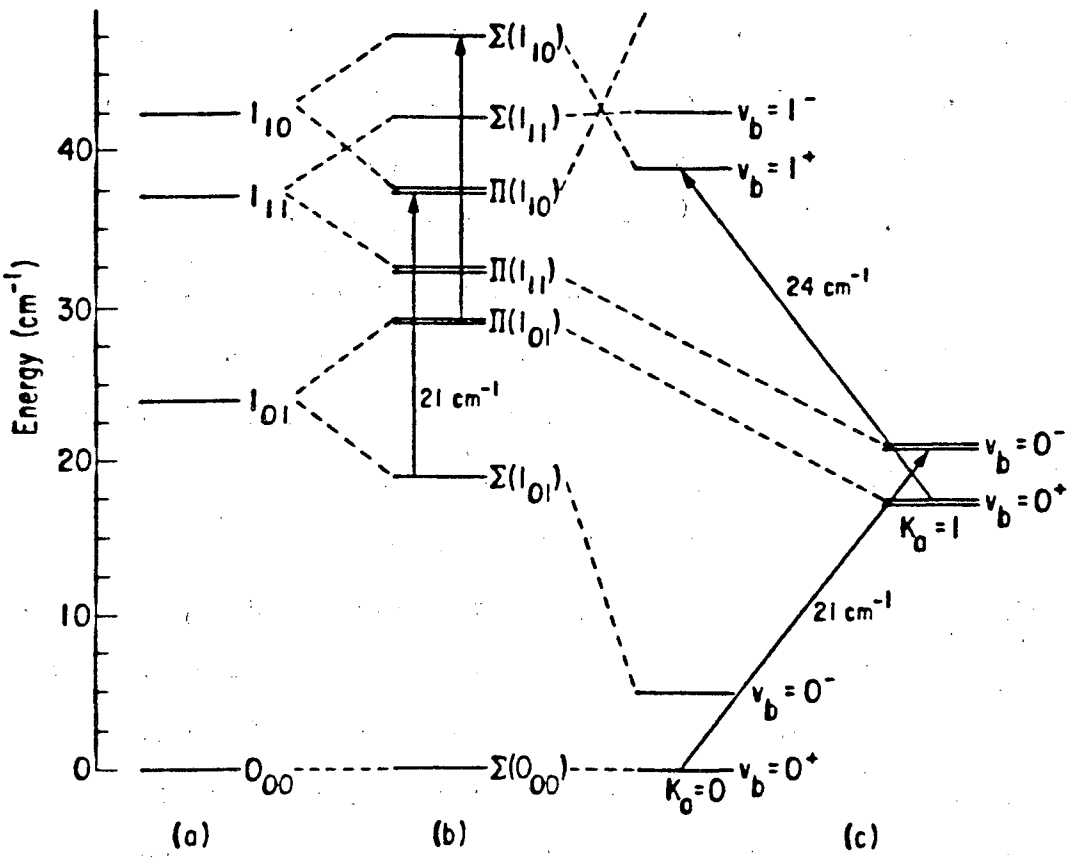

to an argon atom. An A rotational constant is not defined. Superimposed on each level are the rotational states of the complex.

The far right diagram is for the strongly anisotropic case. In this limit, the rotational states of the water monomer are strongly perturbed and mixed. The complex is fairly rigid and undergoes bending and tunneling motions about relatively well-defined minima. A pseudo-diatomic formalism is not appropriate in this case. All three rotational constants are defined. In our first paper, the two hindered rotation bands were discussed and analyzed in terms of this diagram.

The center energy level diagram is the intermediate case in which there is sufficient anisotropy to perturb the rotational states, splitting those states in which $j \neq 0$. However, the states are not significantly mixed, that is, the energy levels are still grouped about the water monomer rotational state energies. One way to envision this energy level diagram is to begin with the unperturbed water monomer rotational energy levels shown on the left of Figure 4.5. As the Ar atom approaches, the $j \neq 0$ states are split according to the absolute value of the projection of the rotational angular momentum along the complex internuclear axis. For example, the 1_{01} level is split into a Σ and a doubly degenerate Π component, corresponding to a projection of 0 and ± 1 along the complex axis, respectively. This scheme can again be thought of in terms of the pseudo-diatomic formalism. Our second paper

treated all four bands using this intermediate picture. Instead of bending or tunneling motions, the complex is thought to undergo slightly hindered rotations of the water. As in the other diagrams, superimposed on these levels are the rotational manifolds associated with the complex end-over-end rotation.

In Figure 4.7 is the expanded intermediate case diagram showing the four observed bands. As in the pure rotational energy levels for water monomer, there are two separate sets of levels corresponding to the ortho and para states of water. These states are not connected through dipole transitions or collisional relaxation. The state labels include the label of the water monomer level to which it is correlated, the projection of that water monomer angular momentum on the complex axis, and the number of van der Waals stretching quanta. For example, the lowest ortho state is labelled $\Sigma(1_{01}, v_s=0)$, where Σ refers to the projection. The degeneracy in the Π states is split due to Coriolis interactions with the Σ state.

In the cold supersonic expansion, there are only three levels that have sufficient population to have been observed thus far as the lower states in an absorption experiment. These are the lowest para state, the $\Sigma(0_{00}, v_s=0)$, and the two lowest ortho levels, the $\Sigma(1_{01}, v_s=0)$ and the $\Pi(1_{01}, v_s=0)$. The Π state is approximately 10 cm^{-1} above the Σ state and therefore still has some population, but transitions are 15-40

Figure 4.7 A detailed diagram of the intermediate case in Figure 4.6 showing the observed hindered rotation bands as well as the observed van der Waals stretching bands.

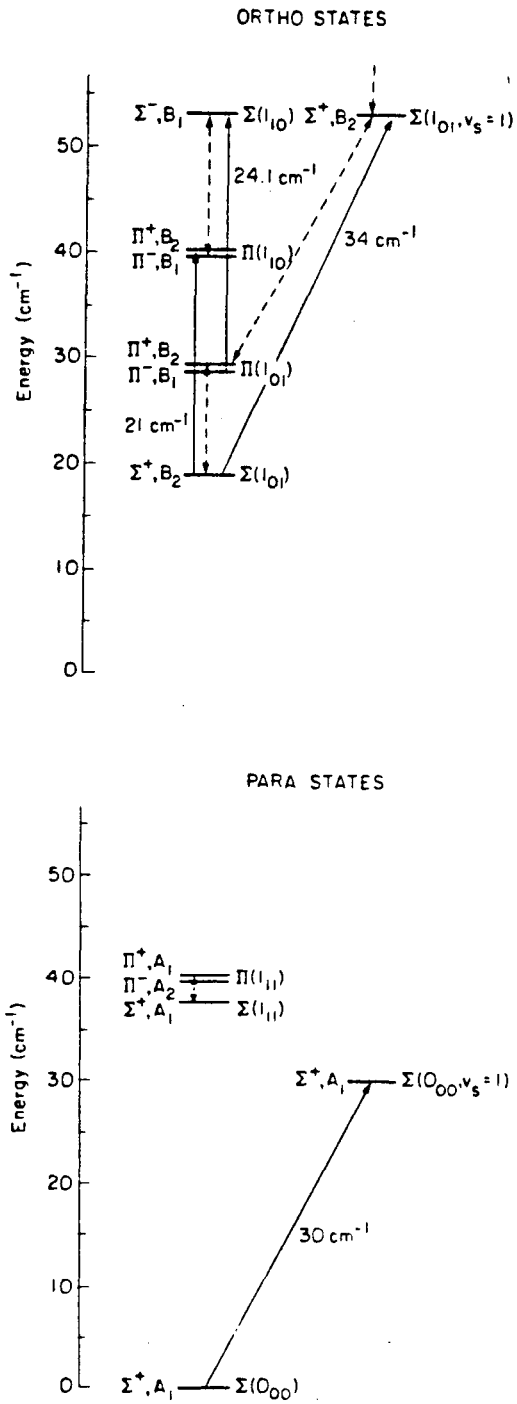

times less intense than the Σ state transitions. The most intense of the observed bands is the $\Sigma(1_{01})\rightarrow\Pi(1_{10})$ band at 21 cm^{-1}. This is due in part to the fact that the hindered rotation band is expected to have a larger transition moment than a stretching band and also because the ortho states have a three times larger statistical weight than the para states.

4.3.3 Comparing ArH_2O to $CH_4 \cdot H_2O$ Spectra

Before attempting to derive a $CH_4 \cdot H_2O$ energy level diagram, it is important to first use the knowledge gained in the ArH_2O work to simplify the problem. The bands and partial bands observed are listed in Table 4.1. Included in this table are the band origins, rotational line assignments, and the band type, based on the lines observed in the region of the origin. For example, in a $\Sigma\rightarrow\Pi$ band, R(0) will be observed, however P(1) will not observed. Of the seven bands in which a band origin could be identified, four have band origins near 545 GHz (18.2 cm^{-1}) and three have band origins near 572 GHz (19.1 cm^{-1}). Based on combination differences, none of them appear to share a common state. The unassigned lines are listed in Table 4.2.

These seven bands were fit using a standard Watson's S-reduced Hamiltonian, using Ron Cohen's ART program available in the group library. The results of these fits are given in Table 4.3. The rotational constants among these bands are quite similar. Also, the variation between the lower and upper

Table 4.1 A list of the rotationally assigned bands and partial bands in $CH_4 \cdot H_2O$.

Band B ν_0 = 537.087GHz $\Pi \rightarrow \Sigma$

481.3748	P(7)
489.9680	P(6)
498.5513	P(5)
507.1261	P(4)
515.6927	P(3)
524.2541	P(2)
532.8120	P(1)
540.2210	Q(11)
540.4580	Q(10)
540.6643	Q(9)
540.8412	Q(8)
540.9891	Q(7)
541.1089	Q(6)
541.2022	Q(5)
541.2703	Q(4)
541.3161	Q(3)
541.3443	Q(2)
541.3595	Q(1)
558.5354	R(1)

Band A ν_0 = 542.524 GHz $\Pi \rightarrow \Sigma$

494.7832	P(6)
503.4493	P(5)
512.1234	P(4)
520.8051	P(3)
529.4958	P(2)
538.1883	P(1)
543.8807	Q(10)
544.4020	Q(9)
544.8804	Q(8)
545.3120	Q(7)
545.6951	Q(6)
546.0291	Q(5)
546.3119	Q(4)
546.5409	Q(3)
546.7152	Q(2)
546.8315	Q(1)
564.2872	R(1)
572.9865	R(2)
581.6699	R(3)
590.3398	R(4)
598.9862	R(5)
607.6028	R(6)
616.1812	R(7)

624.7123	R(8)

Band H ν_0 = 545.383 GHz $\Sigma \rightarrow \Sigma$

471.4348	P(9)
487.4469	P(7)
495.5457	P(6)
503.7054	P(5)
511.9242	P(4)
520.2019	P(3)
528.5390	P(2)
536.9310	P(1)
553.8910	R(0)
562.4436	R(1)
571.0555	R(2)
579.7150	R(3)
588.4227	R(4)
597.1751	R(5)
605.9682	R(6)
614.7983	R(7)
623.6614	R(8)

Band J ν_0 = 546.996 $\Delta \rightarrow \Delta$

491.8128	P(6)
500.1945	P(5)
508.6228	P(4)
517.0928	P(3)
542.7448	Q(2)
542.8137	Q(3)
542.9134	Q(4)
543.0473	Q(5)
543.2181	Q(6)
543.4263	Q(7)
543.6720	Q(8)
568.4665	R(2)
577.1043	R(3)
585.7658	R(4)
594.4533	R(5)
603.1632	R(6)
611.8930	R(7)
620.6339	R(8)

Band F ν_0 = 564.590 GHz $\Pi \rightarrow \Delta$

486.9362	P(9)
495.4654	P(8)
504.0267	P(7)
512.6170	P(6)
521.2322	P(5)
538.5271	P(3)
582.0135	R(1)

590.7337	R(2)
599.4540	R(3)
608.1732	R(4)
616.8888	R(5)
625.5999	R(6)
642.9952	R(8)

Band C ν_0 = 567.871 $\Sigma \rightarrow \Pi$

500.4941	P(7)
509.7690	P(6)
518.9499	P(5)
528.0235	P(4)
536.9854	P(3)
545.8600	P(2)
562.7860	Q(5)
563.0604	Q(4)
563.2614	Q(3)
563.3831	Q(2)
563.4320	Q(1)

Band G ν_0 = 570.187 $\Pi \rightarrow \Delta$

473.0645	P(11)
489.4133	P(9)
497.6839	P(8)
506.0158	P(7)
514.4060	P(6)
522.8526	P(5)
531.3535	P(4)
539.9054	P(3)
548.5067	P(2)
564.4089	Q(7)
564.7732	Q(6)
565.0822	Q(5)
565.3379	Q(4)
565.5415	Q(3)
565.6942	Q(2)
565.7947	Q(1)
574.5749	R(0)
583.3438	R(1)
592.1502	R(2)
600.9887	R(3)
609.8562	R(4)
618.7508	R(5)
627.6686	R(6)

Band E

486.0577
494.6143
503.2215

511.8815
520.5974
529.3715
538.1898
547.0789
592.3448 (?)

Band D

581.9714
590.6405
599.3258
608.0346
616.7580
625.4863
642.6276

Band I

559.2823
559.3291
559.3291
560.2403
561.1893
561.9506
562.4491
562.6229

Band K

733.2151
734.7957
736.1860
737.3913
738.4148
739.2634
739.9392
740.4432
740.7781
741.2654

Band L

771.7993
781.3958
790.8346
800.1199
818.2232

Band M

562.7860

563.0604
563.2614
563.3831
563.4320

Table 4.2 A list of the unassigned lines in an $Ar/CH_4/H_2O$ expansion.

Frequency (GHz)	Intensity (Arbitrary units)
495.8733	9
497.6780	145
508.5823	75
514.9089	30
515.1920	92
529.3679	10
531.8089	45
539.4403	16
540.3400	16
541.7807	23
544.0472	185
553.7938	9
553.8383	9
553.8663	14
553.8819	16
553.8871	14
553.9395	24
562.9824	23
563.0011	9
563.4360	20
563.5163	17
563.5553	360
564.9103	32
566.0297	200
566.9694	155
575.4614	135
600.7254	40
610.9308	60
612.7472	28
614.9764	22
615.8529	30
617.3432	15
617.3985	15
618.8493	124
624.6266	70
634.3290	5
641.4709	63
642.9952	12
643.7914	400
665.5495	16
666.1552	34
723.6565	66
725.6335	240
726.8001	78
728.0483	1
728.2644	108

729.3705	150
729.4457	50
732.2941	100
735.2851	45
738.1887	60
740.3476	60
741.6983	180
742.1078	115
742.4881	230
742.5984	135
742.8343	245
743.1411	220
743.6195	80
744.9870	50
746.9964	45
747.3964	30
776.2230	60
778.2070	50
778.6047	100
779.3427	30
779.6100	40
780.4739	75
781.1696	230
781.3224	130
781.6428	65
781.7251	70
781.7536	85
781.8478	62
782.1113	60
782.3345	92
782.6227	50
782.8951	60
785.1692	50
787.2130	35
788.6659	45
792.2460	36
795.8116	40
795.9660	86
796.8617	66

Table 4.3 The results of the fits of the assigned bands in $CH_4 \cdot H_2O$ using a Watson's S-reduced Hamiltonian. In the Π states, the centrifugal distortion (D) for the two states are determined seperately, rather than fitting a Coriolis coupling constant. All units are in MHz.

Band	Band Origin	B"	B'	D"	D'	H"	H'	q_l	σ	Band Type
B	537087.05	4285.29	4285.05	-0.312 -0.440	-0.385	1.60 $\times 10^{-4}$		-4.826	1.79	Π→Σ
A	542525.18	4364.99	4351.02	0.1081 0.1571			-4.57 $\times 10^{-5}$	-15.058	0.46	Π→Σ
H	545383.25	4225.34	4252.63	0.0598	0.0615		-6.2 $\times 10^{-5}$		1.31	Σ→Σ
J	555552.7	4277.11	4287.39	0.1085	0.0400		-3.3 $\times 10^{-4}$		0.32	Δ→Δ
C	567870.6	4394.03	4403.77	-2.57	-3.21 -2.28			19.3	4.89	Σ→Π
G	570187.03	4345.53	4342.99	0.1114	0.121 0.113			-22.79	0.50	Π→Δ
F	577656.83	4350.02	4353.82	0.1091	0.1067				0.34	Π→Δ

state rotational constants for each band are very small, less than 1%. This indicates that it is unlikely that these bands are related to the van der Waals stretch. In ArH_2O, the rotational constants varied by at least 5% in the stretching bands and less than 1% in the hindered rotation bands.[2] From the distortion constants, as will be shown in a later section, it is possible to predict the van der Waals stretching frequency. These calculations indicate that the stretching frequency is near 60 cm^{-1}. Taking into account that the calculation assumes a harmonic potential, the actual stretching frequency will probably be at 40 or more cm^{-1}. Again, this reinforces the notion that these bands at 19 cm^{-1} are not likely to be related to the stretch, but rather to some hindered rotation band.

The search for this spectra was begun near the band origin of the strongest ArH_2O band, the $\Sigma(1_{01})\rightarrow\Pi(1_{10})$ at ~21 cm^{-1}. Many of the spectra are observed within 2 cm^{-1} of the ArH_2O band origin. Therefore, it is assumed that these $CH_4\cdot H_2O$ bands are related to this ArH_2O band. Another possibility is the $\Sigma(0_{00})\rightarrow\Pi(1_{11})$, however, in ArH_2O, that band is predicted to be near 32 cm^{-1}. The third possible hindered rotor band is the $\Pi(1_{01})\rightarrow\Sigma(1_{10})$. This is observed at 24.7 cm^{-1} in ArH_2O, which is not too far from the 19 cm^{-1} bands in $CH_4\cdot H_2O$. However, in ArH_2O, this band is weaker by a factor of 15-40 than the $\Sigma(1_{01})\rightarrow\Pi(1_{10})$ and it is unlikely that it would be observed without also seeing a second stronger set of bands associated

with the ArH_2O $\Sigma(1_{01})\rightarrow\Pi(1_{10})$ band. This band in ArH_2O also appears to be quite sensitive to beam conditions, i.e. beam temperature, due to the population being approximately 10 cm^{-1} above the lowest ortho state. The $CH_4 \cdot H_2O$ spectra do not appear to show any such temperature instability. Therefore, in order to simplify the proposed energy level diagrams, the assumption will be made that the $CH_4 \cdot H_2O$ bands are somehow related to the ArH_2O $\Sigma(1_{01})\rightarrow\Pi(1_{10})$ band. If this assumption later proves incorrect, modifications to the proposed energy level diagrams should be straightforward.

4.3.4 Hund's Coupling Cases for Diatomic Molecules

In $CH_4 \cdot H_2O$ it is required that the angular momenta of the two monomer subunits and the complex rotation be coupled together. Similarly, in the spectroscopy of diatomic molecules, it is often necessary to consider the coupling between the angular momentum associated with the electronic motion and the angular momentum associated with the rotational motion of the molecule. There are a number of ways in which these angular momenta can be coupled and Hund was the first to outline these different coupling schemes.[7,8] These are referred to as Hund's coupling cases. Analogies to two of Hund's cases will be used to first couple the methane and water angular momenta and the complex rotational angular momenta together and then two plausible energy level schemes for $CH_4 \cdot H_2O$ will be derived. A review of the these two Hund's cases will first

be given in terms of diatomic molecules. Later these coupling schemes will be adapted for the $CH_4 \cdot H_2O$ system.

In all of the Hund's coupling cases, the purpose is to couple several different angular momentum vectors together, namely the electronic orbital angular momentum, the electron spin, and the rotational angular momentum of the molecule. The electronic orbital angular momentum is labelled **L** and its projection along the internuclear axis is Λ. The electron spin is labelled **S** and its projection is Σ. The angular momentum generated by the rotation of the nuclei is referred to as **R** and because it is a diatomic molecule, it is always perpendicular to the internuclear axis and can have no projection. The sum of these vectors gives the total angular momentum labelled **J**.

The first case considered is Hund's case (a). In this case, the coupling between the electronic angular momentum, both **L** and **S**, and the nuclear motion, **R**, is very weak. However, the electronic angular momentum is strongly coupled to the internuclear axis. The vector diagram for this case is shown in Figure 4.8. This diagram shows that both **L** and **S** are individually coupled to the molecular axis, that is, they precess about the axis, both having well-defined projections. The sum of their projections, Λ and Σ, is labelled Ω. This Ω is then coupled to the rotational angular momentum, **R**, to give the total angular momentum **J**. **J** is constant and **R** and Ω precess about it. It is assumed in case (a) that this

Figure 4.8 The Hund's case (a) vector diagram taken from Herzberg.[5] **L** is the electronic orbital angular momentum, **S** is the spin angular momentum, **R** is the molecular rotational angular momentum, and **J** is the total angular momentum.

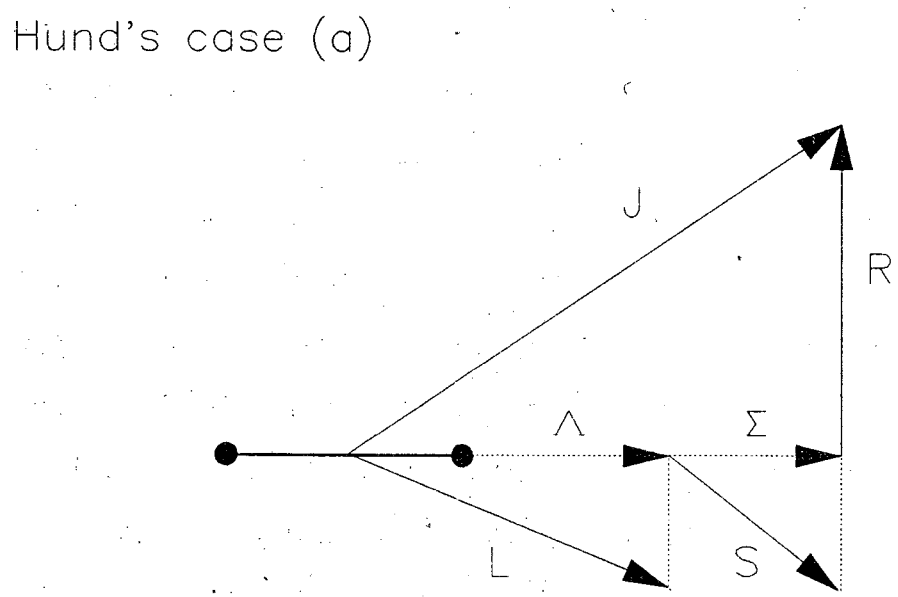

precession about **J** is much slower than the precession of **L** and **S** about the internuclear axis.

The second coupling case considered is case (b). The vector diagram for this case is shown in Figure 4.9. In this case, **L** is once again coupled to the internuclear axis, but **S** is only very weakly coupled to it. Therefore, Ω is not defined in this scheme. The projection of **L**, Λ is coupled to the molecular rotation, **R**, to give **N**. This vector **N** is then coupled to the spin, **S**, to yield the total angular momentum **J**.

In the $CH_4 \cdot H_2O$ system, the angular momenta which must be coupled are the water monomer rotational angular momentum, $\mathbf{j}_w$, the methane monomer rotational angular momentum, $\mathbf{j}_m$, and the rotational angular momentum of the complex, $\boldsymbol{\ell}$. These two Hund's cases can be adapted to the $CH_4 \cdot H_2O$ system by simply replacing the electronic angular momentum vectors, **L** and **S**, with the rotational angular momentum vectors associated with the monomer rotations, $\mathbf{j}_w$ and $\mathbf{j}_m$, respectively. The projection of these vectors on the complex axis are labelled $\mathbf{m}_{jw}$ and $\mathbf{m}_{jm}$, respectively. These labels replace the Λ and Σ labels. The end-over-end rotational angular momentum of the complex is labelled $\boldsymbol{\ell}$. This replaces the label **R** in the diatomic molecule case. The other vector labels will remain the same. Table 4.4 shows the various vector labels in the diatomic cases and the analogous labels used in the $CH_4 \cdot H_2O$ cases.

In terms of $CH_4 \cdot H_2O$, these two different cases present two very different qualitative pictures of the angular momentum

Figure 4.9 The Hund's case (b) vector diagram taken from Herzberg.[5]

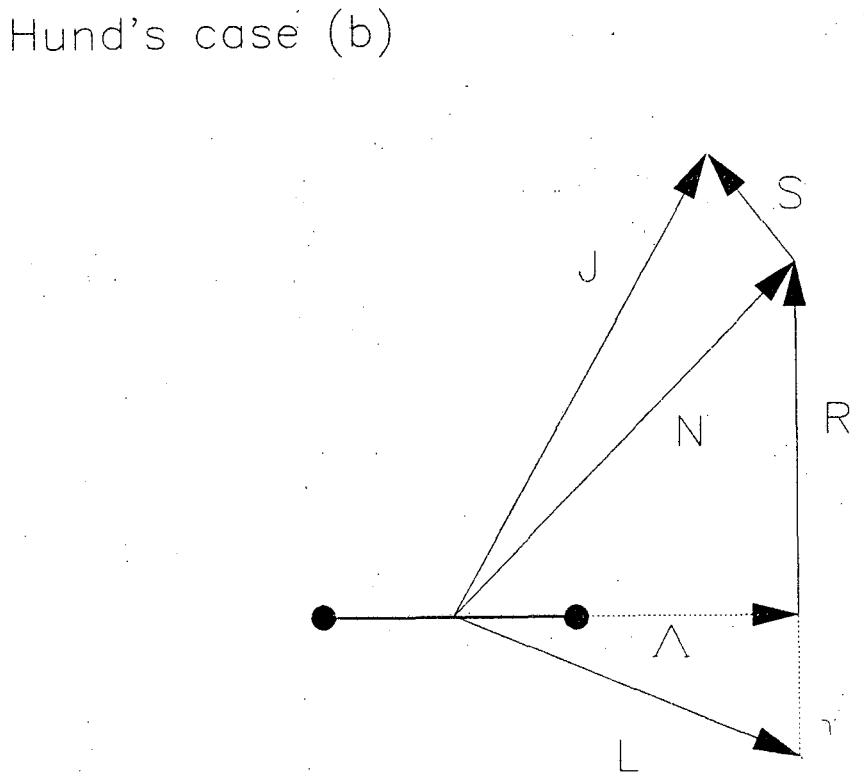

Table 4.4 Correlation of the vector labels in Hund's cases for a diatomic molecule to the $CH_4 \cdot H_2O$ complex.

Case (a)

Diatomic Molecule	$CH_4 \cdot H_2O$
L	j_w
Λ	m_{jw}
S	j_m
Σ	m_{jm}
Ω	Ω
R	ℓ
J	J

Case (b)

Diatomic Molecule	$CH_4 \cdot H_2O$
L	j_w
Λ	m_{jw}
R	ℓ
N	N
S	j_m
J	J

coupling. In case (a), j_w and j_m are both individually coupled to the complex axis with well-defined projections m_{jw} and m_{jm}. The sum of these projections (Ω) is coupled to the complex rotation, ℓ, to give J. This implies that j_w and j_m are both coupled to the axis by a similar degree of potential anisotropy. In case (b), j_w is strongly coupled to the axis, but j_m is only weakly coupled. In our preliminary work on developing an energy level diagram, we considered only case (a). It was on the advice of Jeremy Hutson[9] that we also considered case (b). He suggested that case (b) should be considered because there is no strong evidence or precedent to suggest that the water and methane angular momenta would behave similarly. It is quite conceivable that j_w would couple more strongly than j_m. Hutson did not suggest that case (a) should not be considered, he simply felt that both were plausible. It will later become clear that the two cases result in very different energy level diagrams, neither of which can at this time be definitively judged more appropriate. It is possible that through the calculation of the potential surface, the various coupling terms will indicate which scheme is most appropriate. The potential surface is currently being calculated by Ronald Cohen in our group.[10]

4.3.4.1 Hund's Case (a) Energy Level Diagram

In the framework of the Hund's case (a) model, it is

possible to construct an energy level diagram for $CH_4 \cdot H_2O$. There are a number of important assumptions being made based on our experience with ArH_2O that should be reiterated. The first assumption is that the spectroscopy is dominated by the rotational spectrum of the water monomer. As in the ArH_2O spectrum, the major features of the spectrum are going to be similar to that of the water monomer. The water is responsible for the majority of the transition moment and therefore has the greatest influence on the spectrum. The methane will essentially act as a perturbation. To extend this even further, and as has been mentioned throughout, the $CH_4 \cdot H_2O$ spectrum should be very similar to the ArH_2O spectrum. Therefore, it is not necessary to consider all of the possible energy levels for $CH_4 \cdot H_2O$. Only those levels directly related to the specific ArH_2O-type transition, namely $\Sigma(1_{01}) \rightarrow \Pi(1_{10})$, must be considered at this time. It is also important to emphasize that these spectra are observed in a cold supersonic jet expansion, and therefore only the lowest rotational states will have significant population and need be considered.

The approach to the angular momentum coupling in case (a) is simple. First the projections of $\mathbf{j}_w$ and $\mathbf{j}_m$, $\mathbf{m}_{jw}$ and $\mathbf{m}_{jm}$, are coupled to give $\mathbf{\Omega}$, then $\mathbf{R}$ is coupled to $\mathbf{\Omega}$ to give the total angular momentum $\mathbf{J}$. The assumption is that the transitions observed here are related to the $\Sigma(1_{01}) \rightarrow \Pi(1_{10})$ transition in ArH_2O. Therefore, in the lower state j_w is equal to one and because it is a Σ state, the projection on the axis, m_{jw}, is

zero. In the upper state, j_w is one and m_{jw} is ±1, because it is a Π state. The methane angular momentum, j_m, can be 0, 1, or 2 in both the lower and upper states. Each of these can then have a projection on the axis, m_{jm}, equal to $+j_m$, j_m-1,...,$-j_m$. In Table 4.5 is a compilation of the sums of the various projection vectors, $\mathbf{m}_{jw}$ and $\mathbf{m}_{jm}$, to give $\mathbf{\Omega}$. This sum projection vector, $\mathbf{\Omega}$, is then coupled to the end-over-end rotation of the complex, $\boldsymbol{\ell}$. $\boldsymbol{\ell}$ can have integer values from zero and up. It is possible to now draw the energy level diagram, showing the possible values of Ω and assume that the complex rotation manifold is superimposed on each level. In Figure 4.10 is the case (a) energy level diagram assuming that the splittings are similar to those observed in ArH_2O. The methane rotational manifolds are drawn parallel to each other, but are actually shifted relative to one another. The j_m=1 manifold is 10.5 cm^{-1} up from j_m=0 and the j_m=2 manifold is 31.5 cm^{-1} above j_m=0. Also included in this diagram is the effect of the CH_4 K-degeneracy, which increases the total number of possible states by $(2j_m+1)$. For j_m=0, the number of states is multiplied by 1, but for j_m=1, the factor is 3, and for j_m=2 the factor is five. However, for j_m=2, three of these five sets of states will have F symmetry and can relax down to the j_m=1 levels. The remaining j_m=2 states are of E symmetry and will be populated; therefore, the number of j_m=2 states is only multiplied by 2. This picture only gives a state count, indicating the number of possible transitions. The ordering of

Table 4.5 The case (a) coupling in $CH_4 \cdot H_2O$ of $\mathbf{m}_{jw}$ and $\mathbf{m}_{jm}$ to give Ω.

Ω in the Lower State

	$j_m=0$ $m_{jm}=0$	$j_m=1$ $m_{jm}=0,\pm1$	$j_m=2$ $m_{jm}=0,\pm1,\pm2$
$j_w=1$ $m_{jw}=0$	$\Omega=0(\Sigma)$	$\Omega=0(\Sigma)$	$\Omega=0(\Sigma)$
		$=\pm1(\Pi)$	$=\pm1(\Pi)$
			$=\pm2(\Delta)$

Ω in the Upper State

	$j_m=0$ $m_{jm}=0$	$j_m=1$ $m_{jm}=0,\pm1$	$j_m=2$ $m_{jm}=0,\pm1,\pm2$
$j_w=1$ $m_{jw}=\pm1$	$\Omega=\pm1(\Pi)$	$\Omega=\pm2(\Delta)$	$\Omega=\pm3(\Phi)$
		$=\pm1(\Pi)$	$=\pm2(\Delta)$
		$=0(\Sigma)$	$=\pm1(\Pi)$
		$=0(\Sigma)$	$=0(\Sigma)$
			$=0(\Sigma)$

Figure 4.10 The case (a) energy level diagram for $CH_4 \cdot H_2O$ for the $\Sigma(1_{01}) \rightarrow \Pi(1_{10})$ type transitions. Superimposed on each state is the complex rotational manifold. The state labels ($\Sigma, \Pi, \Delta, \Phi$) refer to the value of Ω (0,1,2,3, respectively).

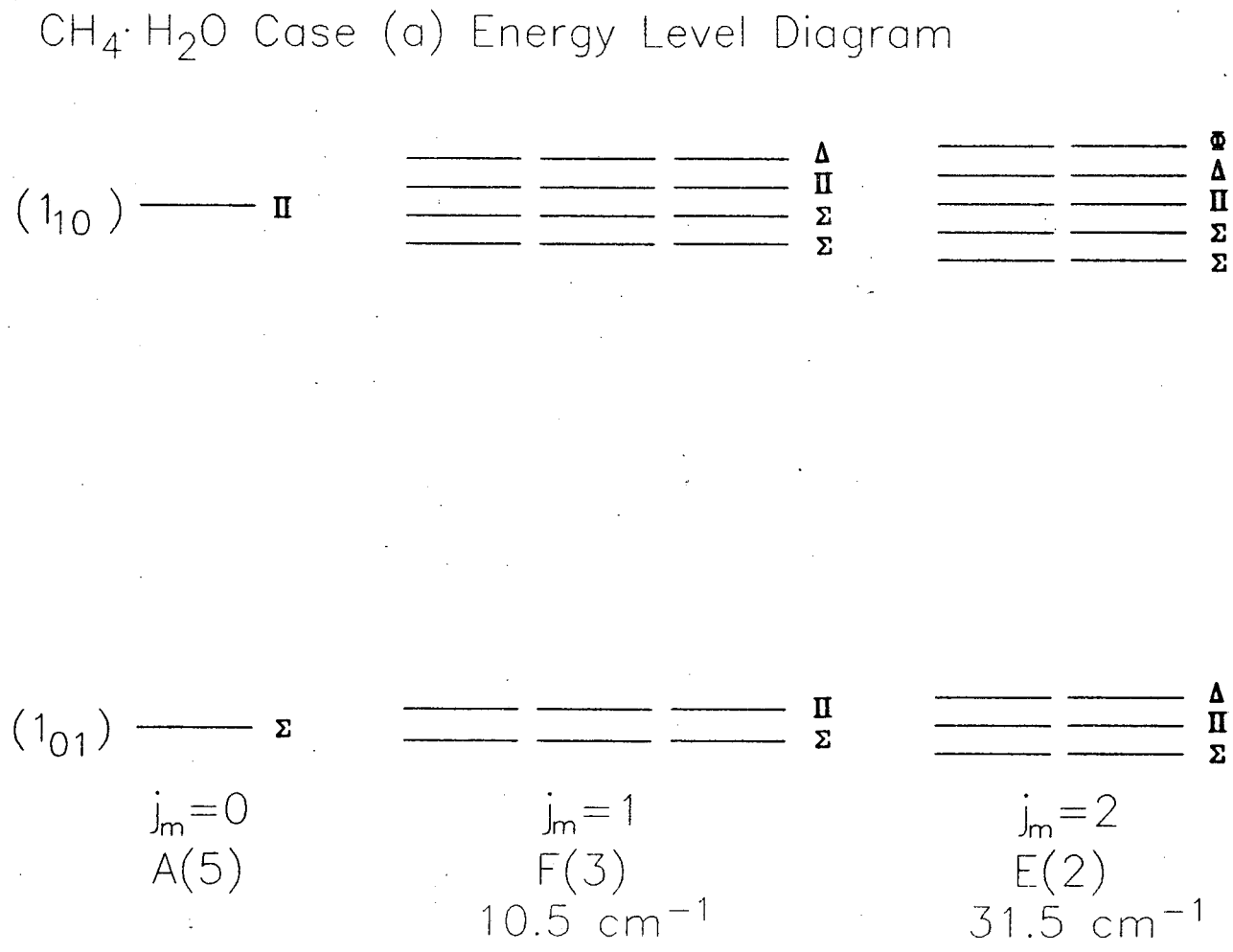

the states as well as the magnitude of the state spacings are unknown at this point. This diagram does explain why there are so many bands observed with nearly the same band origin and why none appear to share a common state. Unfortunately, this picture makes the task of assigning these observed bands seem quite formidable, even knowing the symmetries of the various transitions. For example, the number of different $\Pi \rightarrow \Sigma$ transitions possible is ten.

4.3.4.2 Hund's Case (b) Energy Level Diagram

In the construction of the case (b) energy level diagram, first the projection of the water rotational angular momentum, $\mathbf{m}_{jw}$, is coupled to the end-over-end rotation, $\boldsymbol{\ell}$, to give **N**. This vector **N** is then coupled to the methane rotation vector, $\mathbf{j}_m$, to give the total angular momentum, **J**. Once again, only the transitions related to the ArH_2O $\Sigma(1_{01}) \rightarrow \Pi(1_{10})$ will be considered. Therefore, m_{jw} is going to equal zero in the lower state because it is a Σ state, and ± 1 in the upper state because it is a Π state. ℓ can have any integer value, from 0 on up, therefore, in the lower state, $\ell=0,1,2,...$, and in the upper state, $N=1,2,3,...$

The second step is to couple **N** to $\mathbf{j}_m$, which is going to equal 0,1, or 2 in both the upper and lower states. The resultant vector **J** can equal $(N+j_m),(N+j_m-1),(N+j_m-2),...(|N-j_m|)$. In Figure 4.11 is the energy level diagram derived from the case (b) model. The lower to upper state splitting is

Figure 4.11 The case (b) energy level diagram for $CH_4 \cdot H_2O$ for the $\Sigma 1_{01}) \rightarrow \Pi(1_{10})$ type transitions. In this case, the complex rotational is included in the diagram, it is <u>not</u> superimposed on each state as in the case (a) picture.

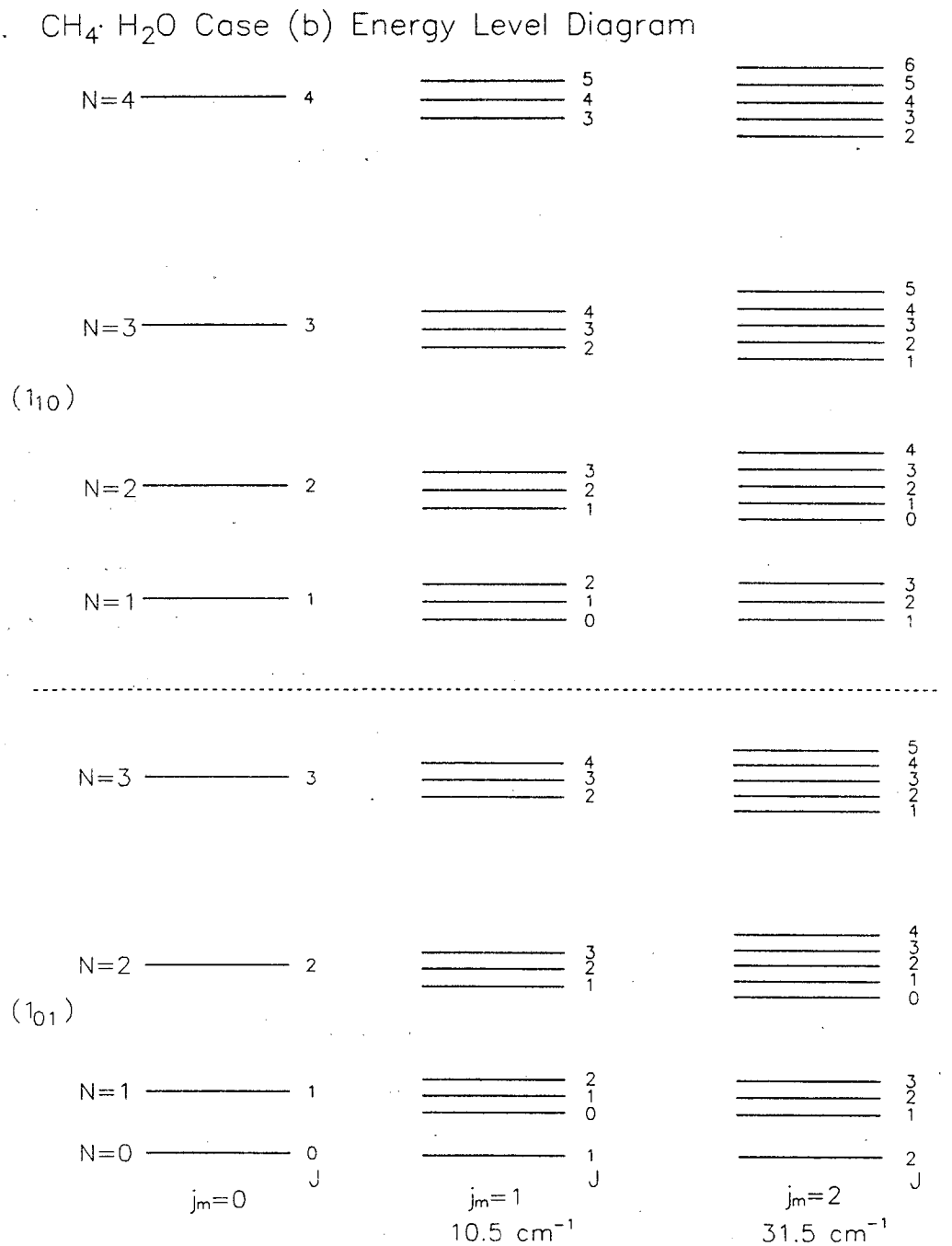

again assumed to be comparable to the ArH_2O $\Sigma(1_{01})\rightarrow\Pi(1_{10})$ transition frequency. The methane j_m manifolds are shifted as in the case (a) diagram. The J state ordering is not determined. It is important to point out that one of the primary differences between this diagram and the case (a) diagram is that in case (a) the end-over-end rotational manifold is not shown for all of the states. It is assumed to be superimposed on top of each level. In the case (b) diagram, the end-over-end rotation, up to $\ell=3$, is included.

4.3.5 Comparison of the Case (a) and Case (b) Predicted Spectra

The very different proposed energy level diagrams imply that the case (a) and case (b) predicted spectra for $CH_4\cdot H_2O$ should be quite different. The two coupling schemes are going to result in different band structure and band spacings. The important question is this: is it possible to take advantage of these differences and point to one of the schemes as the more appropriate representation of the $CH_4\cdot H_2O$ coupling?

4.3.5.1 The Case (a) Spectrum

Before predicting these spectra, the selection rules must be established. In both Hund's case (a) and case (b), the selection rules are $\Delta\Lambda=0,\pm1$ and $\Delta J=0,\pm1$.[8] In case (a), it is also true that $\Delta\Sigma=0$[8], therefore the overall selection rules are $\Delta\Omega=0,\pm1$ and $\Delta J=0,\pm1$. It will also be assumed that $\Delta j_m=0$,

that is, transitions are vertical among the methane stacks. Due to the symmetry species of the j_m states, there is only one non-vertical transition which could possibly occur, namely the $j_m=1 \rightarrow j_m=2$ among the F states. However, these possible transitions will be ignored on the basis of the simple argument that because the $j_m=2$ manifold is 20 cm^{-1} higher the $j_m=1$, these transitions should occur at a much higher frequency. Also, the transition moment lies primarily on the water. The intensity of a transition in which the methane rotation is changed should be relatively small. Similarly, this argument can be extended so that transitions which change the value of the methane projection are also ignored. This assumption is probably rather difficult to prove. However, we are seeking the simplest picture including perhaps only the strongest bands which may make the assignment possible.

In Table 4.6 is a list of the bands that are possible assuming these selection rules. These bands will all be near 21 cm^{-1}. The splitting among the different Ω states is unknown, but is presumed to be small compared to the ArH_2O (1_{01}) Σ-Π splitting (~10 cm^{-1}). The splitting among the Ω states translates to the extent of anisotropy introduced in the complex by the methane. Due to the tetrahedral symmetry of methane, this anisotropy should be quite small compared to the anisotropy introduced by the water. Each of these bands should have a normal P,Q, and R branch structure, except for the $\Omega=0 \rightarrow 0$ bands in which there will be no Q branch. In $\Omega \neq 0$ states,

Table 4.6 The bands possible in the case (a) $CH_4 \cdot H_2O$ spectrum assuming the selection rules $\Delta\Omega=0,\pm1$, $\Delta J=0,\pm1$, $\Delta j_m=0$, and $\Delta m_{jm}=0$.

$j_m=0$	$\Sigma\rightarrow\Pi$	
$j_m=1$ (×3)	$\Sigma\rightarrow\Sigma$	$\Pi\rightarrow\Sigma$
	$\Sigma\rightarrow\Sigma$	$\Pi\rightarrow\Pi$
	$\Sigma\rightarrow\Pi$	$\Pi\rightarrow\Delta$
	$\Pi\rightarrow\Sigma$	
$j_m=2$ (×2)	$\Sigma\rightarrow\Sigma$	$\Pi\rightarrow\Pi$
	$\Sigma\rightarrow\Sigma$	$\Pi\rightarrow\Delta$
	$\Sigma\rightarrow\Pi$	$\Delta\rightarrow\Pi$
	$\Pi\rightarrow\Sigma$	$\Delta\rightarrow\Delta$
	$\Pi\rightarrow\Sigma$	$\Delta\rightarrow\Phi$

there should be a doubling analogous to l-type doubling, however, for $\Omega>1$, this doubling is likely to be very small. Also, for these bands J must be greater than or equal to Ω.

4.3.5.2 The Case (b) Spectrum

As for the case (a) situation, it is important to first outline the assumed selection rules in order to predict the spectrum. In case (b), the selection rules are $\Delta J=0,\pm1$, $\Delta N=0,\pm1$. However, $\Delta N=0$ is not allowed for Σ states, that is $\Sigma\rightarrow\Sigma$ transitions are forbidden.[8] Also, by the same argument as in case (a), $\Delta j_m=0$. Unlike the case (a) spectrum, it does not appear that the case (b) spectrum will yield a large number of individual bands. Instead, a single band-like structure will be observed for each j_m state, in which each "rotational" line will be comprised of a multiplet of lines. It is assumed that the spacing between the N states is essentially B(N(N+1)) and therefore the spacing between transitions is 2B. The spacing between the J states within a given N level is assumed to be small. Figure 4.12 demonstrates how the total spectrum is predicted. The $j_m=0$ manifold gives a simple $\Sigma\rightarrow\Pi$ band structure with no multiplet lines. In the $j_m=1$ manifold again the overall structure is a $\Sigma\rightarrow\Pi$ type band, however, in the R branch, for example, the $N=0\rightarrow1$ transition will be a triplet and all higher transitions will be sextets. The $j_m=2$ transition will have multiplets consisting of up to twelve lines. The intensity of these multiplets, as well as the

Figure 4.12 Predicting the R branch of the case (b) spectrum.

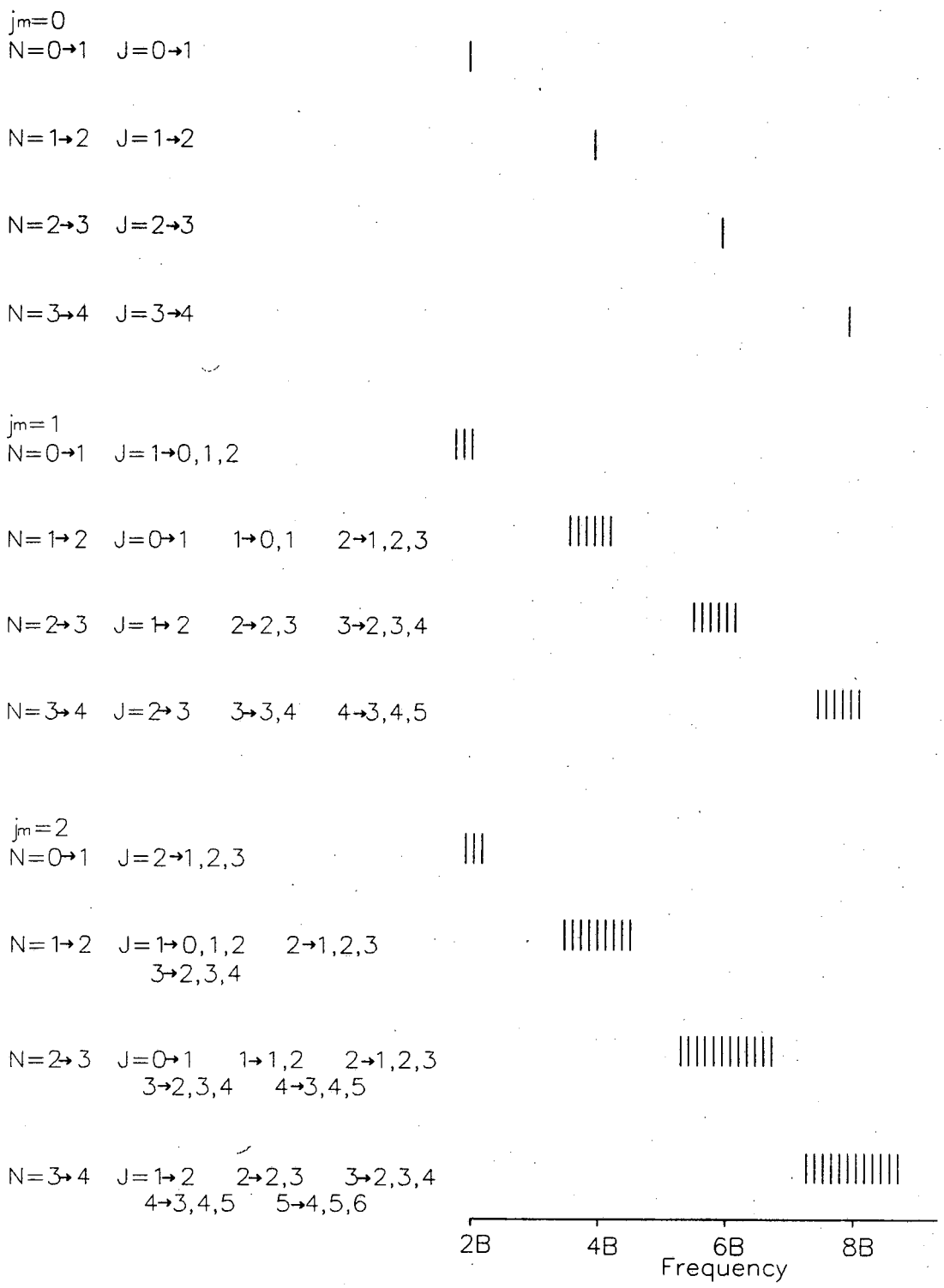

ordering of these lines is unknown. Figure 4.13 gives the qualitative picture of the case (a) and case (b) spectra. In these predicted spectra, the K degeneracy of the CH_4 is ignored. Including it would simply multiply the number of lines in each spectrum by the same factor. Also, in both spectra, the various bands are shown with identical band origins. Our experimental results demonstrate that the bands are slightly shifted, but this provides a zeroth-order picture of the band structure. What is observed in these two cases is that although the energy level diagrams and the individual band structures are very different, in the overall spectrum, combining all of the individual bands, the two cases are nearly indistinguishable. The notable exception is that in the case (b) spectrum there will be no P(1) transitions. These lines would correspond to an $N=1\rightarrow 0$ transition which is not possible in any of the $\mathbf{j}_m$ manifolds. In the observed bands, one is a $\Sigma\rightarrow\Sigma$ type band which does have a P(1) line. In case (b), $\Sigma\rightarrow\Sigma$ bands are not allowed. This implies that the case (a) scheme is more likely to be correct.

It should be mentioned that case (a) and case (b) refer to ideal cases. In reality, many systems are intermediate cases. For these systems, selection rules tend to break down. In particular, case (a) is generally a good approximation for those intermediate case systems in which the overall rotation, J, is small. As J increases, $\mathbf{S}$, or in the case of $CH_4 \cdot H_2O$, $\mathbf{j}_m$, gradually decouples from the complex axis. At high J, case (b)

Figure 4.13 The predicted case (a) and case (b) spectra for $CH_4 \cdot H_2O$ ignoring the K degeneracy of the CH_4. The overall spectra are very similar in the two cases except that in case (b), there will be no P(1) transitions.

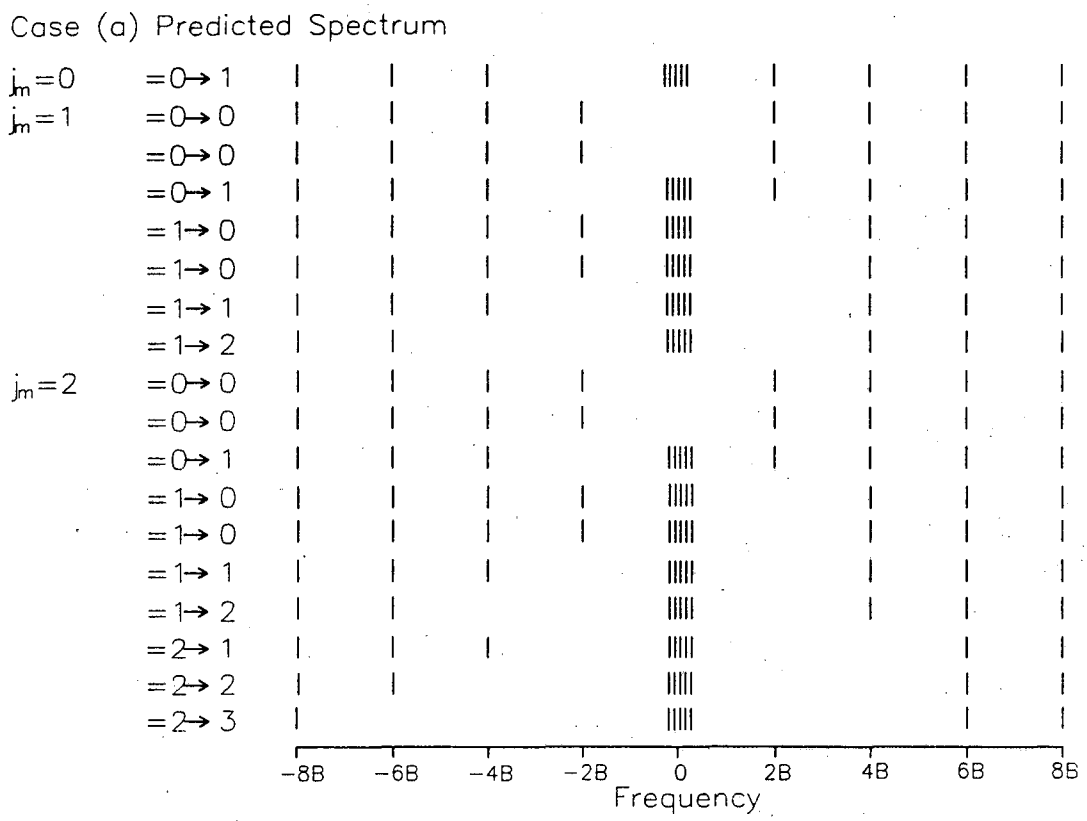

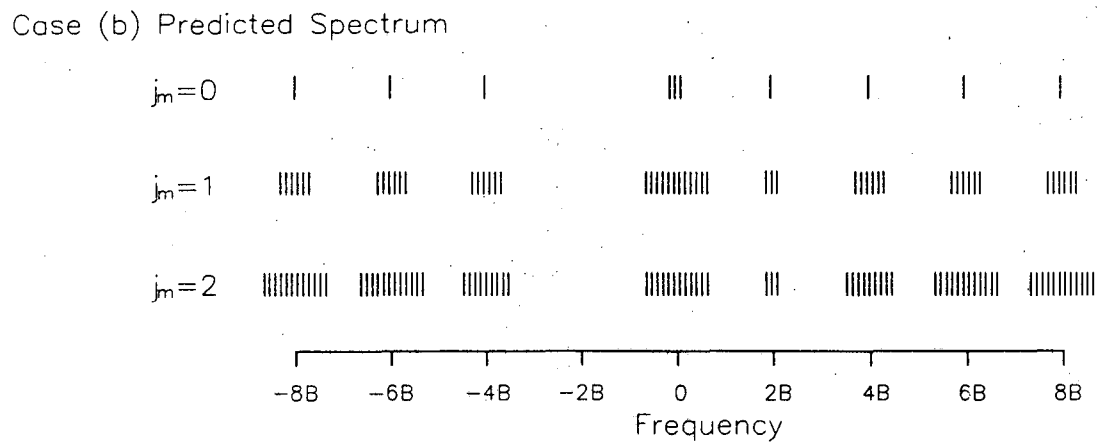

is the better approximation. The problem is, what qualifies as low or high J? In the cold jet, the lowest J levels tend to be the only ones with significant population and therefore, case (a) may be more appropriate. However, at what point the j_m uncoupling becomes significant and consequently, the selection rules break down, is not clear.

4.4 The Binding Energy of $CH_4 \cdot H_2O$

In a potential energy surface determination, a great deal of information about the complex can be obtained. One of the most fundamental characteristics determined for weakly bound complexes is the binding energy. Cohen and Saykally, in the ArH_2O potential surface calculation determined the binding energy for the $\Sigma(0_{00})$ state of 136 cm^{-1} and for the $\Sigma(1_{01})$ state of 175 cm^{-1}.[3] The potential surface for $CH_4 \cdot H_2O$ has yet to be determined, however it is possible to speculate on the binding energy relative to that for ArH_2O.

A very simple means to obtain a qualitative answer about relative binding energies is to compare the polarizability of argon to that for methane. Of the three forces contributing to van der Waals bond formation, electrostatic, induction, and dispersion, the last two are directly dependent on the polarizability of the interacting species. The electrostatic force is nonexistent in ArH_2O because Ar has no permanent moment. Methane does have an octopole moment, but this term is expected to be quite small compared to the dispersion term.

Therefore, the polarizability should provide a reasonable indication of the relative bond strengths. The polarizabilities for Ar and CH_4 are 1.62×10^{-24} cm^3 and 2.60×10^{-24} cm^3, respectively.[11] The polarizability is nearly a factor of two larger for methane and therefore, it may be expected that the $CH_4\cdot H_2O$ binding energy will be larger. Let us assume that the dispersion term represents the largest contribution to the attractive potential. To first order, the dispersion term is proportional to the square of the polarizability.[12] Therefore, assuming comparable bond distances for ArH_2O and $CH_4\cdot H_2O$, a factor of two difference in polarizabilities results in a predicted bond energy for $CH_4\cdot H_2O$ approximately four times larger than ArH_2O.

A somewhat more quantitative means of determining the binding energy involves the centrifugal distortion constants determined in a number of the band fits. This calculation, however, relies on the poor assumption that the potential is harmonic. Assuming that the potential is a Lennard-Jones 6-12 potential, the dissociation energy, D_e, can be calculated using equation 4.1:

$$D_e(ergs) = \frac{4\pi^2}{18}\mu(g)R_e^2(cm)\left(\frac{B_e^3(Hz)}{D_J(Hz)}\right) , \qquad (4.1)$$

where μ is the reduced mass, which is 8.5 g/mole divided by Avogadro's number to give 1.4×10^{-23} g. R_e is the equilibrium bond length, B_e is the equilibrium rotational constant, D_J is the centrifugal distortion constant, and 1 erg equals 5.03×10^{15} cm^{-1}. The equilibrium bond distance and rotational constants are unknown. We can assume that the bond length is approximately the van der Waals radius for methane which is 4.0 Å determined from the $(CH_4)_2$ potential.[13] The rotational constants and distortion constants are simply those determined in the various band fits. There is significant variation among these constants and therefore, there is significant variation in the dissociation energy calculated for the various states. For the lower state of Band H, a dissociation energy of 312 cm^{-1} was obtained. For the lower state of Band G, a value of 182 cm^{-1} was obtained. A similar calculation for the $\Sigma(1_{01})$ state of ArH_2O predicts a dissociation energy of 109 cm^{-1}. These values, although varying dramatically among the $CH_4\cdot H_2O$ states, indicate again that $CH_4\cdot H_2O$ is probably more strongly bound than ArH_2O. A similar calculation can also be used to predict the van der Waals stretching frequency based on the distortion constant. The equation, given in 4.2, again assumes a harmonic potential.

$$\nu_s=\sqrt{\frac{4B^3}{D_J}} \qquad (4.2)$$

For the lower state of Band G, the stretching frequency is calculated to be 57 cm^{-1} and for Band H it is 74 cm^{-1}. This could be helpful in the search for these bands.

An interesting observation was made in scanning for $CH_4 \cdot H_2O$ which may also indicate that $CH_4 \cdot H_2O$ is more strongly bound than ArH_2O. In Figure 4.14, two pairs of scans are shown. In the upper pair, the upper trace shows the strong R(11) line of the ArH_2O $\Sigma(1_{01}) \rightarrow \Pi(1_{10})$ band. The lower trace shows that signal greatly reduced when CH_4 is added to the expansion mixture. The lower pair of scans show a similar result. The P(4) line of the ArH_2O is completely removed when CH_4 is added. However, these scans also show that the R(3) A_2^- line of the $(H_2O)_2$ K=1 lower → K=2 lower band is unaffected by the CH_4 addition. This may indicate that in the competition in the expansion for the available water, methane is more effective than argon, as indicated by the strong ArH_2O depletion. This would imply, once again, that $CH_4 \cdot H_2O$ is more strongly bound. The lack of $(H_2O)_2$ depletion upon CH_4 addition implies that the methane cannot compete with the water. This is quite reasonable because the binding energy of $(H_2O)_2$ is expected to be at least ten times stronger than the $CH_4 \cdot H_2O$ binding energy. Once the $(H_2O)_2$ is formed, CH_4 could not possibly strip off a water molecule and deplete the signal.

It is, however, possible that this ArH_2O depletion is not due to a weaker ArH_2O bond, but may be the result of CH_4 interfering with some step in the ArH_2O formation mechanism.

Figure 4.14 Two sets of scans showing the depletion in the ArH_2O signal upon addition of CH_4 to the expansion mixture. The upper two scans are of the R(11) line of the $\Sigma 1_{01})\rightarrow\Pi(1_{10})$ band of ArH_2O, the top trace without CH_4, the lower trace with CH_4 in the mixture. The lower two scans show the P(4) line of $CH_4 \cdot H_2O$ observed on the third sideband and the R(3) A_2^- line of the $(H_2O)_2$ K=1 lower → K=2 lower band. The upper trace is without CH_4, the lower trace is with CH_4 in the mixture. Note that the $(H_2O)_2$ signal is unaffected by the CH_4.

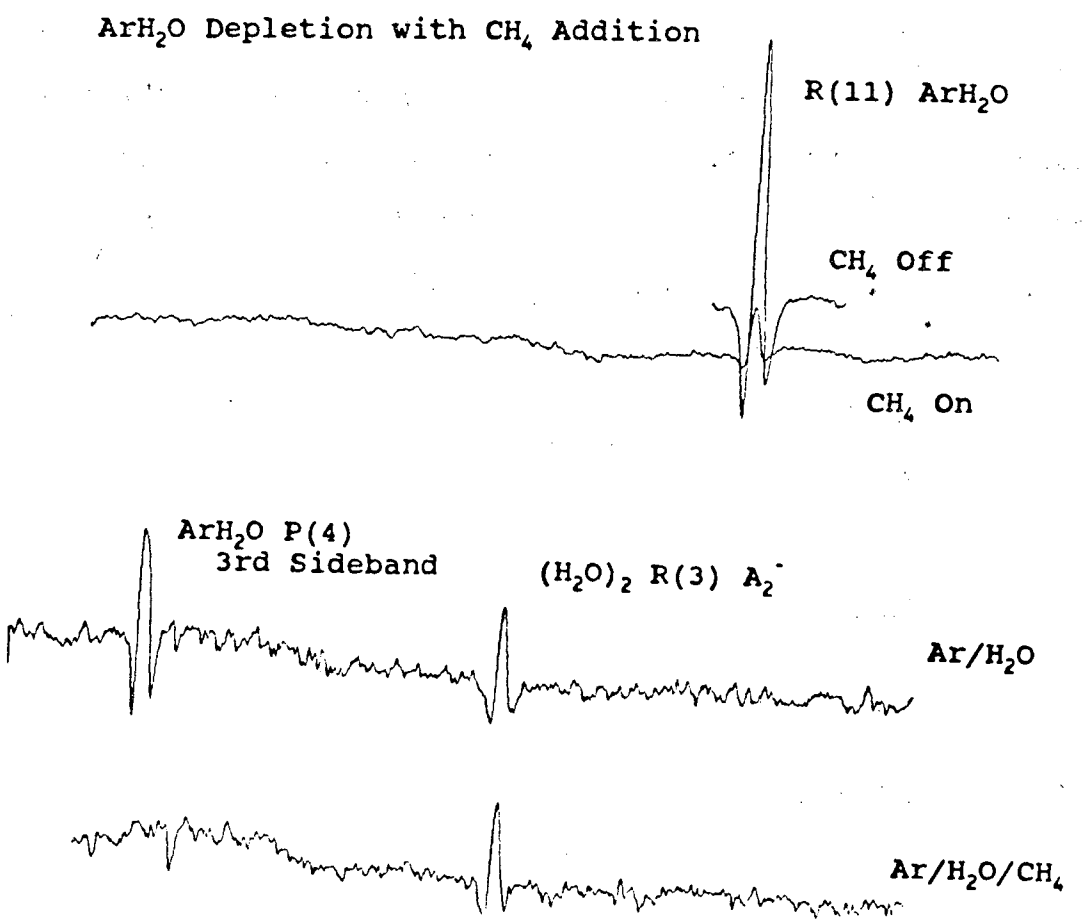

For this argument to be valid, it is important that the mechanism of the formation of these various clusters be considered. In the formation of clusters in a jet, it is important to remember that any dimer formation is the result of a three-body collision. The third body is required to remove excess energy and keep the dimer from immediately dissociating. It is believed that the initial step in any cluster formation is first dimer formation of the carrier gas, in this case, $(Ar)_2$. The argon makes up greater than 95% of the expansion mixture. The CH_4 and H_2O are essentially "impurities" in the expansion. Therefore, most of the three-body collisions which occur are going to involve three argon atoms. It is then the $(Ar)_2$ that is going to lead to the various clusters formed in the beam. The possible mechanisms for ArH_2O and $CH_4 \cdot H_2O$ formation are given below.

<u>ArH_2O Formation Mechanism</u>

$$Ar + Ar + Ar \rightleftharpoons Ar_2 + Ar$$

$$Ar_2 + H_2O \rightleftharpoons Ar + ArH_2O$$

<u>$CH_4 \cdot H_2O$ Formation Mechanisms</u>

Mechanism I

$$Ar + Ar + Ar \rightleftharpoons Ar_2 + Ar$$

$$Ar_2 + H_2O \rightleftharpoons Ar + ArH_2O$$

$$ArH_2O + CH_4 \rightleftharpoons CH_4 \cdot H_2O + Ar$$

$$\rightleftharpoons ArCH_4 + H_2O$$

$$\rightleftharpoons H_2O + CH_4 + Ar$$

or

Mechanism II

$$Ar + Ar + Ar \rightleftharpoons Ar_2 + Ar$$

$$Ar_2 + CH_4 \rightleftharpoons Ar + ArCH_4$$

$$ArCH_4 + H_2O \rightleftharpoons CH_4 \cdot H_2O + Ar$$

$$\rightleftharpoons ArH_2O + CH_4$$

$$\rightleftharpoons Ar + H_2O + CH_4$$

It could be argued that the ArH_2O depletion is due to the loss of Ar_2, a necessary precursor in the ArH_2O mechanism. This loss could be due to the formation of $ArCH_4$, as in the second $CH_4 \cdot H_2O$ mechanism. However, in both of the $CH_4 \cdot H_2O$ mechanisms, CH_4, H_2O, and Ar all come together in the last step in a three-body collision complex. It is at this instant that the most strongly bound complex is likely to form. Looking specifically at the second mechanism, even though the $ArCH_4$ complexation has removed the Ar_2, if the ArH_2O bond is stronger than the $CH_4 \cdot H_2O$ bond, it should form preferentially. The loss of the Ar_2 to $ArCH_4$ should not prevent ArH_2O formation. The fact that the ArH_2O signal is depleted indicates, that based on these mechanisms, the $CH_4 \cdot H_2O$ bond is stronger.

4.5 Discussion

Seven bands were observed in $CH_4 \cdot H_2O$ which appear to share no common states, yet have very similar band origins and rotational constants. There are two energy level diagrams proposed here. Assuming that the proposed selection rules and

splittings are correct, it appears that the case (a) energy level diagram better fits the observed spectra. The predicted spectra for the two cases are essentially superimposable, except that in case (b) there are no P(1) lines. The fact that one of the seven assigned bands has a $\Sigma \rightarrow \Sigma$ band structure in which P(1) is observed indicates that case (a) is the more appropriate scheme. Therefore, those labels will be used to discuss the spectroscopy. A potential calculation which includes the magnitude of various coupling terms could provide additional evidence to support case (a) over the case (b) coupling scheme.

Although many simplifying assumptions have been made in the case (a) scheme, there are still 42 bands possible near 21 cm^{-1}. It is not possible to uniquely assign the seven observed bands. There are however, some conclusions which can be made. One is that any transition in which the lower state Ω is equal to 2, a Δ state, must be in the $j_m=2$ manifold. Also, if any band had been observed with Ω equal to 3, a Φ state, that band would also have to be in $j_m=2$. Any band in which $\Omega'' \rightarrow \Omega' \neq 0 \rightarrow 1$ ($\Sigma \rightarrow \Pi$), cannot be associated with $j_m=0$. Therefore, it can be concluded that Band J must have $j_m=2$ and Band C is the only band that could possibly be in $j_m=0$. Of the seven bands, four bands have band origins near 545 GHz (18.2 cm^{-1}) and three are near 572 GHz (19.1 cm^{-1}). It is plausible that these two sets of bands are associated with different j_m stacks. Band J ($\Delta \rightarrow \Delta$) is in the set of four and must be $j_m=2$. Therefore, we can

speculate that all four bands near 545 GHz are in j_m=2. The other three bands could then be associated with j_m=1. The j_m=0 stack will only have a single $\Sigma \rightarrow \Pi$ band. This speculation still does not uniquely assign the various bands. Also, there appears to be no experimental means to rigorously prove these assignments. One possible method for identifying which j_m level a transition is associated with is to resolve the hydrogen hyperfine splittings for the methane. From the hyperfine structure, one could determine the value of j_m. However, the resolution required for such a measurement is likely to be beyond even the best microwave techniques. A second method is to use an experiment which could determine the Stark splittings. From the Stark structure it would be possible to identify the j_m level associated with the transition.

There certainly remains a great deal of work to be done on this system. It is possible that the measurement of more bands will provide the information necessary to make an assignment. However, this probably cannot be accomplished without simultaneous potential calculations. These calculations could provide the state orderings and the magnitude of various splittings. However, to obtain a "good" potential surface it will be necessary to measure several of the bands associated with different hindered rotations of the water. The para state transitions related to the ArH_2O $\Sigma(0_{00}) \rightarrow \Pi(1_{11})$ should occur near 32 cm^{-1}. Also, the other ortho

state band, $\Pi(1_{01}) \rightarrow \Sigma(1_{10})$, should have a band origin at approximately 24 cm^{-1}. It is expected that these bands will be weaker due to the spin statistical weights and relaxation in the beam, respectively. The bands involving the van der Waals stretch could also provide important information for the potential determination. Based on the centrifugal distortion constants, these bands should occur at greater than 50 cm^{-1}. These bands, because they are stretching bands, will tend to be weaker than the hindered rotor bands. Also, there is a large uncertainty in the predicted frequency because there is a large variation in the values of the centrifugal distortion constants for the different bands and the calculation is based on the poor approximation that the potential is harmonic. Therefore, these bands could present a rather formidable search problem, unlike the hindered rotor bands which should be fairly close in frequency to the analogous bands in ArH_2O.

An important question which must still be addressed is why are there so many partial bands? There are, for example, fairly strong Q branches with no other lines nearby. It is not clear what could cause such marked intensity variations within a band. In some cases, it may simply be that the region has not been thoroughly searched. It is also possible that in some cases these bands involve excited states which are sensitive to beam conditions. Part of a band may be observed and at a later time, the beam temperature may change enough to prevent the rest of the band from being observed. Often, when trying

to extend observed patterns of lines, the previously seen lines will be checked first to verify that the beam conditions are not drastically different. However, with so many lines and so many patterns, it is possible that not all were rechecked. One of the fundamental difficulties with this project is that a very large number of lines have been observed over a fairly broad spectral region, and many of these lines have been grouped into bands and partial bands. Unlike ArH_2O, there are not simply two or three intense band progressions. In $CH_4 \cdot H_2O$, bands are overlapped and have very similar rotational constants. In some cases it is not clear which of several closely spaced Q branches belongs with a certain band. The constants are so similar that all can fit equally well. The answers are going to come through continued searching as well as potential calculations to help in the assignment and predictions.

4.6 Conclusion

At this preliminary point in the $CH_4 \cdot H_2O$ study, it is difficult to make many general conclusions. Over 200 lines were observed in the $CH_4/H_2O/Ar$ expansion. Several bands were found with very similar band origins and rotational constants. None were found to share a common state, indicating that the energy level diagram is quite complex. Two different energy level diagrams were proposed based on the ArH_2O energy level diagram and Hund's case (a) and (b) angular momentum coupling

schemes. Based on a number of assumptions, case (a) appears to be more plausible. Even assuming that the energy level diagram is determined, it is still not possible to assign the seven observed bands because there are so many possible transitions. Several arguments were also presented which indicate that the $CH_4 \cdot H_2O$ is more strongly bound than ArH_2O, which is bound by approximately 175 cm^{-1}.[3]

The ultimate goal of this project is to derive a $CH_4 \cdot H_2O$ potential surface from the spectroscopic results, as was obtained for ArH_2O by Cohen and Saykally.[3] This potential could then be used to study hydrophobic interactions. There remains, however, a great deal of work to be done, including additional scanning for new bands. Work has begun on calculating the energy level diagram using simplistic potential functions.[10] These calculations may aid in the assignment of the existing bands as well as in the search for new bands.

Chapter 4 References

1. R.C. Cohen, K.L. Busarow, K.B. Laughlin, G.A. Blake, M. Havenith, Y.T. Lee, and R.J. Saykally, J. Chem. Phys. **89**, 4494, (1988).

2. R.C. Cohen, K.L. Busarow, Y.T. Lee, and R.J. Saykally, J. Chem. Phys. **92**, 169 (1990).

3. R.C. Cohen and R.J. Saykally, J. Phys. Chem. **94**, 7991 (1990).

4. K.B. Laughlin, Ph.D. Dissertation, University of California, Berkeley, 1988.

5. G. Herzberg, Molecular Spectra and Molecular Structure II. Infrared and Raman Spectra of Polyatomic Molecules (Van Nostrand Reinhold, New York, 1945).

6. J.M. Hutson, J. Chem. Phys. **89**, 4550 (1988).

7. F. Hund, Z. Phys. **42**, 93 (1927); F. Hund, Z. Phys. **63**, 719 (1930); F. Hund, Handbuch d. Phys. **24**, I, 561 (1933).

8. G. Herzberg, Molecular Spectra and Structure I. Spectra of Diatomic Molecules (Van Nostrand Reinhold, New York, 1950).

9. J.M. Hutson, private communication.

10. R.C. Cohen, C.A. Schmuttenmaer, and R.J. Saykally, in preparation.

11. G.M. Barrow, Physical Chemistry (McGraw-Hill, New York, 1979), p. 555.

12. G.C. Maitland, M. Rigby, E.B. Smith, and W.A. Wakeham, Intermolecular Forces: Their Origin and

Determination (Clarendon, Oxford, 1981).

13. B.P. Reid, M.J. O'Loughlin, and R.K. Sparks, J. Chem. Phys. **83**, 5656 (1985).

Appendix A

"Tunable Far Infrared Laser Spectroscopy in a Planar Supersonic Jet: The Σ Bending Vibration of Ar-$H^{35}Cl$"

Kerry L. Busarow, Geoffrey A. Blake, K.B. Laughlin, R.C. Cohen, Y.T. Lee and R.J. Saykally

Chemical Physics Letters, **141**, 289 (1987)

"Tunable Far Infrared Laser Spectroscopy of van der Waals Bonds: Extended Measurements on the Lowest Σ Bend of ArHCl"

Kerry L. Busarow, Geoffrey A. Blake, K.B. Laughlin, R.C. Cohen, Y.T. Lee and R.J. Saykally

Journal of Chemical Physics **89**, 1268 (1988)

Volume 141, number 4 CHEMICAL PHYSICS LETTERS 13 November 1987

TUNABLE FAR-INFRARED LASER SPECTROSCOPY IN A PLANAR SUPERSONIC JET: THE Σ BENDING VIBRATION OF Ar-H^{35}Cl

Kerry L. BUSAROW, Geoffrey A. BLAKE [1], K.B. LAUGHLIN, R.C. COHEN, Y.T. LEE and R.J. SAYKALLY

Department of Chemistry and Materials and Chemical Sciences Division, University of California and Lawrence Berkeley Laboratories, Berkeley, CA 94720, USA

Received 25 September 1987

The lowest Σ bending vibration (02^00) of Ar-H^{35}Cl has been observed near 23.6 cm^{-1} from P(23) to R(17), in a continuous planar jet expansion using a tunable far-infrared laser. A least-squares analysis has been performed to determine the centrifugal distortion constants for the ground and excited states, which will greatly facilitate the determination of an accurate intermolecular potential surface.

Several new spectroscopic techniques have recently been developed for the study of van der Waals molecules. Mid-infrared laser spectroscopy of van der Waals clusters generated in a pulsed planar jet [1] effects both high sensitivity and substantially reduced linewidths. While this approach produces a wealth of both structural and dynamical information, it is not a direct probe of the ground state intermolecular potential surface. The extremely sensitive method of intracavity far-infrared (FIR) laser Stark spectroscopy of the low frequency van der Waals vibrations [2] does provide a direct route to the potential surface, but the search for and assignment of spectra are difficult. In this article we describe a straightforward and versatile new method which avoids this complication. Hyperfine-resolved vibration–rotation absorption spectra of low frequency van der Waals modes are measured by tunable FIR laser spectroscopy of a continuous planar supersonic jet.

Ar-HCl is the prototype system for the study of anisotropic van der Waals interactions. The experimental work of Novick et al. [3], of Marshall et al. [4], and of Ray et al. [2] has provided a characterization of the ground state (00^00) and of the Π bending state (01^10). Recent FIR laser studies by Robinson et al. [5] have provided more detailed information for the three lowest vibrations. Empirical intermolecular potential surfaces obtained by Hutson and Howard [6] indicate that Ar-HCl is bound by approximately 180 cm^{-1} and has a secondary minimum at the Ar–ClH configuration. An experimental characterization of the secondary minimum can be obtained most directly from the spectra of the Σ bending state because this vibration is strongly influenced by the second well. Robinson et al. [5] measured several vibration–rotation lines of the Σ bend, but could not obtain any centrifugal distortion information from this limited data set. In the present work we were able to determine both the quartic and sextic centrifugal distortion constants for the Σ bending state (D and H) as well as more precise values for previously known ground and excited state constants.

The experimental apparatus is shown in fig. 1. The tunable FIR laser has been described elsewhere [7]. Briefly, a cw CO_2 laser is used to optically pump a line tunable FIR laser (10–200 cm^{-1}). The far-infrared radiation is then mixed with continuously tunable microwave radiation (2–40 GHz) in a GaAs Schottky barrier diode. Tunable sum and difference

[1] Berkeley Miller Research Fellow. Present address: Center for Cosmochemistry and Geochemistry, Division of Geology and Planetary Sciences, California Institute of Technology, Pasadena, CA 91125, USA.

Reproduced with permission of Elsevier Science Publishers, B.V., 1991, and of Kerry L. Busarow, Geoffrey A. Blake, K.B. Laughlin, R.C. Cohen, Y.T. Lee, and R.J. Saykally.

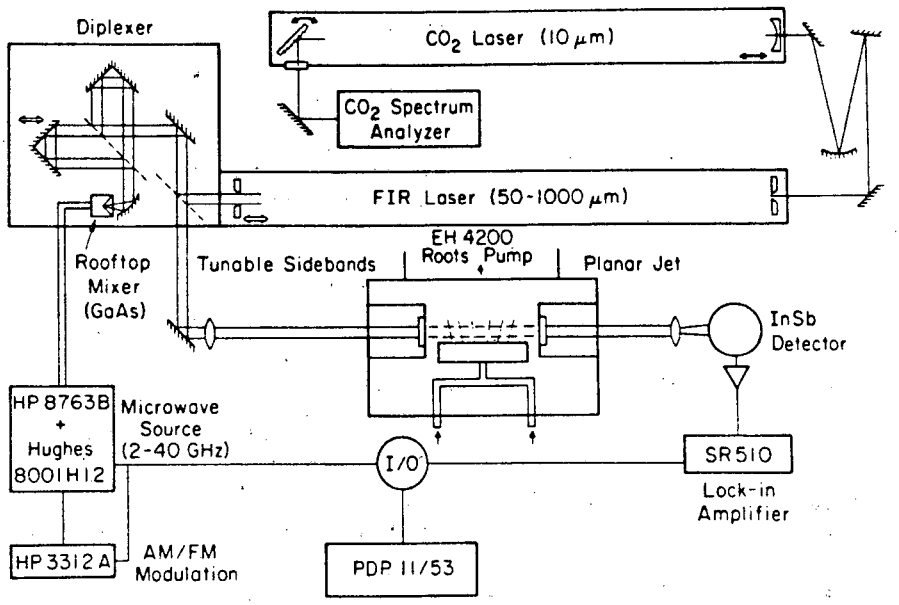

Fig. 1. Tunable FIR laser/planar jet system.

sidebands are separated from the FIR laser carrier with a polarizing diplexer. The collimated tunable FIR radiation laser passes through the plane of the supersonic jet and is detected with an InSb detector.

Ar–HCl was formed by expanding 2–3% HCl in Ar through a 1.5″×25 μm slit at a stagnation pressure of approximately 500 Torr. The chamber was pumped by a 2600 cfm Roots blower and was kept at 120 mTorr. The distance to the Mach disk was determined to be approximately 1″ from the nozzle. The temperature of the expansion is estimated to be less than 10 K. Transitions of Ar–$H^{35}Cl$ were observed with the 692 and 761 GHz HCOOH laser lines from P(23) to R(17), with the exception of P(5), P(6), and R(11) which lie too close to the FIR laser frequency to be observed, and R(9) which is nearly coincident with an atmospheric water line. A typical spectrum is shown in fig. 2. The optimum S/N is about 2000:1. Narrow linewidths (≈300 kHz fwhm) result from the use of a planar jet, representing approximately a threefold reduction in the room temperature Doppler width [8].

All measured transitions were used in this analysis excluding those with $J \leqslant 5$, for which the quadrupole

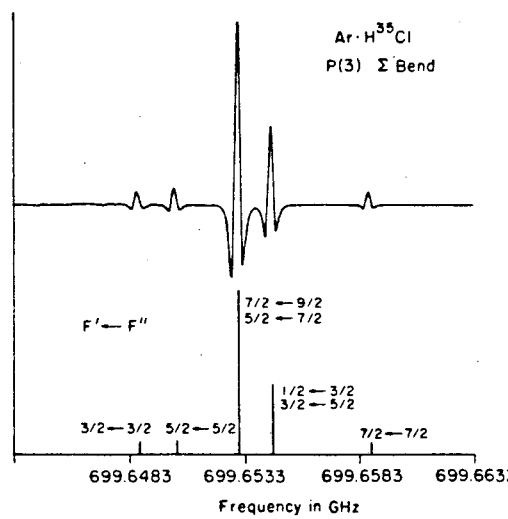

Fig. 2. Tunable FIR laser spectrum showing P(3) of the Σ bend of Ar–$H^{35}Cl$. Below is the predicted spectrum with the quadrupole splittings. The intensity of the 7/2←5/2 and 5/2←3/2 transitions is too small to be shown on this scale.

Table 1
Constants for the lowest Σ bending vibration of Ar–$H^{35}Cl$ (MHz)

	This work [a]	Previous work
ν	709224.68(44)	709219.96(52) [b]
$B(00^00)$	1678.567(18)	1678.511(10) [c]
$D(00^00)$	0.02022(8)	0.02033(40) [c]
$H(00^00)$	$-1.9(1.2)\times10^{-7}$	-
$B(02^00)$	1761.358(20)	1761.204(106) [b]
$D(02^00)$	0.03188(10)	-
$H(02^00)$	$-1.73(17)\times10^{-6}$	-

[a] Standard deviation of the fit is 200 kHz. The errors are expressed as 2σ.
[b] Ref. [5]. [c] Ref. [3].

structure was resolved. The results of the fit are given in table 1. Since the Σ bending state samples the secondary minimum much more completely than do the other two low lying vibrational states, the determination of the centrifugal distortion constants for this state will greatly assist in determining the shape of the potential surface in the region of the secondary minimum.

This work was supported by the Director, Office of Energy Research, Office of Basic Energy Sciences, Chemical Sciences Division of the US Department of Energy under Contract No. DE-AC03-76SF00098. The FIR laser system was funded by the National Science Foundation (Grant CHE-8612296).

References

[1] C.M. Lovejoy, M.D. Schuder and D.J. Nesbitt, J. Chem. Phys. 86 (1987) 5337.
[2] D. Ray, R.L. Robinson, D.-H. Gwo and R.J. Saykally, J. Chem. Phys. 84 (1986) 1171.
[3] S.E. Novick, K.C. Janda, S.L. Holmgren, M. Waldman and W. Klemperer, J. Chem. Phys. 65 (1976) 1114.
[4] M.D. Marshall, A. Charo, H.O. Leung and W. Klemperer, J. Chem. Phys. 83 (1985) 4924.
[5] R.L. Robinson, D.-H. Gwo, D. Ray and R.J. Saykally, J. Chem. Phys. 86 (1987) 5211;
R.L. Robinson, D. Ray, D.-H. Gwo and R.J. Saykally, J. Chem. Phys. (1987), to be published;
R.L. Robinson, D.-H. Gwo and R.J. Saykally, J. Chem. Phys. (1987), to be published.
[6] J.M. Hutson and B.J. Howard, Mol. Phys. 45 (1982) 769.
[7] K.B. Laughlin, G.A. Blake, R.C. Cohen, D.C. Hovde and R.J. Saykally, Trans. Faraday Soc., to be published.
[8] K. Veeken and J. Reuss, Appl. Phys. B38 (1985) 117.

Tunable far infrared laser spectroscopy of van der Waals bonds: Extended measurements on the lowest Σ bend of ArHCl

Kerry L. Busarow, Geoffrey A. Blake,[a] K. B. Laughlin, R. C. Cohen, Y. T. Lee, and R. J. Saykally
Department of Chemistry and Materials and Chemical Sciences Division, University of California and Lawrence Berkeley Laboratories, Berkeley, California 94720

(Received 23 February 1988; accepted 18 April 1988)

A tunable far infrared laser system has been used to measure the vibration–rotation spectrum of the lowest Σ bending state of ArHCl near 24 cm^{-1} in a cw planar jet operating with a terminal jet temperature near 3 K. Over 60 transitions have been observed for both ^{35}Cl and ^{37}Cl isotopes with resolution of the quadrupole hyperfine structure. An improved set of molecular parameters was determined, including B, D, H, and eqQ for both upper and lower states. Very narrow linewidths (approximately 300 kHz) resulting in high resolution and sensitivity make this technique a powerful new method for the detailed investigation of intermolecular forces.

INTRODUCTION

There is a great deal of current interest in the study of weakly bound van der Waals clusters. Much of this activity has been stimulated by recent advances in experimental and theoretical techniques designed to address these systems. Methods now exist for measuring spectroscopic transitions in weakly bound complexes from the microwave through UV-visible frequencies. These techniques are yielding much detailed information regarding the structures and dynamics of complexes, and are revealing subtle features of van der Waals forces never before accessible by either theory or experiment. Clearly, this type of information ultimately contributes a great deal to our general understanding of condensed phase systems.

ArHCl has become the prototype for the study of anisotropic van der Waals interactions. The reason is that it is accessible from both theoretical and experimental approaches, while still exhibiting a substantial degree of complexity as a result of the strong anisotropy of the intermolecular potential. There have been numerous investigations of this system. The earliest studies were performed using static gas cells and low resolution infrared spectroscopy. It was observed that in the null gap between $P(1)$ and $R(0)$ of the HCl vibration–rotation spectrum ($\sim$2900 cm^{-1}), extra peaks appeared, which could be attributed to ArHCl and $(HCl)_2$.[1–4] Shortly thereafter, matrix IR studies probed the same region.[5–8] Low resolution far infrared spectroscopy studies were carried out in the wavelength interval between the $J = 1 \leftarrow 0$ and $2 \leftarrow 1$ lines of the pure rotational spectrum of HCl using both matrix techniques[9,10] and static gas cells.[11–13] Differential cross sections from molecular beam elastic scattering experiments provided a value for the isotropic well depth and an isotropic intermolecular potential surface.[14–16]

The most informative studies have been those utilizing high resolution spectroscopic techniques. Most of these investigations used supersonic molecular beams to generate high densities of rotationally cold complexes. Molecular beam electric resonance (MBER) spectroscopy first determined ground state properties from the pure rotational spectrum of ArHCl.[17–19] High resolution laser spectroscopy has been used to study vibrational bands occurring in the near infrared region.[20] These transitions are combination bands of the high frequency HCl stretching vibration and low frequency van der Waals vibrations.

The advantage of high resolution far infrared studies is that the van der Waals vibrations are probed directly, without the additional complications caused by simultaneous high frequency vibrational excitation. The first high resolution FIR spectrum of ArHCl was recorded by Marshall *et al.* using MBER detection.[21] In their study, hyperfine-resolved components of vibration–rotation transitions between the ground state and the lowest Π bending state were probed near 34 cm^{-1}, but the inherently low sensitivity of this otherwise elegant method precluded more extensive measurements. Shortly thereafter, Ray *et al.*[22] measured a greatly expanded set of transitions in this same vibration–rotation band using intracavity FIR laser absorption spectroscopy. More recently, Robinson *et al.* measured extended spectra for the Π bend[23] as well as for the two other lowest frequency vibrations, the Σ bend (24 cm^{-1})[24] and the Σ stretch (32 cm^{-1}).[25]

In addition to these experimental investigations, there has been considerable theoretical work carried out on the ArHCl system.[15,26–30] In particular, the very important work of Hutson and Howard has provided potential surfaces and spectroscopic predictions which have greatly facilitated spectroscopic investigations. *Ab initio* calculations of potential surfaces have also been performed at a fairly high level of theory, but these are not expected to be reliable at the level of precision required for high resolution spectroscopy.[31]

In this paper we describe a new technique for studying low frequency vibration–rotation transitions in weakly bound complexes with very high resolution, discuss its application for greatly extended measurements of the Σ bending vibration of ArHCl, and elaborate on the preliminary results

[a] Berkeley Miller Postdoctoral Fellow. Present address: Center for Cosmochemistry and Geochemistry, Division of Geology and Planetary Sciences, California Institute of Technology, Pasadena, CA 91125.

 0021-9606/88/151268-09$02.10 © 1988 American Institute of Physics

Reproduced with permission of the American Institute of Physics, 1991, and of Kerry L. Busarow, Geoffrey A. Blake, K.B. Laughlin, R.C. Cohen, Y.T. Lee, and R.J. Saykally.

reported elsewhere.[32] This new method involves a combination of two relatively new techniques. A tunable far infrared laser is used to probe ArHCl complexes produced in a continuous planar supersonic jet expansion. The advantage of the continuous planar jet is that it provides a long path length for the light absorption as well as an order of magnitude reduction in the Doppler width relative to a conventional circular nozzle, and operates with a 100% duty cycle. The obvious disadvantage is that this nozzle design requires large vacuum pumps for continuous operation. This difficulty can be overcome to some extent by pulsing the nozzle, thereby reducing the duty cycle and consequent load on the vacuum pumps. Pulsed planar nozzles have been developed by several groups for use in spectroscopic applications,[33,34] and the recent studies by Nesbitt and co-workers are particularly noteworthy.[35] Some additional investigations have been carried out on continuous planar jets, primarily to characterize them.[36–38] In the present experiment, we operate a 1.5 in. long slit nozzle continuously, using a large Roots blower (2600 cfm) to pump the system.

The evolution of tunable far infrared lasers is a very recent development.[39–41] FIR laser spectroscopy has previously involved the use of fixed frequency optically pumped FIR lasers combined with either Stark or Zeeman tuning of the energy levels of the species of interest (see, e.g., Ref. 23). In these experiments, the requirement for strong tuning fields seriously complicates the observed spectra, and often makes spectral assignments difficult. Also, the extent to which the molecular energy levels can be tuned is usually quite limited, requiring the rather tedious employment of numerous FIR laser lines in order to obtain the spectrum. The development of tunable far infrared lasers now permits spectroscopy to be carried out in the absence of these strong perturbing fields with both high sensitivity and high resolution, and with substantially enhanced generality and versatility. This has been demonstrated by our recent observation of the tunneling–rotation and vibration–rotation spectra of $(HCl)_2$[42] and ArH_2O.[43]

EXPERIMENTAL

A schematic diagram of the experimental arrangement is shown in Fig. 1. The tunable FIR laser system has been described elsewhere[44] in conjunction with studies of molecular ions and will only be discussed briefly here. A 150 W, discharge pumped, cw CO_2 laser (Apollo model 150) is used to optically pump a 2.5 m far infrared laser. A large number (>65) of simple organic molecules can be pumped to produce over 2000 laser frequencies from 10–200 cm^{-1}.[45] In the present experiments, formic acid was used for the production of the 432 and 394 μm laser lines. The narrow band FIR laser output, approximately 100 kHz FWHM,[46] is directed through a polarizing Michelson diplexer into a cornercube in which a GaAs Shottky barrier diode is mounted. The FIR laser output is coupled onto the diode through a small (0.001 in. diameter) whisker antenna contacting the diode. Tunable microwave radiation (2–75 GHz) is also coupled onto the diode, either directly through the whisker mount or through the post on which the diode is mounted. The FIR and microwave radiation are mixed in the diode and sidebands are produced at the sum and difference of the microwave and the FIR laser frequencies. Therefore, tunable sidebands are generated from 2 to 75 GHz on either side of the laser frequency, yielding a 5 cm^{-1} range of tunability for each FIR laser line. Both the FIR laser frequency and the sidebands radiate from the cornercube, and the sidebands are separated from the much more intense FIR carrier by the diplexer. The sidebands are then collimated and directed through the plane of the supersonic jet and detected using an InSb hot electron bolometer. The FIR laser beam is approximately 1 cm in diameter at the nozzle. The microwave radi-

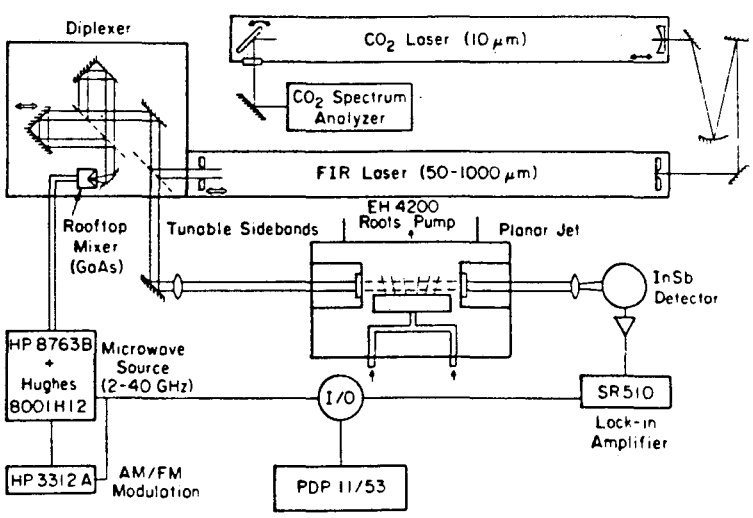

FIG. 1. Tunable far infrared laser/planar supersonic jet apparatus

ation is frequency modulated at 50 kHz with a deviation of approximately 125 kHz, which results in a corresponding frequency modulation of the sidebands. Lock-in detection is referenced at twice the modulation frequency, producing second derivative line shapes. A PDP11/53 is used to control the experiment and to manipulate the data.

ArHCl was formed in 1%–3% mixtures of HCl in Ar expanded continuously from a 500 Torr backing pressure into a 120 mTorr chamber pressure. The chamber is pumped by a 2600 cfm Roots blower (Edwards EH4200) which is backed by two 145 cfm two-stage mechanical pumps (Edwards E2M275). The pumps are connected to the chamber through 40 ft of 8 in. PVC pipe, reducing the pumping speed to approximately 1600 cfm. The planar nozzle, shown in Fig. 2, is constructed from a rectangular block of stainless steel (2 in. × 1 in. × 1 in.), through the length of which a 0.5 in. diameter hole is drilled to hollow out the block. Caps were then welded on the ends, and a hole was drilled through the back side for the gas inlet line. A 1.5 in. × 0.25 in. slot was milled through the front side. Four blind tapped holes were drilled on either side of the slot for mounting the plates which formed the slit. These two stainless steel plates are 0.125 in. thick, except on the edge that forms the slit, where it is tapered down to a thickness of 0.031 in. The separation of the plates is established by using 0.001 in. shims. Hence, the size of the slit is 1.5 in. × 0.001 in. There is no gasket between the block and the plates. The surfaces of each plate and the nozzle block are polished to a mirror finish. The nozzle can be readily cooled to 77 K with liquid nitrogen. However, this cooling did not improve the ArHCl signals, therefore the nozzle was operated without temperature control in the present study.

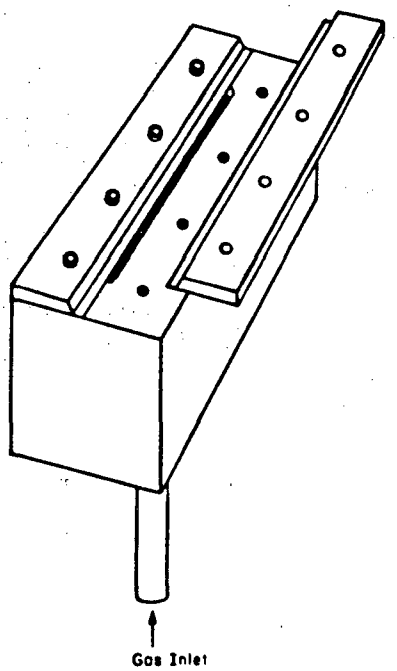

FIG. 2. Planar jet nozzle, drawn to scale, the length of the longest side is 2 in.

RESULTS AND ANALYSIS

Spectra

A total of 61 transitions for $ArH^{35}Cl$ and 63 transitions for $ArH^{37}Cl$ were measured for the lowest Σ bend. The optimum S/N was 2000, obtained for $P(3)$ of $ArH^{35}Cl$ (Fig. 3), while the typical S/N is approximately 200. Due to the fact that the FIR laser frequency undergoes a slow drift, it is necessary to calibrate the absorption frequencies using a standard reference gas. The HCl $J = 1 \leftarrow 0$ rotational transition was chosen as the reference and was measured in the jet expansion to obtain a narrower linewidth than in a gas cell. The value of the frequency used for this transition was taken from DeLucia *et al.* and has an uncertainty of approximately 20 kHz.[47] The HCl transition was measured, followed imme-

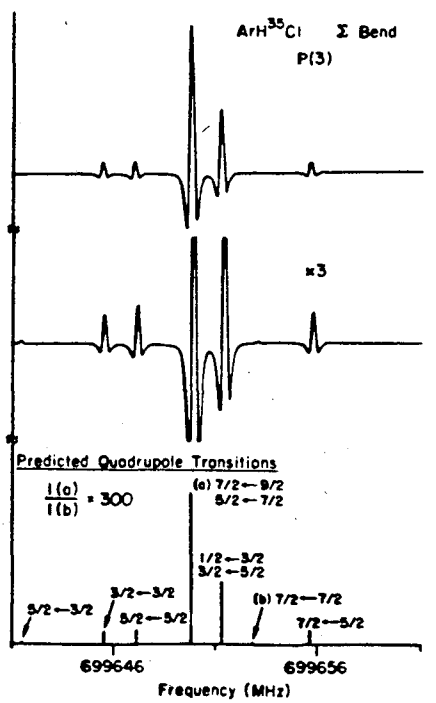

FIG. 3. $P(3)$ of $ArH^{35}Cl$. In the lowest scan the sensitivity is increased by a factor of 3 to show the smallest hyperfine components. The bottom graph shows the predicted hyperfine structure with the intensities. The smallest components, $5/2 \leftarrow 3/2$ and $7/2 \leftarrow 5/2$, are too small to be seen on this scale. The predicted intensity ratio of the largest central peak, labeled (a), to the smallest peak, labeled (b), is 300:1. The overall S/N of this, our best scan, is 2000. ($\tau = 1$ s.)

diately by the measurement of $P(10)$ of $ArH^{35}Cl$, thereby calibrating that peak. The remainder of the ArHCl transitions, both the Cl-35 and the Cl-37 isotopes were then referenced to $P(10)$. The $P(10)$ transition of $ArH^{35}Cl$ is measured using the 692 GHz HCOOH far infrared laser line. Those ArHCl transitions on this laser line are referenced directly to $P(10)$, measuring $P(10)$ before and after each line measurement. Those transitions measured on the 761 GHz HCOOH laser line must be referenced to a line accessible from both laser lines and previously referenced to $P(10)$, such as a lower R branch line. This calibration procedure allowed us to obtain reproducibilities on the order of 50 kHz or less for the FIR transition frequencies. Each peak was also measured twice with up–down scanning to minimize any line shifts caused by time constant effects.

Also included in the fit were rotational transition frequencies measured in the microwave region by Novick and co-workers.[17,19] However, only those transitions measured with better than ~100 kHz uncertainties were included. A list of all of the transitions used in the fit is given in Table I.

The Hamiltonian used to fit the FIR data was of the standard form appropriate for a linear triatomic molecule, including the effects of nuclear quadrupole hyperfine structure:

$$\begin{aligned} H = {} & \nu(v+1/2) + B(02^00)J'(J'+1) - D(02^00)[J'(J'+1)]^2 + H(02^00)[J'(J'+1)]^3 \\ & + L(02^00)[J'(J'+1)]^4 - eqQ(02^00)[3/4C'(C'+1) - I(I+1)J'(J'+1)]/[2I(2I-1) \\ & \times(2J'-1)(2J'+3)] - B(000)J''(J''+1) + D(000)[J''(J''+1)]^2 - H(000)[J''(J''+1)]^3 - L(000) \\ & \times[J''(J''+1)]^4 + eqQ(000)[(3/4C''(C''+1) - I(I+1)J''(J''+1)]/[2I(2I-1)(2J''-1)(2J''+3)], \end{aligned} \tag{1}$$

where

$$C' = F'(F'+1) - I(I+1) - J'(J'+1),$$

$$C'' = F''(F''+1) - I(I+1) - J''(J''+1),$$

and

$$F = I+J, I+J-1, \ldots, |I-J|.$$

We have obtained values for the rotational constants of the upper and lower states, as well as for the quartic and sextic centrifugal distortion constants (D and H) for both vibrational states (Table II). The next higher (octic) centrifugal distortion constant (L) was also included in the preliminary analysis. Including L improved the standard deviation of the fit by about 25% for both the Cl-35 and Cl-37 isotopes. In the Cl-35 case, however, it was not possible to meaningfully determine L for the ground state; therefore, L was not included in the final fits. Our values of B, D, and H for the ground state are slightly more precise than the results obtained by microwave spectroscopy.[19] Although the single line measurement precision of microwave spectroscopy generally exceeds that of the present experiment by approximately a factor of 10, we were able to measure much higher values of J (up to $J = 23$), which allowed us to better determine these constants. For the upper state, the present values of the determined constants are more precise than previous results from FIR laser Stark spectroscopy due to the combined effects of smaller linewidths, measuring to higher J, and careful calibration of the observed transitions.

Both chlorine isotopes have nuclear spins of 3/2 and quadrupole splittings were observed in both cases for transitions involving $J<5$. Our values for the quadrupole coupling constants are not as precise as the $ArH^{35}Cl$ ground state value obtained from MBER studies.[18] The energy level splittings resulted from the nuclear quadrupole interactions decrease rapidly with increasing J; hence there is no advantage in measuring high values of J because hyperfine splittings are observable only up to $J = 5$ or 6, the $P(6)$ splitting for Cl-37 was resolvable but for $R(6)$ it was not resolvable. Therefore, in the Cl-35 fit, the ground state quadrupole coupling constant, eqQ, was fixed at the MBER value. Between $J = 6$ and $J = 8$, the quadrupole structure is blended and broadens the peaks significantly, this makes accurate determination of the line centers more difficult. Therefore, $P(7)$, $P(8)$, $P(9)$, $R(6)$, $R(7)$, $R(8)$, are not included in either fit. This improves the overall standard deviation of the fit slightly. Of the lines not listed in Table I, several lines, including $P(5)$, $P(6)$, and $R(11)$ of $ArH^{35}Cl$ and $P(5)$ of $ArH^{37}Cl$, lie within 2 GHz of the FIR laser frequency and cannot be observed. Moreover, $R(9)$ of both isotopes and $R(11)$ of $ArH^{37}Cl$ are close to an atmospheric water absorption line at 752 GHz, which absorbs most of the available laser power, precluding their measurement. The fit deteriorates at high J, because above $J = 16$, the single peaks begin to split into Doppler doublets, as will be discussed in a later section. The center frequency of these split peaks is used in the fit, which may result in a somewhat larger error. The standard deviation of the fit is very good for FIR spectroscopy (~1 part in 10^7). The $ArH^{37}Cl$ fit is actually about a factor of 3 better than that of $ArH^{35}Cl$, in part due to the fact that we did not measure to as high a value of J, where the fit tends to deteriorate. This does not, however, account for the entire factor of 3 difference.

Linewidths

It was shown by Veeken and Reuss[34] and more recently by Lovejoy and Nesbitt[35] that the absorption linewidths are substantially reduced in a planar free jet expansion compared with those observed with a circular nozzle jet. In a planar jet, the expansion along the slit is inhibited which results in a reduction in the Doppler broadening when the measurements are carried out with the laser beam propagated parallel to the long slit. In the present experiment, the measured linewidths are approximately ten times smaller than for the case of a circular nozzle, and approximately three times smaller than those found in a room temperature low pressure gas cell. Linewidths of transitions occurring

TABLE I. List of all lines measured for the ArHCl Σ bending vibration. Those lines which do not have an associated obs − calc value were not included in the fit.

		Chlorine-35 measured lines		
I	Line	F′←F″	OBS (MHz)	OMC (kHz)
1	*P*(23)		671 708.028	−230
2	*P*(22)		671 842.823	172
3	*P*(21)		672 079.177	216
4	*P*(20)		672 424.272	5
5	*P*(19)		672 885.192	60
6	*P*(18)		673 467.576	−55
7	*P*(17)		674 177.279	−94
8	*P*(16)		675 019.387	−128
9	*P*(15)		675 998.665	−124
10	*P*(14)		677 119.446	−65
11	*P*(13)		678 385.638	30
12	*P*(12)		679 800.702	79
13	*P*(11)		681 367.791	54
14	*P*(10)		683 089.872	93
15	*P*(9)		684 969.337	
16	*P*(8)		687 008.387	
17	*P*(7)		689 208.849	
18	*P*(4)	4.50←5.50	696 792.406	10
19	*P*(3)	3.50←4.50	699 650.823	−15
20	*P*(2)	1.50←0.50	702 665.329	−105
21	*P*(2)	1.50←1.50	702 671.114	−82
22	*P*(2)	2.50←3.50	702 675.239	−68
23	*P*(2)	0.50←0.50	702 675.790	−6
24	*P*(2)	2.50←2.50	702 681.222	152
25	*P*(2)	0.50←1.50	702 681.564	5
26	*P*(1)	1.50←0.50	705 860.894	−58
27	*P*(1)	1.50←2.50	705 865.520	−42
28	*P*(1)	1.50←1.50	705 871.236	−88
29	*R*(0)	1.50←1.50	712 741.503	−28
30	*R*(0)	2.50←1.50	712 747.239	−49
31	*R*(0)	0.50←1.50	712 751.972	78
32	*R*(1)	1.50←0.50	716 427.603	−40
33	*R*(1)	2.50←2.50	716 428.039	−102
34	*R*(1)	1.50←2.50	716 432.270	16
35	*R*(1)	3.50←2.50	716 433.917	18
36	*R*(1)	1.50←1.50	716 437.906	−109
37	*R*(1)	0.50←1.50	716 443.796	24
38	*R*(2)	3.50←3.50	720 278.934	−0
39	*R*(2)	2.50←1.50	720 283.282	14
40	*R*(2)	4.50←3.50	720 284.695	3
41	*R*(2)	2.50←2.50	720 287.416	32
42	*R*(2)	1.50←1.50	720 289.123	99
43	*R*(3)	4.50←4.50	724 292.273	7
44	*R*(3)	3.50←2.50	724 297.380	22
45	*R*(3)	5.50←4.50	724 298.066	43
46	*R*(3)	3.50←3.50	724 300.077	30
47	*R*(3)	2.50←2.50	724 303.203	89
48	*R*(4)	4.50←3.50	728 471.856	43
49	*R*(4)	6.50←5.50	728 472.239	35
50	*R*(5)	5.50←4.50	732 805.064	18
51	*R*(5)	7.50←6.50	732 805.330	25
52	*R*(6)		737 295.071	
53	*R*(7)		741 939.369	
54	*R*(8)		746 734.680	
55	*R*(10)		756 766.394	120
56	*R*(12)		767 361.327	−21
57	*R*(13)		772 859.353	−29
58	*R*(14)		778 484.608	−4
59	*R*(15)		784 231.615	−68
60	*R*(16)		790 094 716	−105
61	*R*(17)		796 067.937	124
62	*J* = 1←0	2.50←1.50	3 358.0900[c]	0.5
63	*J* = 1←0	0.50←1.50	3 362.6975[c]	2.8
64	*J* = 2←1	0.50←0.50	6 713.3940[c]	3.1
65	*J* = 2←1	0.50←1.50	6 723.7560[c]	−6.5
66	*J* = 3←2	1.50←0.50	10 067.7320[c]	−5.7

TABLE I (*continued*).

I	Line	Chlorine-37 measured lines F′←F″	OBS (MHz)	OMC (kHz)
1	*P*(17)		674 426.964	3
2	*P*(16)		675 171.423	1
3	*P*(15)		676 053.095	27
4	*P*(14)		677 076.227	−30
5	*P*(13)		678 244.920	−27
6	*P*(12)		679 562.694	−16
7	*P*(11)		681 032.773	20
8	*P*(10)		682 657.940	14
9	*P*(9)		684 440.819	
10	*P*(8)		686 383.464	
11	*P*(7)		688 487.704	
12	*P*(6)	6.50←7.50	690 755.234	53
13	*P*(6)	4.50←5.50	690 755.424	36
14	*P*(4)	2.50←2.50	695 780.660	40
15	*P*(4)	3.50←3.50	695 783.098	51
16	*P*(4)	4.50←5.50	695 784.660	16
17	*P*(4)	2.50←3.50	695 785.180	9
18	*P*(4)	4.50←4.50	695 789.213	18
19	*P*(3)	1.50←1.50	698 544.699	−42
20	*P*(3)	2.50←2.50	698 545.991	−49
21	*P*(3)	3.50←4.50	698 548.122	−43
22	*P*(3)	1.50←2.50	698 549.252	−39
23	*P*(3)	3.50←3.50	698 552.698	−17
24	*P*(2)	1.50←0.50	701 470.256	−29
25	*P*(2)	1.50←1.50	701 474.795	−40
26	*P*(2)	2.50←3.50	701 478.056	−31
27	*P*(2)	0.50←0.50	701 478.447	−31
28	*P*(2)	2.50←2.50	701 482.620	−18
29	*P*(2)	0.50←1.50	701 483.014	−15
30	*P*(1)	1.50←0.50	704 570.618	−2
31	*P*(1)	1.50←2.50	704 574.260	−1
32	*P*(1)	1.50←1.50	704 578.821	9
33	*R*(0)	1.50←1.50	711 263.748	14
34	*R*(0)	2.50←1.50	711 268.317	31
35	*R*(0)	0.50←1.50	711 271.930	3
36	*R*(1)	1.50←0.50	714 857.188	40
37	*R*(1)	2.50←2.50	714 857.572	34
38	*R*(1)	0.50←0.50	714 861.709	9
39	*R*(1)	3.50←2.50	714 862.124	34
40	*R*(1)	1.50←1.50	714 865.347	7
41	*R*(2)	3.50←3.50	718 615.927	12
42	*R*(2)	1.50←0.50	718 619.330	−10
43	*R*(2)	4.50←3.50	718 620.478	11
44	*R*(2)	2.50←2.50	718 622.599	9
45	*R*(2)	1.50←1.50	718 623.867	−24
46	*R*(3)	4.50←4.50	722 537.304	−15
47	*R*(3)	3.50←2.50	722 541.347	4
48	*R*(3)	5.50←4.50	722 541.888	17
49	*R*(3)	3.50←3.50	722 543.486	20
50	*R*(3)	2.50←2.50	722 545.902	8
51	*R*(4)	4.50←3.50	726 624.324	−29
52	*R*(4)	6.50←5.50	726 624.646	−20
53	*R*(5)	5.50←4.50	730 866.752	−1
54	*R*(5)	7.50←6.50	730 866.967	5
55	*R*(6)		735 266.528	
56	*R*(7)		739 821.023	
57	*R*(8)		744 527.505	
58	*R*(11)		759 526 724	−60
59	*R*(12)		764 807.060	−26
60	*R*(13)		770 220.456	16
61	*R*(14)		775 761.983	48
62	*R*(15)		781 426.307	55
63	*R*(16)		787 207.592	−55
64	$J=2\leftarrow1$	0.50←1.50	6 533.9730[b]	−0.5
65	$J=1\leftarrow0$	0.50←1.50	3 267.6700[a]	0.8

[a]Reference 17.
[b]Reference 19.

TABLE II. Constants for the ground and Σ bending states of ArHCl.[a]

	Constant	This work (MHz)	Previous work (MHz)	References
Cl-35				
	ν	709 223.654(18)	709 219.96(26)	24
	$B(000)$	1678.5086(25)	1678.511(5)	17
	$D(000)$	0.019 991(13)	0.0200(4)	19
	$H(000)$	$-4.63(20)\times10^{-7}$	···	
	$eqQ(000)$	···[b]	−23.0297(5)	18
	$B(02^00)$	1761.3047(27)	1761.204(53)	24
	$D(02^00)$	0.031 649(15)	···	
	$H(02^00)$	$-20.42(26)\times10^{-7}$	···	
	$eqQ(02^00)$	−23.028(93)	−23.84(98)	24
Cl-37				
	ν	707 838.2889(71)	707 846.9(2.3)	24
	$B(000)$	1631.596 45(88)	1631.604(5)	17,19
	$D(000)$	0.018 900(6)	0.0190(4)	19
	$H(000)$	$-3.37(14)\times10^{-7}$	···	
	$eqQ(000)$	−18.203(34)	−18.201(50)[c]	48
	$B(02^00)$	1714.604 16(86)	1711.46(53)	24
	$D(02^00)$	0.030 470(6)	···	
	$H(02^00)$	$-20.0(13)\times10^{-7}$	···	
	$eqQ(02^00)$	−18.208(33)	−23.(11.)	24

[a] Errors are 1σ.
[b] Fixed at value of previous work.
[c] Uncertainty estimated by present authors.

near 25 cm^{-1} for ArHCl formed in the planar free jet in argon buffer gas are typically 300–350 kHz FWHM.

Several important advantages clearly result from this Doppler narrowing. The first and most obvious is that this yields a higher resolution spectrum. This also requires, however, that the line be scanned more slowly. Second, as the absorption profile narrows, the peak intensity increases, increasing the sensitivity of the spectrometer. Finally because the absorptions are so narrow, the FM deviation required for full modulation of the absorption is much smaller and therefore the magnitude of base line fluctuations that normally accompany source modulation is greatly reduced.

In addition to line narrowing, Veeken and Reuss[34] and Hagena[49] point out that due to the slower drop in density and temperature in a planar jet expansion ($1/R$ dependence), as compared with the circular nozzle expansion ($1/R^2$ dependence), the extent of clustering is higher in a planar jet. It is not clear whether this is an advantage in the present experiment, as it may result in more extensive formation of larger than desired clusters [e.g., $Ar_n(HCl)_m$ and HCl polymers].

Beam temperature

In general, it is difficult to obtain accurate relative intensities for many peaks because the sideband power varies considerably as the microwave frequency is swept over large regions. In the case of $ArH^{37}Cl$, $P(2)$ and $P(9)$ fortuitously appeared in the same scan. This occurred because both the upper and lower sidebands are scanned and directed through the jet simultaneously. $P(9)$ appears on the lower frequency sideband, while $P(2)$ appears on the upper sideband at nearly the same microwave frequency (Fig. 4). The sideband responsible for each absorption can be determined by lengthening the FIR laser cavity slightly, thereby shifting the laser frequency slight to the red. This then results in a shift in the microwave frequency at which the absorption occurs, either higher or lower depending on which sideband is being absorbed. The importance of this $P(9)/P(2)$ spectrum is that it provides a ratio of the intensities under approximately identical spectrometer conditions. Using a Fabry–Perot, we were able to determine the actual ratio of the power of the upper sideband to lower sideband. From the corrected ratio of these two peaks a beam temperature of 3(±1)K is obtained. This is not an unreasonable temperature for a circular nozzle; it is, however, colder than expected for a planar jet operating under the present conditions. This is only a

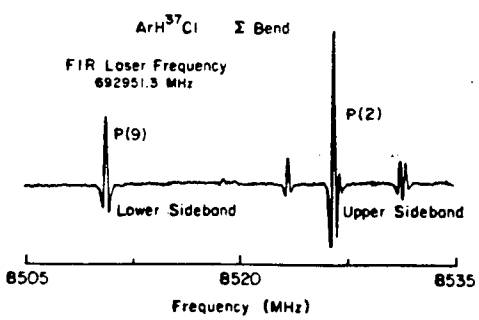

FIG. 4. In this 30 MHz wide scan both $P(2)$ and $P(9)$ of $ArH^{37}Cl$ appear. This results from both the upper and lower sidebands being detected simultaneously. $P(2)$ is on the upper sideband and $P(9)$ is on the lower sideband. This scan gives us an estimate of the jet temperature of 3 K based on the intensities of these two peaks.

single ratio and may not accurately characterize the actual beam temperature, but it certainly does indicate that the expansion is very cold.

High *J* splitting

An interesting feature observed in the tunable FIR laser spectra for $J > 15$, is that instead of a single line, a doublet is observed. The width of each line in the doublet is the same as for the low J lines (~ 350 kHz) and the splitting between the lines is approximately the same. The transition out of $J = 16$ produces a broad, flat-topped line, and at higher J, the flat top becomes two peaks. As shown in Fig. 5, the transition out of $J = 19$ is a resolved doublet. The signal to noise ratio for these high J transitions is quite low.

We believe that this splitting is due to the incomplete rotational cooling of clusters sampled at the shock wave boundaries of the expansion. The number of cold (3 K) clusters in the main body of the expansion (moving perpendicular to the laser beam) is much greater than the number formed in the shock boundary, therefore only a narrow intense peak is observed for low J transitions. However, for higher rotational quantum numbers, the linewidth increases, indicating that the number of clusters in the shock boundary is becoming comparable to that in the beam; finally, for higher J states the density in the beam becomes still smaller and the dip between the peaks becomes more pronounced. We also find that this splitting does not change significantly with J, indicating that these warmer clusters are all found in essentially the same region of the shock. The doublets are very narrow, indicating that the shock boundary region is quite sharply defined.

The information that we can obtain from this data is that there are actually two temperatures associated with the jet, the inner jet temperature, and the shock boundary temperature, which is considerably higher. From the observed Doppler splitting, we can obtain an estimate of the divergence of the planar jet. From the Doppler shift of each peak we find a parallel velocity of 67 m/s. In order to determine the angular divergence of the jet, we need to know the perpendicular velocity of the jet. For pure argon expanded from a circular nozzle a velocity of 560 m/s has been found.[50] Using this value for the perpendicular velocity we obtain $\Theta = 7°$. This angular divergence is obviously quite small compared to that observed with a circular nozzle, which exhibits a broad, cosine-type distribution.[51] Veeken and Reuss have measured a divergence for their pulsed planar jet of 3°.[34]

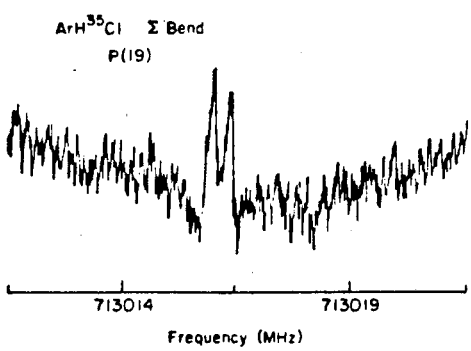

FIG. 5. $P(19)$ of ArH^{35}Cl which shows a splitting characteristic of all the high J scans ($J > 15$). We propose that this splitting occurs because these high J levels are only populated in the warmer boundary regions of the jet, and therefore, are Doppler shifted

DISCUSSION

The molecular constants determined from the tunable FIR spectra are presented in Table II, and are compared with the results obtained previously for the Σ bending state and for the ground state. The band origins for both isotopes are shifted from the FIR laser Stark values. A possible explanation for the large difference in band origin ν for both isotopes is that in the work of Robinson *et al.*,[25] although they were able to measure $P(1)$, they were unable to use it in the fit because the FIR laser frequency had not been accurately determined. Only $R(0)$, $R(1)$, and $R(2)$ were included in the fit. Accurate determination of the band origin without P branch lines is very difficult. The present results are considerably more accurate, as well as more precise, because of the extensive frequency calibrations carried out in this study, the large increase in the number of lines measured, and the reduction in linewidth compared to other FIR techniques.

The recent studies of vibrational spectra of ArHCl were greatly facilitated by the work of Hutson and Howard. By utilizing much of the previously obtained ArHCl data, including line broadening, virial coefficients, scattering, and high resolution microwave spectroscopy, they developed two very different potential surfaces, labeled M3 and M5, both of which fit the available data. The primary difference between these two surfaces is that M5 has a secondary minimum at the ArClH configuration, where M3 does not and is constrained to be flat in this region. Using these two surfaces, the energy levels of the lowest few vibrational states and the associated rotational constants were predicted. Of the lowest three excited states, the Σ stretch, the Σ bend, and the Π bend, the constants associated with the Σ bend most strongly reflect the existence of the secondary minimum. Robinson *et al.* were the first to measure this Σ bend and their results gave strong evidence for this minimum.[24] Our work greatly extends this data set and provides additional constants, particularly the centrifugal distortion constants, which will yield a better characterization of this second well.

From the quadrupole coupling constant we can obtain qualitative information regarding the extent of bending of the complex. The projection of the quadrupole coupling constant on the molecular axis is

$$eqQ_{\mathrm{ArHCl}} = eqQ_{\mathrm{HCl}} \langle P_2(\cos\theta)\rangle,$$

where θ is the angle between the line connecting the Ar to the HCl center of mass and the HCl molecular axis. This assumes that the quadrupole coupling constant of the HCl subunit is unperturbed in the complex. The constant eqQ_{HCl} is well determined,[52] and therefore we can determine the value for $\langle P_2(\cos\theta)\rangle$ as 0.3406 for ArH^{35}Cl in the Σ bending state. If we then make the assumption that $\langle\cos\theta\rangle$ is equal to

$\cos\langle\theta\rangle$, we can calculate an approximate average bending angle of either 41.5° or 138.5°, since we cannot rigorously distinguish between an acute or obtuse angle from this measurement. Based on the predictions from Hutson and Howard's M5 potential[29] and calculations of Marshall *et al.* using the BOARS method,[21] it is apparent that the Σ bending state wave function is predominantly localized in the second minimum, i.e., it is closer to the ArClH configuration. The work of Robinson *et al.* strongly favors this description and indicates that the dipole moment for this state is opposite in sign from that in the other low lying vibrational states, implying that the HCl subunit is oriented in the opposite direction. This assumption could not, however, be proven in the Stark experiment, since the sign of the dipole moment could not be determined. On the basis of these prior results, we propose that this angle is the projection on the molecular axis in the ArClH configuration, and is therefore, the obtuse angle. As in the Stark experiment, we cannot prove this assumption. It is interesting to note, however, that the value of $\langle P_2(\cos\theta)\rangle$ is essentially identical in both the Σ bend and the ground state.

The most significant result presented in this article is the development of sensitive, precise, and versatile tunable FIR laser spectroscopy of planar jets as a powerful new technique for detailed investigations of van der Waals interactions. As has been demonstrated recently by Hutson,[53] very accurate anisotropic intermolecular potential surfaces can be determined exclusively from high resolution spectroscopic measurements of the corresponding weakly bound complexes. In particular, Hutson was able to extract a very well-determined surface for ArHCl, conclusively establishing the existence of a secondary minimum (130 cm^{-1} deep) at the ArClH geometry, in addition to the 180 cm^{-1} primary ArHCl well and the 76 cm^{-1} barrier to HCl rotation, exclusively from the measurements of Robinson *et al.*[23–25] of the lowest Π bend, Σ bend, and Σ stretch vibrations and from Pine's determination of the onset of rotational predissociation.[20] Such a detailed description of the van der Waals' potential surface cannot be obtained by any other means. The generality and simplicity inherent in the use of tunable FIR laser spectroscopy for measurement of low frequency vibrational modes in weakly bound complexes will permit spectroscopists to address a wide variety of systems, and should help to advance a new level of detail in our understanding of the nature of intermolecular forces.

ACKNOWLEDGMENTS

This work was supported by the Director, Office of Energy Research, Office of Basic Energy Sciences, Chemical Sciences Division of the U.S. Department of Energy under Contract No. DE-AC03-76F00098. The FIR laser system was funded by the National Science Foundation (Grant No. CHE-8612296).

[1] D. H. Rank, B. S. Rao, and T. A. Wiggins, J. Chem. Phys. 37, 2511 (1962).
[2] D. H. Rank, P. Sitaram, W. A. Glickman, and T. A. Wiggins, J. Chem. Phys. 39, 2673 (1963).
[3] A. W. Miziolek and G. C. Pimentel, J. Chem. Phys. 65, 4462 (1976).
[4] S. Bratož and M. L. Martin, J. Chem. Phys. 42, 1051 (1965).
[5] L. F. Keyser and G. W. Robinson, J. Chem. Phys. 44, 3225 (1966).
[6] M. T. Bowers and W. H. Flygare, J. Chem. Phys. 44, 1389 (1966).
[7] J. M. P. J. Verstegen, H. Goldring, S. Kimel, and B. Katz, J. Chem. Phys. 44, 3216 (1966).
[8] D. E. Mann, N. Acquista, and D. White, J. Chem. Phys. 44, 3453 (1966).
[9] H. Friedmann and S. Kimel, J. Chem. Phys. 44, 4359 (1966).
[10] W. G. Von Holle and D. W. Robinson, J. Chem. Phys. 53, 3768 (1970).
[11] E. W. Boom, D. Frenkel, and J. van der Elsken, J. Chem. Phys. 66, 1826 (1977).
[12] E. W. Boom and J. van der Elsken, J. Chem. Phys. 73, 15 (1980).
[13] E. W. Boom and J. van der Elsken, J. Chem. Phys. 77, 625 (1982).
[14] J. M. Farrar and Y. T. Lee, Chem. Phys. Lett. 26, 428 (1974).
[15] W. B. Neilsen and R. G. Gordon, J. Chem. Phys. 58, 4149 (1973).
[16] U. Buck and J. Schleusener, J. Chem. Phys. 75, 2470 (1981).
[17] S. E. Novick, P. Davies, S. J. Harris, and W. Klemperer, J. Chem. Phys. 59, 2273 (1973).
[18] J. M. Hutson and B. J. Howard, J. Chem. Phys. 74, 6520 (1981).
[19] S. E. Novick, K. C. Janda, S. L. Holmgren, M. Waldman, and W. Klemperer, J. Chem. Phys. 65, 1114 (1976).
[20] B. J. Howard and A. S. Pine, Chem. Phys. Lett. 122, 1 (1985).
[21] M. D. Marshall, A. Charo, H. O. Leung, and W. Klemperer, J. Chem. Phys. 83, 4924 (1985).
[22] D. Ray, R. L. Robinson, D.-H. Gwo, and R. J. Saykally, J. Chem. Phys. 84, 1171 (1986).
[23] R. L. Robinson, D. Ray, D.-H. Gwo, and R. J. Saykally, J. Chem. Phys. 87, 5149 (1987).
[24] R. L. Robinson, D.-H. Gwo, D. Ray, and R. J. Saykally, J. Chem. Phys. 86, 5211 (1987); R. L. Robinson, D.-H. Gwo, and R. J. Saykally, Mol. Phys. 63, 1021 (1988).
[25] R. L. Robinson, D.-H. Gwo, and R. J. Saykally, J. Chem. Phys. 87, 5156 (1987).
[26] S. L. Holmgren, M. Waldman, and W. Klemperer, J. Chem. Phys. 69, 1661 (1978).
[27] J. M. Hutson and B. J. Howard, Mol. Phys. 41, 1123 (1980).
[28] J. M. Hutson and B. J. Howard, Mol. Phys. 43, 493 (1981).
[29] J. M. Hutson and B. J. Howard, Mol. Phys. 45, 769 (1982).
[30] J. M. Hutson, J. Chem. Phys. 81, 2357 (1984).
[31] T. van Dam, A. Rozendaal, J. A. Vliengenthart, and F. B. van Duijneveldt (to be published).
[32] K. L. Busarow, G. A. Blake, K. B. Laughlin, R. C. Cohen, Y. T. Lee, and R. J. Saykally, Chem. Phys. Lett. 141, 289 (1987).
[33] A. Amirav, U. Even, and J. Jortner, Chem. Phys. Lett. 83, 1 (1981).
[34] K. Veeken and J. Reuss, Appl. Phys. B 38, 117 (1985).
[35] C. M. Lovejoy, M. D. Schuder, and D. J. Nesbitt, J. Chem. Phys. 85, 4890 (1986); C. M. Lovejoy and D. J. Nesbitt, Rev. Sci. Instrum. 58, 807 (1987).
[36] A. E. Beylich, 12th Int. Symp. on Rarefied Gas Dynamics, p. 710.
[37] M. Sulkes, C. Jouvet, and S. A. Rice, Chem. Phys. Lett. 87, 515 (1982).
[38] G. Dupeyrat, 12th Int. Symp. on Rarefied Gas Dynamics, p. 812.
[39] D. D. Bicanić, B. F. J. Zuidberg, and A. Dymanus, Appl. Phys. Lett. 32, 367 (1978); D. D. Bicanić, Int. J. Infrared Millimeter Waves 2, 247 (1981).
[40] K. M. Evenson, D. A. Jennings, and F. R. Petersen, Appl. Phys. Lett. 44, 576 (1984).
[41] J. Farhoomand, G. A. Blake, M. A. Frerking, and H. M. Pickett, J. Appl. Phys. 57, 1763 (1985).
[42] G. A. Blake, K. L. Busarow, R. C. Cohen, K. B. Laughlin, Y. T. Lee, and R. J. Saykally, J. Chem. Phys. (submitted).
[43] R. C. Cohen, K. L. Busarow, K. B. Laughlin, G. A. Blake, Y. T. Lee, and R. J. Saykally, J. Chem. Phys. (submitted).
[44] K. B. Laughlin, G. A. Blake, R. C. Cohen, D. C. Hovde, and R. J. Saykally, Philos. Trans. R. Soc. London Ser. A 324, 97 (1987).
[45] M. Ignuscio, G. Moruzzi, K. M. Evenson, and D. A. Jennings, J. Appl. Phys. 60, R161 (1986).
[46] H. P. Röser, E. J. Durwen, R. Wattenbach, and G. V. Schultz, Int. J. Infrared Millimeter Waves 5, 301 (1984).
[47] F. C. DeLucia, P. Helminger, and W. Gordy, Phys. Rev. A 3, 1849 (1971).
[48] E. J. Campbell and W. G. Read, J. Chem. Phys. 78, 6490 (1983).
[49] O. F. Hagena, Surf. Sci. 106, 101 (1981).
[50] R. B. Bernstein, *Chemical Dynamics via Molecular Beam and Laser Techniques*, 1st ed. (Oxford, New York, 1982), p. 32.
[51] Y. Mizugai, H. Kuze, H. Jones, and M. Takami, Appl. Phys. B 32, 43 (1983).
[52] E. W. Kaiser, J. Chem. Phys. 53, 1686 (1970).
[53] J. M. Hutson, J. Chem. Phys. (accepted).

Appendix B

"Measurement of the Perpendicular Rotation-Tunneling Spectrum of the Water Dimer by Tunable Far Infrared Laser Spectroscopy in a Planar Supersonic Jet"

Kerry L. Busarow, R.C. Cohen, Geoffrey A. Blake, K.B. Laughlin, Y.T. Lee, and R.J. Saykally

Journal of Chemical Physics **90**, 3937 (1989)

Measurement of the perpendicular rotation-tunneling spectrum of the water dimer by tunable far infrared laser spectroscopy in a planar supersonic jet

Kerry L. Busarow, R. C. Cohen, Geoffrey A. Blake,[a] K. B. Laughlin,[b] Y. T. Lee, and R. J. Saykally
Department of Chemistry and Materials and Chemical Sciences Division, University of California and Lawrence Berkeley Laboratories, Berkeley, California 94720

(Received 31 October 1988; accepted 19 December 1988)

Fifty-six transitions from the $K = 1$ lower $\rightarrow K = 2$ lower tunneling–rotation band of water dimer have been measured and assigned at 22 cm^{-1} by direct absorption spectroscopy in a cw planar supersonic jet expansion using a tunable far infrared laser spectrometer. Two different models were used to fit the data and several spectroscopic constants were determined for the upper and lower states. This work supports the local IAM model recently proposed by Coudert and Hougen for the hydrogen bond tunneling dynamics of the water dimer. This model includes four different tunneling motions, all of which contribute to the observed tunneling splittings. This is the most complicated hydrogen bonded system considered to be well understood at this time, at least in the lowest few K states.

INTRODUCTION

The water dimer is of considerable significance in chemistry and biology as a prototype for understanding local structure and hydrogen bond dynamics in condensed phases. The molecular beam electric resonance (MBER) studies of Dyke and co-workers[1–5] have provided an important initial basis for establishing a quantitative undertanding of this very complex system. In particular, the molecular structure of $(H_2O)_2$ deduced from the MBER experiments has confirmed *ab initio* predictions of a tetrahedrally bonded "*trans*-linear" ground state[6] (Fig. 1) and these results clearly evidenced the complicated nature of hydrogen exchange tunneling motions. However, progess in obtaining a more complete understanding of this important phenomenon has been severely impeded by the lack of an appropriate theoretical model for such multidimensional tunneling processes. The recent work of Coudert and Hougen[7] promises important new advances in this endeavor.

Very recently, Fourier transform microwave spectroscopy of $(H_2O)_2$ carried out by Coudert *et al.*[8] and measurements of the OH stretching vibration–rotation spectrum by Huang and Miller[9] have yielded a considerable amount of new data, supplemented by additional MBER measurements from the Dyke group.[10] Altogether, these high resolution spectroscopy experiments have produced precise measurements of over 90 rotation–tunneling transitions, and it would seem that such a large amount of data would be sufficient to characterize most of the relevant tunneling dynamics, given an appropriate theoretical formalism. In fact, this is not the case. The microwave and MBER transitions are all a-type ($\Delta K = 0$) and are restricted to sampling only one of the two principal tunneling motions, viz., the low frequency donor–acceptor tunneling. As a result, both the A rotational constant and the much larger acceptor tunneling splittings remain to be determined, and these properties are clearly essential for developing a meaningful model for the hydrogen tunneling dynamics.

In this paper we report the measurement of perpendicular ($\Delta K = +1$) rotation–tunneling transitions of $(H_2O)_2$ by a new technique developed recently at Berkeley—tunable far infrared laser spectroscopy of planar supersonic jets. Over 350 transitions have been measured in an argon–water supersonic jet expansion in the range from 510 to 835 GHz. Of these, 56 have been assigned to a rotation–tunneling band originating in the lower acceptor tunneling level of $K = 1$ and terminating at the lower acceptor tunneling level of $K = 2$. Over 85 of the remaining lines have been assigned to ArH_2O,[11] and 200 remain unassigned.

EXPERIMENTAL

The experimental apparatus has been described in detail elsewhere.[12,13] In the present experiments, conditions were identical to those in the ArH_2O study.[11] The water dimers are formed in a cw planar supersonic expansion. The nozzle is 1.5 in. long and 0.002 in. wide and is operated without temperature control. Argon is blown over water at room temperature to produce the gas mixture. Previously, the ar-

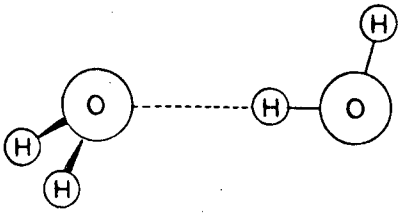

FIG. 1. The *trans*-linear structure of the water dimer

[a] Berkeley Miller Postdoctoral Fellow, present address: Center for Cosmochemistry and Geochemistry, Division of Geology and Planetary Sciences, California Institute of Technology, Pasadena, CA 91125
[b] Present address: Department of Chemistry, Massachusetts Institute of Technology, Cambridge, MA 02139

Reproduced with permission of the American Institute of Physics, 1991, and of Kerry L. Busarow, R.C. Cohen, Geoffrey A. Blake, K.B. Laughlin, Y.T. Lee, and R.J. Saykally.

gon was bubbled through the water, however, this resulted in a prohibitive amount of water being bumped into the gas manifold and signals were not consistent in time. The water was obtained from the distilled water tap and the Ar is 99.99% pure (liquid air). The expansion was typically operated with between 800 and 1000 Torr behind the nozzle and approximately 100 mTorr in the vacuum chamber, which is pumped by a 2650 cfm Roots blower. Far infrared radiation is produced with a cw tunable far infrared laser system similar to that of Pickett and co-workers.[14] Production of coherent FIR radiation occurs through nonlinear mixing of fixed frequency FIR radiation with tunable microwave radiation in a GaAs Schottky barrier diode. Linewidths observed are approximately 400 kHz (FWHM), resulting from residual Doppler broadening in the planar jet.

The precision of the frequency measurement is approximately 1 MHz, resulting from the necessity of shifting the fixed frequency FIR laser slightly to determine which sideband is responsible for a given absorption. The FIR laser is then reset to the maximum of the gain curve. This is a rather imprecise procedure. When we carefully calibrate each line with a known reference, we can obtain uncertainties of less than 50 kHz,[13] however, this is a painstaking process for a large number of lines, and it is seldom that the available models require that high a level of precision.

The typical signal to noise ratio in the water dimer spectra is less than 50, with a time constant of 300 ms. For other van der Waals clusters, such as ArH_2O, ArHCl, and $(HCl)_2$, under similar conditions, S/N of >1000 was achieved. This indicates that the perpendicular dipole moment of water dimer is quite small, assuming that we are producing a similar density of dimers, in agreement with the MBER results of Dyke and co-workers.[4]

ANALYSIS

The rotation–tunneling energy level diagram for the water dimer is explained in the papers of Coudert *et al.*[8] and by Odutola *et al.*[10] and will only be discussed here as is necessary to describe the assignment of the far infrared spectra. The equilibrium structure of water dimer is the *trans*-linear form, determined from the experimental work of Dyke and co-workers,[4] in agreement with theoretical predictions[6] (Fig. 1). It contains a single nearly linear hydrogen bond, with a strength of approximately 5 kcal/mol, and has a plane of symmetry (C_s). The A rotational constant is estimated to be approximately 6 cm^{-1}, and B and C are ~6 GHz (0.2 cm^{-1}).

There are several different types of feasible proton tunneling motions considered in this model. The first, which Coudert *et al.* refer to as a 1→4 tunneling,[8] involves the exchange of the two hydrogens on the acceptor molecule. We will refer to this as the *acceptor* tunneling. The numbers 1 and 4 refer to tunneling between the frameworks 1 and 4 of the eight possible frameworks for water dimer as labeled by Coudert *et al.*[8] (Fig. 2). No hydrogen bond is broken in this exchange. The second tunneling motion, referred to by Coudert *et al.* as a 1→5,6 tunneling, or a geared internal rotation, exchanges the donor proton involved in the hydrogen bond with a proton from the acceptor molecule. Hence, we refer to

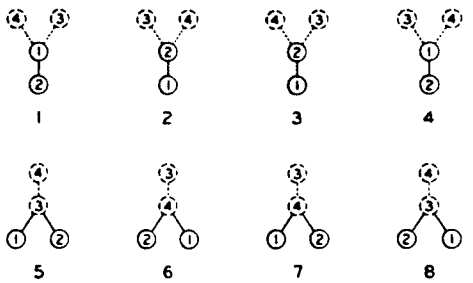

FIG. 2: The eight equivalent frameworks for the water dimer from Coudert *et al.* (Ref. 8) are used to label the various tunneling motions between frameworks. In this representation, the oxygen atoms are not shown, only the hydrogens, labeled 1 through 4. The dashed lines indicate the hydrogens are behind the plane of the figure and solid lines indicate the hydrogens are above the plane.

this as the *geared donor–acceptor* tunneling. In this tunneling motion, the roles as hydrogen acceptor and donor are reversed. This motion does involve breaking and reforming the hydrogen bond and is analogous to the trans geared motion in $(HF)_2$.[15] The donor–acceptor tunneling leads to a splitting of each rotational state into four levels, two of which are degenerate, thereby resulting in three actual levels for each value of J (for $K = 0$). The overall tunneling splitting associated with this motion is 19 GHz for $K = 0$.[10] The acceptor tunneling motion causes an additional doublet splitting of all these levels. Because this motion does not involve any bond breakage, it is expected to result in a considerably larger tunneling splitting than the geared donor–acceptor tunneling; Coudert *et al.*[8] have estimated it to be 6 cm^{-1} for $K = 0$. Therefore, for each J in $K = 0$, there are six levels, two of which are doubly degenerate (the E states). An additional possible tunneling motion is the 1→2 tunneling, also called a geared inversion. Although the 1→4 and the 1→5 tunneling motions split the levels into the maximum number of levels allowed by the group theory (into six states for each J), the 1→2 tunneling can cause an additional shift in the energy of these states. Coudert and Hougen[7] have proposed that for K even states, the A/B states would be shifted upward relative to the energies from the other two tunneling splittings, and the E states would be pushed down, where for K odd, the levels would shift in the opposite direction. The extent of the perturbation due to the 1→2 tunneling on the energy of the states is yet to be determined. One final tunneling motion considered by Coudert and Hougen is the 1→7 or the antigeared donor–acceptor tunneling, analogous to an antigeared motion in $(HF)_2$. This tunneling would also cause a shift in the energies and would result in slightly different selection rules. For the present discussion, we will ignore the 1→7 tunneling and assume that the 1→2 tunneling need not be explicitly considered because it will result in a systematic shift of all the lines that we measure. Although the E state transitions would be shifted in the opposite direction, we have not observed these transitions due to their low population in the jet, as will be discussed below. The 1→2 tunneling, however, most likely plays a significant

role in the observed transition frequencies. Therefore, for $K = 0$ there exist six levels. For each value of J, the lower set of three levels, which we will henceforth refer to as "$K = 0$ lower," and the upper set of three levels, "$K = 0$ upper," are separated by the acceptor tunneling splitting ($\sim 6\ \mathrm{cm}^{-1}$). For $K \neq 0$, there is an additional splitting caused by the asymmetry doubling. This asymmetry splitting is significantly smaller than the other two tunneling splittings, such that for $K \neq 0$, there will be twelve levels for each value of J, six lower levels and six upper levels. An energy level diagram is shown in Fig. 3, including the two lowest rotational states for each value of K. The asymmetry splitting is not shown on this diagram because it is too small to be visible on this scale.

In the present work, we have measured transitions from the $K = 1$ lower states to the $K = 2$ lower states (Fig. 3). Coudert *et al.*[8] point out that they had made an arbitrary choice between two different possible schemes for labeling the state symmetries in $K \neq 0$, due to the ambiguity in the sign of the asymmetry splitting. The experimental results then available could not establish which of these was correct. The recent work of Huang and Miller[9] demonstrated that their choice was incorrect, based on the relative intensities of the observed lines (the statistical weights for the $A_2^{\pm}$ and $B_2^{\pm}$ states are three and six, respectively). Our work confirms this conclusion. In Fig. 4 we present spectra for two transitions originally labeled $Q(3)A_2^+$ and $Q(3)B_2^-$ by Coudert *et al.* However, the 2:1 intensity ratio clearly indicates that these labels should be switched, in agreement with Huang and Miller. It is difficult to measure intensity ratios over a large frequency range on this spectrometer due to laser power fluctuations. However, the fluctuation in laser power decreases for closely spaced transitions and in the case of Q branch transitions, we believe that these intensity measurements are quite reliable.

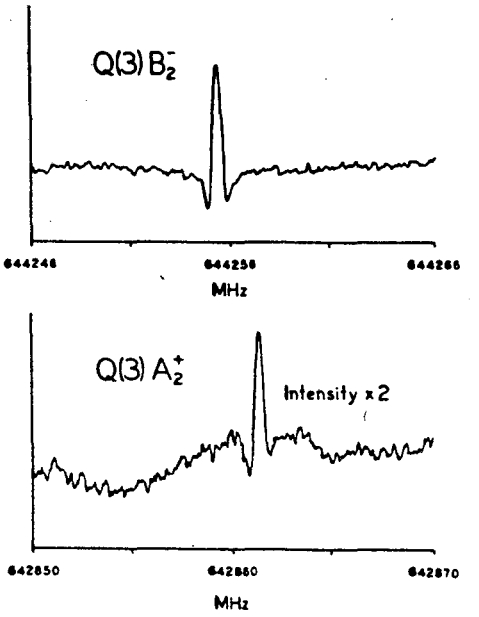

FIG. 4. A comparison of the intensities for two of the $Q(3)$ transitions. The upper scan is B_2^- symmetry, spin weight equal to six, and the lower scan is A_2^+ symmetry, spin weight equal to three. The lower scan intensity is multiplied by a factor of 2.

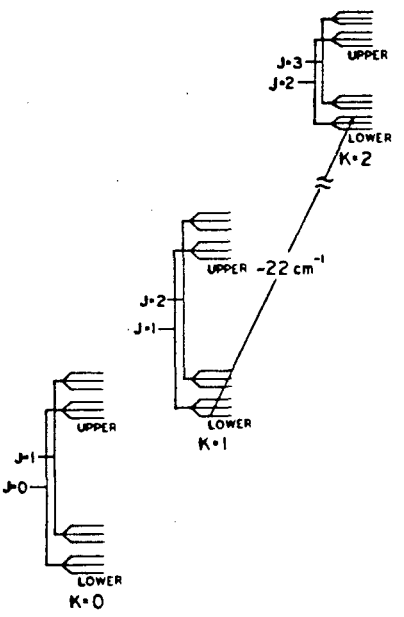

FIG. 3. The energy level diagram for the water dimer including the two lowest rotational states for each K. The asymmetry splittings for $K = 1$ and 2 are not shown. The splitting between the states labeled "lower" and "upper" is the result of the $1 \rightarrow 4$ (acceptor) tunneling. The smaller triplet splitting is the result of the $1 \rightarrow 5$ (greated donor–acceptor) tunneling.

Given the triplet level structure of each J state resulting from the donor–acceptor tunneling splitting (ignoring the asymmetry splitting), one expects to observe three bands slightly shifted from one another, each exhibiting P, Q, and R branches. In our spectra, however, only two bands are observed, with Q branches at 644 and 670 GHz. We find no transitions originating from the $E^{\pm}$ states. This results from the fact that in the cold jet expansion, the population in the $E^{\pm}$ states can relax to the $K = 0$ lower $E^{\pm}$ states. The other states, of $A_2^{\pm}$ and $B_2^{\pm}$ symmetry, can only relax to the $K = 0$ upper state because of the selection rules, $A_2 \leftrightarrow A_2$ and $B_2 \leftrightarrow B_2$. Coudert and co-workers[8] were the first to assign transitions originating in $K = 1$ lower in a cold jet, and because they observed transitions in $K = 0$ upper as well, they proposed that the $K = 0$ upper and $K = 1$ lower levels must be nearly degenerate for there to be significant population in both states in the 1 K supersonic expansion. Based on this assumption, they proposed that the $K = 0$ lower to $K = 0$ upper splitting (the acceptor tunneling splitting) was 6 cm^{-1}, assuming that $A = 6\ \mathrm{cm}^{-1}$. As in the present spectra, Coudert and co-workers only observed $A_2^{\pm}/B_2^{\pm}$ transitions

TABLE I. Frequencies for transitions from $K = 1$ lower to $K = 2$ lower in $(H_2O)_2$. Calculated frequencies are determined from the constants of the first two fits shown in Table II. Transitions are labeled by the symmetry and rotational level of the initial state. The lower band originates in the lower pairs of K-type doublets of $K = 1$ lower and terminates in the upper pairs of K-type doublets of $K = 2$ lower. The upper band originates in the upper pairs of K-type doublets of $K = 1$ lower and terminates in the lower pairs of K-type doublets in $K = 2$ lower. The last four transitions in each band are calculated from observed microwave transitions of Coudert *et al.* (Ref. 8). All frequencies are in MHz.

	Lower band $K = 1$ lower $\rightarrow K = 2$ lower		
Transition	Observed frequency	Calculated frequency	Obs.-calc.
$P(5)B_2^+$	607 247.3	607 240.0	7.3
$P(5)A_2^-$	610 301.8	610 305.1	−3.3
$P(4)B_2^+$	622 426.4	622 427.6	−1.2
$P(3)B_2^+$	633 305.1	633 310.8	−5.7
$P(3)A_2^-$	634 590.0	634 589.0	1.0
$Q(7)B_2^+$	666 904.4	666 913.6	−9.2
$Q(6)A_2^-$	667 883.5	667 873.6	9.9
$Q(6)B_2^+$	672 042.4	672 043.2	−0.8
$Q(5)B_2^+$	668 777.2	668 769.1	8.1
$Q(5)A_2^-$	671 832.6	671 834.3	−1.7
$Q(4)A_2^-$	669 565.3	669 566.6	−1.3
$Q(4)B_2^+$	671 659.4	671 658.4	1.0
$Q(3)B_2^+$	670 232.4	670 238.3	−5.9
$Q(3)A_2^-$	671 519.8	671 516.5	3.3
$Q(2)A_2^-$	670 757.1	670 761.6	−4.5
$Q(2)B_2^+$	671 414.8	671 409.4	5.4
$R(1)B_2^+$	695 741.2	695 740.3	0.9
$R(1)A_2^-$	695 963.1	695 958.1	5.0
$R(2)A_2^-$	707 684.0	707 689.1	−5.1
$R(2)B_2^+$	708 339.2	708 336.9	2.3
$R(3)B_2^+$	719 463.0	719 469.1	−6.1
$R(3)A_2^-$	720 749.1	720 747.3	1.8
$R(4)A_2^-$	731 095.0	731 095.8	−0.8
$R(4)B_2^+$	733 185.6	733 187.5	−1.9
$R(5)B_2^+$	742 598.5	742 590.3	8.2
$R(5)A_2^-$	745 652.1	745 655.5	−3.4
$R(6)B_2^+$	758 144.0	758 149.0	−5.0
$R(7)B_2^+$	765 293.9	765 295.3	−1.4
$R(8)B_2^+$	783 204.9	783 201.8	3.1
$K = 1$ lower			
$J = 1B_2^+ \rightarrow J = 2B_2^+$	24 327.462	24 330.8	−3.3
$J = 1A_2^- \rightarrow J = 2A_2^-$	25 206.003	25 196.5	9.5
$J = 2A_2^- \rightarrow J = 3A_2^-$	36 164.855	36 172.6	−7.7
$J = 2B_2^+ \rightarrow J = 3B_2^+$	38 108.343	38 098.6	9.7

	Upper band $K = 1$ lower $\rightarrow K = 2$ lower		
Transition	Observed frequency	Calculated frequency	Obs.-calc.
$P(4)B_2^-$	592 927.3	592 934.0	−6.7
$P(3)B_2^-$	607 318.0	607 315.6	2.4
$Q(8)B_2^-$	638 504.6	638 535.6	−31.0
$Q(7)A_2^+$	639 522.6	639 491.4	31.1
$Q(6)B_2^-$	640 478.9	640 447.9	31.0
$Q(5)A_2^+$	641 367.0	641 357.2	9.8
$Q(5)B_2^-$	644 611.4	644 610.9	0.5
$Q(4)B_2^-$	642 167.6	642 178.1	−10.5
$Q(4)A_2^+$	644 412.4	644 415.1	−2.7
$Q(3)A_2^+$	642 859.2	642 876.2	−17.0
$Q(3)B_2^-$	644 253.0	644 251.0	2.0
$Q(2)B_2^-$	643 415.8	643 423.9	−8.1
$Q(2)A_2^+$	644 133.3	644 123.5	9.8
$R(1)A_2^+$	668 437.5	668 425.3	12.2
$R(1)B_2^-$	668 681.7	668 661.2	20.5
$R(2)B_2^-$	680 351.9	680 359.3	−7.4
$R(2)A_2^+$	681 070.0	681 059.0	11.0
$R(3)A_2^+$	692 100.3	692 120.3	−20.0

TABLE I. (continued).

Transition	Upper band $K = 1$ lower $- K = 2$ lower		
	Observed frequency	Calculated frequency	Obs.-calc.
$R(3)B_2^-$	693 494.4	693 495.1	− 0.7
$R(4)B_2^-$	703 712.5	703 728.2	− 15.7
$R(4)A_2^+$	705 953.9	705 965.2	− 11.3
$R(5)A_2^+$	715 212.8	715 210.0	2.8
$R(5)B_2^-$	718 448.9	718 463.6	− 14.7
$R(6)B_2^-$	726 612.7	726 599.4	13.3
$R(6)A_2^+$	730 972.8	730 983.2	− 10.4
$R(7)A_2^+$	737 936.0	737 936.8	− 0.8
$R(7)B_2^-$	743 526.1	743 515.7	10.4
$K = 1$ lower			
$J = 1A_2^+ \rightarrow J = 2A_2^+$	24 300.784	24 301.7	− 0.9
$J = 1B_2^- \rightarrow J = 2B_2^-$	25 263.115	25 237.3	25.8
$J = 2B_2^- \rightarrow J = 3B_2^-$	36 097.344	36 108.3	− 11.0
$J = 2A_2^+ \rightarrow J = 3A_2^+$	38 209.060	38 182.8	26.3

and assumed that the $E^{\pm}$ state population had thermally relaxed. Our planar supersonic jet expansion is nearly as cold, yielding a jet temperature of 3 K for ArHCl.[13] Under warmer conditions, the E states are observable, as reported by Dyke and co-workers,[2-4] who have measured E state transitions up to $K = 4$.

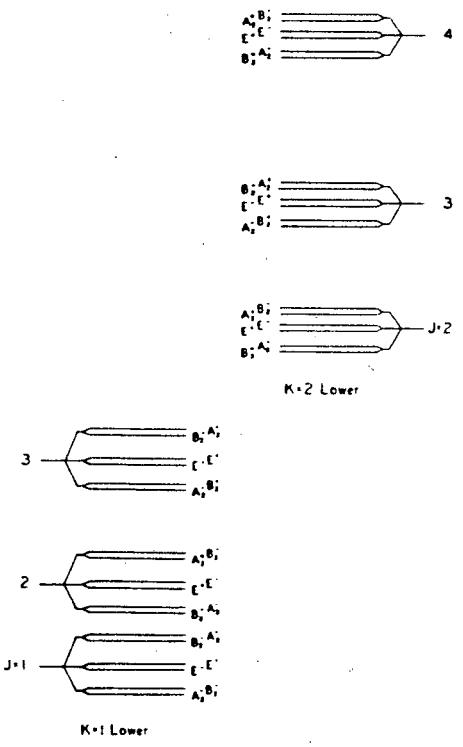

FIG. 5. The energy level diagram for the $K = 1$ lower and $K = 2$ lower states. For $(H_2O)_2$, the nuclear spin statistical weights are three for A_2 and E states and six for B_2 states.

The 56 rotation–tunneling transitions assigned in this work are listed in Table I and a detailed energy level diagram is shown in Fig. 5. We were able to assign the lowest J states from combination differences calculated from measured transitions in $K = 1$ lower from the work of Coudert *et al.*[8] A large number of lines were measured, with essentially no recognizable pattern, and without these combination differences the assignment would have been very difficult. Coudert and Hougen[16] have recently developed a model in which they can include both pure rotational transitions and tunneling–rotational transitions in a combined fit. They included our initial assignments in their fit, along with the microwave data, and they provided us with predictions for higher J transitions. We were subsequently able to either assign new lines from the large number of unassigned spectra, or we went back and searched for new predicted lines. In this way, transitions were eventually assigned as high as $Q(8)$ and $R(8)$. However, the intensity of the P branch was significantly lower and we were not able to measure transitions to as high in J. The assignment of $K = 1$ lower as the initial state of these transitions was confirmed by microwave combination differences, which matched to within 2 MHz. For the upper state assignment, there were no combination differences available, and we were not able to determine independently whether it was actually $K = 2$ lower or upper. Based only on the fit of Coudert and Hougen, we assign the upper state as $K = 2$ lower. Determination of the sign of the asymmetry doubling in $K = 2$ lower was unambiguous, given the ordering of the $K = 1$ lower states.

The model used here in fitting the present data set is rather simplistic. Because Coudert and Hougen have now developed a much more sophisticated model, it does not seem worthwhile to expend a great deal of effort in improving our model. As discussed previously, in $K = 1$ lower, there are three pairs of levels for each J. One pair is made up of the two E states, which were not observed in these experiments. Therefore, two pairs of K-type doublets are observed for each J, split by the geared donor–acceptor tunneling mo-

TABLE II. Fits in which the lower and upper bands are fit independently as two asymmetric vibration–rotation bands. Those constants not listed were set to zero in the fit. Uncertainties are 1σ.

Lower band	Upper band
$(B'' + C'')/2 = 6192.2(4)$ MHz	$(B'' + C'')/2 = 6194.3(10)$ MHz
$(B'' - C'') = 218.8(4)$ MHz	$(B'' - C'') = 238.7(10)$ MHz
$D_J'' = 0.163(7)$ MHz	$D_J'' = 0.133(12)$ MHz
$d_1'' = -0.121(2)$ MHz	$d_1'' = -0.178(7)$ MHz
$(B' + C')/2 = 6155.5(6)$ MHz	$(B' + C')/2 = 6155.3(11)$ MHz
$D_J' = 0.052(5)$ MHz	$\nu = 62\,437.5(69)$ MHz
$\nu = 89\,731.6(26)$ MHz	A(fixed) = 200 000 MHz
A(fixed) = 200 000 MHz	
Standard deviation = 5.9 MHz	Standard deviation = 17.4 MHz

tion. In the present analysis, the transitions originating from the lower pairs of K-type doublets are treated as a vibration–rotation band, and the transitions from the upper pairs of K-type doublets are treated as a second such band. In Table I, lines originating from the lower pairs of states are designated the lower band, and those originating from the upper pairs are designated the upper band. Each band is then fit to a Watson S-reduced Hamiltonian. The vibration in this case, is actually the difference of the acceptor tunneling splittings in $K = 1$ and 2. The approximate frequency for these two bands is then

$$3A + 1/2\nu_{\text{tun}}(K = 1) - 1/2\nu_{\text{tun}}(K = 2),$$

where, in this fit, the sum of the second two terms is the effective vibrational frequency. This is not to imply that the value of A is uniquely determined, however, we assume that it has the proposed value of 6 cm^{-1}. The only quantity actually determined is the sum of the three terms, which is approximately 22 cm^{-1}.

The two vibrational bands were fit separately and the results are shown in Table II. The higher frequency band centered at 670 GHz consisted of the transitions from the lower pairs of states in $K = 1$ lower (A_2^-/B_2^+ symmetry) to the upper pairs of levels in $K = 2$ lower (A_2^+/B_2^- symmetry). Figure 6 contains a plot of the lines observed in this band as well as a characteristic spectrum of one of the transitions. The lower frequency band centered at 644 GHz consisted of the transitions from the upper pairs in $K = 1$ lower (A_2^+/B_2^-) to the lower pairs in $K = 2$ lower (A_2^-/B_2^+). Figure 7 contains a plot of the lines observed as well as a characteristic spectrum of one of the transitions. Also included in the fits of these two bands are several combination differences calculated from the microwave measurements of Coudert *et al.*[8] The difference in frequency between the two bands is the sum of the donor-acceptor tunneling splittings for $K = 1$ lower and $K = 2$ lower, approximately 26 GHz. For the $J = 1$ state of $K = 1$ lower, this splitting has been measured to be 16 GHz; therefore, for $K = 2$ lower it is 10 GHz. The corresponding measured splitting for $K = 0$ lower is 19 GHz.[10]

Fitting these transitions as two vibrational bands is a very simplistic approach and does not explicitly account for

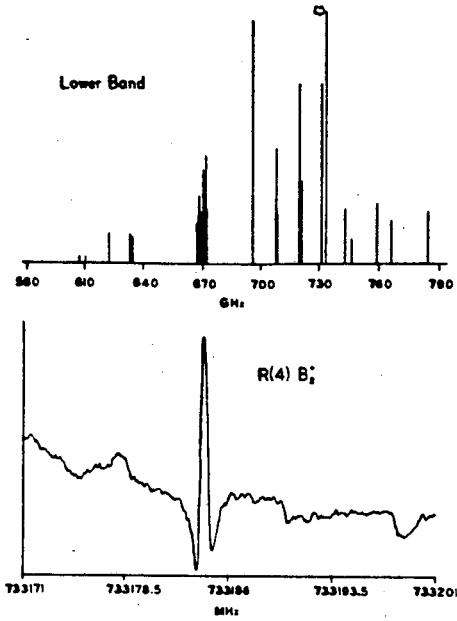

FIG. 6. The upper plot is a stick spectrum of the 670 GHz band for $K = 1$ lower $-K = 2$ lower, with the observed intensities. Below is shown a scan of the $R(4)\ B_2^+$ transition, marked with an arrow in the stick spectrum.

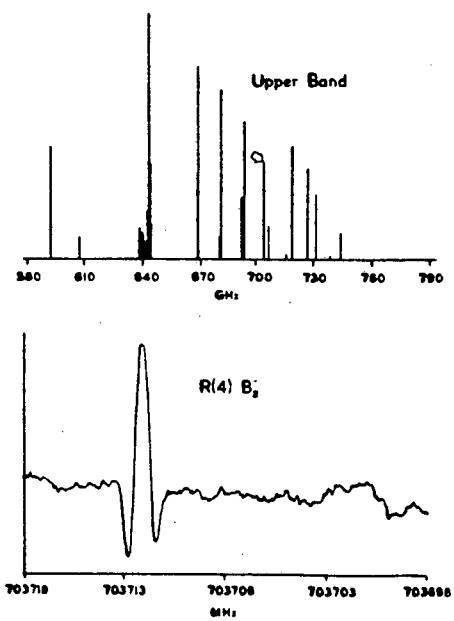

FIG. 7. The upper plot is the stick spectrum for the 644 GHz band of the $K = 1$ lower $-K = 2$ lower, with the observed intensities. Below is shown a scan of the $R(4)B_2^-$ transition, marked with an arrow in the stick spectrum

TABLE III. Fit in which all transitions are fit as a single band including the geared donor–acceptor tunneling splitting. Those constants not listed were set to zero in the fit. Uncertainties are 1σ.

$(B^{\prime\prime}+C^{\prime\prime})/2 = 6190.2(17)$ MHz
$(B^{\prime\prime}-C^{\prime\prime}) = 228.3(17)$ MHz
$\nu_{1,2}^{\prime\prime} = 16\,225(13)$ MHz
$D_J^{\prime\prime} = 0.092(15)$ MHz
$d_1^{\prime\prime} = -0.152(9)$ MHz
$(B^{\prime}+C^{\prime})/2 = 6153.7(17)$ MHz
$\nu_{1,2}^{\prime} = 11\,083(17)$ MHz
$\nu = 76\,072(13)$ MHz
A(fixed) = 200 000 MHz
Standard deviation = 40.9 MHz

the J dependence of the geared donor-acceptor tunneling splitting or the correlation between the rotational constants in the various states. As would be expected, the fit is good for low J (up to approximately $J=4$), with a few MHz standard deviation, but at higher J it deteriorates rapidly. This implies that even for the low J fit, the centrifugal distortion constants are of limited value because they are most likely shifted by the J dependence of the tunneling splitting. It is interesting to note that the higher frequency band, that originating from the lower pair of states, fits much better. A fit was obtained for this entire band with a standard deviation of less than 6 MHz, where for the lower frequency band, the best fit obtained was worse by a factor of three.

A second fit was attempted in which all of the data were fit in a single band, by including a tunneling term in the energy expressions for the upper and lower states. This tunneling term then represents the effective geared donor-acceptor tunneling splitting. Those transitions assigned to the lower band are given a tunneling quantum number equal to -1 and those in the upper band are $+1$. In this fit, an attempt was made to also fit the J dependence of this tunneling; however, it could not be determined. Only a constant tunneling term was determined for $K=1$ lower and $K=2$ lower. The results of this fit are shown in Table III. The large standard deviation of the fit (40 MHz) indicates that this is still a grossly oversimplified model for the energy level spacings of the water dimer. However, the analysis is carried out in terms of a single band fit, unlike the first method and a value for the donor–acceptor tunneling splitting is determined for each K state.

One important observation that may be deduced from the results of the fits is that the use of the high barrier approximation in the model of Hougen and Coudert is supported, at least for the states included in the present data set. A comparison of the rotational constants for the lower and upper bands in each K indicates that they are identical within the quoted statistical uncertainties, as expected in the high barrier limit.

There are several possibilities for future work on this project. The first of which would be to measure other rotation-tunneling bands. However, the only allowed transition expected to be sufficiently populated in a supersonic jet is the $K=0$ lower $\rightarrow K=1$ upper band. This band is predicted to be at approximately 12 cm^{-1}. In that band, unlike that studied in this paper, the E state transitions, as well as the A_1 transitions, would be observed, which would improve the model and result in a better understanding of the relative contribution of the various tunneling motions to the overall energy level structure. An alternative direction in the study of water dimer is to search for an intermolecular vibrational band. The lowest predicted vibration is the torsion about the acceptor molecule C_2 axis. The lowest energy prediction for this vibration is approximately 80 cm^{-1}, others are as high as 130 cm^{-1}.[17] A third logical step is to attempt to study larger clusters such as the water trimer. We presently have over two hundred lines that are unassigned, many of which are in regions where one would not expect to find dimer transitions, if our understanding of that system is correct. It is very possible that these lines may be due to the trimers, $Ar_2(H_2O)$, $Ar(H_2O)_2$ or $(H_2O)_3$. The water trimer itself is a very complicated system about which very little is known. It has been deduced from deflection experiments[1] that it is only slightly polar and therefore most likely cyclic, having three hydrogen bonds. There is no assigned high resolution spectroscopic data available. Some work has been done on the permutation-inversion theory for water trimer.[18] Our current understanding of water dimer and similar clusters should prove very helpful in assigning the trimer spectrum.

ACKNOWLEDGMENTS

This work was supported by the Director, Office of Energy Research, Office of Basic Energy Sciences, Chemical Sciences Division of the U.S. Department of Energy under Contract No. DE-AC03-76SF00098. The FIR laser system was funded by the National Science Foundation (Grant No. CHE-8612296). We thank Dr. J. T. Hougen and Dr. L. H. Coudert for their interest and guidance in this project.

[1] T. R. Dyke and J. S. Muenter, J. Chem. Phys. 57, 5011 (1972).
[2] T. R. Dyke and J. S. Muenter, J. Chem. Phys. 60, 2929 (1974).
[3] T. R. Dyke, J. Chem. Phys. 66, 492 (1977).
[4] T. R. Dyke, K. M. Mack, and J. S. Muenter, J. Chem. Phys. 66, 498 (1977).
[5] J. A. Odutola and T. R. Dyke, J. Chem. Phys. 72, 5062 (1980).
[6] L. A. Curtiss and J. A. Pople, J. Mol. Spectrosc. 55, 1 (1975).
[7] L. H. Coudert and J. T. Hougen, J. Mol. Spectrosc. 130, 86 (1988).
[8] L. H. Coudert, F. J. Lovas, R. D. Suenram, and J. T. Hougen, J. Chem. Phys. 87, 6290 (1987).
[9] Z. S. Huang and R. E. Miller, J. Chem. Phys. 88, 8008 (1988).
[10] J. A. Odutola, T. A. Hu, D. Prinslow, S. E. O'dell, and T. R. Dyke, J. Chem. Phys. 88, 5352 (1988).
[11] R. C. Cohen, K. L. Busarow, K. B. Laughlin, G. A. Blake, M. Havenith, Y. T. Lee, and R. J. Saykally, J. Chem. Phys. 89, 4494 (1988).
[12] K. L. Busarow, G. A. Blake, K. B. Laughlin, R. C. Cohen, Y. T. Lee, and R. J. Saykally, J. Chem. Phys. 89, 1268 (1988).
[13] K. B. Laughlin, G. A. Blake, R. C. Cohen, D. C. Hovde, and R. J. Saykally, Phil. Trans. R. Soc. London Ser. A 324, 97 (1987).
[14] J. Farhoomand, G. A. Blake, M. A. Frerking, and H. M. Pickett, J. Appl. Phys. 57, 1763 (1985).
[15] T. R. Dyke, B. J. Howard, and W. Klemperer, J. Chem. Phys. 56, 2442 (1972); J. T. Hougen and N. Ohashi, J. Mol. Spectrosc. 109, 134 (1985).
[16] Coudert and Hougen fit (to be published).
[17] M. J. Frisch, J. A. Pople, and J. E. Del Bene, J. Phys. Chem. 89, 3664 (1985); R. D. Amos, Chem. Phys. 104, 145 (1986).
[18] K. Balasubramanian and T. R. Dyke, J. Phys. Chem. 88, 4688 (1984).

Appendix C: Unassigned Lines in an Argon/Water Expansion

In the course of our scanning for $(H_2O)_2$ and ArH_2O, we also observed 260 lines which remain unassigned. These lines are listed in Table C.1 with the intensities. A stick spectrum of these lines is shown in Figure C.1. Several approaches, which were used in attempting to assign some of these lines, will be discussed.

Combination differences are very useful in identifying spectral features associated with the same ground or excited state. The concept is simple. In a given perpendicular band, regardless of whether it is a vibration-rotation or tunneling-rotation band, the differences between certain pairs of lines is going to be identical. For example, the frequency difference between R(2) and Q(3) exactly equals the difference between Q(2) and P(3). That difference is simply the energy difference between J=2 and 3 in the lower state. One method for using the combination differences is to write a simple computer program which takes the difference between the first two lines of the list and determines if that difference occurs between any other pairs of lines. If a match is found, these pairs are tabulated. Then the difference between the first and third lines is searched and so on. The hope is that certain patterns can be picked out with this additional information. Unfortunately, in our case, the line density is so high that there were an enormous number of matches found for nearly every difference. It was simply not possible to sort out any

Table C.1 Unassigned lines observed in an Ar/H_2O expansion. The intensities are given in arbitrary units.

487.963	50
488.423	50
488.667	50
489.695	50
490.211	50
490.504	50
491.702	50
493.566	50
494.166	50
495.430	50
495.632	50
497.606	50
513.694	24
514.810	10
515.193	21
515.289	17
516.039	27
516.194	30
517.147	28
517.162	14
518.261	19
520.252	22
520.905	18
522.6526	49
523.2807	30
523.2883	43
523.3349	48
524.8191	57
525.8313	82
526.6438	33
527.4201	15
527.5351	25
527.6510	76
527.7115	7
527.8206	12
528.5424	56
528.8437	74
529.2862	66
529.5960	47
530.0223	73
530.1856	43
531.2047	25
531.2675	75
531.2788	67
532.4266	31
544.8256	17
545.1110	34
546.836	88
566.811	50
618.4785	12
621.5249	27
621.8328	30
623.2433	15
623.7480	41
623.7839	12
632.9236	8
632.3335	15
632.8827	28
633.3374	26
633.4673	10
633.4854	14
633.5434	56
634.1901	20
635.2246	20
636.2037	13
636.5988	12
642.5056	6
642.6162	10
642.7600	9
642.9194	52
644.0481	7
646.0293	8
646.0336	10
654.302	50
655.182	14
655.173	7
655.177	12
655.178	9
668.4523	80
670.2630	21
679.890	100
683.7886	52
697.4673	25
700.344	5
705.775	14
717.178	13
718.447	72
718.627	50
727.7160	52
727.8012	40
728.532	13
728.6739	90
730.0631	56
730.1480	60
733.1874	125
736.4478	13
737.7341	29
737.7713	24
737.8791	11
738.556	50
738.9085	9
739.1944	29
740.0095	14
750.6991	20
750.8119	19
756.8987	11
757.0590	12
757.2591	14
765.8022	36
765.8554	12
766.3415	30
767.0053	46
767.9452	30
768.0328	22
768.2146	22
768.3942	26
768.8673	30
769.0847	48
772.0346	12
774.6973	13
774.7021	48
774.7339	14
776.2876	38
777.2069	46
778.2040	108
779.6083	48
780.4732	95
781.3217	26
781.6588	14
781.6675	20
781.7224	28
781.7507	40
781.8465	95
782.1088	46
782.3331	40
782.6219	24
782.8926	32
782.8803	28
783.0844	30
783.4873	48
783.5394	54
783.7465	74
783.8973	56
783.9463	34
784.2022	9
784.2037	50
784.2759	23
784.5758	83
784.6787	94
784.7831	33
784.8140	15
784.9313	61
785.0073	69
785.1043	50
785.1075	42
785.2529	52
785.3423	53
785.4576	37
785.5530	55
785.9157	52
786.0257	42
786.0561	66
787.1228	35
787.3143	29
787.5200	27
787.5349	34
788.0689	44
788.6610	40
791.189	50
793.736	50
811.2123	10
818.8666	7
819.2333	14
820.2371	8
821.5208	8
822.2980	16
822.3735	8
823.5452	10
824.2780	16
825.5943	22
829.4856	27
829.5119	29
832.4594	24
832.6750	25
833.4145	15

Figure C.1 The stick spectrum of the unassigned lines observed in an Ar/H_2O expansion. The intensities are in arbitrary units.

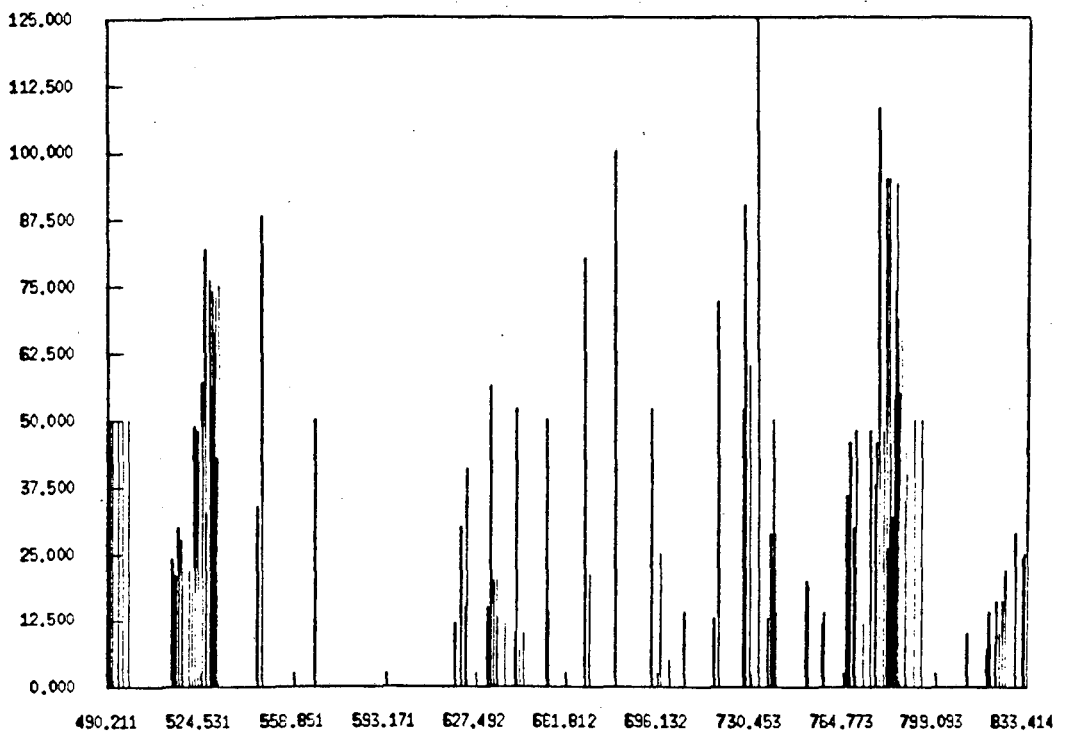

kinds of patterns from so many matches.

A second computer program was written, which was similar, but the concept was even simpler. The idea was to simply to take the difference between every possible pair of lines in the list and count how many occurred within a certain small range. For example, there may have been 24 differences between 100 and 110 MHz and 34 differences between 110 and 120 MHz. These results could then be plotted as a histogram. The goal of this method is to find certain ranges which have significantly higher counts than the others. The assumption is that this difference may be close to twice the rotational constant. In Table C.2 is the histogram for the differences of 1-11.5 GHz for the unassigned lines in the range of 550 to 840 GHz. The actual number of differences associated with each asterisk is unknown, but was scaled to keep the graph on the page. It is difficult to see exactly what is a significant deviation from the background. It appears that in the range of 8.9 to 9.2 GHz there is a somewhat larger signal. It is not clear to which cluster this could be attributed.

A third approach was to predict the spectra of a number of argon-water clusters. Again, with such a large number of lines, we were not expecting a direct match with our observed spectrum, but were instead, concerned primarily with the line density expected for the various clusters. In particular, we were looking for a cluster that could be responsible for the enormous line density near 780 GHz.

Table C.2 The histogram of line differences between 1 and 11.5 GHz

```
1.0 - 1.1      ************************************
1.1 - 1.2      *********************************
1.2 - 1.3      ************************************
1.3 - 1.4      **********************
1.4 - 1.5      *********************
1.5 - 1.6      **********************
1.6 - 1.7      ************************
1.7 - 1.8      ****************************
1.8 - 1.9      *********************
1.9 - 2.0      **********************************
2.0 - 2.1      ****************************
2.1 - 2.2      ****************************
2.2 - 2.3      *********************
2.3 - 2.4      ****************************
2.4 - 2.5      ***************************
2.5 - 2.6      **********************
2.6 - 2.7      *********************
2.7 - 2.8      *****************
2.8 - 2.9      **********************
2.9 - 3.0      *******************
3.0 - 3.1      ****************************
3.1 - 3.2      *****************************
3.2 - 3.3      **********************
3.3 - 3.4      ************************
3.4 - 3.5      **********************
3.5 - 3.6      ***************
3.6 - 3.7      ****************
3.7 - 3.8      ***************
3.8 - 3.9      **************
3.9 - 4.0      ************
4.0 - 4.1      **************
4.1 - 4.2      *****************
4.2 - 4.3      *****************
4.3 - 4.4      ************
4.4 - 4.5      **************
4.5 - 4.6      **************
4.6 - 4.7      *******
4.7 - 4.8      *****
4.8 - 4.9      ************
4.9 - 5.0      *********
5.0 - 5.1      ***********
5.1 - 5.2      **********
5.2 - 5.3      ***********
5.3 - 5.4      *******************
5.4 - 5.5      *********
5.5 - 5.6      ***************
5.6 - 5.7      **************
```

```
5.7 - 5.8       **************
5.8 - 5.9       ********
5.9 - 6.0       ******
6.0 - 6.1       ********
6.1 - 6.2       **********
6.2 - 6.3       ***************
6.3 - 6.4       **********
6.4 - 6.5       ***********
6.5 - 6.6       *******
6.6 - 6.7       **********
6.7 - 6.8       ******
6.8 - 6.9       ****************
6.9 - 7.0       *************
7.0 - 7.1       ********
7.1 - 7.2       *****
7.2 - 7.3       *****
7.3 - 7.4       *******
7.4 - 7.5       ***********
7.5 - 7.6       **********
7.6 - 7.7       *******
7.7 - 7.8       ********
7.8 - 7.9       ************
7.9 - 8.0       ***
8 0 - 8.1       ***********
8.1 - 8.2       ***
8.2 - 8.3       **************
8.3 - 8.4       *****
8.4 - 8.5       ********
8.5 - 8.6       **
8.6 - 8.7       **********
8.7 - 8.8       *****************
8.8 - 8.9       ******
8.9 - 9.0       *****************
9.0 - 9.1       **************************
9.1 - 9.2       ******************
9.2 - 9.3       *******
9.3 - 9.4       *****
9.4 - 9.5       ***********
9.5 - 9.6       ************
9.6 - 9.7       **********
9.7 - 9.8       **************
9.8 - 9.9       ************
9.9 - 10.0      *************
10.0 - 10.1     **********
10.1 - 10.2     ************
10.2 - 10.3     ************
10.3 - 10.4     ************
10.4 - 10.5     ****************
10.5 - 10.6     *********
10.6 - 10.7     *******
10.7 - 10.8     *************
10.8 - 10.9     ********
```

```
10.9 - 11.0     *******
11.0 - 11.1     *****************
11.1 - 11.2     ********
11.2 - 11.3     ***************
11.3 - 11.4     **************
11.4 - 11.5     *******
```

The first step in predicting the spectra is to draw a plausible structure, and assuming that it is rigid, determine the rotational constants. One program for determining the rotational constants is MOMIRT and is available in the group library. For the larger complexes, it is very difficult to input the structure correctly. Therefore, in some cases, the structures were simplified, under the assumption that we were only concerned with the overall line density and band structure. The structures investigated, as well as the rotational constants are given in Figure C.2. For the reader that is seriously interested in a particular cluster, it is strongly recommended that they work through the geometry required by MOMIRT themselves. The next step is then to use a second program, WANGMAIN, also available in the group. This program predicts the spectra for asymmetric rotors. Some of the stick spectra are shown in Figure C.3. A band origin or vibrational frequency of 25 cm^{-1} was arbitrarily chosen for all of these predictions. Unless otherwise noted, the excited state rotational constants are the same as the ground state constants. The Ar_2H_2O spectra show fairly high line densities. However, none of these spectra predict the very high density Q-branch seen at 780 GHz. It is possible that this is due to the overlap of several fairly dense bands. The water trimer bands, on the other hand, show a very simple band structure. A similar spectrum is anticipated for the cyclic tetramer.

One last effort taken was to use the rotational constants

Figure C.2 The $Ar_m(H_2O)_n$ structures investigated with the rotational constants given in MHz.

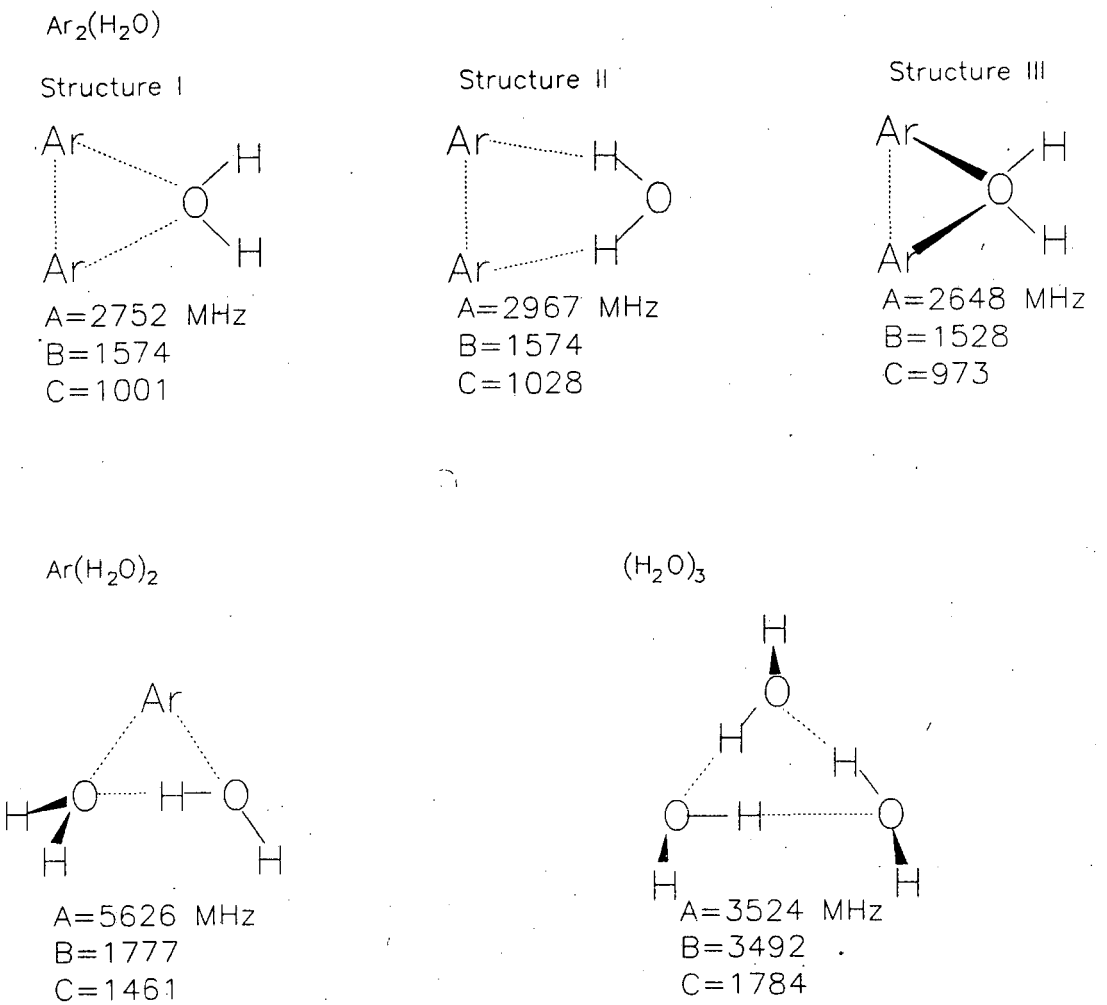

Figure C.3 Several of the predicted spectra for some of the structures given in Figure C.2. All spectra have an arbitrarily chosen band origin at 25 cm^{-1} and all spectra are predicted assuming a 1K rotational temperature. The frequency scale is given in cm^{-1}.

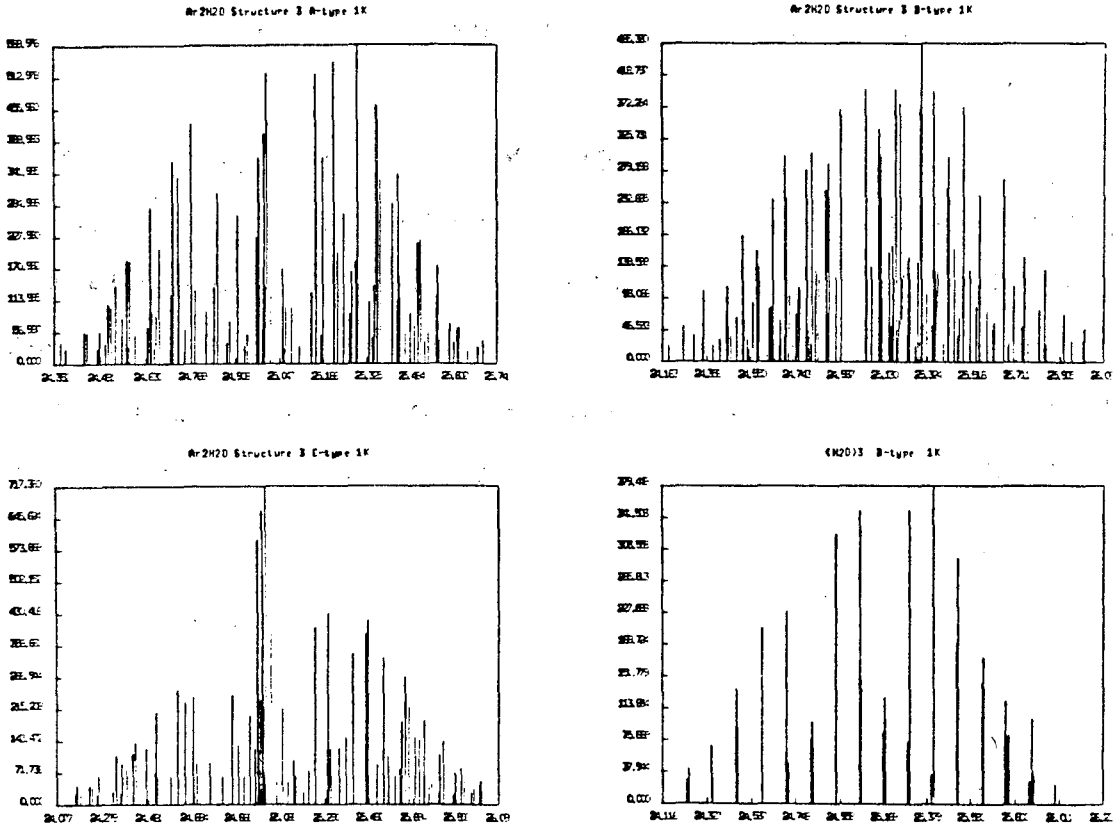

generated by MOMIRT for these various structures and search for differences in our frequency list that were roughly twice the rotational constant. This is similar to the histogram study, but we were only looking for specific differences. As could have been predicted from our previous results, the list of matches for several of the differences we tried were simply too long to be useful. The results for two of differences tried are given in Table C.3.

It is certainly very likely that many of these structures are being produced in the jet expansion, the difficulty is sorting through the many lines obtained. It may be worthwhile to scan to higher frequency to see if less dense patterns appear. We have found that the line density does drop as we go to higher frequency, so that may be the best place to start.

Table C.3 Two sets of line differences, the first lists the lines in which the difference is 3.2 ± 0.2 GHz, which is approximately 2B for the Ar_2H_2O structures. The second set lists the lines in which the difference is 7.0 ± 0.2 GHz, which is 2((A+B)/2) for $(H_2O)_3$. All frequencies are given in GHz.

I. Difference = 3.2 ± .2 GHz

Line 1	Line 2	Δ
488.4235	491.7020	3.2785
488.6670	491.7020	3.0350
490.2110	493.5660	3.3550
490.5040	493.5660	3.0620
522.6526	525.9313	3.2787
523.2807	526.6438	3.3631
523.2807	520.2526	3.0281
523.2883	526.6438	3.3555
523.2883	520.2526	3.0357
523.3349	526.6438	3.3089
523.3349	520.2526	3.0823
524.8191	527.8206	3.0015
525.9313	528.9437	3.0124
525.9313	529.2862	3.3549
526.6438	530.0223	3.3785
527.8206	531.2047	3.3841
529.2862	532.4266	3.1404
621.5249	618.3947	3.1302
632.9236	636.2037	3.2801
632.8827	636.2037	3.3210
635.2246	638.5012	3.2766
635.2246	638.5998	3.3752
642.7600	646.0293	3.2693
642.7600	646.0336	3.2736
642.9194	646.0293	3.1099
642.9194	646.0336	3.1142
730.0631	733.1874	3.1243
730.1480	733.1874	3.0394
733.1874	736.4478	3.2604
765.8022	768.8673	3.0651
765.8022	769.0847	3.2825
765.8554	768.8673	3.0119
765.8554	769.0847	3.2293
768.8673	772.0346	3.1673
776.2978	779.6083	3.3105

777.2069	780.4732	3.2663	781.7224	785.0073	3.2849
778.2040	781.3217	3.1177	781.7224	785.1043	3.3819
779.6083	782.6219	3.0136	781.7224	785.1075	3.3851
779.6083	782.8926	3.2843	781.7507	784.7931	3.0424
779.6083	782.8803	3.2720	781.7507	784.8140	3.0633
778.9701	782.1098	3.1397	781.7507	784.9313	3.1806
778.9701	782.3331	3.3630	781.7507	785.0073	3.2566
780.4732	783.4873	3.0141	781.7507	785.1043	3.3536
780.4732	783.5394	3.0662	781.7507	785.1075	3.3568
780.4732	783.7465	3.2733	781.8465	784.9613	3.0848
Line 1	Line 2	Δ	781.8465	785.0073	3.1608
781.3217	784.5758	3.2541	781.8465	785.1043	3.2578
781.3217	784.6787	3.3570	781.8465	785.1075	3.2610
781.6588	784.6787	3.0199	782.1098	785.2529	3.1431
781.6588	784.7931	3.1343	782.1098	785.3423	3.2325
781.6588	784.8140	3.1552	782.1098	785.4576	3.3478
781.6588	784.9313	3.2725	782.3331	785.3423	3.0092
781.6588	785.0073	3.3485	782.3331	785.4576	3.1245
781.6675	784.6787	3.0112	782.3331	785.5530	3.2199
781.6675	784.7931	3.1256	782.6219	785.9157	3.2938
781.6675	784.8140	3.1465	782.8926	785.9157	3.0231
781.6675	784.9313	3.2638	782.8926	786.0257	3.1331
781.6675	785.0073	3.3398	782.8926	786.0561	3.1635
781.7224	784.7931	3.0707	782.8803	785.9157	3.0354
781.7224	784.8140	3.0916	782.8803	786.0257	3.1454
781.7224	784.9313	3.2089	782.8803	786.0561	3.1758

783.7465	787.1228	3.3763
783.8973	787.1228	3.2255
783.9463	787.1228	3.1765
783.9463	787.3143	3.3680
Line 1	Line 2	Δ
784.2022	787.3143	3.1121
784.2022	787.5200	3.3178
784.2022	787.5349	3.3327
784.2037	787.3143	3.1106
784.2037	787.5200	3.3163
784.2037	787.5349	3.3312
784.2759	787.3143	3.0384
784.2759	787.5200	3.2441
784.2759	787.5349	3.2590
784.6787	788.0689	3.3902
784.7931	788.0689	3.2758
784.8140	788.0689	3.2549
784.9313	788.0689	3.1376
785.0073	788.0689	3.0616
785.3423	788.6610	3.3187
785.4576	788.6610	3.2034
785.5530	788.6610	3.1080
788.0689	791.1890	3.1201
819.2333	822.2980	3.0647
819.2333	822.3735	3.1402
820.2371	823.5452	3.3081
822.2980	825.5943	3.2963
822.3735	825.5943	3.2208
829.4856	832.6750	3.1894
829.5119	832.6750	3.1631
520.2526	517.1627	3.0899
520.2526	517.1476	3.1050
518.2614	515.1934	3.0680
518.2614	514.9106	3.3508

II. Difference = 7.0 ± 0.2 GHz

Line 1	Line2	Δ
488.4235	495.4300	7.0065
488.6670	495.6320	6.9650
490.5040	497.6060	7.1020
522.6526	529.5960	6.9434
523.2807	530.1956	6.9149
523.2807	516.1946	7.0861
523.2883	530.1956	6.9073
523.2883	516.1946	7.0937
523.3349	530.1956	6.8607
523.3349	516.1946	7.1403
527.4201	520.2526	7.1675
527.7115	520.9054	6.8061
527.8206	520.9054	6.9152
733.1874	740.0095	6.8221
772.0346	778.9701	6.9355
774.6973	781.6588	6.9615
774.6973	781.6675	6.9702
774.6973	781.7224	7.0251
774.6973	781.7507	7.0534
774.6973	781.8465	7.1492
Line 1	Line 2	Δ
774.7021	781.6588	6.9567
774.7021	781.6675	6.9654
774.7021	781.7224	7.0203
774.7021	781.7507	7.0486
774.7021	781.8465	7.1444
774.7339	781.6588	6.9249
774.7339	781.6675	6.9336
774.7339	781.7224	6.9885
774.7339	781.7507	7.0168
774.7339	781.8465	7.1126
776.2978	783.4873	7.1895
777.2069	784.2022	6.9953
777.2069	784.2037	6.9968
777.2069	784.2759	7.0690
778.2040	785.0073	6.8033
778.2040	785.1043	6.9003
778.2040	785.1075	6.9035
778.2040	785.2529	7.0489
778.2040	785.3423	7.1383
778.9701	785.9157	6.9456
Line 1	Line 2	Δ
778.9701	786.0257	7.0556
778.9701	786.0561	7.0860
780.4732	787.3143	6.8411
780.4732	787.5200	7.0468
780.4732	787.5349	7.0617

781.6588	788.6610	7.0022
781.6675	788.6610	6.9935
781.7224	788.6610	6.9386
781.7507	788.6610	6.9103
781.8465	788.6610	6.8145
784.2022	791.1890	6.9868
784.2037	791.1890	6.9853
784.2759	791.1890	6.9131
811.2123	818.0550	6.8427
822.2980	829.4856	7.1876
822.3735	829.4856	7.1121
822.3735	829.5119	7.1384
825.5943	832.4594	6.8651
825.5943	832.6750	7.0807
1000.6820	1007.5510	6.8690

LAWRENCE BERKELEY LABORATORY
UNIVERSITY OF CALIFORNIA
INFORMATION RESOURCES DEPARTMENT
BERKELEY, CALIFORNIA 94720